Cavity-enhanced quantum network nodes in diamond

Ruf, M.T.

DOI
10.4233/uuid:933b37d4-7f00-4070-becc-9c462bf9d8df

Publication date
2021

Document Version
Final published version

Citation (APA)
Ruf, M. T. (2021). *Cavity-enhanced quantum network nodes in diamond*. [Dissertation (TU Delft), Delft University of Technology]. https://doi.org/10.4233/uuid:933b37d4-7f00-4070-becc-9c462bf9d8df

Important note
To cite this publication, please use the final published version (if applicable).
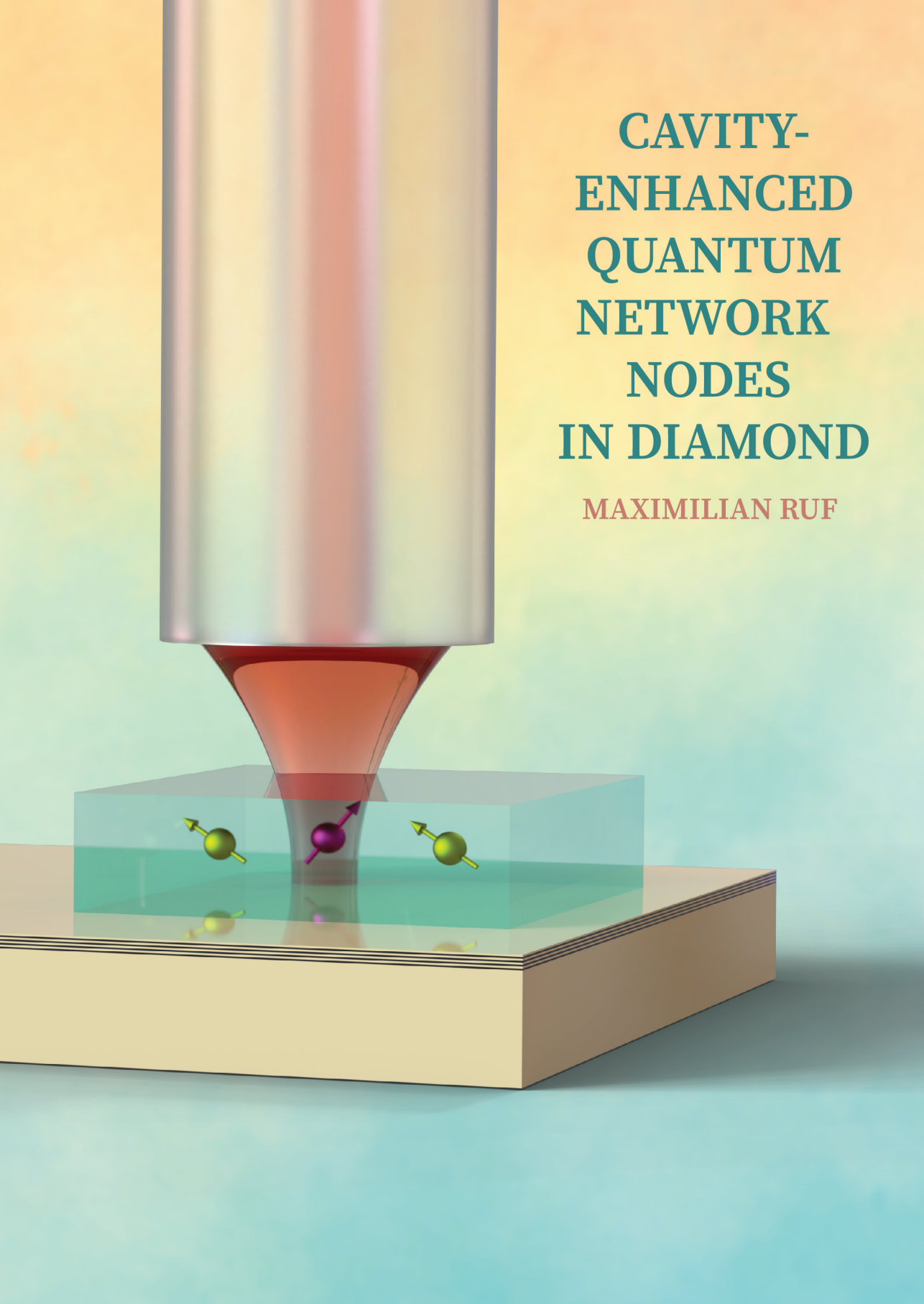Please check the document version above.

CAVITY-ENHANCED QUANTUM NETWORK NODES IN DIAMOND

MAXIMILIAN RUF

CAVITY-ENHANCED QUANTUM NETWORK NODES IN DIAMOND

CAVITY-ENHANCED QUANTUM NETWORK NODES IN DIAMOND

Dissertation

for the purpose of obtaining the degree of doctor
at Delft University of Technology,
by the authority of the Rector Magnificus Prof.dr.ir. T.H.J.J. van der Hagen,
Chair of the Board for Doctorates,
to be defended publicly on
Tuesday 21 September 2021 at 10:00 o'clock

by

Maximilian Thomas Ruf

Master of Science in Physics,
McGill University, Montreal, Canada,
born in Santa Clara, California, United States of America.

This dissertation has been approved by the promotor, Prof.dr.ir. R. Hanson.

Composition of the doctoral committee:

Rector Magnificus,	Chairperson
Prof.dr.ir. R. Hanson	Delft University of Technology, promotor
Dr.ir. T.H. Taminiau,	Delft University of Technology, copromotor

Independent members:

Prof.dr. P. Maletinsky	University of Basel, Switzerland
Prof.dr. A.F. Koenderink	AMOLF and University of Amsterdam
Prof.dr. L. DiCarlo	Delft University of Technology
Dr. M. Blaauboer	Delft University of Technology
Dr.ir. T. van der Sar	Delft University of Technology

Reserve member:

Prof.dr. W. Tittel	Delft University of Technology

CONTENTS

SUMMARY

With their ability to process and transfer quantum information, large-scale entanglement-based quantum networks could be at the heart of a new age of quantum information, enabling fundamentally new applications such as distributed quantum computation, quantum communication, and quantum enhanced sensing. Due to their long spin coherence, controllable local qubit registers and optically active spins, color centers in diamond are prime candidates for nodes of such a network, and have enabled some of the most advanced quantum network demonstrations to date. These demonstrations include the distribution of a 3-node GHZ state across a quantum network, entanglement swapping, entanglement distillation, and memory-enhanced quantum communication. To move beyond current proof-of-principle networks, a further increase of entanglement generation rates is crucial. This thesis presents theoretical and experimental work on enhancing the spin-photon interface of color centers in diamond to achieve this goal, making use of the Purcell effect. The discussed work follows two main directions: embedding of color centers in open, tuneable Fabry-Perot micro-cavities, and in all-diamond photonic crystal cavities.

First, we describe theoretical and experimental progress towards cavity-enhanced quantum networks based on nitrogen-vacancy (NV) centers in diamond. Due to their first order sensitivity to electric fields, we choose to embed NV centers in microns-thin diamond membranes that can be integrated into open fiber-based micro-cavities. We develop analytical methods to optimize the design of such open cavity systems for maximum Purcell enhancement of embedded color centers (Chapter 4). We demonstrate a method to fabricate optically coherent NV centers in microns-thin diamond membranes (Chapter 5), and use such structures to demonstrate the resonant excitation and detection of coherent, Purcell enhanced NV emission (Chapter 6). A theoretical model in excellent agreement with our results suggests our system can improve entanglement rates between distant NV centers by two orders of magnitude with near-term improvements to the setup.

Second, we describe progress towards an efficient spin-photon interface of group-IV color centers in diamond by coupling them to photonic nanostructures, allowing for large-scale integration. Due to their first-order insensitivity to electric fields, group-IV color centers can be brought in close proximity to surfaces (~ 100 nm), allowing for sub-wavelength mode volumes and thus very high Purcell factors. We numerically optimize photonic crystal cavity designs to maximize the Purcell enhancement of embedded emitters, test the robustness of our designs to real-world fabrication imperfections, and devise a method to efficiently interface nanophotonic structures (Chapter 7). We then proceed to fabricate all-diamond photonic crystal cavities, making use of a dry etching technique that is selective to different crystallographic directions, and characterize the resulting optical quality factors (Chapter 8). Finally, we marry the fabrication methods developed in Chapters 5 and 8 to fabricate microns-sized diamond platelets that can

be transferred from a holding frame in a controlled fashion (Chapter 9). This capability could be crucial for the realization of hybrid photonic circuits that we expect to be at the heart of future large-scale quantum networks (Chapter 10).

SAMENVATTING

Met hun vermogen om quantuminformatie te verwerken en over te dragen, kunnen grootschalige op verstrengeling gebaseerde quantumnetwerken de basis vormen van een nieuw tijdperk van quantuminformatie. Waarin fundamenteel nieuwe toepassingen mogelijk worden, zoals gedistribueerde quantumberekening, quantumcommunicatie en quverbeterde sensoren. Vanwege hun lange spincoherentie, de aanwezigheid van aanstuurbare lokale qubit-registers en optisch actieve spins, zijn kleurcentra in diamant de belangrijkste kandidaten voor knooppunten van een dergelijk netwerk en kleurcentra hebben enkele van de meest geavanceerde quantumnetwerkdemonstraties tot nu toe mogelijk gemaakt. Zoals onder andere de distributie van een GHZ-toestand over 3 knooppunten in een quantumnetwerk, het doorgeven van verstrengeling, verstrengelingsdestillatie en verbeterde quantumcommunicatie met behulp van een geheugenqubit. Om verder te gaan dan de huidige proof-of-principle-netwerke is een verdere toename van de snelheid waarmee verstrengeling gegenereerd kan worden cruciaal. Om dit doel te bereiken presenteert dit proefschrift theoretisch en experimenteel werk om de spin-foton-interface van kleurcentra in diamant te verbeteren, door middel van het Purcell-effect. Het besproken werk volgt twee hoofdrichtingen: het gebruik van kleurcentra in open, afstembare Fabry-Perot microholtes, en kleurcentra in volledig diamanten fotonische kristalholten.

Eerst beschrijven we theoretische en experimentele vooruitgang op het gebied van holte-versterkte quantumnetwerken op basis van het stikstofholte (NV) centrum in diamant. Vanwege hun gevoeligheid in de eerste orde voor elektrische velden, kiezen we ervoor om NV-centra in te bedden in micrometerdunne diamantmembranen die kunnen worden geïntegreerd in open microholtes op basis van glasvezelkabels. We ontwikkelen analytische methoden om het ontwerp van dergelijke open-cavity-systemen te optimaliseren voor maximale Purcell-verbetering van ingebedde kleurcentra (hoofdstuk 4). We demonstreren een methode om optisch coherente NV-centra te fabriceren in micronmeterdunne diamantmembranen (hoofdstuk 5) en gebruiken dergelijke structuren om de resonante excitatie en detectie van coherente door Purcell versterkte NV-emissie aan te tonen (hoofdstuk 6). Een theoretisch model dat uitstekend overeenkomt met onze resultaten suggereert dat ons systeem de verstrengelingspercentages tussen NV-centra op afstand met twee ordes van grootte kan verbeteren met verbeteringen aan de opstelling die op korte termijn uitgevoerd kunnen worden.

Ten tweede beschrijven we de voortgang naar een efficiënte spin-foton-interface van groep-IV-kleurcentra in diamant door ze te koppelen aan fotonische nanostructuren, waardoor grootschalige integratie mogelijk wordt. Vanwege hun ongevoeligheid in de eerste orde voor elektrische velden, kunnen kleurcentra van groep IV dicht aan de oppervlakte worden aangebracht (~ 100 nm), waardoor sub-golflengtemodusvolumes en dus zeer hoge Purcell-factoren mogelijk zijn. Met numerieke methoden optimaliseren we de ontwerpen van fotonische kristalholtes om de Purcell-verbetering van ingebedde emit-

ters te maximaliseren, testen we de robuustheid van onze ontwerpen voor fabricage-imperfecties, en bedenken we een methode om nanofotonische structuren efficiënt te koppelen (hoofdstuk 7). We gaan dan verder met het fabriceren van volledig diamanten fotonische kristalholtes, gebruikmakend van een droge etstechniek die selectief is voor verschillende kristallografische richtingen en karakteriseren de resulterende optische kwaliteitsfactoren (hoofdstuk 8). Ten slotte combineren we de fabricagemethoden die zijn ontwikkeld in de hoofdstukken 5 en 8 om micrometers grote diamanten plaatjes te fabriceren die op een gecontroleerde manier kunnen worden overgebracht van het frame waarin ze gemaakt worden naar de experimentele chips(hoofdstuk 9). Deze mogelijkheid is cruciaal voor de realisatie van hybride fotonische circuits waarvan we verwachten dat ze de basis zullen vormen van grootschalige toekomstige quantumnetwerken (hoofdstuk 10).

1

INTRODUCTION

"I think that this present century in a sense will see a great upsurge and development of this whole information business." Claude Shannon, 1959 [2]

Often termed the age of information, the 20th century has seen fundamental changes in society and economy, fueled by radically new means of communication. The rapid rise of quantum technologies over the past decades, as well as their inherent disruptive potential for information technology, suggests that we could find ourselves at yet another decisive point in history. Here, we give a brief introduction to the evolution and state of the art of quantum technologies, focusing in particular on large-scale entanglement-based quantum networks. With their ability to transfer and process quantum information, such networks could enable a suite of fundamentally new applications, from quantum communications to distributed quantum sensing and quantum computing. Thus, such quantum networks could be at the heart of a new age of quantum information.

1

1.1. THE AGE OF (QUANTUM) INFORMATION*

With the Panama-Pacific International Exposition of 1914 fast approaching, AT&T's leadership grew increasingly alarmed: it was still impossible to hold a coast-to-coast telephone call, despite the company touting it for years. The essential problem "was a satisfactory telephone repeater," recalled an AT&T senior manager from conversations with the company's chief engineer John J. Carty [2]. Whereas mechanical repeaters adequately boosted voice signals on the metro-scale, they added so much noise that signals quickly became unintelligible over longer distances. A fundamentally new repeater technology was needed. Tasked with this urgent mission, Bell Laboratories developed the "audion" trion vacuum tube, just in time for the 1914 Exposition. Over the ensuing decades, the triode made way to the transistor, copper wires yielded to optical fiber, and binary digits ("bits") became the universal language of information, transcending physical modality. Today, the world is at the cusp of the next information revolution, as quantum bits ("qubits") have become the universal units fueling a new generation of 'quantum information technologies'. And once again, an essential challenge is to develop a "satisfactory repeater" – this time, capable of relaying (but not amplifying! [3]) *quantum information* signals. This thesis focuses on quantum technology using color centers in diamond to connect quantum information among spins and photons, with the goal of realizing one such "quantum repeater".

1.2. A BRIEF INTRODUCTION TO QUANTUM TECHNOLOGY

Around the same time that Bell Laboratories rolled out the "audion" repeater to enable long-distance telephone communication, quantum theory was developed and formalized by a group of European scientists. This new quantum theory spurred many debates amongst the theory's founding fathers on its possible "ridiculous consequences", often carried out in *"Gedankenexperimenten"* (at the time, the prevailing language in quantum research was German). These thought experiments were meant to test the interpretations of quantum mechanics, and often used in debates about the correct interpretations of the theory. In fact, the founding fathers themselves thought that it would not be possible to perform most of these experiments. Schrödinger, for example, famously wrote in 1952 [4]:

> *"We never experiment with just one electron or atom or (small) molecule. In thought-experiments we sometimes assume that we do; this invariably entails ridiculous consequences."*

Less than a century later we find ourselves in a situation in which many of these thought experiments can be routinely tested in the lab [5]. One famous example is the contradiction of the Einstein–Podolsky–Rosen paradox [6] via loophole-free "Bell tests", independently reported for the first time by three research groups in 2015 [7–9]. In their 1935 paper, Podolsky, Einstein and Rosen argued that the principles of entanglement violated the theory of relativity, as it would allow faster-than-light communication. From this, they concluded that quantum theory in its current form could not be considered complete, and needed some local "hidden" variables (i. e. variables that are not contained in the formulation of quantum theory) to explain the results. In 1964, John Bell

devised a quantifiable test of the existence of such hidden variables in the form of an equality [10], and the results in 2015 demonstrated that such local hidden variables do not exist.

The past decades have seen a rapid progression from laboratory-scale experiments aimed at understanding nature, confirming the predictions of quantum mechanics, and experimentally testing thought experiments, to harnessing the powers of quantum theory for technologies with real-world applications. The technologies that are currently being developed can be loosely grouped in three main categories:

1. **Quantum sensing:** A broad class of quantum technologies can be grouped under the term of quantum sensing. While there exist different flavors of quantum sensing [11], it is most commonly defined as exploiting quantum systems to measure physical properties, sometimes in combination with quantum entanglement to increase sensitivity beyond classical limits [12, 13]. Typically measured properties include magnetic and electric fields, accelerations, forces and displacements [11], and some of the most sensitive and commonly used sensing devices, such as superconducting quantum interference device (SQUID) magnetometers [14] and optical atomic clocks that can serve as the global time standard [15] are based on quantum sensing techniques. Recently, it has been demonstrated that color centers in diamond, such as the nitrogen-vacancy center, can be used to non-invasively image the action potential of single neurons in live worms [16], and resolve the spatial composition of a coupled spin system in their surroundings with atomic scale resolution [17], paving the way towards imaging and inferring the structure of single molecules [18].

2. **Quantum computing**: Around the year 1980, scientists started to realize that the exponentially-growing state space of quantum mechanical systems would pose a fundamental limitation on their ability to simulate quantum mechanical systems with classical computers [19]. As Feynman famously noted in 1981 [20]:

   > *"Nature isn't classical, dammit, and if you want to make a simulation of Nature, you'd better make it quantum mechanical, and by golly it's a wonderful problem because it doesn't look so easy."*

   In the 1990's, around 90 years after the refinement of the "audion", it was again at AT&T's Bell labs that two of the most influential quantum algorithms that offer a speed-up over their classical counterparts were developed: Grover's algorithm [21] to search a large unstructured database with a quadratic speedup[1], and Shor's algorithm [22] to factor large numbers into their prime factors in polynomial time, in contrast to an exponential runtime on classical computers. While Shor's algorithm led to tremendous interest in quantum research due to its practical implications for information security[2], building a universal quantum machine was

---

[1] Although applicable to a wide range of problems in computer science that use exhaustive search, the problem was not by coincidence formulated in terms of finding someone's phone number in a large phone directory.

[2] Current communication protocols are based on RSA encryption [23], which exploits the computational hardness of factoring prime numbers on classical computers

1

thought to be impossible due to quantum decoherence [24]. It was not until another invention by Shor, a quantum error correction code that could overcome the fragile nature of quantum states [25], that the consensus view changed. Indeed, shortly after, it was demonstrated (yet again by Shor!) that building a fault-tolerant quantum computer, i. e. a quantum computer resilient to both decoherence and faulty quantum gates themselves, could be feasible [26]. These developments led to a large influx of resources — both financial and human — aimed at experimentally demonstrating these protocols, recently culminating in hallmark experiments showing the first demonstrations of quantum algorithms that can not be simulated with the best available supercomputers [27–29], developing what currently is an industry with yearly investments of billions of dollars [30]. While reaching this "quantum supremacy" threshold signals an important milestone on the path towards real-world quantum computation, these experiments are performed for carefully chosen algorithms that are hard to simulate on classical machines, and are of no explicit practical use. We expect the next years to see rapid developments on several fronts, including quantum computing hardware [31, 32], quantum algorithms [33], as well as the further development of end user platforms that allow accessing different quantum hardware in the cloud [34–36]. We also note that the last years have seen tremendous progress in the field of analog quantum simulators on various platforms [37–41]. In contrast to the universal quantum computers described above, these systems can simulate a subset of problems that can be mapped to the system's specific Hamiltonian. Here, the problems studied are typically restricted to ones that are robust to disturbance from noisy operations [19]. Thus, while analog quantum simulations are currently a powerful tool, they might be replaced in the future by universal, fault-tolerant quantum computers.

3. **Quantum communication**: Around the year 1970, Stephen Wiesner designed a protocol that — despite being practically infeasible — can be seen as the beginnings of the field of quantum cryptography [42]. His idea was to exploit Heisenberg's uncertainty principle to design unforgeable bank notes, by storing photons with a certain polarization in each bank note. Using two conjugate bases of polarization encoding (chosen randomly with 50% probability), a person without knowledge of this encoding would inevitably induce an error in a quarter of cases when trying to obtain information about the photons polarization. Thus, if the bank has a register in which all serial notes of bank notes together with the corresponding photon polarizations are stored, they can at any time verify the authenticity of bank notes, while any attempt of copying the money can be detected. Initially, this was of little practical interest, and Wiesner's work remained unpublished until 1983 [43]. As Charles Bennett later noted [42]:

> *"Initially, quantum cryptography was thought of by everyone (including ourselves) mostly as a work of science-fiction, because the technology required to implement it was out of reach (for instance, quantum bank notes [43] require the ability to store a single polarized photon or spin half particle for days without significant absorption or loss of polarization). [...] The main breakthrough came when we realized that photons were never meant to <u>store</u> information, but rather to <u>transmit</u> it [...]."*

Indeed, in 1984, Charles Bennett and Gilles Brassard published the BB84 protocol, which used the idea of two conjugate bases to encode information. By sending photons from an information encoder (sender) to a decoder that measures the photons randomly in the two bases (reciever), and using an authenticated classical communication channel to compare bases and measurement results, the amount of information an evesdropper could have gained about the information sent can be inferred [44], and a secure key can be shared. Importantly, as it is not possible to create a perfect copy of a quantum state (known as the no cloning theorem [3]), this key is thus secured by the laws of nature. It was not long after, in 1989, that the experimental feasibility of this protocol was demonstrated [42, 45]. Soon after, another important class of quantum key distribution protocol that exploits the monogamy of entanglement to secure communication was formulated [46], and many more protocols based on these principles have followed since [47]. The last years have seen the first demonstrations of *trusted* repeater networks[3], and today there are several companies that offer quantum key distribution as a commercial service [48, 49]. Current research is focused on extending the functionality and security of these networks beyond trusted repeater networks focused on quantum key distribution, to networks in which entangled states are distributed between the parties at high rates. As discussed in the following section, the realization of a large-scale entanglement-based quantum network shows promise to combine all three quantum technologies in one physical platform [50].

1.3. A BRIEF INTRODUCTION TO QUANTUM NETWORKS*

In a future quantum network (see Fig. 1.1), remote parties are connected by sharing long-lived entangled states [50, 51]. Arguably, the most promising way of linking distant nodes is to employ fiber- or free-space photonic communication channels to establish entanglement. While all photon-based schemes are associated with losses that scale with distance [52], motivating the need for quantum repeaters [53], heralding entanglement generation on successful photon transmission events maps these losses into reduced entanglement generation rates without lowering entanglement fidelities [54–56].

Optically-mediated remote entanglement of individually controllable qubits has been generated for different materials platforms, including quantum dots [57, 58], trapped ions [59–61], neutral atoms [62–65], and nitrogen-vacancy centers in diamond [7, 66]. Other promising systems, including so-called group-IV defects in diamond [67–70], defects in SiC [71–75], and rare-earth ions in solid-state hosts [76–78], show great potential for quantum network applications, although remote entanglement has not yet been generated. Another less explored approach is to link distant superconducting quantum processors using coherent conversion of microwave photons to telecom frequencies [79–83].

Apart from fundamental tests of physics [7], small-scale quantum networks have been used to demonstrate key network protocols such as non-local quantum gates [64], entanglement distillation [84], and very recently entanglement swapping [85]. These

---

[3]In this scenario, the two commuting parties have to trust middle stations in between them. These stations are required to achieve sufficient communication rates due to exponential photon losses in fiber with transmission distance (see below).
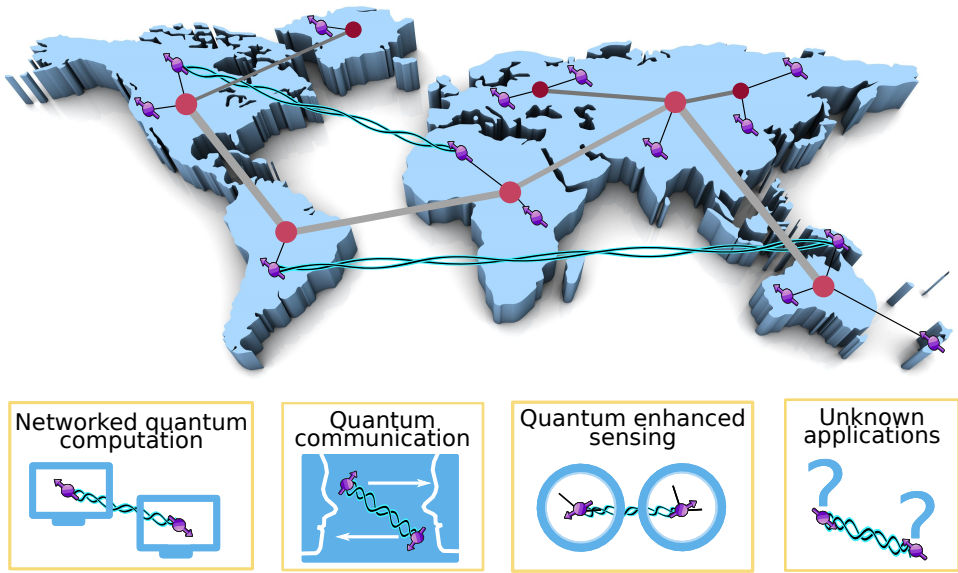
Figure 1.1: Schematic overview of a future large-scale quantum network, consisting of nodes containing optically interfaced qubits (purple) with long coherence times. Photons routed via optical fibers or free-space channels serve as mediators to create entanglement (blue wiggled lines). Local area and trunk backbone quantum repeaters (dark and light red circles, respectively) are used to enable a high entanglement generation rate over large distances, overcoming photon transmission loss. The entanglement generation is heralded, meaning that detection of certain photon statistics signals the successful generation of an entangled state that is available to a network user for further processing and applications such as networked quantum computation, quantum secured communication, quantum enhanced sensing, and potential not yet discovered tasks.

networks are currently limited to a few nodes [85], distances of up to one kilometer [7], and entanglement generation rates in the Hz to kHz regime [7, 57–63, 66]. A major challenge for the coming decade is to transition from the current proof-of-principle experiments to large-scale quantum networks for use in fields such as distributed quantum computation [86, 87], quantum enhanced sensing [12, 13], and quantum secure communication [47].

1.4. REQUIREMENTS FOR A QUANTUM NETWORK NODE*

To make a material platform suitable for a node in a quantum network in which entanglement is mediated by photons, it has to fulfill three main requirements [50]. First, the capability to interface at least one qubit efficiently with optical photons (at telecommunication wavelengths for fiber-based systems), to establish remote entanglement at high rates. Second, the ability to store quantum states during entanglement generation; in particular, this requires qubit coherence times under full network activity to be longer than the time it takes to generate entanglement between nodes. Third, the capability to store several entangled states per node with a capability for high-fidelity operations between them, to enable multi-qubit protocols such as error correction.

Color centers in diamond satisfy most of these requirements, and have enabled some
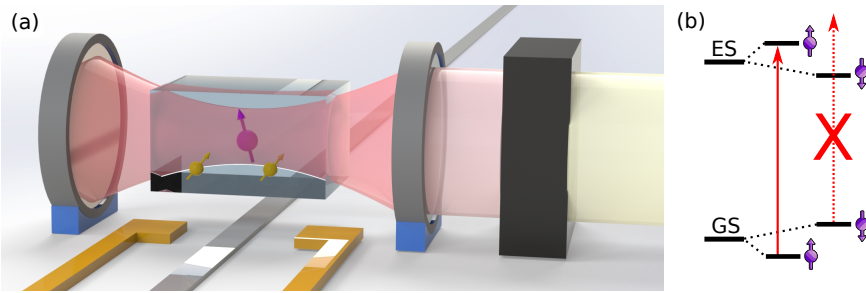
Figure 1.2: Overview of a quantum network node based on color centers in diamond and simplified optical level scheme. (a) Schematic of a quantum network node in diamond, consisting of an optically-active (communication) qubit (purple) embedded between two highly reflective mirrors (an optical cavity) to enhance the interaction strength of photons with the qubit. The state of the color center qubit can be swapped onto long-lived nuclear spin (memory) qubits in the surroundings (orange) using high fidelity gates that employ microwave or RF pulses delivered via dedicated lines (gray). Tuning of network nodes to an optimal frequency operation point is e.g. enabled by applying a static electric field via electrodes (yellow). Frequency-conversion (black box) can be used to down-convert photons entangled with the state of the communication qubit to telecommunication wavelengths, for which photon transmission losses are low. The color center features spin-resolved optical transitions between an optical ground (GS) and excited state (ES), enabling optically-mediated remote entanglement generation (b).

of the most advanced experimental demonstrations of quantum network protocols to date. We here give a concise, high level overview of the achieved and projected key capabilities of color centers in diamond [see Fig. 1.2(a)], motivating a detailed treatment (and also including the relevant literature) in the remainder of this thesis:

1. The color center contains an individually controllable, optically active spin (communication qubit), with access to several long-lived nuclear spins (memory qubits) in its surrounding. These memory qubits can be manipulated with high fidelity to free up the communication qubit and enable multi-qubit protocols. They have a long coherence time enabling robust state storage during subsequent network activity.

2. The internal level structure is suited to generate remote entanglement. In particular, color centers feature spin-state-selective optical transitions that can entangle the color center's spin state with a photonic state, e.g. in the number / polarization / time basis [see Fig. 1.2(b)].

3. Optical emission of color centers is bright and can be collected with high efficiency, enabling high entanglement generation rates. This emission is in the visible to near-IR spectrum, and thus at wavelengths that are associated with higher fiber transmission losses than for photons in the telecom band. However, it is possible to efficiently convert this emission to the telecom band while maintaining quantum correlations.

4. Diamond is a solid-state material, potentially enabling nanophotonic device fabrication at a large scale. Such devices can also be integrated with photonic cir-

1

cuits, and efficient interfacing of color centers embedded in such systems has been demonstrated.

1.5. THESIS OVERVIEW

This thesis presents theoretical and experimental progress on enhancing the spin-photon interface of color centers in diamond for a quantum network, and is organized as follows:

- Chapter 2 gives a brief introduction to properties of NV centers at cryogenic temperatures, focusing in particular on their spin-photon interface. We discuss different schemes that have been used to generate remote entanglement between NV centers, and give an overview to the state of the art of NV-based quantum networks. Current limits to entanglement rates and possibilities for improvement are introduced.

- Chapter 3 describes the theory behind one such improvement method, namely enhancing the spin-photon interface efficiency by embedding NV centers in an optical cavity, making use of the Purcell effect.

- In chapter 4, we develop analytical methods to optimize the design of fiber-based open micro-cavities. These methods are then used to find experimentally feasible parameter values that maximize Purcell enhancement in such cavities.

- Chapter 5 develops a method to fabricate microns-thin diamond membranes that contain NV centers with bulk-like optical coherence.

- Similar devices are used in chapter 6 to demonstrate resonant excitation and detection of coherently emitted photons, Purcell enhanced by an optical cavity. A theoretical model shows excellent agreement with the results and suggests that our system can improve entanglement generation rates between distant NV centers by two orders of magnitude using near-term improvements to the setup.

- Chapter 7 motivates the development of all-diamond photonic crystal cavities as a tool for realizing efficient spin-photon interfaces for group-IV color centers in diamond. We discuss the differences between group-IV color centers in diamond and NV centers, and describe the theory, design, and optimization of photonic crystal cavities for highest Purcell enhancement. We evaluate the robustness of our design to real-world fabrication imperfections, and devise a method to efficiently interface these structures using tapered optical fibers.

- Chapter 8 presents a process flow to fabricate such cavities. We characterize the resulting photonic crystal cavities, and outline a path for further improvements of these systems.

- Chapter 9 focuses on the fabrication of diamond "platelets" as next-generation diamond devices for open cavities. These small, thin diamond rectangles are attached to a diamond frame, fabricated by marrying the methods developed in chapters 5 and 8, and can be positioned and bonded on a mirror with microns-scale accuracy using a micromanipulator.

- Finally, chapter 10 summarizes the results obtained in this thesis and discusses future avenues and challenges on the path towards a large-scale entanglement-based quantum network using color centers in diamond.

1

REFERENCES

[1] M. Ruf, N. H. Wan, H. Choi, D. Englund and R. Hanson, *Quantum networks based on color centers in diamond,* Journal of Applied Physics **130**, 070901 (2021).

[2] J. Gertner, *The Idea Factory* (Penguin, New York, 2012).

[3] J. L. Park, *The concept of transition in quantum mechanics,* Foundations of Physics **1**, 23 (1970).

[4] E. Schrödinger, *Are there quantum jumps?* The British Journal for the Philosophy of Science **3**, 233 (1952).

[5] I. Georgescu, *Nobel Prize 2012: Haroche and Wineland,* Nature Physics **8**, 777 (2012).

[6] A. Einstein, B. Podolsky and N. Rosen, *Can Quantum-Mechanical Description of Physical Reality Be Considered Complete?* Physical Review **47**, 777 (1935).

[7] B. Hensen *et al.*, *Loophole-free Bell inequality violation using electron spins separated by 1.3 kilometres,* Nature **526**, 682 (2015).

[8] M. Giustina *et al.*, *Significant-Loophole-Free Test of Bell's Theorem with Entangled Photons,* Physical Review Letters **115**, 250401 (2015).

[9] L. K. Shalm *et al.*, *Strong Loophole-Free Test of Local Realism,* Physical Review Letters **115**, 250402 (2015).

[10] J. S. Bell, *The Einstein Podolsky Rosen Paradox and Local Hidden—Variables Theories,* Physics **1**, 195 (1964).

[11] C. L. Degen, F. Reinhard and P. Cappellaro, *Quantum sensing,* Reviews of Modern Physics **89**, 035002 (2017).

[12] D. Gottesman, T. Jennewein and S. Croke, *Longer-baseline telescopes using quantum repeaters,* Physical Review Letters **109**, 1 (2012).

[13] P. Kómár, E. M. Kessler, M. Bishof, L. Jiang, A. S. Sørensen, J. Ye and M. D. Lukin, *A quantum network of clocks,* Nature Physics **10**, 582 (2014).

[14] R. C. Jaklevic, J. Lambe, J. E. Mercereau and A. H. Silver, *Macroscopic Quantum Interference in Superconductors,* Physical Review **140**, A1628 (1965).

[15] K. Beloy *et al.*, *Frequency ratio measurements at 18-digit accuracy using an optical clock network,* Nature **591**, 564 (2021).

[16] F. Barry *et al.*, *Optical magnetic detection of single-neuron action potentials using quantum defects in diamond,* Proceedings of the National Academy of Sciences **114**, E6730 (2017).

[17] M. H. Abobeih, J. Randall, C. E. Bradley, H. P. Bartling, M. A. Bakker, M. J. Degen, M. Markham, D. J. Twitchen and T. H. Taminiau, *Atomic-scale imaging of a 27-nuclear-spin cluster using a quantum sensor,* Nature **576**, 411 (2019).

[18] I. Lovchinsky *et al.*, *Magnetic resonance spectroscopy of an atomically thin material using a single-spin qubit,* Science **355**, 503 (2017).

[19] J. Preskill, *Quantum computing 40 years later,* arXiv preprint (2021), arXiv:2106.10522 .

[20] R. P. Feynman, *Simulating physics with computers,* International Journal of Theoretical Physics **21**, 467 (1982).

[21] L. K. Grover, *A fast quantum mechanical algorithm for database search,* in *Proceedings of the twenty-eighth annual ACM symposium on Theory of computing,* Vol. 41 (ACM Press, New York, New York, USA, 1996) pp. 212–219.

[22] P. Shor, *Algorithms for quantum computation: discrete logarithms and factoring,* in *Proceedings 35th Annual Symposium on Foundations of Computer Science* (IEEE Comput. Soc. Press, 1994) pp. 124–134.

[23] R. Rivest, A. Shamir and L. Adleman, *Cryptographic communications system and method,* U.S. Patent 4405829 (1977).

[24] S. Haroche and J. Raimond, *Quantum Computing: Dream or Nightmare?* Physics Today **49**, 51 (1996).

[25] P. W. Shor, *Scheme for reducing decoherence in quantum computer memory,* Physical Review A **52**, R2493 (1995).

[26] P. W. Shor, *Fault-tolerant quantum computation,* Annual Symposium on Foundations of Computer Science - Proceedings , 56 (1996).

[27] F. Arute *et al.*, *Quantum supremacy using a programmable superconducting processor,* Nature **574**, 505 (2019).

[28] H. S. Zhong *et al.*, *Quantum computational advantage using photons,* Science **370**, 1460 (2021).

[29] Y. Wu *et al.*, *Strong quantum computational advantage using a superconducting quantum processor,* arXiv preprint (2021), arXiv:2106.14734 .

[30] McKinsey, *McKinsey Quantum Computing Monitor,* (2020).

[31] M. McEwen *et al.*, *Resolving catastrophic error bursts from cosmic rays in large arrays of superconducting qubits,* arXiv preprint (2021), arXiv:2104.05219 .

[32] K. C. Chen, E. Bersin and D. Englund, *A polarization encoded photon-to-spin interface,* npj Quantum Information **7**, 1 (2021).

1

[33] A. Montanaro, *Quantum algorithms: An overview,* npj Quantum Information **2**, 1 (2016).

[34] Microsoft, *Azure Quantum, retrieved 2021-07-15,* (2021).

[35] Google, *Google Quantum Computing Service, retrieved 2021-07-15,* (2021).

[36] Amazon Web Services, *Amazon Braket, retrieved 2021-07-15,* (2021).

[37] M. Greiner, O. Mandel, T. Rom, A. Altmeyer, A. Widera, T. Hänsch and I. Bloch, *Quantum phase transition from a superfluid to a Mott insulator in an ultracold gas of atoms,* Physica B: Condensed Matter **329-333**, 11 (2003).

[38] J. Zhang, G. Pagano, P. W. Hess, A. Kyprianidis, P. Becker, H. Kaplan, A. V. Gorshkov, Z.-X. Gong and C. Monroe, *Observation of a many-body dynamical phase transition with a 53-qubit quantum simulator,* Nature **551**, 601 (2017).

[39] H. Bernien, S. Schwartz, A. Keesling, H. Levine, A. Omran, H. Pichler, S. Choi, A. S. Zibrov, M. Endres, M. Greiner, V. Vuletić and M. D. Lukin, *Probing many-body dynamics on a 51-atom quantum simulator,* Nature **551**, 579 (2017).

[40] S. Ebadi *et al.*, *Quantum phases of matter on a 256-atom programmable quantum simulator,* Nature **595**, 227 (2021).

[41] J. Randall, C. E. Bradley, F. V. van der Gronden, A. Galicia, M. H. Abobeih, M. Markham, D. J. Twitchen, F. Machado, N. Y. Yao and T. H. Taminiau, *Observation of a many-body-localized discrete time crystal with a programmable spin-based quantum simulator,* arXiv preprint (2021), arXiv:2107.00736 .

[42] C. H. Bennett, F. Bessette, G. Brassard, L. Salvail and J. Smolin, *Experimental quantum cryptography,* Journal of Cryptology **5**, 3 (1992).

[43] S. Wiesner, *Conjugate coding,* ACM SIGACT News **15**, 78 (1983).

[44] C. H. Bennett and G. Brassard, *Quantum cryptography: Public key distribution and coin tossing,* Theoretical Computer Science **560**, 7 (2014).

[45] C. H. Bennett and G. Brassard, *Experimental quantum cryptography: the dawn of a new era for quantum cryptography: the experimental prototype is working],* ACM SIGACT News **20**, 78 (1989).

[46] A. K. Ekert, *Quantum Cryptography and Bell's Theorem* (Springer, New York, 1992) pp. 412–416.

[47] A. Ekert and R. Renner, *The ultimate physical limits of privacy,* Nature **507**, 443 (2014).

[48] E. Diamanti, H.-K. Lo, B. Qi and Z. Yuan, *Practical challenges in quantum key distribution,* npj Quantum Information **2**, 16025 (2016).

[49] F. Xu, X. Ma, Q. Zhang, H.-K. Lo and J.-W. Pan, *Secure quantum key distribution with realistic devices,* Reviews of Modern Physics **92**, 025002 (2020).

[50] S. Wehner, D. Elkouss and R. Hanson, *Quantum internet : A vision for the road ahead,* Science **362**, 303 (2018).

[51] H. J. Kimble, *The quantum internet,* Nature **453**, 1023 (2008).

[52] S. Pirandola, R. Laurenza, C. Ottaviani and L. Banchi, *Fundamental limits of repeaterless quantum communications,* Nature Communications **8**, 1 (2017).

[53] H.-J. Briegel, W. Dür, J. I. Cirac and P. Zoller, *Quantum Repeaters: The Role of Imperfect Local Operations in Quantum Communication,* Physical Review Letters **81**, 5932 (1998).

[54] C. Cabrillo, J. I. Cirac, P. García-Fernández and P. Zoller, *Creation of entangled states of distant atoms by interference,* Physical Review A **59**, 1025 (1999).

[55] S. D. Barrett and P. Kok, *Efficient high-fidelity quantum computation using matter qubits and linear optics,* Physical Review A **71**, 060310 (2005).

[56] L. M. Duan and H. J. Kimble, *Scalable photonic quantum computation through cavity-assisted interactions,* Physical Review Letters **92**, 1 (2004).

[57] A. Delteil, Z. Sun, W. B. Gao, E. Togan, S. Faelt and A. Imamoglu, *Generation of heralded entanglement between distant hole spins,* Nature Physics **12**, 218 (2016).

[58] R. Stockill, M. J. Stanley, L. Huthmacher, E. Clarke, M. Hugues, A. J. Miller, C. Matthiesen, C. Le Gall and M. Atatüre, *Phase-Tuned Entangled State Generation between Distant Spin Qubits,* Physical Review Letters **119**, 1 (2017).

[59] D. L. Moehring, P. Maunz, S. Olmschenk, K. C. Younge, D. N. Matsukevich, L. M. Duan and C. Monroe, *Entanglement of single-atom quantum bits at a distance,* Nature **449**, 68 (2007).

[60] D. Hucul, I. V. Inlek, G. Vittorini, C. Crocker, S. Debnath, S. M. Clark and C. Monroe, *Modular entanglement of atomic qubits using photons and phonons,* Nature Physics **11**, 37 (2015).

[61] L. J. Stephenson, D. P. Nadlinger, B. C. Nichol, S. An, P. Drmota, T. G. Ballance, K. Thirumalai, J. F. Goodwin, D. M. Lucas and C. J. Ballance, *High-Rate, High-Fidelity Entanglement of Qubits Across an Elementary Quantum Network,* Physical Review Letters **124**, 1 (2020).

[62] S. Ritter, C. Nölleke, C. Hahn, A. Reiserer, A. Neuzner, M. Uphoff, M. Mücke, E. Figueroa, J. Bochmann and G. Rempe, *An elementary quantum network of single atoms in optical cavities,* Nature **484**, 195 (2012).

[63] J. Hofmann, M. Krug, N. Ortegel, L. Gérard, M. Weber, W. Rosenfeld and H. Weinfurter, *Heralded Entanglement Between Widely Separated Atoms,* Science **337**, 72 (2012).

[64] S. Daiss, S. Langenfeld, S. Welte, E. Distante, P. Thomas, L. Hartung, O. Morin and G. Rempe, *A quantum-logic gate between distant quantum-network modules,* Science **371**, 614 (2021).

[65] S. Langenfeld, S. Welte, L. Hartung, S. Daiss, P. Thomas, O. Morin, E. Distante and G. Rempe, *Quantum Teleportation between Remote Qubit Memories with Only a Single Photon as a Resource,* Physical Review Letters **126**, 130502 (2021).

[66] H. Bernien, B. Hensen, W. Pfaff, G. Koolstra, M. S. Blok, L. Robledo, T. H. Taminiau, M. Markham, D. J. Twitchen, L. Childress and R. Hanson, *Heralded entanglement between solid-state qubits separated by three metres,* Nature **497**, 86 (2013).

[67] M. K. Bhaskar *et al.*, *Quantum Nonlinear Optics with a Germanium-Vacancy Color Center in a Nanoscale Diamond Waveguide,* Physical Review Letters **118**, 223603 (2017).

[68] C. T. Nguyen, D. D. Sukachev, M. K. Bhaskar, B. Machielse, D. S. Levonian, E. N. Knall, P. Stroganov, R. Riedinger, H. Park, M. Lončar and M. D. Lukin, *Quantum Network Nodes Based on Diamond Qubits with an Efficient Nanophotonic Interface,* Physical Review Letters **123**, 1 (2019).

[69] M. K. Bhaskar, R. Riedinger, B. Machielse, D. S. Levonian, C. T. Nguyen, E. N. Knall, H. Park, D. Englund, M. Lončar, D. D. Sukachev and M. D. Lukin, *Experimental demonstration of memory-enhanced quantum communication,* Nature **580**, 60 (2020).

[70] M. E. Trusheim *et al.*, *Transform-Limited Photons from a Coherent Tin-Vacancy Spin in Diamond,* Physical Review Letters **124**, 1 (2020).

[71] S. A. Zargaleh, S. Hameau, B. Eble, F. Margaillan, H. J. von Bardeleben, J. L. Cantin and W. Gao, *Nitrogen vacancy center in cubic silicon carbide: A promising qubit in the 1.5 um spectral range for photonic quantum networks,* Physical Review B **98**, 165203 (2018).

[72] R. Nagy *et al.*, *High-fidelity spin and optical control of single silicon-vacancy centres in silicon carbide,* Nature Communications **10**, 1954 (2019).

[73] A. Bourassa, C. P. Anderson, K. C. Miao, M. Onizhuk, H. Ma, A. L. Crook, H. Abe, J. Ul-Hassan, T. Ohshima, N. T. Son, G. Galli and D. D. Awschalom, *Entanglement and control of single nuclear spins in isotopically engineered silicon carbide,* Nature Materials **19**, 1319 (2020).

[74] D. M. Lukin, M. A. Guidry and J. Vučković, *Integrated Quantum Photonics with Silicon Carbide: Challenges and Prospects,* PRX Quantum **1**, 020102 (2020).

[75] J.-F. Wang *et al.*, *Coherent Control of Nitrogen-Vacancy Center Spins in Silicon Carbide at Room Temperature,* Physical Review Letters **124**, 223601 (2020).

[76] M. Raha, S. Chen, C. M. Phenicie, S. Ourari, A. M. Dibos and J. D. Thompson, *Optical quantum nondemolition measurement of a single rare earth ion qubit,* Nature Communications **11**, 1 (2020).

[77] J. M. Kindem, A. Ruskuc, J. G. Bartholomew, J. Rochman, Y. Q. Huan and A. Faraon, *Control and single-shot readout of an ion embedded in a nanophotonic cavity,* Nature **580**, 201 (2020).

[78] B. Merkel, A. Ulanowski and A. Reiserer, *Coherent and Purcell-Enhanced Emission from Erbium Dopants in a Cryogenic High-Q Resonator,* Physical Review X **10**, 041025 (2020).

[79] Y. Chu and S. Gröblacher, *A perspective on hybrid quantum opto- and electromechanical systems,* Applied Physics Letters **117**, 150503 (2020).

[80] M. Mirhosseini, A. Sipahigil, M. Kalaee and O. Painter, *Superconducting qubit to optical photon transduction,* Nature **588**, 599 (2020).

[81] M. Forsch, R. Stockill, A. Wallucks, I. Marinković, C. Gärtner, R. A. Norte, F. van Otten, A. Fiore, K. Srinivasan and S. Gröblacher, *Microwave-to-optics conversion using a mechanical oscillator in its quantum ground state,* Nature Physics **16**, 69 (2020).

[82] W. Hease, A. Rueda, R. Sahu, M. Wulf, G. Arnold, H. G. Schwefel and J. M. Fink, *Bidirectional Electro-Optic Wavelength Conversion in the Quantum Ground State,* PRX Quantum **1**, 1 (2020).

[83] S. Krastanov, H. Raniwala, J. Holzgrafe, K. Jacobs, M. Lončar, M. J. Reagor and D. R. Englund, *Optically Heralded Entanglement of Superconducting Systems in Quantum Networks,* Physical Review Letters **127**, 040503 (2021).

[84] N. Kalb, A. A. Reiserer, P. C. Humphreys, J. J. Bakermans, S. J. Kamerling, N. H. Nickerson, S. C. Benjamin, D. J. Twitchen, M. Markham and R. Hanson, *Entanglement distillation between solid-state quantum network nodes,* Science **356**, 928 (2017).

[85] M. Pompili, S. L. N. Hermans, S. Baier, H. K. C. Beukers, P. C. Humphreys, R. N. Schouten, R. F. L. Vermeulen, M. J. Tiggelman, L. dos Santos Martins, B. Dirkse, S. Wehner and R. Hanson, *Realization of a multinode quantum network of remote solid-state qubits,* Science **372**, 259 (2021).

[86] N. H. Nickerson, J. F. Fitzsimons and S. C. Benjamin, *Freely scalable quantum technologies using cells of 5-to-50 qubits with very lossy and noisy photonic links,* Physical Review X **4**, 1 (2014).

[87] H. Choi, M. Pant, S. Guha and D. Englund, *Percolation-based architecture for cluster state creation using photon-mediated entanglement between atomic memories,* npj Quantum Information **5**, 104 (2019).

2

THE NITROGEN-VACANCY (NV) CENTER IN DIAMOND AS A QUANTUM NETWORK NODE

The nitrogen-vacancy (NV) center is a color center in diamond that is a promising node candidate for future quantum networks, as it combines excellent spin coherence properties, spin-conserving optical transitions, and extensive control capabilities over nearby carbon nuclear spins with long coherence times. Here, we give a brief introduction to the electronic level structure of the negative charge state of the NV center, discuss its creation mechanisms, and explore the origins for the small emission fraction of photons in the zero phonon line (ZPL). We compare different entanglement generation protocols for NV centers, outline the state of the art of NV-based quantum networks, and establish current limitations to entanglement generation rates. Finally, we propose solutions to overcome the current constraints in entanglement rates, setting the stage for the work discussed in this thesis.
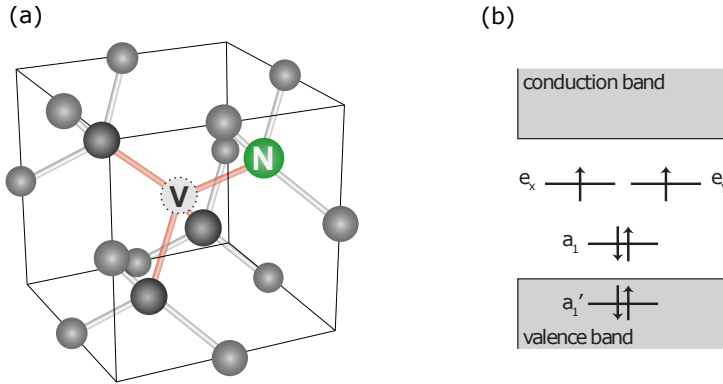
Figure 2.1: The nitrogen-vacancy (NV) center in diamond. (a) Crystallographic structure of a diamond lattice unit cell containing an NV center, consisting of a substitutional nitrogen atom, N, and a neighbouring lattice vacancy, V. Carbon atoms that contribute electrons to the NV complex via dangling bonds are shaded in dark gray. The resulting NV complex has C_{3v} symmetry (NV axis along the [111] crystallographic direction). (b) Molecular orbitals (MO) and their electron occupation for the ground state of the NV center, following from Pauli's exclusion principle; symmetry of the MOs is indicated by the labels. Fig. (b) from Pfaff, Bernien [6, 7].

2.1. THE NITROGEN-VACANCY (NV) CENTER IN DIAMOND

The nitrogen-vacancy (NV) center in diamond is an atomic point defect in the diamond lattice, for which two neighbouring carbon atoms of the diamond lattice are replaced with a nitrogen atom, and a vacant lattice site, see Fig. 2.1(a). In the neutral charge state (discussed in Refs. [1–3]), the resulting system is comprised of five electrons, resulting from dangling bonds: two from the nitrogen atom, and three from the carbon atoms surrounding the vacancy. In this work, we are solely concerned with the negative charge state of the defect, for which an additional electron from a charge donor in the environment is added to the defect; unless stated explicitly otherwise, we will we will refer to the negative charge state NV center simply as "the" nitrogen-vacancy (NV) center. In this chapter, we give a brief introduction to the most important aspects of the NV center as required to understand the rest of this thesis, and refer the reader to Refs. [1, 4, 5] for further details.

2.2. NV CENTER CREATION METHODS

While NV centers occur at low density in diamond grown using chemical vapour deposition, their occurrence can be increased using techniques that either create vacancies in the lattice (laser writing [8, 9], non-nitrogen ion implantation [10], electron irradiation [11–15]), or substitute a carbon atom with a nitrogen one (delta-doped layers [16, 17], nitrogen ion implantation [10, 18–22]). In a subsequent high temperature annealing step ($T \sim (800 - 1200)°C$), vacancies in the diamond become mobile and form NV centers [20] by combining with nitrogen that is implanted, or residual nitrogen that is left from the growth process. In this thesis, we use NV centers created via electron irradiation, as this maintains bulk-like optical coherence properties even in µm-thin diamond samples (see Ch. 5), in contrast to NV centers formed via ion implantation [22, 23].

2.3. ELECTRONIC LEVEL STRUCTURE OF THE NV CENTER IN DIAMOND

A schematic of the molecular orbitals (MOs) of the NV center ground state, obtained via a linear combination of the atomic orbitals (LCAO, taking the C_{3v} symmetry group of the defect into account [1, 25, 26]) can be seen in Fig. 2.1(b). In the ground state, the electronic occupation of the MOs is $a_1'^2 a_1^2 e^2$, while one a_1-orbital electron occupies one of the degenerate e orbitals in the excited state, resulting in the configuration $a_1'^2 a_1 e^3$. Thus, the two unpaired electrons of both the NV ground and excited state are situated in the bandgap of diamond (see Fig. 2.1(b)), explaining the atom-like coherence properties of the NV center, despite its solid-state host.

As a consequence of coulomb repulsion, the otherwise degenerate ground and excited state spin singlet and triplet states shift in energy, resulting in their relative spacing as indicated in Figs. 2.2(a,b). Transitions between the ground and excited state triplet states (Fig. 2.2(b)) can occur resonantly (~ 637 nm excitation or emission light) in the zero-phonon line (ZPL) and off-resonantly in the phonon side band (PSB), for which additional accompanying localized NV vibrations take or provide part of the energy of the transition (see Sec. 2.4). While most of the decay from the excited states occurs through these transitions, the excited triplet state also has a state-dependent probability of transitioning to the singlet state: levels with $m_s = \pm 1$ spin character are more likely to decay to the singlet, which then decays predominantly to the $m_s = 0$ triplet ground state level [27–29] (Fig. 2.2(a)).

Taking spin-spin and spin-orbit interactions into account leads to the electronic level structure of the NV centre as shown in Fig. 2.2(c). The orbital singlet spin triplet ground state splits into two states at zero magnetic field: when the electrons are co-aligned ($m_s = \pm 1$), (mostly) spin-spin interaction leads to an energy shift of $D \approx 2.88$ GHz (zero field splitting), compared to the case for which the electrons are anti-parallel ($m_s = 0$). Applying a magnetic field parallel to the NV axis splits the degenerate $m_s = \pm 1$ levels via the Zeeman effect (see Fig. 2.2(e)), such that a qubit subspace can be defined. Excellent coherence times ($T_2 > 1$ s) have recently been observed for these qubits under cryogenic conditions using dynamical decoupling sequences [30].

The nitrogen atom of the NV center carries a nuclear spin with either $I = 1$ (^{14}N, 99.3% natural occurrence) or $I = 1/2$ (^{15}N, 0.7% natural occurrence), which leads to an additional splitting of the ground state levels on the order of 2 MHz; by applying microwave pulses that are sufficiently broad in frequency, and utilizing high Rabi frequencies, one can address all nitrogen states simultaneously [31]. Furthermore, the nitrogen spin can also be used as an additional qubit, as demonstrated e.g. in Refs. [32, 33] by employing selective radio-frequency (RF) pulses.

The NV center spin also couples to nearby nuclear spins of ^{13}C atoms ($I = 1/2$, natural occurrence of 1.1% in the otherwise spinless diamond lattice) via a distance and position dependent hyperfine interaction. These nuclear spins can be used as memory qubits with coherence times exceeding ten seconds [33] and can be coherently controlled via tailored dynamical decoupling sequences that either exploit a NV spin-state-dependent precession axis and frequency shift [34, 35], or use additional interleaved RF pulses to selectively drive individual carbon nuclear spins [33, 36]. Such spins have been

2
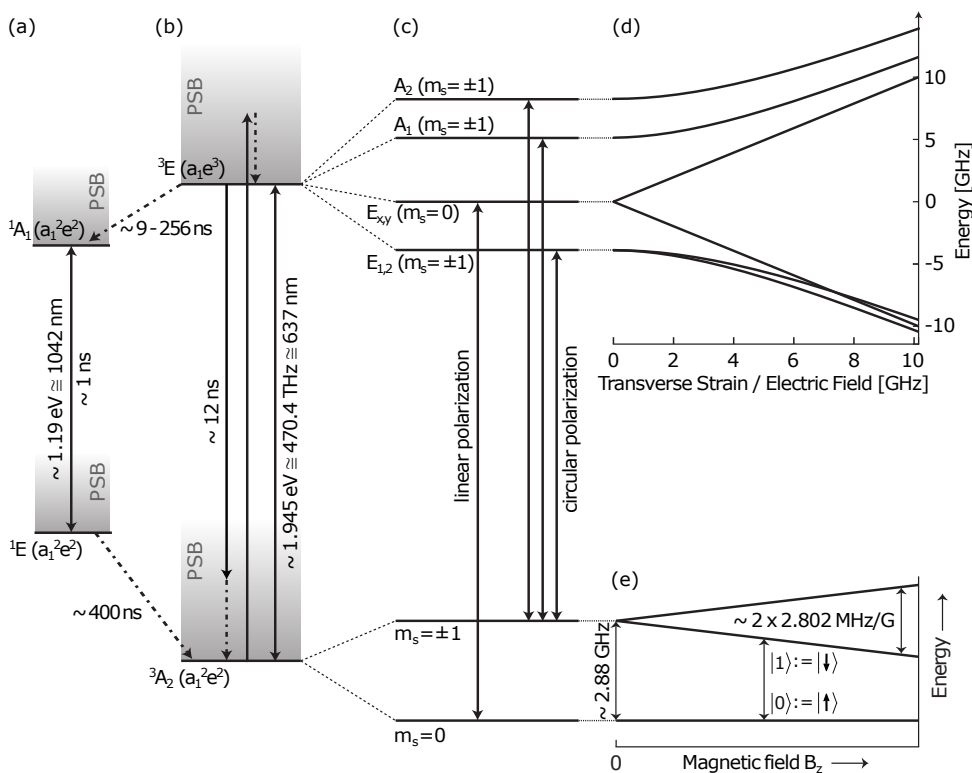
Figure 2.2: Electronic level structure of the NV$^-$ center in diamond. Figure adapted from Pfaff, Bernien, Kalb [6, 7, 24]. The NV electron wave function is described by an orbital- and a spin-state-dependent part. The otherwise degenerate ground and excited spin singlet (a) and triplet (b) states shift in energy when introducing coulomb repulsion. Transitions between the excited state ^3E and the ground state triplet $^3A_2$ (b, molecular orbital electron occupation in brackets) can occur resonantly (solid lines, transition frequency ∼ 470.4 THz), but are mostly accompanied by lattice vibrations that quickly relax to the vibrational ground state (∼ 97 %, dashed lines, PSB, see text). While most decay from ^3E to $^3A_2$ follows this radiative decay path, a spin-state dependent decay mechanism through the singlet states (a, non-radiative parts dashed lines) allows for optical spin polarization (see text). Including spin-spin and spin-orbit interactions, the excited state orbital doublet splits into six levels, two pairs of which are doubly degenerate (c), while the ground state splits into three levels, one pair of which is doubly degenerate. Transitions between the ground and excited state follow selection rules (allowed transitions indicated with solid lines, polarization indicated) and are spin-selective (spin states in brackets). Application of a transverse strain (or equivalent transverse electric field) modifies the excited state energy levels (d), while having no effect on ground state energy levels to first order. Application of a longitudinal strain, in contrast, changes the energy splitting between the ground and excited states. Application of a magnetic field along the NV axis splits the $m_s = \pm 1$ spin levels (e) and thus allows to define a qubit ($|0\rangle$ / $|1\rangle$) that can be coherently addressed with microwave pulses.

used to store entangled quantum states to free up the NV electron for up to ~ 2000 subsequent entanglement generation tries in non-purified samples used for entanglement generation [29, 37, 38].

In the excited state, the orbital doublet spin triplet state splits into six levels when including spin-spin and spin-orbit interactions. The double degeneracy of two pairs of these levels is lifted under application of external electric fields or strain perpendicular (transverse) to the NV axis (leading to a deformation of the contributing orbitals), as shown in Fig. 2.2(d) [39, 40]; axial strain or electric fields (i.e. applied along the axis of the NV center), on the other hand, lead to an overall shift of the excited state energy with respect to the ground state energy. Optical transitions from the ground to the excited state follow optical selection rules as indicated with solid lines in Fig. 2.2(c). By solving the Hamiltonian for the ground and excited state of the NV centre as introduced in Ref. [1] using the parameters found in Refs. [1, 41], we can extract the transverse strain of an NV center by fitting the measured optical transition energies to this model. This technique is used in Ch. 5 of this thesis. The excited state fine structure can be observed at cryogenic temperatures, while the orbital states mix via a T^5 dependent two phonon process at higher temperatures, leading to broadened ZPL transition and thus removing the capability of spin-state dependent resonant addressing of optical transitions [42], as required for entanglement generation protocols (see Sec. 2.5).

The spin-state dependent decay from the excited state to the ground state via the singlet states offers a path of spin polarization of the NV center even at ambient temperatures [1]. In addition, it also displays a straightforward way to read out the spin state of the NV center with non-selective off-resonant addressing: decay between the triplet and singlet levels is non-radiative, and decay through the singlet states only emits a photon at infrared frequencies, and is slow compared to the radiative triplet decay (see Figs. 2.2(a,b)). Thus, one detects less photons from an NV center in the $m_s = \pm 1$ state, compared to the $m_s = 0$ state, which allows to perform optically detected magnetic resonance (ODMR) measurements with non-selective off-resonant excitation, as performed in Ch. 5 of this thesis [15].

Addressing individual ZPL transitions resonantly allows readout of the NV center spin state in a single shot with high fidelity (> 95 % [38, 43]), owing to the high cyclicity of the $m_s = 0$ transitions (spin flip probability per optical excitation ~ 0.5 %). On the other hand, addressing the $m_s = \pm 1$ ZPL transitions can be used to initialize the NV center in the $m_s = 0$ spin state, due to a finite cyclicity of the optical transitions [27]. These spin-resolved optical addressing techniques are at the heart of protocols employed to create entanglement between NV centers, as discussed in Sec. 2.5.

2.4. ELECTRONIC TRANSITIONS VIA VIBRATIONAL LEVELS

As indicated in the discussion of Fig. 2.2, transitions between electronic levels can occur both without involvement of vibrational modes (zero-phonon line, ZPL), and via one or more vibrational modes (phonon sideband, PSB). In this section, we introduce the Huang-Rhys model (see Fig. 2.3(a)), which describes the effects of vibrational modes on electronic transitions as a consequence of electron-phonon coupling [1, 44, 45].

The electronic energies of the ground and excited state are described by quantum harmonic oscillators that depend on the displacement coordinate of an effective vibra-
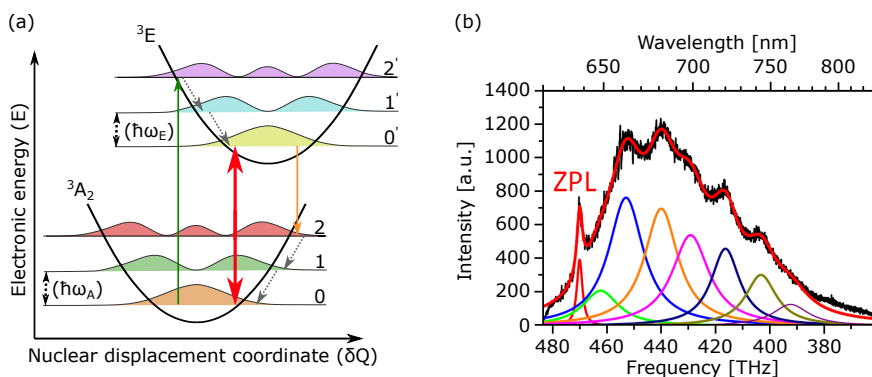
2

Figure 2.3: NV transitions via vibrational states. (a) Electron energy as a function of collective nuclear displacement coordinate for the ground ($^3A_2$) and excited (^3E) state. A different electron configuration in the ground and excited state leads to a relative displacement between equilibrium nuclear coordinates, δQ, and a difference in energy spacing between vibrational modes ($\hbar\omega_A$ and $\hbar\omega_E$). Optical transitions between the ground and the excited state are instantaneous compared to movements of the nuclei, leading to absorption and emission spectra that are comprised of the ZPL (red solid line) and blue- (example green solid line) and red- (example orange solid line) detuned emission components, respectively. Their relative strength is dependent on the wavefunction overlap. Transitions between vibrational states are non-radiative and immediate compared to optical transitions (indicated with grey dotted lines for the example red-detuned optical transition lines). (b) Emission spectrum of an NV center at room temperature under ∼ 532 nm excitation (black). Red top line shows the sum of 8 transition lines (ZPL + 7 transitions that involve vibrational modes in the ground state), whose relative strength is given by the overlap of vibrational wavefunctions between the modes. Figure (b) reprinted with permission from Ref. [49]. Copyright (2013) by the American Physical Society.

tional mode which describes the displacement of the nuclei from their equilibrium position. A difference in charge distribution in the ground and excited state leads to a different nuclear equilibrium position, and a slight difference in the energy spacing of vibrational modes [1]. As transitions between electronic states are instantaneous compared to the timescales of the movement of nuclei (Born-Oppenheimer approximation [46]), optical transitions between the ground and the excited NV state occur with high probability between states that have different vibrational occupation. The strength of a particular transition is then determined by the overlap of vibrational wavefunctions (Franck-Condon principle [47, 48]). As the excited vibrational states decay rapidly to the ground vibrational state, this effect gives rise to an NV emission spectrum that consists of the ZPL transition and several red-shifted lines, while absorption of light can occur at the wavelength of the ZPL transition and for blue-detuned light [49]. Approximately 2.6% of light emission occurs into the ZPL, while the remaining radiative emission is assisted by a lattice vibration [23]; this limits entanglement generation rates, as discussed in Sec. 2.7.

Fig. 2.3(b) shows the emission spectrum for an NV center in a nanodiamond at room temperature, and the contribution of different vibrational modes of the electronic ground state to the spectrum. The ZPL transition linewidths are broadened by phonon-induced mixing of excited states via a T^5-dependent two-phonon Raman process [42], while the transitions via vibrational modes are broadened by the fast decay times of lattice vibrations at room temperature [49].
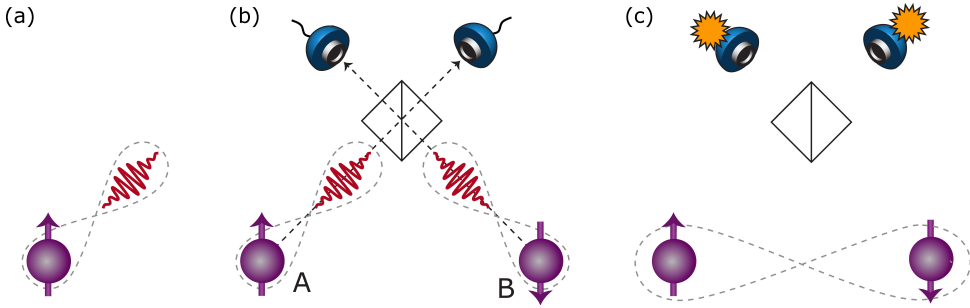
Figure 2.4: Schematic of entanglement generation between NV centers. (a) Spin-photon entanglement is locally generated at each NV center. (b) Interfering the indistinguishable radiative modes of two spin-photon entangled states on a beamsplitter removes the which path information. (c) Creation of a spin-spin entangled state is heralded by a photon detection event. Figure adapted from Bernien, Pfaff [6, 7].

2.5. Entanglement generation between NV centers

The generation of heralded entanglement between distant NV centers critically relies on the interference of indistinguishable photons that are entangled with the spin-state of the NV centers, as depicted schematically in Fig. 2.4 [50]. Entanglement generation protocols start by initializing the NV qubit in one ground state, followed by the creation of a superposition of two ground state spin states (forming the qubit subspace) using microwave pulses. Exploiting the spin-selectivity of the optical transitions of an NV center (see Sec. 2.3), an optical π-pulse that is resonant only for one of the two spin states then excites the NV center to the excited state, from where it decays under the spontaneous emission of a photon with a characteristic lifetime ~ 12 ns, creating a spin-photon entangled state (Fig. 2.4(a)). Interfering the indistinguishable photonic parts of two such spin-photon entangled states from distant different NV centers on a beamsplitter (removing the which path information, Fig. 2.4(b)) and detecting a photon click then leads to the generation of a state with density matrix of form [51]

$$(1-\alpha)|\Psi^\pm\rangle\langle\Psi^\pm| + \alpha|\uparrow\rangle_A|\uparrow\rangle_B\langle\uparrow|_A\langle\uparrow|_B. \tag{2.1}$$

Here, α is the probability to be in the "bright" state after initial NV ground state spin initialization, $|\uparrow\rangle$ denotes the bright qubit state, A and B label the two setups, and $|\Psi^\pm\rangle = \left(1/\sqrt{2}\right) \times \left(|\uparrow_A\downarrow_B\rangle \pm e^{-i\Phi}|\downarrow_A\uparrow_B\rangle\right)$ is the spin-spin entangled state (Fig. 2.4(c)), with Φ the phase of the state[1].

There exist different protocols that utilize states with density matrix of the form of eq. 2.1 to generate entanglement between NV centers. In the two-photon scheme [31, 50, 52–55], a first photon detection event generates a state of form of eq. 2.1, with $\alpha = 0.5$. The NV center spin states are then flipped, and detection of a second photon in a subsequent round generates the state $\Psi^\pm$, where the phase has canceled, i.e. $\Phi = 0$, as the

---

[1] Here, the sign of $|\Psi^\pm\rangle$ is given by which detector clicked. We assume non-photon number resolving detectors, symmetric excitation and detection efficiencies, and operation in the high photon loss regime, as justified later in this section. The phase Φ contains the laser excitation pulse phases, the phase difference due to different photon path lengths, and fluctuations in the NV center frequency that lead to a difference in phase accumulation.

2

path length difference is quasi static on the timescale of a single experimental repetition (∼ 250 ns). While this is the most straightforward scheme to implement, entanglement generation rates scale with $0.5p_p^2$, where p_p is the probability to detect a photon per optical excitation pulse if the NV center is initialized in the bright state. Using this scheme, entanglement fidelities ∼ 90% at ∼ mHz rates have been demonstrated [31].

A second scheme uses a nearby ^{13}C memory qubit in the vicinity of each NV center to serve as an entangled state storage after a first photon detection [37, 56]. This then frees up the NV electrons for a second entangled state generation attempt, which, upon photon detection, is used to project the memory qubits into an entangled state with a global phase by performing a CNOT gate between the NV and memory qubits and measuring out the NV center qubit. Importantly, $\Phi = 0$ for this protocol as long as the phases in eq. 2.1 are the same for the two generated entangled states (∼ 2 ms due to slow carbon nuclear spin gate times). This scheme can in principle scale with αp_p, if the entangled state swapped to the carbon nuclear spin memories does not dephase during additional entanglement generation attempts on the NV center electron spin. However, this condition is not yet met in state-of-the-art experiments [29, 38]. Combined with the increased control complexity at the NV center nodes, compared to the two-photon scheme, this renders this protocol unsuited for current experimental parameters.

A third entanglement generation protocol only requires a single photon click [51, 57] and directly generates a state of form of eq. 2.1; thus, active optical phase control throughout the whole experiment to keep Φ constant is required. It scales advantageously as ∼ $2\alpha p_p$, trading off entanglement generation rate (scaling with the bright state population α) with the entanglement fidelity (scaling with 1-α), yet necessitates tight control over the excitation pulse phase, NV center frequency fluctuations, and, most importantly, over path length fluctuations in the optical interferometer [38, 51], which all contribute to Φ. This scheme is the primary method for entanglement generation with high rates in our group at this moment, with demonstrated fidelities ∼ 82% at rates of ∼ 10 Hz [38].

2.6. STATE OF THE ART OF NV-BASED QUANTUM NETWORKS[2]

A recent experiment showcasing the potential of NV centers in diamond as quantum network node candidates can be seen in Fig. 2.5, which shows a laboratory-scale quantum network based on nitrogen-vacancy (NV) centers in diamond [38]. Three NV centers in separate cryostats, linked via optical fiber channels in a line configuration, are operated as independent quantum network nodes. The centers are set to a common optical emission frequency via electric field tuning (DC Stark shift) [50]. The network is used to demonstrate distribution of three-partite Greenberger-Horne-Zeilinger (GHZ) entangled states across the nodes, as well as entanglement swapping to achieve any-to-any connectivity in the network [38]. This network sets the state of the art for entanglement-based quantum networks.

Entanglement between the nodes is generated using the single-photon-emission-based scheme described in Sec. 2.5 above. In the vicinity of the NV center, a ^{13}C nuclear spin is used as a memory qubit at the middle node, coupled to the NV center electron

---

[2]This section has been published in Journal of Applied Physics **130**, 070901 (2021) [58].
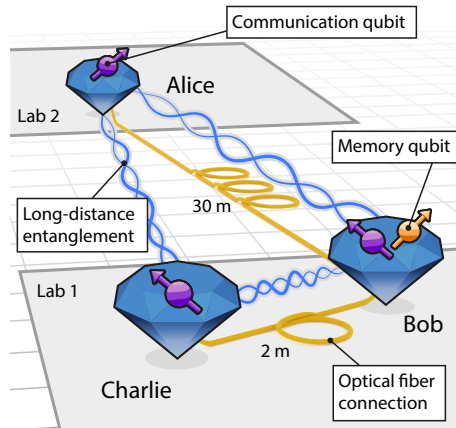
Figure 2.5: Schematic of a state-of-the-art 3-node quantum network based on nitrogen-vacancy (NV) centers in diamond, linked with optical fibers. One of the network nodes features a ^{13}C nuclear spin that is used as a memory qubit to store (part of) an entangled state and free up the communication qubit, while subsequent entanglement is created using this communication qubit a second time. Figure from [38], reprinted with permission from AAAS.

spin via the hyperfine interaction. The nuclear spin is controlled via tailored microwave pulses applied to the NV center spin [35] that simultaneously decouple the NV electron spin from the other nuclear spins. Characterization of the nuclear spin environment of an NV center has enabled communication qubit coherence times above one second [30]. In addition, entangled states have been stored in ^{13}C memory qubits for up to ~ 500 subsequent entanglement generation attempts [29, 38, 59]. Combined with the demonstrated capability of entanglement distillation (generating one higher fidelity state from two lower fidelity states) [37] and deterministic entanglement delivery (by generating entanglement between two nodes faster than it is lost, albeit not under full network activity) [51], these experiments highlight the potential of the NV center as a quantum network node. As we discuss in detail below, a main challenge for the NV center is the low fraction of emitted and detected coherent photons, limiting the entanglement rates.

2.7. PHOTON DETECTION IN ENTANGLEMENT GENERATION PRO-TOCOLS

As discussed in Sec. 2.5, entanglement generation protocols between NV centers scale linearly or quadratically with the probability to detect a photon after an optical excitation pulse for an NV center in the bright state, p_p. This makes p_p a critical parameter in entanglement generation protocols. Here, we discuss the most important contributions that currently limit p_p, as summarized in Fig. 2.6.

- **Probability to excite the NV center to the excited state,** p_e: A finite probability of exciting the NV center to the excited state per optical excitation pulse limits the photon generation rate. There are three main mechanisms that can contribute to

2

Figure 2.6: Schematic of main loss contributions to detection of a photon emitted from an NV center after resonant excitation, p_p. An NV center in the bright spin state is excited with probability p_e. Spontaneously emitted coherent photons at the ZPL frequency are filtered, p_{zpl}, and collected with efficiency p_c. Subsequent travel of the photon in a fiber succeeds with probability p_f, before a photon is detected with efficiency p_{det}. Time windowing to remove residual exci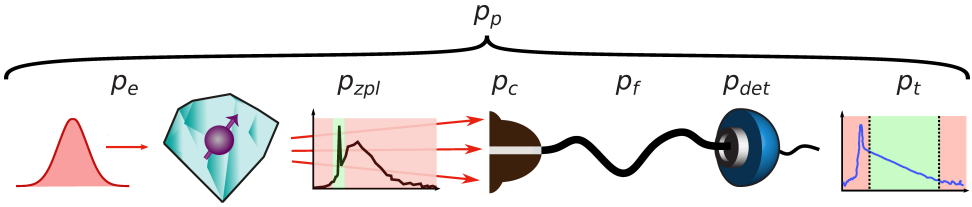tation light and to spectrally narrow NV centers finally reduces p_p by 1-p_t. See text for a discussion of these effects.

limited p_e:

– **Insufficient optical driving power:** To make the NV center spontaneously emit a photon, it is brought to the excited state using resonant laser driving [60]. To achieve Rabi frequencies that allow for ns-long excitation pulses (shorter than the NV lifetime to allow for efficient excitation pulse suppression via time filtering), sufficient laser power is needed; recent experimental data suggests that we are typically operating in this regime [51].

– **Probability to be off-resonant, or in the wrong charge state**: A two-photon process can lead to photo-ionization of the NV center, during which the charge state is altered from the negative to the neutral state [51, 61], which has different transition energies and different energy levels, causing subsequent entanglement generation attempts to fail. Additionally, the NV center transition frequency can be detuned from the excitation laser, reducing the effective optical driving power, and thus the probability to excite the NV electron to the excited state. This can be caused by a fluctuating charge environment in the vicinity of the NV center, which leads to spectral shifts of the transition frequencies [15, 50]. We note, however, that due to the high Rabi frequencies associated with the driving powers typically used for optical pulses, this effect plays a minor role for p_p, and instead rather limits entanglement fidelities.

In practice, charge resonance checks can be employed to guarantee that the NV center is in the negative charge state, and that the excitation lasers are on resonance with the NV ZPL transition used for entanglement generation. Such a check is realized by driving both $m_s = 0$ and $m_s = \pm 1$ transitions simultaneously using two lasers, realizing a scheme in which the NV center does not go dark due to spin-flips, but only due to being off-resonance with one of the lasers, or due to being in the neutral charge state. Once the detected photon number drops below a set threshold, green (non-resonant) [43] or yellow (resonant) [3, 32] laser pulses can be employed to bring the NV center back to the negative charge state, and the excitation laser frequencies can be slightly tuned to restore maximum counts.

- **Probability of zero-phonon line (ZPL) photon emission, p_{zpl}:** As introduced in Sec. 2.4, only ~ 2.6% of the spontaneously emitted light from the NV excited state is emitted in the zero-phonon line [23]. However, only ZPL photons can be used for entanglement generation, as the phonons assisting a photon during PSB transitions dephase rapidly: for photons emitted in the PSB, the spin state is thus entangled with both the presence or absence of a photon and the presence or absence of a phonon. However, as the phonon is leaked to the environment, the spin-photon state gets fully mixed. Additionally, photons emitted in the PSB occur at a broad range of frequencies, and are therefore distinguishable after sub-ns timescales already, eliminating the possibility of entanglement generation at high rates.

- **Probability of photon collection, p_c:** Due to the high refractive index of diamond (~ 2.41; compared to the refractive index of air of 1, in which the next stage of the collection path is located), total internal reflection limits the collection of emitted NV photons. State-of-the art solid-immersion lens collection enhancement tools that have been used in entanglement generation experiments increase the collection of photons to ~ 15% [31, 43]. Additionally, deviations from an ideal shape due to fabrication imperfections in the ion beam milling process limit subsequent collection of photons in a single mode fiber (as needed to guarantee spatial indistinguishability) in practice to ~ 50%, resulting in a total photon collection efficiency ~ 7.5%.

- **Probability of photon transmission through fibers, p_f:** Connecting distant setups is typically realized through single mode optical fibers to achieve spatial indistinguishability of photons, and low-loss photon transmission. However, commonly employed fibers have losses at ~ 637 nm (~ 8 dB/km) that are significantly higher than at their transmission optimum (1310 nm / 1550 nm, ~ 0.2 dB/km) [31, 62].

- **Probability of photon detection, p_{det}:** State of the art superconducting nanowire single photon detectors feature detection efficiencies up to ~ 95% at photon wavelengths of ~ 637 nm [38]. We note that the experiments reported in this thesis were conducted using silicon avalanche photodetectors, with typical efficiencies ~ 70%.

- **Probability of photon detection in time window, p_t:** As discussed above, entanglement generation relies on the interference of indistinguishable photons. Thus, it is important to filter out reflected light from the optical π-pulse used to excite the NV center. Common techniques involve a combination of cross-polarization detection and time filtering, i.e. restricting the window during which photon counts are accepted as heralding events [50, 63]. Additionally, time filtering can be employed to mitigate the effects of unwanted spectral diffusion [64, 65]. The exact allowable time window and thus fraction of all emitted photons that contribute to the entanglement generation depends on the experimental requirements and settings, and varies between setups and samples.

Combining all factors (including time filtering, but not fiber transmission losses), current state-of-the art photon detection probabilities per NV excitation pulse, p_p, are

$\sim 1 \times 10^{-3}$ if the NV center is initialized in the bright state [31]. This limits entanglement generation rates in the single-photon detection protocol to ~ 10 Hz for single link fidelities ~ 0.8 [38].

2.8. INCREASING PHOTON DETECTION RATES

There are two major ways to improve the coherent photon detection probability per resonant excitation pulse, p_p, for distant NV entanglement generation. The first approach is to increase the probability of fiber transmission, p_f, by conversion of NV photons to telecom frequencies. As discussed above, fiber transmission losses at NV ZPL wavelengths are ~ 6 times higher (per kilometer) than at telecom wavelengths. Thus, for long fiber transmission distances, it can be advantageous to convert the NV photons to telecom frequencies using a difference frequency generation process [66–68], with reported system conversion efficiencies of up to ~ 20 % (including in- and out-coupling, as well as filtering). As this process requires strong pump light with a wavelength ~ 1064 nm (creating background photons throughout the whole telecom band), it is important to filter the downconverted light with narrow frequency filters ($\sim$ a few NV center linewidths), to limit false heralding events by maintaining high signal to noise ratios. At the time of writing this thesis, work towards entanglement generation between NV centers using down-converted photons is under way, but has not yet been demonstrated.

A second approach is to increase the fraction of photons emitted in the zero-phonon line, p_{zpl}, and their subsequent collection efficiency, p_c, by embedding the NV center in an optical cavity. This selectively enhances the fraction of emitted light at the resonance frequency of the cavity, as introduced in Ch. 3 of this thesis. Furthermore, this enhanced emission is funneled into the well-defined cavity mode that is relatively straightforward to pick up with high efficiencies (up to ~ 75 %). This thesis focuses on embedding diamond color centers in optical cavities to enhance their spin-photon interface; recent experiments (including the results presented in this thesis) suggest that entanglement generation rates between NV centers for protocols that scale linearly with photon detection probability p_p could be improved by up to two orders of magnitude using this approach [23, 69, 70], bringing metropolitan-scale quantum networks based on NV center end nodes within reach.

REFERENCES

[1] M. W. Doherty, N. B. Manson, P. Delaney, F. Jelezko, J. Wrachtrup and L. C. Hollenberg, *The nitrogen-vacancy colour centre in diamond,* Physics Reports **528,** 1 (2013).

[2] M. S. Barson, E. Krausz, N. B. Manson and M. W. Doherty, *The fine structure of the neutral nitrogen-vacancy center in diamond,* Nanophotonics **8,** 1985 (2019).

[3] S. Baier, C. E. Bradley, T. Middelburg, V. V. Dobrovitski, T. H. Taminiau and R. Hanson, *Orbital and Spin Dynamics of Single Neutrally-Charged Nitrogen-Vacancy Centers in Diamond,* Physical Review Letters **125,** 193601 (2020).

[4] L. Childress and R. Hanson, *Diamond NV centers for quantum computing and quantum networks,* MRS Bulletin **38,** 134 (2013).

[5] W. B. Gao, A. Imamoglu, H. Bernien and R. Hanson, *Coherent manipulation, measurement and entanglement of individual solid-state spins using optical fields,* Nature Photonics **9,** 363 (2015).

[6] H. Bernien, *Control, Measurement and Entanglement of Remote Quantum Spin Registers in Diamond,* Ph.D. thesis, TU Delft (2014).

[7] W. Pfaff, *Quantum Measurement and Entanglement of Spin Quantum Bits in Diamond,* Ph.D. thesis, TU Delft (2013).

[8] Y.-C. Chen *et al., Laser writing of coherent colour centres in diamond,* Nature Photonics **11,** 77 (2017).

[9] Y.-C. Chen *et al., Laser writing of individual nitrogen-vacancy defects in diamond with near-unity yield,* Optica **6,** 662 (2019).

[10] T. Lühmann, R. John, R. Wunderlich, J. Meijer and S. Pezzagna, *Coulomb-driven single defect engineering for scalable qubits and spin sensors in diamond,* Nature Communications **10,** 4956 (2019).

[11] G. Davies, S. C. Lawson, A. T. Collins, A. Mainwood and S. J. Sharp, *Vacancy-related centers in diamond,* Physical Review B **46,** 13157 (1992).

[12] A. Gruber, *Scanning Confocal Optical Microscopy and Magnetic Resonance on Single Defect Centers,* Science **276,** 2012 (1997).

[13] D. Twitchen, D. Hunt, M. Newton, J. Baker, T. Anthony and W. Banholzer, *Electron paramagnetic resonance (EPR) and optical absorption studies of defects created in diamond by electron irradiation damage at 100 and 350K,* Physica B: Condensed Matter **273-274,** 628 (1999).

[14] B. Campbell and A. Mainwood, *Radiation Damage of Diamond by Electron and Gamma Irradiation,* Physica Status Solidi (A) **181,** 99 (2000).

[15] M. Ruf, M. IJspeert, S. van Dam, N. de Jong, H. van den Berg, G. Evers and R. Hanson, *Optically Coherent Nitrogen-Vacancy Centers in Micrometer-Thin Etched Diamond Membranes,* Nano Letters **19,** 3987 (2019).

[16] K. Ohno, F. Joseph Heremans, L. C. Bassett, B. A. Myers, D. M. Toyli, A. C. Bleszynski Jayich, C. J. Palmstrøm and D. D. Awschalom, *Engineering shallow spins in diamond with nitrogen delta-doping,* Applied Physics Letters **101**, 082413 (2012).

[17] C. A. McLellan, B. A. Myers, S. Kraemer, K. Ohno, D. D. Awschalom and A. C. Bleszynski Jayich, *Patterned Formation of Highly Coherent Nitrogen-Vacancy Centers Using a Focused Electron Irradiation Technique,* Nano Letters **16**, 2450 (2016).

[18] J. Meijer, B. Burchard, M. Domhan, C. Wittmann, T. Gaebel, I. Popa, F. Jelezko and J. Wrachtrup, *Generation of single color centers by focused nitrogen implantation,* Applied Physics Letters **87**, 261909 (2005).

[19] J. R. Rabeau, P. Reichart, G. Tamanyan, D. N. Jamieson, S. Prawer, F. Jelezko, T. Gaebel, I. Popa, M. Domhan and J. Wrachtrup, *Implantation of labelled single nitrogen vacancy centers in diamond using N15,* Applied Physics Letters **88**, 023113 (2006).

[20] Y. Chu *et al.*, *Coherent Optical Transitions in Implanted Nitrogen Vacancy Centers,* Nano Letters **14**, 1982 (2014).

[21] F. Fávaro de Oliveira, D. Antonov, Y. Wang, P. Neumann, S. A. Momenzadeh, T. Häußermann, A. Pasquarelli, A. Denisenko and J. Wrachtrup, *Tailoring spin defects in diamond by lattice charging,* Nature Communications **8**, 15409 (2017).

[22] S. B. van Dam, M. Walsh, M. J. Degen, E. Bersin, S. L. Mouradian, A. Galiullin, M. Ruf, M. IJspeert, T. H. Taminiau, R. Hanson and D. R. Englund, *Optical coherence of diamond nitrogen-vacancy centers formed by ion implantation and annealing,* Physical Review B **99**, 161203 (2019).

[23] D. Riedel, I. Söllner, B. J. Shields, S. Starosielec, P. Appel, E. Neu, P. Maletinsky and R. J. Warburton, *Deterministic enhancement of coherent photon generation from a nitrogen-vacancy center in ultrapure diamond,* Physical Review X **7**, 1 (2017).

[24] N. Kalb, *Diamond-Based Quantum Networks with Multi-qubit Nodes,* Ph.D. thesis, TU Delft (2018).

[25] M. W. Doherty, N. B. Manson, P. Delaney and L. C. L. Hollenberg, *The negatively charged nitrogen-vacancy centre in diamond: the electronic solution,* New Journal of Physics **13**, 025019 (2011).

[26] J. R. Maze, A. Gali, E. Togan, Y. Chu, A. Trifonov, E. Kaxiras and M. D. Lukin, *Properties of nitrogen-vacancy centers in diamond: the group theoretic approach,* New Journal of Physics **13**, 025025 (2011).

[27] L. Robledo, H. Bernien, T. V. D. Sar and R. Hanson, *Spin dynamics in the optical cycle of single nitrogen-vacancy centres in diamond,* New Journal of Physics **13**, 025013 (2011).

[28] M. Gould, E. R. Schmidgall, S. Dadgostar, F. Hatami and K. M. C. Fu, *Efficient Extraction of Zero-Phonon-Line Photons from Single Nitrogen-Vacancy Centers in an Integrated GaP-on-Diamond Platform,* Physical Review Applied **6**, 2 (2016).

[29] N. Kalb, P. C. Humphreys, J. J. Slim and R. Hanson, *Dephasing mechanisms of diamond-based nuclear-spin memories for quantum networks,* Physical Review A **97**, 062330 (2018).

[30] M. H. Abobeih, J. Cramer, M. A. Bakker, N. Kalb, M. Markham, D. J. Twitchen and T. H. Taminiau, *One-second coherence for a single electron spin coupled to a multi-qubit nuclear-spin environment,* Nature Communications **9**, 1 (2018).

[31] B. Hensen *et al.*, *Loophole-free Bell inequality violation using electron spins separated by 1.3 kilometres,* Nature **526**, 682 (2015).

[32] W. Pfaff, B. J. Hensen, H. Bernien, S. B. van Dam, M. S. Blok, T. H. Taminiau, M. J. Tiggelman, R. N. Schouten, M. Markham, D. J. Twitchen and R. Hanson, *Unconditional quantum teleportation between distant solid-state quantum bits,* Science **345**, 532 (2014).

[33] C. E. Bradley, J. Randall, M. H. Abobeih, R. C. Berrevoets, M. J. Degen, M. A. Bakker, M. Markham, D. J. Twitchen and T. H. Taminiau, *A Ten-Qubit Solid-State Spin Register with Quantum Memory up to One Minute,* Physical Review X **9**, 31045 (2019).

[34] T. H. Taminiau, J. J. T. Wagenaar, T. van der Sar, F. Jelezko, V. V. Dobrovitski and R. Hanson, *Detection and Control of Individual Nuclear Spins Using a Weakly Coupled Electron Spin,* Physical Review Letters **109**, 137602 (2012).

[35] T. H. Taminiau, J. Cramer, T. Van Der Sar, V. V. Dobrovitski and R. Hanson, *Universal control and error correction in multi-qubit spin registers in diamond,* Nature Nanotechnology **9**, 171 (2014).

[36] M. H. Abobeih, J. Randall, C. E. Bradley, H. P. Bartling, M. A. Bakker, M. J. Degen, M. Markham, D. J. Twitchen and T. H. Taminiau, *Atomic-scale imaging of a 27-nuclear-spin cluster using a quantum sensor,* Nature **576**, 411 (2019).

[37] N. Kalb, A. A. Reiserer, P. C. Humphreys, J. J. Bakermans, S. J. Kamerling, N. H. Nickerson, S. C. Benjamin, D. J. Twitchen, M. Markham and R. Hanson, *Entanglement distillation between solid-state quantum network nodes,* Science **356**, 928 (2017).

[38] M. Pompili, S. L. N. Hermans, S. Baier, H. K. C. Beukers, P. C. Humphreys, R. N. Schouten, R. F. L. Vermeulen, M. J. Tiggelman, L. dos Santos Martins, B. Dirkse, S. Wehner and R. Hanson, *Realization of a multinode quantum network of remote solid-state qubits,* Science **372**, 259 (2021).

[39] P. Tamarat, T. Gaebel, J. R. Rabeau, M. Khan, A. D. Greentree, H. Wilson, L. C. L. Hollenberg, S. Prawer, P. Hemmer, F. Jelezko and J. Wrachtrup, *Stark Shift Control of Single Optical Centers in Diamond,* Physical Review Letters **97**, 083002 (2006).

2

[40] L. C. Bassett, F. J. Heremans, C. G. Yale, B. B. Buckley and D. D. Awschalom, *Electrical Tuning of Single Nitrogen-Vacancy Center Optical Transitions Enhanced by Photoinduced Fields*, Physical Review Letters **107**, 266403 (2011).

[41] H. Beukers, *Improving coherence of quantum memory during entanglement creation between nitrogen vacancy centres in diamond*, M.Sc. thesis, TU Delft and University of Groningen (2019).

[42] K.-M. C. Fu, C. Santori, P. E. Barclay, L. J. Rogers, N. B. Manson and R. G. Beausoleil, *Observation of the Dynamic Jahn-Teller Effect in the Excited States of Nitrogen-Vacancy Centers in Diamond*, Physical Review Letters **103**, 256404 (2009).

[43] L. Robledo, L. Childress, H. Bernien, B. Hensen, P. F. A. Alkemade and R. Hanson, *High-fidelity projective read-out of a solid-state spin quantum register*, Nature **477**, 574 (2011).

[44] K. Huang and A. Rhys, *Theory of Light Absorption and Non-Radiative Transitions in F-Centres*, Proceedings of the Royal Society of London. Series A, Mathematical and Physical Sciences **204** (1950).

[45] A. M. Stoneham, *Theory of Defects in Solids: Electronic Structure of Defects in Insulators and Semiconductors* (Oxford University Press, Oxford, 1975).

[46] M. Born and R. Oppenheimer, *Zur Quantentheorie der Molekeln*, Annalen der Physik **389**, 457 (1927).

[47] J. Franck and E. G. Dymond, *Elementary processes of photochemical reactions*, Transactions of the Faraday Society **21**, 536 (1926).

[48] E. Condon, *A Theory of Intensity Distribution in Band Systems*, Physical Review **28**, 1182 (1926).

[49] R. Albrecht, A. Bommer, C. Deutsch, J. Reichel and C. Becher, *Coupling of a Single Nitrogen-Vacancy Center in Diamond to a Fiber-Based Microcavity*, Physical Review Letters **110**, 243602 (2013).

[50] H. Bernien, B. Hensen, W. Pfaff, G. Koolstra, M. S. Blok, L. Robledo, T. H. Taminiau, M. Markham, D. J. Twitchen, L. Childress and R. Hanson, *Heralded entanglement between solid-state qubits separated by three metres*, Nature **497**, 86 (2013).

[51] P. C. Humphreys, N. Kalb, J. P. Morits, R. N. Schouten, R. F. Vermeulen, D. J. Twitchen, M. Markham and R. Hanson, *Deterministic delivery of remote entanglement on a quantum network*, Nature **558**, 268 (2018).

[52] S. D. Barrett and P. Kok, *Efficient high-fidelity quantum computation using matter qubits and linear optics*, Physical Review A **71**, 060310 (2005).

[53] D. L. Moehring, P. Maunz, S. Olmschenk, K. C. Younge, D. N. Matsukevich, L.-M. Duan and C. Monroe, *Entanglement of single-atom quantum bits at a distance*, Nature **449**, 68 (2007).

[54] J. Hofmann, M. Krug, N. Ortegel, L. Gérard, M. Weber, W. Rosenfeld and H. Weinfurter, *Heralded Entanglement Between Widely Separated Atoms,* Science **337**, 72 (2012).

[55] A. Narla, S. Shankar, M. Hatridge, Z. Leghtas, K. M. Sliwa, E. Zalys-Geller, S. O. Mundhada, W. Pfaff, L. Frunzio, R. J. Schoelkopf and M. H. Devoret, *Robust Concurrent Remote Entanglement Between Two Superconducting Qubits,* Physical Review X **6**, 031036 (2016).

[56] E. T. Campbell and S. C. Benjamin, *Measurement-Based Entanglement under Conditions of Extreme Photon Loss,* Physical Review Letters **101**, 130502 (2008).

[57] C. Cabrillo, J. I. Cirac, P. García-Fernández and P. Zoller, *Creation of entangled states of distant atoms by interference,* Physical Review A **59**, 1025 (1999).

[58] M. Ruf, N. H. Wan, H. Choi, D. Englund and R. Hanson, *Quantum networks based on color centers in diamond,* Journal of Applied Physics **130**, 070901 (2021).

[59] A. Reiserer, N. Kalb, M. S. Blok, K. J. M. van Bemmelen, T. H. Taminiau, R. Hanson, D. J. Twitchen and M. Markham, *Robust Quantum-Network Memory Using Decoherence-Protected Subspaces of Nuclear Spins,* Physical Review X **6**, 021040 (2016).

[60] L. Robledo, H. Bernien, I. van Weperen and R. Hanson, *Control and Coherence of the Optical Transition of Single Nitrogen Vacancy Centers in Diamond,* Physical Review Letters **105**, 177403 (2010).

[61] N. Aslam, G. Waldherr, P. Neumann, F. Jelezko and J. Wrachtrup, *Photo-induced ionization dynamics of the nitrogen vacancy defect in diamond investigated by single-shot charge state detection,* New Journal of Physics **15**, 013064 (2013).

[62] F. Rozpędek, R. Yehia, K. Goodenough, M. Ruf, P. C. Humphreys, R. Hanson, S. Wehner and D. Elkouss, *Near-term quantum-repeater experiments with nitrogen-vacancy centers: Overcoming the limitations of direct transmission,* Physical Review A **99**, 052330 (2019).

[63] H. Bernien, L. Childress, L. Robledo, M. Markham, D. Twitchen and R. Hanson, *Two-Photon Quantum Interference from Separate Nitrogen Vacancy Centers in Diamond,* Physical Review Letters **108**, 043604 (2012).

[64] T. Legero, T. Wilk, A. Kuhn and G. Rempe, *Time-resolved two-photon quantum interference,* Applied Physics B: Lasers and Optics **77**, 797 (2003).

[65] T. Legero, T. Wilk, A. Kuhn and G. Rempe, *Characterization of Single Photons Using Two-Photon Interference,* Advances in Atomic, Molecular and Optical Physics **53**, 253 (2006).

[66] M. Bock, P. Eich, S. Kucera, M. Kreis, A. Lenhard, C. Becher and J. Eschner, *High-fidelity entanglement between a trapped ion and a telecom photon via quantum frequency conversion,* Nature Communications **9**, 1998 (2018).

2

[67] A. Dréau, A. Tcheborateva, A. E. Mahdaoui, C. Bonato and R. Hanson, *Quantum Frequency Conversion of Single Photons from a Nitrogen-Vacancy Center in Diamond to Telecommunication Wavelengths,* Physical Review Applied **9**, 064031 (2018).

[68] A. Tchebotareva, S. L. Hermans, P. C. Humphreys, D. Voigt, P. J. Harmsma, L. K. Cheng, A. L. Verlaan, N. Dijkhuizen, W. de Jong, A. Dréau and R. Hanson, *Entanglement between a Diamond Spin Qubit and a Photonic Time-Bin Qubit at Telecom Wavelength,* Physical Review Letters **123**, 063601 (2019).

[69] A. Faraon, C. Santori, Z. Huang, V. M. Acosta and R. G. Beausoleil, *Coupling of Nitrogen-Vacancy Centers to Photonic Crystal Cavities in Monocrystalline Diamond,* Physical Review Letters **109**, 033604 (2012).

[70] M. Ruf, M. Weaver, S. van Dam and R. Hanson, *Resonant Excitation and Purcell Enhancement of Coherent Nitrogen-Vacancy Centers Coupled to a Fabry-Perot Microcavity,* Physical Review Applied **15**, 024049 (2021).

3

PURCELL ENHANCEMENT OF COLOR CENTERS IN DIAMOND

Future quantum networks are at the heart of quantum technologies, and may enable a suite of novel applications. Entanglement generation rates between distant color centers in diamond are currently limited by the emission probability of a spin-selective photon in the zero-phonon line, as well as the photon collection efficiency. Here, we introduce the spontaneous emission rate of a dipole emitter in a homogeneous medium, and outline a path to increase this rate via the Purcell effect in an optical cavity. We explore different parameter regimes of color center - cavity coupling (including regimes that can allow for near-deterministic spin-photon gates), and determine a strategy to quantify Purcell enhancement experimentally. We conclude by giving an overview of different implementations of embedding color centers in diamond in optical cavities. We focus in particular on all-diamond photonic crystal cavities and open fiber-based micro-cavities; these designs are theoretically and experimentally considered in the rest of this thesis.

3.1. IMPROVING THE OPTICAL INTERFACE OF COLOR CENTERS IN DIAMOND

Fast generation of photon-mediated entanglement between color centers in diamond requires an efficient spin-photon interface with indistinguishable, spin-selective, coherent color center transitions. In this section, we introduce the spontaneous emission rate of a dipole emitter, and how we can enhance this rate using optical cavities. Apart from enhancing the relative photon emission fraction into the zero-phonon line (only this light can be used for entanglement generation, see Ch. 2), a cavity also funnels emitted light into a well defined mode that can be readily collected. In case the squared coupling of the light field to the emitter can be made greater than the product of cavity and emitter decay rates, near deterministic spin-photon gates can become feasible, a regime that we also discuss in this chapter.

3.1.1. TRANSITION RATE FOR AN EMITTER IN A HOMOGENEOUS MEDIUM

The transition rate between two eigenstates of a dipole emitter in a homogeneous medium due to an external perturbation is described by Fermi's golden rule [1, 2] (see e.g. Ref. [3] for a derivation). In the case of spontaneous emission of a two level dipole emitter, the coupling of vacuum electric field fluctuations, $\vec{E}_{vac}$, to the dipole moment of the emitter, $\vec{\mu}_{eg}$, takes up the role of this perturbation, and leads to a spontaneous emission decay rate from an excited state, $|e\rangle$, to a ground state, $|g\rangle$, of

$$\Gamma_{e \to g}(\omega) = \frac{2\pi}{\hbar^2} |M_{e \to g}|^2 D(\omega) = \frac{2\pi}{\hbar^2} |\vec{\mu}_{eg} \cdot \vec{E}_{vac}|^2 D(\omega), \tag{3.1}$$

where $D(\omega)$ is the density of ground states at the transition frequency, ω, and $|M_{e \to g}|$ is a matrix element describing the transition. We can furthermore introduce a coupling of the emitter to the vacuum field, g, and quantize the electric field, yielding

$$\vec{E}_{vac} = |\vec{E}_{vac}| \cdot \hat{e} = \sqrt{\frac{\hbar\omega}{2\epsilon_0 \epsilon_r V}} \cdot \hat{e}, \qquad (3.2) \qquad\qquad g = \sqrt{\frac{\omega \mu_{eg}^2}{2\hbar\epsilon_0 \epsilon_r V}}, \qquad (3.3)$$

where $\hat{e}$ is the electric field polarization, V is the vacuum field quantization volume, and ϵ_0 and ϵ_r are the vacuum and relative electric permittivity, respectively [3, 4]. Substituting $\vec{\mu}_{eg} = \mu_{eg} \cdot \hat{d}$, as well as eqs. 3.3 and 3.2 in eq. 3.1 gives

$$\Gamma_{e \to g}(\omega) = 2\pi g^2 |\hat{d} \cdot \hat{e}|^2 D(\omega) = \frac{\pi\omega}{\hbar\epsilon_0 \epsilon_r V} \mu_{eg}^2 |\hat{d} \cdot \hat{e}|^2 D(\omega). \tag{3.4}$$

The photon density of states in a homogeneous medium with refractive index n can be calculated as [5]

$$D_{hom}(\omega) = \frac{\omega^2 V}{\pi^2 (c/n)^3}, \tag{3.5}$$

with c the speed of light. Furthermore, the vaccum electric field fluctuations and a dipole emitter in a homgeneous medium have a random orientation to each other, giving on average $|\hat{d} \cdot \hat{e}|^2 = 1/3$. Together, this yields the spontaneous emission rate of a dipole
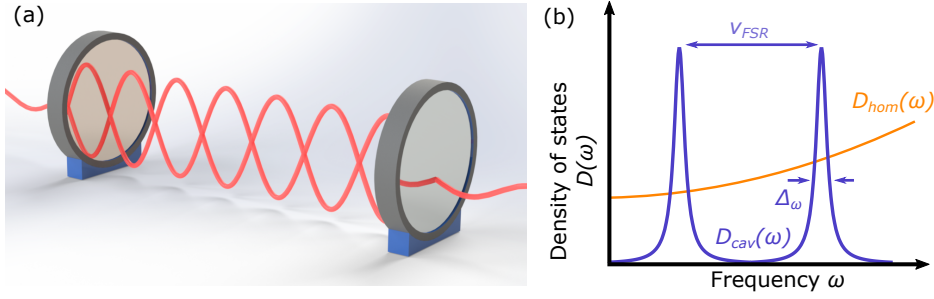
Figure 3.1: Schematic overview of an optical cavity and comparison of the density of states in an optical cavity and in a homogeneous material. (a) Canonical model of an optical cavity, clamping the electric field between two highly reflective mirrors. (b) Density of states as a function of frequency in a homogeneous material (orange) and in an optical cavity (purple). A cavity has allowed fundamental modes spaced by the free spectral range ν_{FSR}, leading to Lorentzian spikes in the density of states; this can enhance the transition rate of an embedded solid-state emitter (see text).

emitter in a homogeneous medium

$$\Gamma_{hom} = \frac{\omega^3 n^3 \mu_{eg}^2}{3\hbar\pi\epsilon_0\epsilon_r c^3}. \tag{3.6}$$

3.1.2. TRANSITION RATE FOR AN EMITTER IN AN OPTICAL CAVITY

Evaluating eq. 3.1, we can see that the spontaneous emission rate increases along with the density of states. In this work, we make use of an optical cavity, which can enhance the density of states around its resonances above the one in a homogeneous medium. We will only give a brief introduction to the most important aspects of an optical cavity here, and refer the reader to Refs. [5–7] for a detailed introduction.

A canonical one-dimensional model for an optical cavity consists of two highly reflective mirrors separated by a length L_{cav} in a medium with refractive index n, see Fig. 3.1(a). The mirrors introduce a clamping boundary condition for the electric field, which leads to the formation of standing waves inside this optical resonator - in analogy to a guitar, where clamping the strings at their mounting points defines nodes of the supported modes. Constructive interference of the light field exiting the resonator can be achieved at specific lengths which are integer multiples, m, of half of the wavelength, λ, of the electric field: $L_{cav} = m\frac{\lambda}{2}$. Using $c = n\lambda\nu$, where ν is the frequency of the light mode, we find that neighbouring modes of the cavity are spaced by the free spectral range, ν_{FSR}:

$$\nu_{FSR} = \frac{c}{2nL_{cav}}. \tag{3.7}$$

The density of states in the cavity, D_{cav}, with angular cavity frequency, ω_c, is given as [5]:

$$D_{cav}(\omega) = \frac{2}{\pi\Delta_\omega}\frac{\Delta_\omega^2}{4(\omega-\omega_c)^2 + \Delta_\omega^2}, \tag{3.8}$$

where we have introduced the full width at half maximum of the cavity, Δ_ω which is

related to the exponential decay rate of light out of the resonator, κ, via the relation $\kappa = 2\pi\Delta_\omega$. A common quantity to compare different optical cavities is the quality factor, Q, which quantifies how long a light mode stays inside the resonator before its energy has decayed to $\frac{1}{e}$, and is defined as

$$Q = \frac{\omega}{\Delta_\omega} = \frac{2nL_{cav}F}{\lambda}, \tag{3.9}$$

where the finesse, $F = \frac{v_{FSR}}{\Delta_v}$, is a commonly used parameter that describes how many times a photon bounces between the cavity mirrors before it is lost (modulo a factor of π). Thus, the transmission of the cavity (as well as its density of states) is highly peaked, following a Lorentzian profile (recall that the Fourier transform of an exponential decay is a Lorentzian); it is this effect of a highly peaked density of states around its resonance frequencies that enhances the spontaneous emission rate of a dipole emitter inside a cavity, compared to the situation in a homogeneous medium discussed in Sec. 3.1.1 (see also Fig. 3.1(b)).

If the cavity resonance matches the transition frequency of the dipole emitter, we can simplify eq. 3.8 to read

$$D_{cav}(\omega = \omega_c) = \frac{2}{\pi\Delta_\omega} = \frac{2Q}{\pi\omega}. \tag{3.10}$$

Thus, using eq. 3.4, the spontaneous emission rate of a dipole emitter on resonance with an optical cavity becomes

$$\Gamma_{cav}(\omega = \omega_c) = \frac{2\mu_{eg}^2}{\hbar\epsilon_0\epsilon_r}|\hat{d}\cdot\hat{e}|^2\frac{Q}{V}. \tag{3.11}$$

3.1.3. PURCELL ENHANCEMENT AND ITS INTERPRETATION

Having calculated the spontaneous emission rates of a dipole emitter in a homogeneous medium and in an optical cavity, we can quantify the emission rate enhancement by introducing the Purcell factor, F_P, which compares the two rates:

$$F_P = \frac{\Gamma_{cav}}{\Gamma_{hom}} = \frac{|\hat{d}\cdot\hat{e}|^2}{\frac{1}{3}}\frac{D_{cav}(\omega)}{D_{hom}(\omega)} = \frac{3c^3}{4\pi^2n^3}\times\frac{\zeta^2}{v^3}\times\frac{Q}{V}, \tag{3.12}$$

where $\omega = 2\pi v$. Note that a cavity mode has a certain polarization (as opposed to the random orientation for the vacuum electric field fluctuations), and thus the factor $\zeta^2 = |\hat{d}\cdot\hat{e}|^2$ remains. Here, the quantization volume (which equals the cavity mode volume, see also Ch. 4) does not cancel out, as opposed to the free space case. Thus, for highest Purcell enhancement, we want to maximize the ratio of Q/V. We will discuss different regimes of Purcell enhancement in Sec. 3.2 below.

In Ch. 4, we will derive that the mode volume of an optical cavity is given as $V = \frac{\pi w_0^2}{4}L_{\text{eff}}$, where L_{eff} is the effective cavity length (taking electric field penetration depth into the mirrors and the effect of the Gouy phase into account). For the simple one-dimensional model considered here, we can set $L_{\text{eff}} = L_{cav}$, and — using eq. 3.9 — rewrite eq. 3.12 as

$$F_P \quad = \quad \underbrace{\frac{3}{2\pi}\frac{\lambda^2}{n^2}}_{\substack{\text{Dipole absorption} \\ \text{cross section}}} \times \underbrace{\frac{F}{\pi}}_{\substack{\text{Photon bounces} \\ \text{in cavity}}} \times \underbrace{\frac{4}{w_0^2 \pi}}_{\substack{\text{Inverse cavity} \\ \text{beam area}}} \times \underbrace{|\hat{d}\cdot\hat{e}|^2}_{\substack{\text{Polarization overlap} \\ \text{cavity - dipole}}}. \tag{3.13}$$

$$\underbrace{F_P}_{\substack{\text{Purcell} \\ \text{factor}}}$$

This gives us an intuitive understanding of the Purcell factor: the cavity enhances the emission with a factor determined by the ratio of the beam area in the cavity to the absorption cross section of the dipole [4], multiplied by the number of round trips a photon makes between the cavity mirrors before it leaks out the resonator, taking into account the overlap of the direction of the emission dipole with the electric field polarization in the cavity.

3.1.4. FRACTION OF ZERO-PHONON LINE EMISSION FOR THE NV CENTER

So far, we have focused on a dipole emitter with only one ground and one excited energy state. In the case of color centers in diamond, the situation is more complicated: Their radiative emission rate, γ_{rad}, is divided into a zero-phonon line (ZPL) emission fraction, β_0, given by the Debye-Waller factor, and a phonon sideband (PSB) emission fraction $(1-\beta_0)$, as introduced in Ch. 2 for the nitrogen-vacancy (NV) center. Additionally, some states decay partly via additional transitions to singlet states (see Ch. 2), which we model as a non-radiative decay at rate γ_{dark}. Thus, without interaction with a cavity, we can model the decay from the NV center excited state as:

$$\gamma_0 = \beta_0\gamma_{rad} + (1-\beta_0)\gamma_{rad} + \gamma_{dark}. \tag{3.14}$$

As introduced above, coupling ZPL transitions of an NV center to the mode of the cavity opens up another decay channel, which we can quantify with a ZPL enhancement factor, F_P^{ZPL}. For a cavity on resonance with a NV ZPL transition, the decay rate from the NV excited state, modified by the cavity, γ', is then given as

$$\gamma' = F_P^{ZPL}\beta_0\gamma_{rad} + \beta_0\gamma_{rad} + (1-\beta_0)\gamma_{rad} + \gamma_{dark}. \tag{3.15}$$

Thus, in our definition, F_P^{ZPL} characterizes the enhancement of the ZPL from the cavity mode, rather than the overall increase in emission in all directions. This better represents the increase in coherent light emitted from the NV dipole that we can readily pick up, as it is emitted in a well defined mode of the optical cavity (as opposed to the case of emission into a homogeneous medium, for which emission happens in all directions).

Under the assumption that $\gamma_{rad} \gg \gamma_{dark}$, which is satisfied for the NV center measurements in this thesis (see Ch. 6), we can combine eq. 3.14 and eq. 3.15, and obtain

$$\frac{\gamma'}{\gamma_0} = \frac{\tau_0}{\tau'} = 1 + F_P^{ZPL}\beta_0\frac{\gamma_{rad}}{\gamma_{rad}+\gamma_{dark}} \tag{3.16}$$

$$\approx 1 + F_P^{ZPL}\beta_0,$$

where $\tau_0 = 1/\gamma_0$ is the NV center lifetime without the cavity and $\tau' = 1/\gamma'$ is the modified lifetime with the cavity. We can then re-write eq. 3.16 as

$$F_P^{ZPL} = \frac{1}{\beta_0}\left(\frac{\tau_0}{\tau'} - 1\right). \tag{3.17}$$

Thus, comparing the lifetime of an NV center on and off-resonance with a cavity allows us to extract the Purcell factor for a certain NV center transition. We will make use of this technique in Ch. 6.

From eq. 3.16, we see that the fraction of light emitted into the ZPL in the cavity mode, β_{cav} is

$$\beta_{cav} = \frac{F_P^{ZPL}\beta_0}{F_P^{ZPL}\beta_0 + 1}. \tag{3.18}$$

If the assumption that γ_{dark} is negligible is incorrect, then $F_P^{ZPL}\beta_0$ is increased by a factor of $(\gamma_{rad} + \gamma_{dark})/\gamma_{rad}$. Thus, this method allows us to extract a lower bound on the Purcell enhancement in the cavity. In reverse, this means that by measuring the Purcell factor for different cavity lengths (and building a full transfer matrix model of the cavity, see Ch. 4), we can extract the quantum efficiency of an emitter, $\eta_q = \frac{\gamma_{rad}}{\gamma_{rad}+\gamma_{dark}}$, as the cavity only enhances the radiative decay rate; this method assumes that by changing the cavity length, the cavity field - emitter overlap remains constant. If the experimental setup does not allow to tune the cavity length while keeping the emitter - cavity lateral field overlap constant, we can still extract a lower bound on the quantum efficiency by measuring the maximum Purcell enhancement for many emitters (thus sampling from different cavity field - emitter overlaps), and comparing the highest Purcell value with a theoretical model.

3.2. COOPERATIVITY AND EMITTER BROADENING

In Sec. 3.1, we quantified the enhancement of radiative emission in the zero-phonon line using the Purcell factor, F_P^{ZPL}; the radiative emission rate enhancement in the cavity mode is given as $F_P^{ZPL} \times \beta_0$ when taking the considerations of Sec. 3.1.4 into account. We can then re-write eq. 3.12, using $\kappa = 2\pi\Delta_\omega$, and eqs. 3.3 and 3.11 as

$$F_P^{ZPL}\beta_0 = \frac{\Gamma_{cav}}{\Gamma_{hom}} = \frac{4g^2}{\kappa\gamma_0} = C, \tag{3.19}$$

where C is known as the cooperativity. While this quantifies the efficiency of the spin-photon interface, it does not take into account the coherence of the emitter: in practice, solid-state emitters often experience additional decay due to unwanted interactions with the environment of the solid-state host, γ_{dep}, which manifests in broadening of the optical transitions above the lifetime limited value [8–13]. Therefore, it is useful to introduce the coherent cooperativity, C_{coh}, which quantifies the ratio of coherent decay into the cavity mode to undesired decay, and is given as

$$C_{coh} = \frac{4g^2}{\kappa\gamma} = C\frac{\gamma_0}{\gamma} = F_P^{ZPL}\beta_0\frac{\gamma_0}{\gamma}, \tag{3.20}$$

where $\gamma = \gamma_0 + \gamma_{dep}$ [14, 15]; C_{coh} can be interpreted as the probability of coherent atom-photon interaction, and plays an important role in the fidelity and efficiency of many near-deterministic quantum protocols [14].

In the following sections, we will investigate the implications of different coherent cooperativity regimes for enhancement of the spin-photon interface of color centers in diamond.

REGIME OF LOW COHERENT COOPERATIVITY ($C_{coh} \lesssim 1$)

In the regime of low coherent cooperativity, $C_{coh} \lesssim 1$, the coupling between the emitter and the cavity is less than or equal to the decay rates, meaning that there is a low chance for a photon to interact with the emitter before it leaks out of the resonator or the emitter dephases. The total cavity decay rate, κ, consists of inevitable losses (such as scattering and absorption), κ_l, and the coupling to an output mode, κ_c, which can be chosen by design, i.e. $\kappa = \kappa_c + \kappa_l$. Typical emitter-cavity systems in the weak coupling regime operate with $\kappa \gg \{g, \gamma\}$, which is favourable for photon collection when engineering $\kappa_c \gg \kappa_l$ (note that this design choice comes at the expense of lowering the Purcell enhancement).

Notably, all low-temperature NV center-cavity systems studied to date have been operated in the limit of low coherent cooperativity, mostly limited by inhomogeneous broadening of optical transitions, induced by surface effects. This has limited optical coherence of cavity-coupled NV centers to minimal values of $\gamma \gtrsim 1$ GHz [10], and thus $C_{coh} << 1$, even for systems for which $F_P^{ZPL}\beta_0 = C \gtrsim 1$ [10, 16].

The low cooperativity regime is optimal for an enhancement of collected photons; we note that cooperativites on the order of one for an NV-based cavity system would allow for quantum repeaters which outperform direct transmission [17] . As discussed in Ch. 5, entanglement generation requires indistinguishable photons, necessitating photon detection in a time window $\propto 1/\gamma$. Here, Purcell enhancement in a cavity can be of help to counteract spectral diffusion at rate γ_{dep}: it leads to Purcell broadened linewidths with decay rate (for the ZPL transition on resonance with the cavity)

$$\gamma_P = \gamma + \frac{4g^2}{\kappa} = (\gamma_0 + \gamma_{dep}) + \frac{4g^2}{\kappa}. \tag{3.21}$$

Thus, for sufficiently large Purcell factors F_P^{ZPL} and low spectral diffusion dephasing rates γ_{dep}, Purcell broadening of the lines can recover near-to-ideal photon indistinguishability, for which $\gamma_{dep} \ll \gamma_P$.

REGIME OF HIGH COHERENT COOPERATIVITY ($C_{coh} \gg 1$)

In the regime of high coherent cooperativity, $C_{coh} \gg 1$, on the other hand, the squared coupling between the emitter and the cavity is stronger than the multiplied decay rates, so there is a high probability for a photon to interact with the emitter before it leaks out of the resonator or the emitter dephases. This regime enables near-deterministic interactions between the emitter and photon, whose efficiency and fidelity scale with the cooperativity [14].

As discussed above, reaching $C_{coh} \gg 1$ has remained elusive for the NV center, due to poor optical properties near surfaces, resulting from a first order sensitivity of the NV center to electric field fluctuations (see Ch. 2); however, bringing the emitter close to surfaces (to reduce the mode volume) is crucial to increase g sufficiently to achieve $C_{coh} \gg 1$, see eq. 3.12, even more so because of the low intrinsic optical emission in the zero phonon line.

Due to their first order insensitivity to electric fields, group IV vacancy centers in diamond display a promising alternative to nitrogen vacancy centers in diamond for efficient spin-photon interfaces. This electric field insensitivity means that their optical transitions feature close-to-lifetime limited values even in heavily fabricated nanopho-

tonic (cavity) structures [13, 18, 19]; this has recently allowed such systems to exceed $C_{coh} > 100$ [20]. Here, spin-photon entanglement has been generated using reflection based schemes, in which weak coherent photon states are reflected off of the cavity. The spin-dependant reflection amplitude then discriminates the spin states of silicon vacancy centers [12, 18] (see Ch. 7); notably, current state-of-the art cavities operate in the "bad cavity limit" ($\kappa \gg g \gg \gamma$).

3.3. OVERVIEW OF CAVITY DESIGNS FOR DEFECTS IN DIAMOND

Having discussed the fundamentals of emitter-cavity coupling, we here give a brief overview of cavity systems that have been realized to date to enhance the spin-photon interface of color centers in diamond; Fig. 3.2 shows an overview of these systems.

3.3.1. MONOLITHIC CAVITY DESIGNS

A first class of cavities are monolithic designs, which are either fabricated in diamond containing color centers, or in another host material that is brought in close proximity to couple evanescently to the diamond color center emitters. While such structures are inherently insusceptible to cavity length fluctuations due to their monolithic design, cavity-frequency tuning ranges (most commonly done via gas condensation and selective gas removal via controlled laser-induced heating [18]) are typically limited. However, these structures can produce very large Purcell factors due to their low mode volume.

WHISPERING GALLERY MODE AND RING RESONATORS

Fig. 3.2(a) shows an image of a whispering gallery mode resonator in diamond, for which quality factors exceeding $Q > 10^5$ have been realized at telecommunication wavelengths [21–23]. These structures are conceptually similar to ring resonators, which feature an additional hole in the middle [22, 24], and have typical mode volumes $\sim (15 - 30)(\lambda / n)^3$, where λ is the wavelength of the resonance, and n is the refractive index of diamond.

PHOTONIC CRYSTAL CAVITIES

Fig. 3.2(b) shows an image of an all diamond one dimensional nanobeam photonic crystal cavity (PCC), with the potential to embed a color center in the middle of the beam. Light is confined to the nanobeam via index-guiding along off-axial directions (when taking the axis along the nanobeam), while a periodic modulation of the refractive index (achieved by creating regularly spaced holes in the diamond) confines light along the axis of the beam (see Ch. 7). The advantage of PCC structures compared to whispering gallery mode and ring resonators is that very small optical mode volumes $V \ll (\lambda / n)^3$ are readily achievable. PCC-coupling of NV centers at low temperatures has been shown in many works, including Refs. [16, 27–31]. Yet, as discussed above, spectral diffusion originating from heavily fabricated surfaces has substantially broadened NV transition linewidths in such devices, preventing coherent cooperativities $C_{coh} \geq 1$. Despite a decade of active research, embedding NV centers in nanophotonic devices in a way that maintains their optical coherence has remained elusive.

Instead, the focus of the diamond PCC community has shifted to enhancing the spin-photon interface of inversion symmetric group IV color centers in diamond, which include Si, Ge, Sn, and Pb related defects [13, 32–36]. To date, PCC coupling of group IV
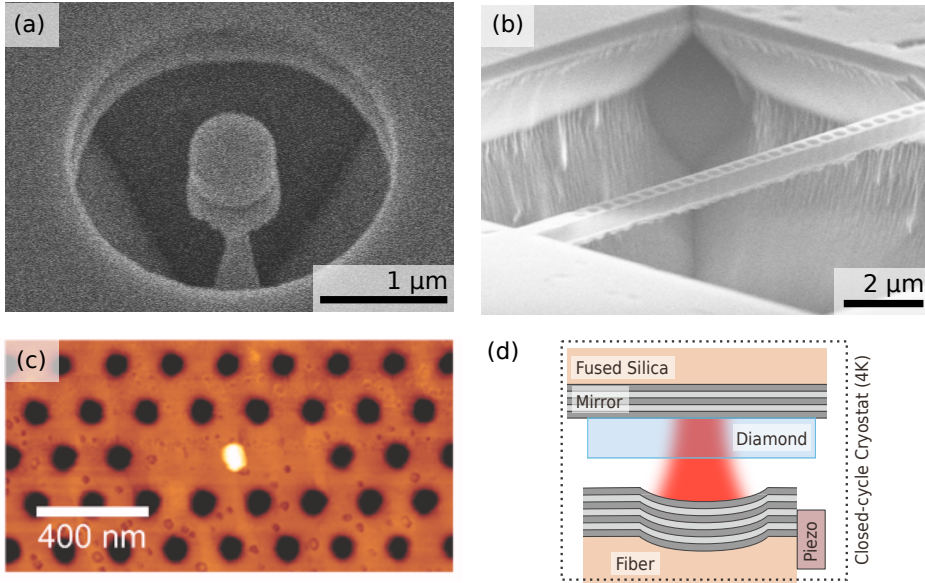
Figure 3.2: Overview of different cavity geometries used to enhance the zero-phonon line emission of color centers in diamond to date. (a) Whispering gallery mode like resonator. (b) One dimensional photonic crystal cavity in diamond (c) Evanescently coupled GaP two dimensional photonic crystal cavity with a nanodiamond positioned in the middle of the mode. Figure reprinted from Ref. [25], with the permission of AIP Publishing. (d) Open, tuneable Fabry-Perot microcavity containing a μm-thin diamond membrane. Figure adapted with permission from Ref. [26], in accordance with creativecommons.org/licenses/by/4.0/legalcode

color centers in diamond at low temperatures has been demonstrated for the SiV [12, 18, 20, 37, 38] and SnV [39] center (for GeV centers, all-diamond waveguide emitter coupling has been demonstrated [40]), with recent SiV-cavity systems achieving coherent cooperativities $C_{coh} > 100$ [20].

Ch. 7 of this thesis gives an introduction to group IV color centers in diamond. We focus on the theoretical understanding and design of photonic crystal cavities in diamond, on methods to optimize structures for highest Q/V ratios, and on a strategy for efficient in- and outcoupling to/from these devices. In Ch. 8, we discuss different methods that have been used to fabricate all-diamond photonic crystal cavities (ADPCC) to date, present a process flow that allows to fabricate rectangular ADPCCs, and present measurements of the quality factors of these structures.

CAVITIES WITH EVANESCENTLY COUPLED COLOR CENTERS

Another method of enhancing the zero-phonon line (ZPL) emission of color centers in diamond is to bring an emitter close to a cavity fabricated in a different host material. Historically, this method has been explored before fabrication of photonic crystal cavities (PCC) in diamond itself, since techniques for fabricating PCCs in different materials were readily available, and devices thus more straightforward to achieve.

One method is to fabricate a photonic crystal cavity in a common wide-bandgap

material such as GaP or Si_3N_4, and then place a nanodiamond containing a color center close to its field maximum using micromanipulators; this technique has been explored for both NV centers [25, 41, 42] and SiV centers [43], see Fig. 3.2(c). An opposite strategy was followed in Ref. [44], in which nanodiamonds were encapsulated in a polymer film, and a GaP photonic crystal cavity (fabricated on a different substrate) was placed on top using micromanipulators. Another method used to enhance the ZPL emission of NV centers is to deposit a thin semiconductor film on top of a bulk diamond substrate containing color centers close to its top surface, and fabricate a photonic crystal cavity in the semiconductor [45, 46].

Such evanescently coupled systems suffer from the fundamental trade-off of placing the dipole emitter as close to the electric field maximum of the cavity as possible (i.e. as close to the diamond surface as possible), while maintaining good optical coherence to allow for high coherent cooperativity. As discussed above, reaching this regime has remained elusive for color centers in diamond, including NV and SiV centers.

3.3.2. Open Fabry-Perot micro-cavities

In contrast to the monolithic cavity designs discussed above, a cavity can also be formed around a color center by embedding a microns-thin piece of diamond in between two macroscopic highly reflective mirrors, see Fig. 3.2(d). To achieve small mode volume, such cavities are typically formed from one super-polished macroscopic substrate, and one sub-mm sized substrate. Most commonly, the latter is the cleaved tip of an optical fiber, in which a Gaussian shaped dimple is formed via laser ablation of the substrate, evaporating and re-flowing the surface [47–51]; this can create structures with sub-nanometer surface roughness. Both substrates can then be coated with high reflectivity mirror coatings, with demonstrated finesse values $F \gg 10^5$. In principle, using a fiber as one of the mirrors offers a straightforward way of in- (out-) coupling of light to (from) the cavity, while its small diameter allows for low mode volumes (tens of $[\lambda/n]^3$) even if the two mirror surfaces are not perfectly parallel (as the substrates touching at the edges would otherwise prevent reaching small cavity lengths). Mounting one of the mirrors on a piezoelectric element allows for spatial and spectral tuneability of the cavity, at the cost of increasing susceptibility to vibrations in the system (compared to a monolithic design) [26, 52].

Cavity enhancement of color centers in nanodiamonds embedded in an open Fabry-Perot microcavity at room temperature has been demonstrated for both NV centers [53–57] and SiV centers [58], with the only low temperature (77 K) realization in Ref. [56]. However, these experiments suffered from poor optical coherence (see discussion above), and / or significant additional losses introduced by scattering or absorption in the nanodiamond.

Another method is to embed microns-thin diamond membranes in a cavity in an effort to retain bulk-like optical properties; initial work showed the realization of cavities with finesse $F \gg 10^4$ at room-temperature [59] and $T \sim 10$ K [52]. Before this thesis, the only work showcasing Purcell enhancement of NV centers at 4 K in a diamond membrane was done in Ref. [10], with achieved Purcell factors $F_P^{ZPL} \sim 30$. However, spectral diffusion (≥ 1 GHz) of implanted NV centers in these devices prevented resonant excitation and subsequent detection of coherent photons, a crucial component of entangle-

ment protocols involving the NV center [60]. Recently, both GeV centers [61] and SiV centers[62, 63] have been coupled to open microcavities at room temperature, demonstrating the versatility of the open microcavity platform.

In Ch. 5 of this thesis, we demonstrate that combining diamond electron irradiation (creating vacancies throughout the diamond), high temperature annealing (to recombine vacancies with naturally occurring nitrogen in the diamond, forming NV centers), and an optimized etching sequence (to obtain sub-nanometer surface roughness in microns-thin etched membranes) allows the fabrication of diamond membranes containing NV centers with optical properties that are compatible with entanglement generation protocols. In Ch. 6, we use such a device to demonstrate the first pulsed resonant excitation and detection of coherent NV center emission in optical cavities, paving the way for efficient quantum networks based on Purcell-enhanced NV centers in diamond.

3

REFERENCES

[1] P. A. M. Dirac, *The Quantum Theory of the Emission and Absorption of Radiation,* Proceedings of the Royal Society of London **114** (1927).

[2] E. Fermi, *Nuclear Physics: A Course Given by Enrico Fermi at the University of Chicago* (University of Chicago Press, Chicago, 1950).

[3] B. Simons, *Advanced Quantum Mechanics* (Lecture Notes, University of Cambridge, Cambridge, 2009).

[4] A. Reiserer and G. Rempe, *Cavity-based quantum networks with single atoms and optical photons,* Reviews of Modern Physics **87**, 1379 (2015).

[5] M. Fox, *Quantum Optics* (Oxford University Press, Oxford, 2006).

[6] B. E. Saleh and M. C. Teich, *Fundamentals of Photonics, Vol. 22* (Wiley, New York, 1991).

[7] M. Ruf, *Fiber-based Fabry-Perot Microcavities,* MSc thesis, McGill University (2016).

[8] L. Robledo, H. Bernien, I. van Weperen and R. Hanson, *Control and Coherence of the Optical Transition of Single Nitrogen Vacancy Centers in Diamond,* Physical Review Letters **105**, 177403 (2010).

[9] C. Santori, P. E. Barclay, K.-M. C. Fu, R. G. Beausoleil, S. Spillane and M. Fisch, *Nanophotonics for quantum optics using nitrogen-vacancy centers in diamond,* Nanotechnology **21**, 274008 (2010).

[10] D. Riedel, I. Söllner, B. J. Shields, S. Starosielec, P. Appel, E. Neu, P. Maletinsky and R. J. Warburton, *Deterministic enhancement of coherent photon generation from a nitrogen-vacancy center in ultrapure diamond,* Physical Review X **7**, 1 (2017).

[11] U. Jantzen, A. B. Kurz, D. S. Rudnicki, C. Schäfermeier, K. D. Jahnke, U. L. Andersen, V. A. Davydov, V. N. Agafonov, A. Kubanek, L. J. Rogers and F. Jelezko, *Nanodiamonds carrying silicon-vacancy quantum emitters with almost lifetime-limited linewidths,* New Journal of Physics **18**, 073036 (2016).

[12] C. T. Nguyen, D. D. Sukachev, M. K. Bhaskar, B. MacHielse, D. S. Levonian, E. N. Knall, P. Stroganov, R. Riedinger, H. Park, M. Lončar and M. D. Lukin, *Quantum Network Nodes Based on Diamond Qubits with an Efficient Nanophotonic Interface,* Physical Review Letters **123**, 1 (2019).

[13] A. E. Rugar, C. Dory, S. Aghaeimeibodi, H. Lu, S. Sun, S. D. Mishra, Z.-X. Shen, N. A. Melosh and J. Vučković, *Narrow-Linewidth Tin-Vacancy Centers in a Diamond Waveguide,* ACS Photonics **7**, 2356 (2020).

[14] J. Borregaard, A. S. Sørensen and P. Lodahl, *Quantum Networks with Deterministic Spin–Photon Interfaces,* Advanced Quantum Technologies **2**, 1800091 (2019).

[15] E. Janitz, M. K. Bhaskar and L. Childress, *Cavity quantum electrodynamics with color centers in diamond*, Optica **7**, 1232 (2020).

[16] A. Faraon, C. Santori, Z. Huang, V. M. Acosta and R. G. Beausoleil, *Coupling of Nitrogen-Vacancy Centers to Photonic Crystal Cavities in Monocrystalline Diamond*, Physical Review Letters **109**, 033604 (2012).

[17] F. Rozpędek, R. Yehia, K. Goodenough, M. Ruf, P. C. Humphreys, R. Hanson, S. Wehner and D. Elkouss, *Near-term quantum-repeater experiments with nitrogen-vacancy centers: Overcoming the limitations of direct transmission*, Physical Review A **99**, 052330 (2019).

[18] C. T. Nguyen *et al.*, *An integrated nanophotonic quantum register based on silicon-vacancy spins in diamond*, Physical Review B **100**, 1 (2019).

[19] N. H. Wan, T.-J. Lu, K. C. Chen, M. P. Walsh, M. E. Trusheim, L. De Santis, E. A. Bersin, I. B. Harris, S. L. Mouradian, I. R. Christen, E. S. Bielejec and D. Englund, *Large-scale integration of artificial atoms in hybrid photonic circuits*, Nature **583**, 226 (2020).

[20] M. K. Bhaskar, R. Riedinger, B. Machielse, D. S. Levonian, C. T. Nguyen, E. N. Knall, H. Park, D. Englund, M. Lončar, D. D. Sukachev and M. D. Lukin, *Experimental demonstration of memory-enhanced quantum communication*, Nature **580**, 60 (2020).

[21] B. J. Hausmann, B. Shields, Q. Quan, P. Maletinsky, M. McCutcheon, J. T. Choy, T. M. Babinec, A. Kubanek, A. Yacoby, M. D. Lukin and M. Lončar, *Integrated diamond networks for quantum nanophotonics*, Nano Letters **12**, 1578 (2012).

[22] M. J. Burek, Y. Chu, M. S. Z. Liddy, P. Patel, J. Rochman, S. Meesala, W. Hong, Q. Quan, M. D. Lukin and M. Lončar, *High quality-factor optical nanocavities in bulk single-crystal diamond*, Nature Communications **5**, 5718 (2014).

[23] M. Mitchell, D. P. Lake and P. E. Barclay, *Realizing Q > 300 000 in diamond microdisks for optomechanics via etch optimization*, APL Photonics **4**, 016101 (2019).

[24] A. Faraon, P. E. Barclay, C. Santori, K. M. C. Fu and R. G. Beausoleil, *Resonant enhancement of the zero-phonon emission from a colour centre in a diamond cavity*, Nature Photonics **5**, 301 (2011).

[25] J. Wolters, A. W. Schell, G. Kewes, N. Nüsse, M. Schoengen, H. Döscher, T. Hannappel, B. Löchel, M. Barth and O. Benson, *Enhancement of the zero phonon line emission from a single nitrogen vacancy center in a nanodiamond via coupling to a photonic crystal cavity*, Applied Physics Letters **97**, 141108 (2010).

[26] M. Ruf, M. Weaver, S. van Dam and R. Hanson, *Resonant Excitation and Purcell Enhancement of Coherent Nitrogen-Vacancy Centers Coupled to a Fabry-Perot Microcavity*, Physical Review Applied **15**, 024049 (2021).

[27] B. J. M. Hausmann *et al.*, *Coupling of NV Centers to Photonic Crystal Nanobeams in Diamond*, Nano Letters **13**, 5791 (2013).

3

[28] L. Li *et al.*, *Coherent spin control of a nanocavity-enhanced qubit in diamond*, Nature Communications **6**, 6173 (2015).

[29] J. Riedrich-Möller, S. Pezzagna, J. Meijer, C. Pauly, F. Mücklich, M. Markham, A. M. Edmonds and C. Becher, *Nanoimplantation and Purcell enhancement of single nitrogen-vacancy centers in photonic crystal cavities in diamond*, Applied Physics Letters **106**, 2 (2015).

[30] T. Schröder, M. Walsh, J. Zheng, S. Mouradian, L. Li, G. Malladi, H. Bakhru, M. Lu, A. Stein, M. Heuck and D. Englund, *Scalable fabrication of coupled NV center-photonic crystal cavity systems by self-aligned N ion implantation*, Optical Materials Express **7**, 682 (2017).

[31] T. Jung, J. Görlitz, B. Kambs, C. Pauly, N. Raatz, R. Nelz, E. Neu, A. M. Edmonds, M. Markham, F. Mücklich, J. Meijer and C. Becher, *Spin measurements of NV centers coupled to a photonic crystal cavity*, APL Photonics **4**, 120803 (2019).

[32] G. Thiering and A. Gali, *Ab Initio Magneto-Optical Spectrum of Group-IV Vacancy Color Centers in Diamond*, Physical Review X **8**, 021063 (2018).

[33] T. Müller, C. Hepp, B. Pingault, E. Neu, S. Gsell, M. Schreck, H. Sternschulte, D. Steinmüller-Nethl, C. Becher and M. Atatüre, *Optical signatures of silicon-vacancy spins in diamond*, Nature Communications **5**, 3328 (2014).

[34] T. Iwasaki *et al.*, *Germanium-Vacancy Single Color Centers in Diamond*, Scientific Reports **5**, 1 (2015).

[35] M. E. Trusheim *et al.*, *Transform-Limited Photons from a Coherent Tin-Vacancy Spin in Diamond*, Physical Review Letters **124**, 1 (2020).

[36] M. E. Trusheim *et al.*, *Lead-related quantum emitters in diamond*, Physical Review B **99**, 1 (2019).

[37] A. Sipahigil *et al.*, *An integrated diamond nanophotonics platform for quantum-optical networks*, Science **354**, 847 (2016).

[38] R. E. Evans *et al.*, *Photon-mediated interactions between quantum emitters in a diamond nanocavity*, Science **362**, 662 (2018).

[39] A. E. Rugar, S. Aghaeimeibodi, D. Riedel, C. Dory, H. Lu, P. J. McQuade, Z.-X. Shen, N. A. Melosh and J. Vučković, *Quantum Photonic Interface for Tin-Vacancy Centers in Diamond*, Physical Review X **11**, 031021 (2021).

[40] M. K. Bhaskar *et al.*, *Quantum Nonlinear Optics with a Germanium-Vacancy Color Center in a Nanoscale Diamond Waveguide*, Physical Review Letters **118**, 223603 (2017).

[41] T. Van Der Sar, J. Hagemeier, W. Pfaff, E. C. Heeres, S. M. Thon, H. Kim, P. M. Petroff, T. H. Oosterkamp, D. Bouwmeester and R. Hanson, *Deterministic nanoassembly of a coupled quantum emitter-photonic crystal cavity system*, Applied Physics Letters **98**, 1 (2011).

[42] K. G. Fehler, A. P. Ovvyan, N. Gruhler, W. H. P. Pernice and A. Kubanek, *Efficient Coupling of an Ensemble of Nitrogen Vacancy Center to the Mode of a High-Q, Si3N4 Photonic Crystal Cavity*, ACS Nano **13**, 6891 (2019).

[43] K. G. Fehler, A. P. Ovvyan, L. Antoniuk, N. Lettner, N. Gruhler, V. A. Davydov, V. N. Agafonov, W. H. Pernice and A. Kubanek, *Purcell-enhanced emission from individual SiV-center in nanodiamonds coupled to a Si3N4-based, photonic crystal cavity*, Nanophotonics **9**, 3655 (2020).

[44] D. Englund, B. Shields, K. Rivoire, F. Hatami, J. Vučković, H. Park and M. D. Lukin, *Deterministic coupling of a single nitrogen vacancy center to a photonic crystal cavity*, Nano Letters **10**, 3922 (2010).

[45] P. E. Barclay, K. M. C. Fu, C. Santori, A. Faraon and R. G. Beausoleil, *Hybrid nanocavity resonant enhancement of color center emission in diamond*, Physical Review X **1**, 1 (2011).

[46] M. Gould, E. R. Schmidgall, S. Dadgostar, F. Hatami and K. M. C. Fu, *Efficient Extraction of Zero-Phonon-Line Photons from Single Nitrogen-Vacancy Centers in an Integrated GaP-on-Diamond Platform*, Physical Review Applied **6**, 2 (2016).

[47] D. Hunger, T. Steinmetz, Y. Colombe, C. Deutsch, T. W. Hänsch and J. Reichel, *A fiber Fabry–Perot cavity with high finesse*, New Journal of Physics **12**, 065038 (2010).

[48] D. Hunger, C. Deutsch, R. J. Barbour, R. J. Warburton and J. Reichel, *Laser microfabrication of concave, low-roughness features in silica*, AIP Advances **2**, 012119 (2012).

[49] J. Benedikter, T. Hümmer, M. Mader, B. Schlederer, J. Reichel, T. W. Hänsch and D. Hunger, *Transverse-mode coupling and diffraction loss in tunable Fabry–Pérot microcavities*, New Journal of Physics **17**, 053051 (2015).

[50] M. Uphoff, M. Brekenfeld, G. Rempe and S. Ritter, *Frequency splitting of polarization eigenmodes in microscopic Fabry–Perot cavities*, New Journal of Physics **17**, 013053 (2015).

[51] J. Gallego, S. Ghosh, S. K. Alavi, W. Alt, M. Martinez-Dorantes, D. Meschede and L. Ratschbacher, *High-finesse fiber Fabry–Perot cavities: stabilization and mode matching analysis*, Applied Physics B **122**, 47 (2016).

[52] S. Bogdanović, S. B. van Dam, C. Bonato, L. C. Coenen, A.-M. J. Zwerver, B. Hensen, M. S. Z. Liddy, T. Fink, A. Reiserer, M. Lončar and R. Hanson, *Design and low-temperature characterization of a tunable microcavity for diamond-based quantum networks*, Applied Physics Letters **110**, 171103 (2017).

[53] R. Albrecht, A. Bommer, C. Deutsch, J. Reichel and C. Becher, *Coupling of a Single Nitrogen-Vacancy Center in Diamond to a Fiber-Based Microcavity*, Physical Review Letters **110**, 243602 (2013).

[54] H. Kaupp, C. Deutsch, H. C. Chang, J. Reichel, T. W. Hänsch and D. Hunger, *Scaling laws of the cavity enhancement for nitrogen-vacancy centers in diamond*, Physical Review A - Atomic, Molecular, and Optical Physics **88**, 1 (2013).

[55] R. Albrecht, A. Bommer, C. Pauly, F. Mücklich, A. W. Schell, P. Engel, T. Schröder, O. Benson, J. Reichel and C. Becher, *Narrow-band single photon emission at room temperature based on a single nitrogen-vacancy center coupled to an all-fiber-cavity*, Applied Physics Letters **105**, 073113 (2014).

[56] S. Johnson, P. R. Dolan, T. Grange, A. A. P. Trichet, G. Hornecker, Y. C. Chen, L. Weng, G. M. Hughes, A. A. . R. Watt, A. Auffeves and J. M. Smith, *Tunable cavity coupling of the zero phonon line of a nitrogen-vacancy defect in diamond*, New Journal of Physics **17**, 122003 (2015).

[57] H. Kaupp, T. Hümmer, M. Mader, B. Schlederer, J. Benedikter, P. Haeusser, H.-C. Chang, H. Fedder, T. W. Hänsch and D. Hunger, *Purcell-Enhanced Single-Photon Emission from Nitrogen-Vacancy Centers Coupled to a Tunable Microcavity*, Physical Review Applied **6**, 054010 (2016).

[58] J. Benedikter, H. Kaupp, T. Hümmer, Y. Liang, A. Bommer, C. Becher, A. Krueger, J. M. Smith, T. W. Hänsch and D. Hunger, *Cavity-Enhanced Single-Photon Source Based on the Silicon-Vacancy Center in Diamond*, Physical Review Applied **7**, 024031 (2017).

[59] E. Janitz, M. Ruf, M. Dimock, A. Bourassa, J. Sankey and L. Childress, *Fabry-Perot microcavity for diamond-based photonics*, Physical Review A - Atomic, Molecular, and Optical Physics **92**, 1 (2015).

[60] H. Bernien, B. Hensen, W. Pfaff, G. Koolstra, M. S. Blok, L. Robledo, T. H. Taminiau, M. Markham, D. J. Twitchen, L. Childress and R. Hanson, *Heralded entanglement between solid-state qubits separated by three metres*, Nature **497**, 86 (2013).

[61] R. Høy Jensen, E. Janitz, Y. Fontana, Y. He, O. Gobron, I. P. Radko, M. Bhaskar, R. Evans, C. D. Rodríguez Rosenblueth, L. Childress, A. Huck and U. Lund Andersen, *Cavity-Enhanced Photon Emission from a Single Germanium-Vacancy Center in a Diamond Membrane*, Physical Review Applied **13**, 064016 (2020).

[62] S. Häußler, J. Benedikter, K. Bray, B. Regan, A. Dietrich, J. Twamley, I. Aharonovich, D. Hunger and A. Kubanek, *Diamond photonics platform based on silicon vacancy centers in a single-crystal diamond membrane and a fiber cavity*, Physical Review B **99**, 1 (2019).

[63] M. Salz, Y. Herrmann, A. Nadarajah, A. Stahl, M. Hettrich, A. Stacey, S. Prawer, D. Hunger and F. Schmidt-Kaler, *Cryogenic platform for coupling color centers in diamond membranes to a fiber-based microcavity*, Applied Physics B **126**, 131 (2020).

4

OPTIMAL DESIGN OF DIAMOND-AIR MICROCAVITIES FOR QUANTUM NETWORKS USING AN ANALYTICAL APPROACH

Suzanne van Dam, Maximilian Ruf, and Ronald Hanson

Defect centres in diamond are promising building blocks for quantum networks thanks to a long-lived spin state and bright spin-photon interface. However, their low fraction of emission into a desired optical mode limits the entangling success probability. The key to overcoming this is through Purcell enhancement of the emission. Open Fabry-Pérot cavities with an embedded diamond membrane allow for such enhancement while retaining good emitter properties. To guide the focus for design improvements it is essential to understand the influence of different types of losses and geometry choices. In particular, in the design of these cavities a high Purcell factor has to be weighed against cavity stability and efficient outcoupling. To be able to make these trade-offs we develop analytic descriptions of such hybrid diamond-and-air cavities as an extension to previous numeric methods. The insights provided by this analysis yield an effective tool to find the optimal design parameters for a diamond-air cavity.

4.1. INTRODUCTION

Quantum networks rely on entanglement distributed among distant nodes [2]. Nitrogen-vacancy (NV) defect centers in diamond can be used as building blocks for such networks, with a coherent spin-photon interface that enables the generation of heralded distant entanglement [3, 4]. The long-lived electron spin and nearby nuclear spins provide quantum memories that are crucial for extending entanglement to multiple nodes and longer distances [5–9]. However, to fully exploit the NV centre as a quantum network building block requires increasing the entanglement success probability. One limitation to this probability is the low efficiency of the NV spin-photon interface. Specifically, entanglement protocols depend on coherent photons emitted into the zero-phonon line (ZPL), which is only around 3% of the total emission [10], and collection efficiencies are finite due to limited outcoupling efficiency out of the high-refractive index diamond. These can both be improved by embedding the NV centre in an optical microcavity at cryogenic temperatures, benefiting from Purcell enhancement [11–18]. A promising cavity design for applications in quantum networks is an open Fabry-Pérot microcavity with an embedded diamond membrane [10, 19–21]. Such a design provides spatial and spectral tunability and achieves a strong mode confinement while the NV centre can reside in the diamond membrane far away ($\approx$ μm) from the surface to maintain bulk-like optical properties.

The overall purpose of the cavity system is to maximize the probability to detect a ZPL photon after a resonant excitation pulse. This figure of merit includes both efficient emission into the ZPL into the cavity mode, and efficient outcoupling out of the cavity. The core requirement is accordingly to resonantly enhance the emission rate into the ZPL. However this must be accompanied by vibrational stability of the system; an open cavity design is especially sensitive to mechanical vibrations that change the cavity length, bringing the cavity off-resonance with the NV centre optical transition. Furthermore the design should be such that the photons in the cavity mode are efficiently collected. We aim to optimize the cavity parameters in the face of these (often contradicting) requirements. For this task, analytic expressions allow the influence of individual parameters to be clearly identified and their interplay to be better understood. In this manuscript we take the numerical methods developed in [20] as a starting point, and find the underlying analytic descriptions of hybrid diamond-air cavities. We use these new analytic descriptions to investigate the optimal parameters for a realistic cavity design.

We define two boundary conditions for the design of the cavity, within which we operate to maximize the figure of merit: the probability to detect a ZPL photon. Firstly we require the optical transition to be little influenced by decoherence and spectral diffusion so that the emitted photons can be used for generating entanglement between remote spins [3]. Showing enhancement of the ZPL of narrow linewidth NV centres is still an outstanding challenge. The demonstration in [10] employed NV centres in a 1 μm thick membrane with optical transitions with a linewidth under the influence of spectral diffusion of $\approx$ 1 GHz, significantly broadened compared to the $\approx$ 13 MHz lifetime-limited value. While the mechanism of broadening is not fully understood, using a thicker diamond may be desired. We therefore conservatively use a diamond membrane thickness of 4 μm in the simulations throughout this manuscript. Secondly, we consider a

design that enables long uninterrupted measurements at cryogenic temperatures, potentially at a remote location with no easy access (such as a data center), through the use of a closed-cycle cryostat. The vibrations induced by the cryostat's pulse tube can be largely mitigated passively [21]. Active stabilisation of Fabry-Pérot cavities has been demonstrated [22, 23], including at a high bandwidth [24, 25], however these results have not yet been extended to operation in a pulse-tube cryostat. In the simulations in this manuscript we therefore assume that vibrations lead to passively stabilised cavity length deviations of 0.1 nm RMS [21]. While these boundary conditions influence the simulated maximally achievable probability to detect a ZPL photon, the analytic descriptions in this manuscript are not limited to these parameter regimes.

The layout of this manuscript is the following. We start by describing the one-dimensional properties of the cavities in Sec. 4.2. These are determined by the distribution of the electric field over the diamond and air parts of the cavity and its impact on the losses out of the cavity. In Sec. 4.3 we extend this treatment to the transverse extent of the cavity mode, analyzing the influence of the geometrical parameters. Finally we include real-world influences of vibrations and unwanted losses to determine the optimal mirror transmittivity and resulting emission into the ZPL in Sec. 4.4.

4.2. THE ONE-DIMENSIONAL STRUCTURE OF A HYBRID CAVITY

The resonant enhancement of the emission rate in the ZPL is determined by the Purcell factor [11, 26]:

$$F_p = \xi \frac{3c\lambda_0^2}{4\pi n_d^3} \frac{1}{\delta v V}, \tag{4.1}$$

where ξ describes the spatial and angular overlap between the NV centre's optical transition dipole and the electric field in the cavity; c is the speed of light, λ_0 is the free-space resonant wavelength and n_d the refractive index in diamond. δv is the cavity linewidth (full width at half maximum (FWHM) of the resonance that we assume to be Lorentzian), and V is the mode volume of the cavity. While the ZPL emission rates can be enhanced through the Purcell effect, the off-resonant emission into the phonon side band (PSB) will be nearly unaffected in the parameter regimes considered. This is the result of the broad PSB transition linewidth (δv_{PSB} is several tens of THz), that leads to a reduced effective quality factor, replacing $v/\delta v \rightarrow v/\delta v + v/\delta v_{PSB}$ [27]. This results in a low Purcell factor for the PSB. Selection rules for the optical transitions further prevent enhancement of the ZPL emission rate to ground states other than the desired one. The resulting branching ratio of photons into the ZPL, into the cavity mode is therefore [12, 16]:

$$\beta = \frac{\beta_0 F_p}{\beta_0 F_p + 1}, \tag{4.2}$$

where β_0 is the branching ratio into the ZPL in the absence of the cavity. Values for β_0 have been found in a range $\approx 2.4 - 5\%$ [10, 12]; we here use $\beta_0 = 3\%$. Note that to maximize the branching ratio we should maximize the Purcell factor, but that if $\beta_0 F_p \gg 1$ the gain from increasing F_p is small.

To optimize the Purcell factor through the cavity design we should consider the cavity linewidth and mode volume. In this section we focus on the linewidth of the cavity,
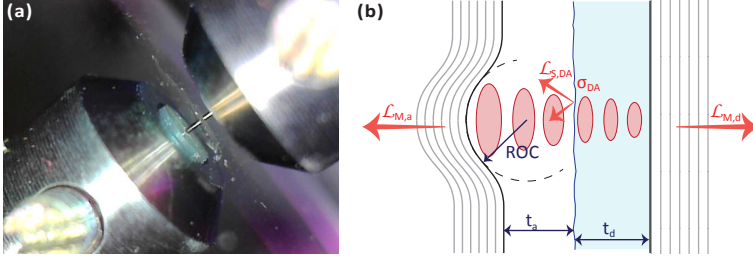
Figure 4.1: **Plane-concave fiber-based microcavities. (a)** Experimental plane-concave fiber-based microcavity. The cavity is formed at the fiber tip. Reflections of the fiber and holders are visible in the mirror. **(b)** The geometry of an open diamond-air cavity is described by the diamond thickness t_d, air gap t_a, and the dimple radius of curvature (ROC). The most important losses are through the mirror on the air-side ($\mathscr{L}_{M,a}$) and on the diamond-side ($\mathscr{L}_{M,d}$), and from scattering on the diamond-air interface ($\mathscr{L}_{S,DA}$) resulting from a rough diamond surface with surface roughness σ_{DA}.

that is determined by the confinement of the light between the mirrors. In Sec. 4.3 we evaluate the mode volume of the cavity.

The cavity linewidth is given by the leak rate out of the cavity: $\delta\nu = \kappa/(2\pi)$. For a general bare cavity this can be expressed as:

$$\delta\nu = \frac{1}{2\pi}\frac{\text{losses per round-trip}}{\text{round-trip duration}} = \frac{1}{2\pi}\frac{\mathscr{L}}{2nL/c} = \frac{c/(2nL)}{2\pi/\mathscr{L}} = \nu_{\text{FSR}}/F, \qquad (4.3)$$

for a cavity of length L in a medium with refractive index n. $\mathscr{L}$ are the losses per round-trip. In the last two steps we have written the expression such that one can recognize the standard definitions of free spectral range ($\nu_{\text{FSR}} = c/(2nL)$) and Finesse ($F = 2\pi/\mathscr{L}$). By using this description we assume that the losses per round trip are independent of the cavity length, which is true if losses appear at surfaces only.

For a hybrid diamond-air cavity (Fig. 4.1) this definition does not work anymore: due to the partially reflective interface between diamond and air, we cannot use the simple picture of a photon bouncing back and forth in a cavity. Instead, we should consider the electric field mode and its relative energy density in each part of the cavity. Staying close to the formulations used for a bare cavity, and choosing the speed of light in the diamond part (c/n_d) as a reference, the duration of an *effective round-trip* is $c/(2n_d L_{\text{eff}})$, where L_{eff} is an effective cavity length. This effective length should contain the diamond thickness and the width of the air gap weighted by the local energy density of the photon mode, relative to the energy density in the diamond membrane. Generalizing this, the effective length of the cavity system can be described by the 'energy distribution length' [28]:

$$L_{\text{eff}} \equiv \frac{\int_{cav}\epsilon(z)|E(z)|^2 dz}{\epsilon_0 n_d^2 |E_{max,d}|^2/2}. \qquad (4.4)$$

In this formulation $\epsilon = \epsilon_0 n^2$ is the permittivity of a medium with refractive index n, $E(z)$ is the electric field in the cavity and $E_{max,d}$ is the maximum electric field in diamond. The integral extends over the full cavity system, such that the effective length automatically includes the penetration depth into the mirrors. The resulting formulation for the

linewidth of a hybrid cavity analogous to eq. 4.3 is:

$$\delta \nu = \frac{c/(2n_d L_{\text{eff}})}{(2\pi/\mathcal{L}_{\text{eff}})},$$

(4.5)

where $\mathcal{L}_{\text{eff}}$ are the losses encountered during the effective round-trip. Here, like in the bare cavity case, we assume these losses to occur only at surfaces. This is a realistic assumption since the most important losses are expected to be from mirror transmission and absorption and diamond surface roughness.

In the above we have taken the field in diamond as reference for the effective round-trip. This choice is motivated by the definition of the mode volume as the integral over the electric field in the cavity relative to the electric field at the position of the NV centre - in diamond. It is given by [27, 29]:

$$V = \frac{\int_{cav} \epsilon(\vec{r})|E(\vec{r})|^2 \mathrm{d}^3\vec{r}}{\epsilon(\vec{r}_0)|E(\vec{r}_0)|^2},$$

(4.6)

with $\vec{r}_0$ the position of the NV centre, that we assume to be optimally positioned in an antinode of the cavity field in diamond, such that $E(\vec{r}_0) = E_{max,d}$. We choose to explicitly include effects from sub-optimal positioning in the factor ξ in the Purcell factor (eq. 4.1) rather than including them here. If we evaluate the integral in the radial direction we see that the remaining integral describes the effective length as defined above:

$$V = \frac{\pi w_0^2}{2} \frac{\int_{cav} \epsilon(z)|E(z)|^2 \mathrm{d}z}{\epsilon_0 n_d^2 |E_{max,d}|^2} = \frac{\pi w_0^2}{4} L_{\text{eff}},$$

(4.7)

where w_0 is the beam width describing the transverse extent of the cavity mode at the NV, that we will come back to in Sec. 4.3. We notice that the effective length appears in both the linewidth and the mode volume. In the Purcell factor ($F_p \sim 1/(\delta \nu V)$), the effective length cancels out. This is the result of our assumption that the losses per round-trip occur only at surfaces in the cavity.

The parameter relevant for Purcell enhancement in eq. 4.5 is thus $\mathcal{L}_{\text{eff}}$. Since these are the losses in an effective round-trip, we expect that they depend on the electric field distribution. We therefore first analyse the electric field distribution in the following section, before finding the effective losses related to the mirror losses and diamond surface scattering in Sec. 4.2.2 and Sec. 4.2.3.

4.2.1. Electric field distribution over diamond and air

The electric field distribution in the cavity on resonance is dictated by the influence of the partially reflective diamond-air interface. If the two parts were separated, the resonant mode in air would have an antinode at this interface, but the mode in diamond would have a node at that position. These cannot be satisfied at the same time, such that in the total diamond-air cavity system the modes hybridize, satisfying a coupled system resonance condition (see Sec. 4.6.1) [20, 21]. Two special cases can be distinguished for these resonant modes: the 'air-like mode', in which the hybridized mode has an antinode at the diamond-air interface, and the 'diamond-like mode' in which there is a node at the interface. For a fixed resonance frequency matching the NV-centre's ZPL emission

frequency ($\approx$ 470.4 THz), the type of mode that the cavity supports is fully determined by the diamond thickness. The tunable air gap allows for tuning the cavity to satisfy the resonance condition for any frequency.

Using a transfer matrix model [20, 30] we find the electric field distribution for both the air-like and the diamond-like modes, as shown in Figs. 4.2(a,b). If the cavity supports a diamond-like mode, the field intensity (proportional to nE_{max}^2[31]) is higher in the diamond-part, and vice-versa for the air-like mode. The relative intensity of the electric field in the cavity in the diamond membrane compared to the air gap is shown in Fig. 4.2(c) for varying diamond thicknesses. The relation that the relative intensity satisfies can be explicitly inferred from the continuity condition of the electric field at the diamond-air interface:

$$E_{max,a} \sin\left(\frac{2\pi t_a}{\lambda_0}\right) = E_{max,d} \sin\left(\frac{2\pi t_d n_d}{\lambda_0}\right); \tag{4.8}$$

where the air gap t_a corresponds to the hybridized diamond-air resonance condition (see Sec. 4.6.1):

$$t_a = \frac{\lambda_0}{2\pi} \arctan\left(-\frac{1}{n_d} \tan\left(\frac{2\pi n_d t_d}{\lambda_0}\right)\right) + \frac{m\lambda_0}{2}, \tag{4.9}$$

for an integer m. We use $n_{air} = 1$. The relative intensity in the air gap can thus be written as

$$\frac{E_{max,a}^2}{n_d E_{max,d}^2} = \frac{1}{n_d} \sin^2\left(\frac{2\pi n_d t_d}{\lambda_0}\right) + n_d \cos^2\left(\frac{2\pi n_d t_d}{\lambda_0}\right). \tag{4.10}$$

This ratio reaches its maximal value n_d for an air-like mode, while the minimal value $1/n_d$ is obtained for a diamond-like mode. This relation is shown in Fig. 4.2(c) as a dashed line, that overlaps with the numerically obtained result.

To remove the mixing of diamond-like and air-like modes, an anti-reflection (AR) coating can be applied on the diamond surface. This is in the ideal case a layer of refractive index $n_{AR} = \sqrt{n_d} \approx 1.55$ and thickness $t_{AR} = \lambda_0/(4n_{AR})$. The effect of a coating with refractive index n_{AR} is shown as a gray line in Fig. 4.2(c). For a realistic coating with a refractive index that deviates from the ideal, a small diamond thickness-dependency remains (see Sec. 4.6.2).

Next we determine the diamond thickness-dependency of an NV centre's branching ratio into the ZPL [32]. For this we need to find the linewidth and mode volume: we use the transfer matrix to numerically find the cavity linewidth from the cavity reflectivity as a function of frequency, and we calculate the mode volume using eq. 4.7. The method with which we determine the beam waist w_0 will be later outlined in Sec. 4.3. We further assume that the NV center is optimally placed in the cavity. To include the effect of surface roughness we extend the Fresnel reflection and transmission coefficients in the matrix model as described in [20, 33–35] (see Sec. 4.6.3). Fig. 4.2(d) shows that the resulting emission into the ZPL is strongly dependent on the electric field distribution over the cavity, both for the cases with and without roughness of the diamond interface.

Since we have already seen that the effective cavity length does not appear in the final Purcell factor, the varying emission into the ZPL with diamond thickness has to originate from varying effective losses in eq. 4.5. In the next paragraphs we develop analytic expressions for the effective losses that indeed exhibit this dependency on the electric field

distribution. We address the two most important sources of losses in our cavity: mirror losses and roughness of the diamond-air interface.
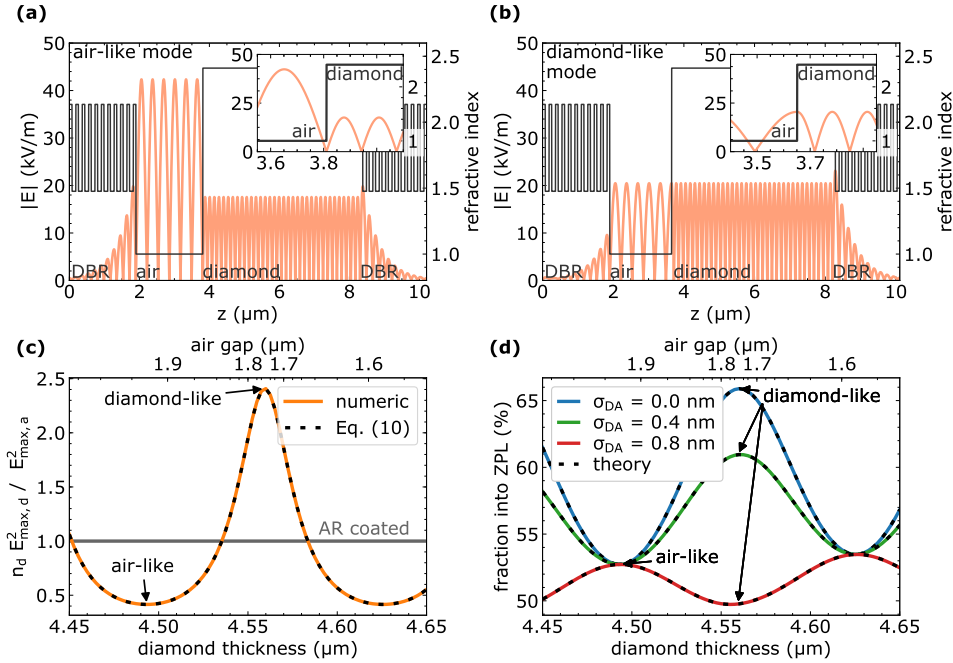

Figure 4.2: **Diamond-like and air-like modes in a diamond-based microcavity.** **(a-b)** The electric field strength (orange, left axis) in a diamond-air cavity satisfying the conditions for **(a)** an air-like mode and **(b)** a diamond-like mode is calculated using a transfer matrix model. **(c)** The relative intensity of light in the diamond membrane and air gap is described by eq. 4.10. It oscillates between $n_d \approx 2.41$ for the diamond-like mode and $1/n_d \approx 0.4$ for the air-like mode. When the diamond is anti-reflection (AR) coated, the oscillations vanish. To stay on the same resonance for varying diamond thickness the air gap is tuned. The corresponding values on the top x-axis do not apply to the cavity with AR coating. **(d)** The fraction of photons emitted into the ZPL shows a strong dependency on the diamond thickness, presented for three values of RMS diamond roughness σ_{DA}. The emission into the ZPL is determined from eqs. 4.1 and 4.2, with the mode volume as described in Sec. 4.3. The linewidth is numerically found from the transfer matrix model (solid lines) or with analytic descriptions using eq. 4.5 together with eqs. 4.11 and 4.15 (black dashed lines). The mirror transmittivity corresponds to a distributed Bragg reflector (DBR) stack with 21 alternating layers of Ta_2O_5 ($n = 2.14$) and SiO_2 ($n = 1.48$) (giving $\mathscr{L}_{M,A} = 260$ ppm and $\mathscr{L}_{M,D} = 630$ ppm). The dimple radius of curvature used is $ROC = 25\,\mu m$.

4.2.2. MIRROR LOSSES

As described at the start of this section the mirrors on either side of a bare cavity are encountered once per round-trip, making the total mirror losses simply the sum of the individual mirror losses. For a hybrid cavity, we have rephrased the definition of linewidth to eq. 4.5 by introducing an effective round-trip. In this picture, the mirrors on the diamond side are encountered once per round-trip, while the losses on the air side should be weighted by the relative field intensity in the air part. The resulting effective mirror

losses are described by:

$$\mathscr{L}_{M,\text{eff}} = \frac{E_{max,a}^2}{n_d E_{max,d}^2} \mathscr{L}_{M,a} + \mathscr{L}_{M,d},\tag{4.11}$$

where $\mathscr{L}_{M,a}$ are the losses of the mirror on the air side, $\mathscr{L}_{M,d}$ the losses of the diamond side mirror and the relative intensity in the air gap is given by eq. 4.10. Since this factor fluctuates between $1/n_d$ for the diamond-like mode and n_d for the air-like mode, the effective losses are lower in the diamond-like mode than in the air-like mode. This results in the strong mode-dependency of the emission into the ZPL in Fig. 4.2(d). The analytic expression for the effective mirror losses can be used to calculate the fraction of NV emission into the ZPL, resulting in the black dashed line in Fig. 4.2(d). This line overlaps with the numerically obtained result. Our model using the effective round-trip thus proves to be a suitable description of the system.

In Fig. 4.3(a) the effective losses are plotted for a relative contribution of $\mathscr{L}_{\text{M,a}}$ to the total mirror losses, that are fixed. If this contribution is larger, the deviations between the effective mirror losses in the diamond-like and air-like mode are stronger.

For a cavity with an AR coating ($E_{max,a}^2 = n_d E_{max,d}^2$) the losses would reduce to the standard case $\mathscr{L}_{M,a} + \mathscr{L}_{M,d}$ as expected. From the perspective of fixed mirror losses the best cavity performance can thus be achieved in a cavity without AR coating, supporting a diamond-like mode.

4.2.3. SCATTERING AT THE DIAMOND-AIR INTERFACE

Next to mirror losses the main losses in this system are from scattering due to diamond roughness. The strength of this effect depends on the electric field intensity at the position of the interface.

The electric field intensity at the diamond-mirror interface depends on the termination of the distributed Bragg reflector (DBR). If the last DBR layer has a high index of refraction, the cavity field has an node at this interface, while if the refractive index is low the field would have a antinode there. The losses due to diamond surface roughness are thus negligible with a high index of refracted mirror. Such a mirror is therefore advantageous in a cavity design, even though a low index of refraction termination interfaced with diamond provides lower transmission in a DBR stack with the same number of layers [20]. We assume a high index of refraction mirror termination and thus negligible surface roughness losses throughout this manuscript. The mirror transmissions specified already take the interfacing with diamond into account.

At the diamond-air interface the field intensity depends on the type of the cavity mode. The air-like mode (with a node at the interface) is unaffected, while the diamond-like mode is strongly influenced (Fig. 4.2(d) and Fig. 4.3(a), green and red lines).

From a matching matrix describing a partially reflective rough interface [20, 33–35], we can find the effective losses at the interface. To get the effective losses on one side of the interface, we find the difference between the intensity of the field travelling towards the surface and the intensity of the field travelling back. The field travelling away from the interface contains contributions both from the reflected field, as well as from the field transmitted through the other side of the interface. For one side, this is thus described

as:

$$\mathscr{L}_{S,12} = 1 - |E_{1,out}|^2 / |E_{1,in}|^2 \tag{4.12}$$

$$= 1 - |\rho'_{12} E_{1,in} + \tau'_{21} E_{2,in}|^2 / |E_{1,in}|^2, \tag{4.13}$$

where $E_{1,in}$ and $E_{2,in}$ are the incoming field from the left-hand side and right-hand side of the interface respectively. $E_{1,out}$ is the outgoing field on the left-hand side of the interface. Furthermore, ρ'_{12} and τ'_{21} are the reflection and transmission coefficients extended to include surface roughness.

We evaluate this expression for losses from the diamond-side and from the air-side, multiplying the latter by the relative intensity (eq. 4.10) as we did in the case for the mirror losses. The resulting losses per effective round-trip are:

$$\mathscr{L}_{S,\text{eff}} = \mathscr{L}_{S,DA} + \frac{E_{max,a}^2}{n_d E_{max,d}^2} \mathscr{L}_{S,AD} \tag{4.14}$$

$$\approx \sin^2\left(\frac{2\pi n_d t_d}{\lambda_0}\right) \frac{(1 + n_d)}{n_d} (1 - n_d)^2 \left(\frac{4\pi \sigma_{DA}}{\lambda_0}\right)^2. \tag{4.15}$$

In the evaluation of this expression we use a Taylor series approximation for the exponents in the reflection and transmission coefficients, and keep terms up to $O\left((4\pi\sigma_{DA}/\lambda_0)^2\right)$; Sec. 4.6.3 contains a detailed derivation. This description matches well with the numerically found result, which is evidenced in Fig. 4.2(d) where the gray dashed lines obtained with eq. 4.15 overlap with the numerical description (green and red lines).

In the case that the diamond would be AR coated, the coating roughness is expected to follow the diamond roughness. In this case, scattering losses are always present, with only a small modification based on the exact diamond thickness. The amount of scattering losses is however lower than in the diamond-like mode.

4.2.4. MINIMIZING THE EFFECTIVE LOSSES

Assuming that mirror losses and scattering at the air-diamond interface are the main contributors to the losses, the total effective losses are $\mathscr{L}_{\text{eff}} = \mathscr{L}_{M,\text{eff}} + \mathscr{L}_{S,\text{eff}}$. Other losses could originate from absorption in the diamond or clipping losses (see Sec. 4.3.2), but have a relatively small contribution in the considered parameter regimes [20].

As described above, an AR coating on the diamond membrane ensures that the intensities of the electric field in diamond and air are the same, while they would otherwise fluctuate with the diamond thickness. The mirror losses are then independent of diamond thickness, and the scattering losses are close to constant. The mirror losses with an AR coating are higher than the losses in the case of no AR coating in the diamond-like mode for the same mirror parameters. The scattering losses however are lower with an AR coating than in the diamond-like mode. Whether the highest Purcell factor can be achieved with or without AR coating thus depends on the relative losses. For the parameters in Fig. 4.2 if the roughness is < 0.4 nm a higher Purcell factor can be achieved in the diamond-like mode without an AR coating than with an AR coating.

If the diamond is not AR coated, we can decide to select either a diamond-like or air-like mode. From the previous section we see that $\mathscr{L}_{M,\text{eff}}$ is lowest for the diamond-

like mode, while $\mathcal{L}_{S,\text{eff}}$ is largest in that case. Whether a system supporting an air-like or a diamond-like mode is preferential depends on their relative strength. To be able to pick this freely requires tuning of the diamond thickness on the scale $\lambda_0/(4n_d) = 66$ nm, or using the thickness gradient of a diamond membrane to select the regions with the preferred diamond thickness. Note that the diamond thickness does not have to be tuned exactly to the thickness corresponding to a diamond-like mode. From Fig. 4.2(c) it is clear that the effective mirror losses are reduced compared to the AR coating value in a thickness range of ≈ 40 nm around the ideal diamond-like value, corresponding to about 35% of all possible diamond thicknesses.

Using the analytic expressions for the losses (eqs. 4.11 and 4.15) we can decide whether being in a diamond-like and air-like is beneficial. If the total losses in the diamond-like mode are less than the total losses in the air-like mode, it is beneficial to have a cavity that supports a diamond-like mode. This is the case if:

$$\left(\frac{4\pi\sigma_{DA}}{\lambda_0}\right)^2 \frac{(n_d+1)(n_d-1)^2}{n_d} < \left(n_d - \frac{1}{n_d}\right)\mathcal{L}_{\text{M,a}}. \tag{4.16}$$

Fig. 4.3(b) shows the $\mathcal{L}_{\text{M,a}}$ for varying σ_{DA} for which both sides of the above expression are equal. In the region above the curve, where eq. 4.16 holds, the best Purcell factor is achieved in the diamond-like mode. In the region below the curve, the Purcell factor is maximized for the air-like mode.

Concluding, to achieve the highest Purcell factor low losses are key. These losses are strongly influenced by whether the cavity supports diamond-like or air-like modes. Analytic descriptions of the mirror losses and losses from diamond surface roughness depending on the electric field distribution, enable to find whether a diamond-like or air-like mode performs better.
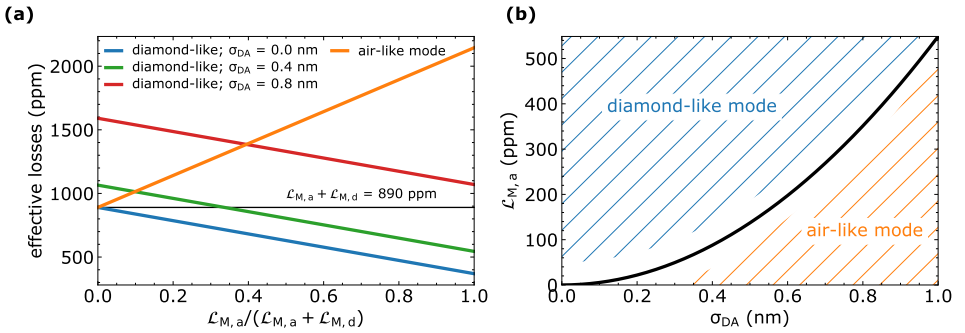

Figure 4.3: **Effective losses in a diamond-based microcavity. (a)** The effective losses in the cavity depend on whether the cavity supports a diamond-like or air-like mode. The difference is most pronounced if the losses on the air side are dominant. For the fixed value of $\mathcal{L}_{\text{M,a}} + \mathcal{L}_{\text{M,d}} = 890$ ppm shown, the effective losses can be up to ≈ 2150 ppm in the air-like mode (orange line), or as low as 470 ppm in the diamond-like mode (blue line). Scattering on the diamond-air interface (green and red lines) increase the losses in the diamond-like mode, but do not affect the air-like mode. **(b)** Depending on the bare losses on the air mirror and the amount of diamond surface roughness the total losses are lowest in the diamond-like mode (shaded region above the black curve) or the air-like mode (below the curve).

4.3. Transverse extent of Gaussian beams in a hybrid cavity

Having analyzed the one-dimensional structure of the cavity, we turn to the transverse electric field confinement. We have seen in eq. 4.7 that the mode volume can be described as

$$V = \frac{\pi w_{0,d}^2}{4} L_{\text{eff}} \equiv g_0 \, (\lambda_0/n_d)^2 \, L_{\text{eff}}, \tag{4.17}$$

where we define a geometrical factor $g_0 \equiv \frac{\pi w_{0,d}^2}{4}/(\frac{\lambda_0}{n_d})^2$, and $w_{0,d}$ is the beam waist in diamond. Since L_{eff} cancels out in the Purcell factor, g_0 captures all relevant geometrical factors in the mode volume. Note that combining eq. 4.1 with eqs. 4.17 and eq. 4.5, the Purcell factor can be written as $F_p = 3\xi/(g_0 \mathscr{L}_{\text{eff}})$.

In this section we describe how to find the beam waist $w_{0,d}$, and which parameters play a role in minimizing it. Furthermore, we quantify the losses resulting if the beam extends outside of the dimple diameter.

4.3.1. Beam waist

We describe the light field in our cavity using a coupled Gaussian beams model [20]. The hybrid cavity supports two Gaussian beams: one that lives in the air gap of the cavity, and one in the diamond (Fig. 4.4(a), indicated in orange and blue respectively). The boundary conditions for the model are provided by the diamond thickness, width of the air gap and the radius of curvature (ROC) of the fiber dimple (see Sec. 4.6.4). In the model we assume that the diamond surface is planar. We note that this deviates from the assumption in [20], where the diamond surface is assumed to follow the beam curvature at the interface. The latter assumption would introduce a lensing effect, leading to a narrower effective beam waist than for a plane surface. The planar interface causes mixing with higher-order modes, but the influence of these effects is expected to be small due to the large radius of curvature of the mode at the interface [20].

A solution to this model provides the beam waist of both beams ($w_{0,d}$ and $w_{0,a}$) and the related Rayleigh lengths ($z_{0,d}$, $z_{0,a}$) as well as the location of the beam waist of the air beam with respect to the plane mirror, Δz_a. Previously such a model has been solved numerically [20], but an analytic solution gives insight in the influence of the individual cavity parameters. The analytic solution that we find is given by (see Sec. 4.6.4):

$$w_{0,a} = w_{0,d}, \quad (\rightarrow z_{0,a} \approx z_{0,d}/n_d); \tag{4.18}$$

$$\Delta z_a = t_d \left(1 - \frac{1}{n_d}\right); \tag{4.19}$$

$$w_{0,d} = \sqrt{\frac{\lambda_0}{\pi} \left(\left(t_a + \frac{t_d}{n_d}\right)\left(ROC - \left(t_a + \frac{t_d}{n_d}\right)\right)\right)^{1/4}}. \tag{4.20}$$

In the last expression for the beam waist we recognize the standard expression for the beam waist of a plane-concave cavity [19], but with a new term taking the position of cavity length:

$$L' \equiv t_a + \frac{t_d}{n_d} \quad (= t_a + t_d - \Delta z_a). \tag{4.21}$$

As an important result, the influence of the diamond thickness is a factor $1/n_d \approx 0.42$ less than that of the width of the air gap. We indeed see in Figs. 4.4(c,d) that increasing the air gap from 1 to 4 μm (green line) has a larger effect on $w_{0,d}$ and g_0 than increasing the diamond thickness from 1 to 4 μm (orange line).

The minimal air gap that can be achieved is set by the dimple geometry (see Fig. 4.4(b)). Smooth dimples with a small ROC can be created in several ways, including with CO_2 laser ablation or focused-ion-beam milling of optical fibers or fused silica plates [19, 36–39]. The dimple depth for dimple parameters as considered here is typically $z_d \approx 0.2 - 0.5$ μm, while a relative tilt between the mirror of an angle θ introduces an extra distance of $z_f = D_f/2\sin(\theta) \approx D_f\theta/2$, which is ≈ 4 μm for a fiber cavity (see Sec. 4.6.5). This last effect if thus dominant over the dimple depth. To reduce the minimal air gap in fiber-based cavities, the most important approach to lowering the mode volume is thus by shaping the fiber tip [40]. For cavities employing silica plates the large extent of the plates demands careful parallel mounting of the mirror substrates.

4.3.2. CLIPPING LOSSES

The laser-ablated dimple has a profile that is approximately Gaussian (Fig. 4.4(b)). Beyond the radius $D_d/2$ the dimple significantly deviates from a spherical shape. If the beam width on the mirror (w_m) approaches this value, significant clipping losses result [19]:

$$\mathscr{L}_{clip} = \exp\left(-2\left(\frac{D_d/2}{w_m}\right)^2\right). \tag{4.22}$$

Using our coupled Gaussian beam model we find a numerical (Fig. 4.4(e), solid line) and analytical (dashed line) solution to the beam width on the mirror and the resulting clipping losses (Fig. 4.4(f)). Like $w_{0,d}$, w_m is influenced more strongly by the air gap width than by the diamond thickness. Consequently, the clipping losses are small even when the diamond membrane is relatively thick. For a Gaussian dimple with $ROC = 25$ μm and $z_d = 0.3$ μm, we expect that $D_d \approx 7.7$ μm. In this case for $t_d \approx 4$ μm and $t_a < 2$ μm, the influence of clipping losses is negligible compared to other losses. The influence of clipping losses can be larger for cavity lengths at which transverse mode mixing appears [41].

Finally we note that the clipping losses should be treated in line with the method developed in Sec. 4.2. The effective clipping losses are the clipping losses as found above, weighted by the relative field intensity in air (eq. 4.10).
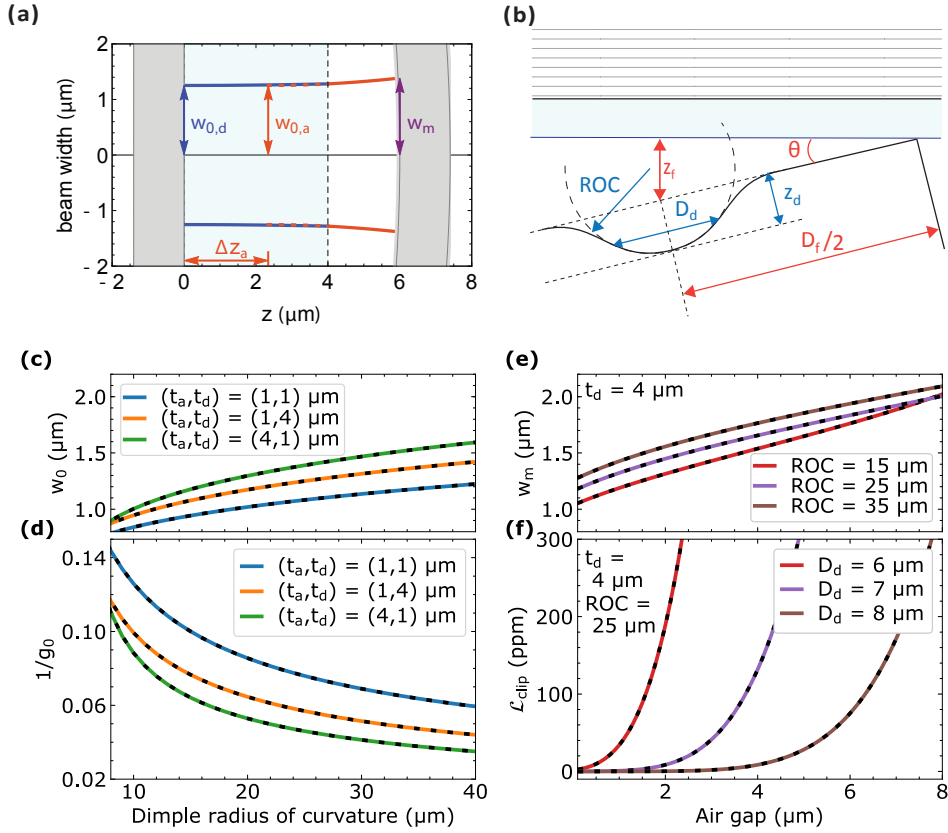
Figure 4.4: **Transverse extent of Gaussian beams in a microcavity. (a)** The transverse extent of the cavity mode is described using a Gaussian beams model [20], with a beam in diamond (blue) and air (orange), that are coupled at the diamond-air interface, where the beam widths match and the beam curvatures satisfy $n_d R_a = R_d$ for a planar diamond surface. The beam curvature of the air beam at the dimple follows the dimple's radius of curvature (ROC, here 25 µm). The beam waist of the diamond beam ($w_{0,d}$) is fixed at the plane mirror, whereas the position of the air beam waist ($w_{0,a}$) at $z = \Delta z_a$ is obtained as a solution to the model. **(b)** Schematic of the cavity geometry. The dimple has a Gaussian shape with diameter D_d (full width at $1/e$ of the Gaussian) and radius of curvature ROC, resulting in a minimum distance from fiber to mirror of z_d. The extent of the fiber (D_f) in combination with a fiber tilt θ result in an minimum extra cavity length of z_f. Figure is not to scale. **(c-d)** Numerical (solid lines) and analytical (dashed lines) solutions for **(c)** $w_{0,d}$ and **(d)** the corresponding factor g_0 (eq. 4.17) exhibit a stronger dependence on the air gap than on the diamond thickness, as described by eq. 4.21. The exact analytic solution overlaps with the numerically obtained result. **(e-f)** The ratio of the beam width on the concave mirror w_m **(e)** and the dimple diameter D_d determine the strength of the clipping losses per round-trip **(f)**. We here fix $t_d = 4$ µm.

4.4. INCLUDING REAL-WORLD IMPERFECTIONS

From the perspective of Purcell enhancement alone the requirements for the mirrors of our Fabry-Pérot cavity are clear: since the Purcell factor is proportional to the quality factor of the cavity, high reflectivity of the cavity mirrors will provide the largest Purcell factor.

But when including real-world imperfections, we have to revisit this conclusion. In an open cavity system, having high-reflectivity mirrors comes with a price: the resulting narrow-linewidth cavity is sensitive to vibrations. And next to that, unwanted losses in the cavity force motivate an increase of the transmission of the outcoupling mirror, to detect the ZPL photons efficiently. In this section we analyse how both these effects influence the optimal mirror parameters.

4.4.1. VIBRATION SENSITIVITY

The benefit of tunability of an open Fabry-Pérot cavity has a related disadvantage: the cavity length is sensitive to vibrations. This issue is especially relevant for systems as considered here that require operation at cryogenic temperatures. Closed-cycle cryostats allow for stable long-term operation, but also induce extra vibrations from their pulse-tube operation. In setups specifically designed to mitigate vibrations passively [21] vibrations modulate the cavity length over a range with a standard deviation of approximately 0.1 nm. Here we discuss how to make a cavity perform optimally in the presence of such vibrations.

If vibrations change the cavity length, the cavity resonance frequency is modulated around the NV center emission frequency. For a bare cavity (with $\nu_{\text{res}} = mc/(2nL)$) the resonance frequency shift $d\nu_{\text{res}}$ due to vibrations over a characteristic (small) length dL can be described by:

$$|d\nu_{\text{res}}| = \nu_{\text{res}}\, dL/L. \tag{4.23}$$

Comparing this to the cavity linewidth $\delta\nu = \nu_{\text{FSR}}/F = c/2nLF$ and using $\nu_{\text{res}} = c/(n\lambda_{0,\text{res}})$ we find:

$$\frac{d\nu_{\text{res}}}{\delta\nu} = 2\frac{dL}{\lambda_{0,res}}F. \tag{4.24}$$

For the impact of the vibrations the cavity length is thus irrelevant: rather the finesse plays an important role. If we demand that $d\nu_{res} < \delta\nu$ we find that we would need to limit the finesse to $F < \lambda_{0,res}/(2dL)$.

For a hybrid cavity the frequency response is modified compared to the bare cavity situation by the influence of diamond-like and air-like modes. To find the modified response we evaluate the derivative of the resonance condition (see Secs. 4.6.1 and 4.6.6) at the diamond-like and air-like mode:

$$\frac{d\nu_{a,d}}{dt_a} = -\frac{c}{(t_a + n_d t_d)\lambda_{0,res}}\left(1 \pm \frac{n_d-1}{n_d+1}\frac{2n_d t_d}{t_a + n_d t_d}\right). \tag{4.25}$$

The plus-sign on the left hand side corresponds to the case for an air-like mode, and the minus-sign corresponds to a diamond-like mode. A diamond-like mode is therefore less sensitive to vibrations than an air-like mode. This difference can be significant. For $t_d \approx 4$ μm and $t_a \approx 2$ μm, $\frac{d\nu_{a,d}}{dt_a} \approx 7$ GHz/Å in the air-like mode, while $\frac{d\nu_{a,d}}{dt_a} \approx 1$ GHz/Å

in the diamond-like mode. The vibration susceptibility of a cavity with an AR coated diamond reduces to the bare cavity expression eq. 4.23, with $L = t_a + n_d t_d + \lambda_0/2$, and thus takes an intermediate value between those for the air-like and diamond-like modes.

We include these vibrations in our model that describes the emission into the ZPL (see Sec. 4.6.6). The results are shown as solid lines in Figs. 4.5(a,b), for the diamond-like and air-like mode respectively. For a system with vibrations $\sigma_{vib} = 0.1$ nm, the emission into the ZPL for the diamond-like mode is $\approx 40\%$ for total losses of ≈ 800 ppm, corresponding to a finesse of $F \approx 8000$.

The optimal losses may thus be higher than the minimal value set by unwanted losses. The losses can be increased by increasing the transmission through the outcoupling mirror. In this way not only vibration stability but also an improved outcoupling efficiency is achieved, as we see below.
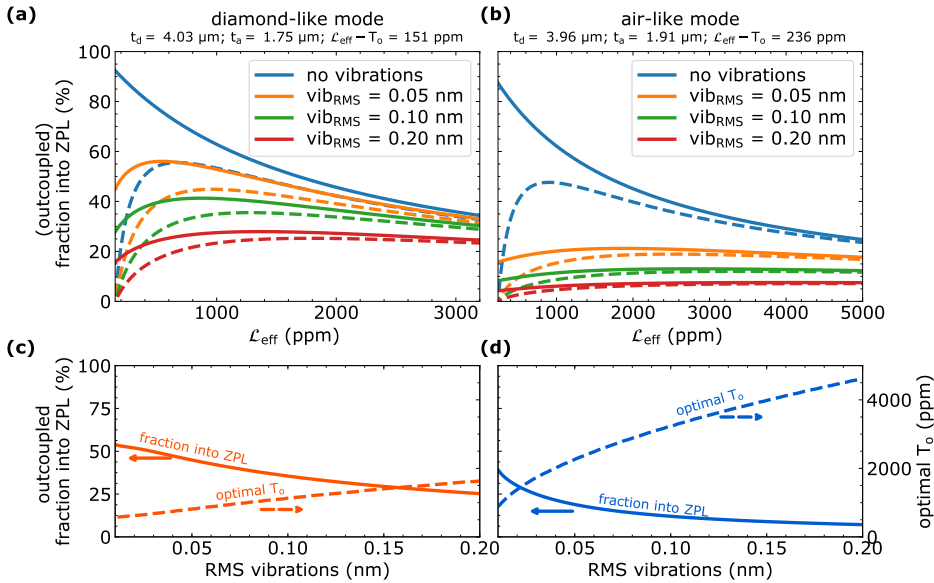

Figure 4.5: **Optimal mirror parameters for a cavity under realistic conditions. (a-b)** Vibrations impact the average emission into the ZPL (solid lines) for **(a)** the diamond-like mode and more strongly for **(b)** the air-like mode. A reduced vibration sensitivity can be achieved for both by increasing the total cavity losses at the expense of a lower on-resonance Purcell factor. The fraction of ZPL photons outcoupled through the desired mirror (dashed line) can be increased by increasing the total losses via the transmittivity of the outcoupling mirror T_o. Outcoupling is assigned to be via the flat mirror, and the used parameters are $\mathscr{L}_{M,a} = 84$ ppm, $\mathscr{L}_{M,d} = T_o + 34$ ppm, $\sigma_{DA} = 0.25$ nm RMS, and $ROC = 20$ μm. **(c-d)** By choosing an optimal T_o (dashed line, right x-axis) the maximum outcoupled fraction into the ZPL for each level of vibrations (solid line, left x-axis) is obtained for **(c)** the diamond-like mode and **(d)** the air-like mode.

4.4.2. OUTCOUPLING EFFICIENCY

We do not only want to enhance the probability to emit a ZPL photon per excitation, but also want to couple this photon out of the cavity into the desired direction. The

outcoupling efficiency is given by $\eta_o = T_o / \mathscr{L}_{\text{eff}}$, with T_o the transmittivity of the outcoupling mirror. We choose to assign the plane mirror on the diamond side of the cavity as the outcoupling mirror. This assignment is motivated by comparison of the mode-matching efficiencies between the cavity mode and the dimpled fiber, and between the cavity mode and the free space path. For the free space path in principle perfect overlap with the Gaussian mode can be achieved, while for the fiber side this is limited to $\approx 50\%$ for a cavity with $ROC = 20\,\mu\text{m}$, $t_d = 4\,\mu\text{m}$, and $t_a = 2\,\mu\text{m}$ (see Sec. 4.6.7) [19, 42]. Moreover, in this regime the mode-matching efficiency can only be improved by increasing each of these parameters, thereby compromising Purcell enhancement. Since the plane mirror is interfaced with diamond, we note that in the transmission T_o this diamond termination has to be taken into account. When using a DBR stack with a high refractive index final layer, T_o is higher than the transmission of the same stack in air.

The larger the unwanted losses ($\mathscr{L}_{\text{eff}} - T_o$) in the cavity are, the higher the transmission through the output mirror has to be to achieve the same outcoupling efficiency. The contributing unwanted losses are transmission through the non-outcoupling mirror, scattering and absorption in both mirrors, and scattering at the diamond-air interface. Using values of ≈ 50 ppm, ≈ 24 ppm and ≈ 10 ppm for mirror transmission, scattering and absorption [21], and a diamond-air interface roughness of $\sigma_{\text{DA}} = 0.25$ nm [10, 43, 44], we find that the unwanted losses are 139 ppm (236 ppm) for the diamond-like (air-like) mode using the analytic expression from eqs. 4.11 and 4.15.

An outcoupling efficiency $\eta_0 > 0.5$ is then achieved for $T_o > 139$ ppm (236 ppm). The additional losses this would add to the cavity system are less than what is optimal for typical vibrations of $\sigma_{\text{vib}} \approx 0.1$ nm ($\rightarrow \mathscr{L}_{\text{eff}} \approx 800$ ppm (3000 ppm)) for both the diamond-like and air-like modes. Vibrations thus have a dominant effect. To improve the cavity performance in this regime focus should thus be on the reduction of vibrations over the reduction of unwanted losses. A possible route for vibration reduction is by extending active cavity stabilisation techniques for Fabry-Pérot cavities [22–25] to operation under pulse-tube conditions.

Including the outcoupling efficiency in our model we find the fraction of photons that upon NV excitation are emitted into the ZPL and subsequently coupled out of the cavity into the preferred mode (dashed lines in Figs. 4.5(a,b)). For each value of vibrations, we can maximize this fraction by picking an optimal T_o. For the diamond-like and air-like mode the results of this optimization are shown in Figs. 4.5(c,d). For vibrations of 0.1 nm, the best results ($\approx 35\%$ probability of outcoupling a ZPL photon) are expected to be achieved in a diamond-like mode with $T_o \approx 1200$ ppm. We note that this corresponds to a modest Purcell factor of 40, leading to an excited state lifetime reduction to 5.2 ns, and a lifetime-limited linewidth of 31 MHz. Purcell factors higher than this lead to increased linebroadening, which should be taken into account for optical excitation, see e.g. Ref [45]. Increased Purcell factors at such levels have a small effect on the resulting emission into the ZPL (eq. 4.2), and thus a limited benefit for an optimal design.

4.5. CONCLUSIONS

In summary, we have developed analytical descriptions giving the influence of key parameters on the performance of a Fabry-Pérot cavity containing a diamond membrane. This analytical treatment allows us to clearly identify sometimes conflicting require-

ments and guide the optimal design choices.

We find that the effective losses in the cavity are strongly dependent on the precise diamond thickness. This thickness dictates the distribution of the electric field in the cavity, with as extreme cases the diamond-like and air-like modes in which the field lives mostly in diamond and air respectively. As a result, the losses due to the mirror on the air side are suppressed by a factor n_d in diamond-like modes while they are increased by the same factor in the air-like modes. In contrast the losses resulting from diamond surface roughness are highest in the diamond-like mode. The two types of losses can therefore be traded-off against each other. If the diamond surface roughness can be made sufficiently low (< 0.4 nm RMS for mirror losses on the air gap side of 85 ppm), the total losses are lowest in the diamond-like mode.

The transverse confinement of the cavity is captured in a geometrical factor g_0 that depends on the beam waist alone. It is determined by the radius of curvature of the dimple and an expression that captures the effect of the cavity component thicknesses: $t_a + t_d/n_d$. The width of the air gap t_a thus has a dominant influence, while the influence of the diamond thickness t_d is reduced by the diamond refractive index n_d. From a geometrical perspective, the focus in the cavity design should thus be on small radii of curvature and small air gaps.

Although the highest Purcell factors are achieved for low cavity losses, vibrational instability of the cavity length and the presence of unwanted losses suggest that lowering the cavity finesse can be advantageous. We find that a cavity supporting an air-like mode is more severely affected by vibrations than one supporting a diamond-like mode. For example, for vibrations of 0.1 nm RMS and unwanted losses of ≈ 190 ppm we find that the optimal fraction of ZPL photons reaching the detector is obtained with a diamond-like mode and an outcoupling mirror transmission of $T_o \approx 1200$ ppm.

The experimentally realistic parameter regimes considered here include a 4 μm diamond thickness to support optically coherent NV centres and vibrations of 0.1 nm RMS under pulse-tube operation with passive stabilisation. In this regime with an optimized design an emission efficiency of ZPL photons into the desired outcoupled optical mode after resonant excitation of 35% can be achieved. This constitutes a two orders of magnitude improvement compared to existing approaches, for which the branching ratio into the ZPL is ≈ 3% and the collection efficiencies are typically ≈ 10% [46].

Purcell enhancement with open Fabry-Pérot cavities will open the door to efficient spin-photon interfaces for diamond-based quantum networks. The analysis presented here clarifies the design criteria for these cavities. Future experimental design and investigation will determine how to combine such cavities with resonant excitation and detection for spin-state measurement [47] and long distance entanglement generation [46, 48, 49].

Acknowledgements

4.6. SUPPLEMENTARY INFORMATION

4.6.1. RESONANCE CONDITION FOR A DIAMOND-AIR CAVITY

To understand how the partially reflective diamond-air interface influences the cavity system, we first look at the resonance condition in diamond and air separately. For the air gap the diamond-air interface from low ($n_a = 1$) to high ($n_d = 2.41$) refractive index results in a field with an antinode at the interface. From the diamond membrane the reflection coefficient is opposite: the field in diamond has a node at this interface. Naturally, when these cavities are coupled, the electric field at the diamond-air interface has to be continuous. It is thus impossible to satisfy the resonance conditions of the two individual cavities at the same time. The result is that the original modes in diamond and air show anti-crossings [20, 21]. The hybridized cavity resonances are given by [20]:

$$v = \frac{c}{2\pi(t_a + n_d t_d)} \left(m\pi - (-1)^m \arcsin\left(\frac{n_d - 1}{n_d + 1} \sin\left(\pi m \frac{t_a - n_d t_d}{t_a + n_d t_d} \right) \right) \right), \tag{4.26}$$

for an air gap of length t_a and a diamond thickness t_d. The resulting spectrum is shown in Fig. 4.6(a). We can distinguish two special cases for these resonant modes: the 'air-like mode', in which the hybridized mode has an antinode at the diamond-air interface, and the 'diamond-like mode' in which there is a node at the interface. They correspond to the values for which the sine term on the right-hand side of the resonant condition vanishes:

$$t_d = m_d \frac{\lambda_0}{2n_d} \qquad \text{and} \quad t_a = m_a \frac{\lambda_0}{2}; \qquad \text{(air-like mode)} \tag{4.27}$$

$$t_d = (2m_d + 1)\frac{\lambda_0}{4n_d} \quad \text{and} \quad t_a = (2m_a - 1)\frac{\lambda_0}{4}; \quad \text{(diamond-like mode)} \tag{4.28}$$

for any integer (m_a, m_d), and $m = m_a + m_d$, and $\lambda_0 = v/c$ the free space wavelength.

We next find the resulting condition on t_a given a diamond thickness t_d. The resonance condition for a diamond-air cavity (eq. 4.26) is derived from the equation [20]:

$$(1 + n_d)\sin\left(\frac{2\pi}{\lambda_0}(t_a + n_d t_d) \right) = (1 - n_d)\sin\left(\frac{2\pi}{\lambda_0}(t_a - n_d t_d) \right). \tag{4.29}$$

To find the on-resonance air gap t_a as a function of diamond thickness t_d, as in eq. 4.9, we rewrite this in the following steps:

$$(1 + n_d)\left(\sin\left(\frac{2\pi}{\lambda_0} t_a \right)\cos\left(\frac{2\pi}{\lambda_0} n_d t_d \right) + \cos\left(\frac{2\pi}{\lambda_0} t_a \right)\sin\left(\frac{2\pi}{\lambda_0} n_d t_d \right) \right) \tag{4.30}$$

$$= (1 - n_d)\left(\sin\left(\frac{2\pi}{\lambda_0} t_a \right)\cos\left(\frac{2\pi}{\lambda_0} n_d t_d \right) - \cos\left(\frac{2\pi}{\lambda_0} t_a \right)\sin\left(\frac{2\pi}{\lambda_0} n_d t_d \right) \right)$$

$$2n_d \sin\left(\frac{2\pi}{\lambda_0} t_a \right)\cos\left(\frac{2\pi}{\lambda_0} n_d t_d \right) = -2\cos\left(\frac{2\pi}{\lambda_0} t_a \right)\sin\left(\frac{2\pi}{\lambda_0} n_d t_d \right) \tag{4.31}$$

$$n_d \tan\left(\frac{2\pi}{\lambda_0} t_a \right) = -\tan\left(\frac{2\pi}{\lambda_0} n_d t_d \right) \tag{4.32}$$

$$t_a = \frac{\lambda_0}{2\pi} \arctan\left(-\frac{1}{n_d} \tan\left(\frac{2\pi n_d t_d}{\lambda_0} \right) \right) \tag{4.33}$$

4.6.2. EFFECT OF AR COATING OF THE DIAMOND MEMBRANE

With an AR coating applied to the diamond membrane, the electric field distribution is altered to the situation as shown in Fig. 4.7. In the ideal case the AR coating is a layer of refractive index $n_{AR} = \sqrt{n_d} \approx 1.55$ and thickness $t_{AR} = \lambda_0/(4n_{AR})$. In practice, it can be created for example with SiO_2 ($n_{SiO_2} \approx 1.46$) or Al_2O_3 ($n_{Al_2O_3} \approx 1.77$) [50, 51].

The resonance condition for a cavity with a non-ideal AR coating with refractive index n_{AR} and a thickness $\lambda_0/(4n_{AR})$ is given by:

$$\nu_{AR} = \frac{c}{2\pi(t_a + t_d n_d)}\left((m+1/2)\pi - (-1)^m \arcsin\left(\frac{n_{AR}^2 - n_{air}n_d}{n_{AR}^2 + n_{air}n_d}\cos\left(\pi(m+1/2)\frac{t_a - n_d t_d}{t_a + n_d t_d}\right)\right)\right).$$

(4.34)

For the ideal AR coating with $n_{AR} = \sqrt{n_{air}n_d}$ the second term on the right-hand-side vanishes, and this reduces to the resonance condition expected for a cavity with a single material of optical length $L = t_a + t_d n_d + \lambda_0/(4n_{AR})n_{AR}$:

$$\nu_{ideal,AR} = \frac{(m+1/2)c}{2(t_a + t_d n_d)}$$

(4.35)

The resonance spectrum for the ideal and non-ideal AR coated diamond-air cavities are compared to the hybridized resonance spectra (eq. 4.26) in Fig. 4.6.
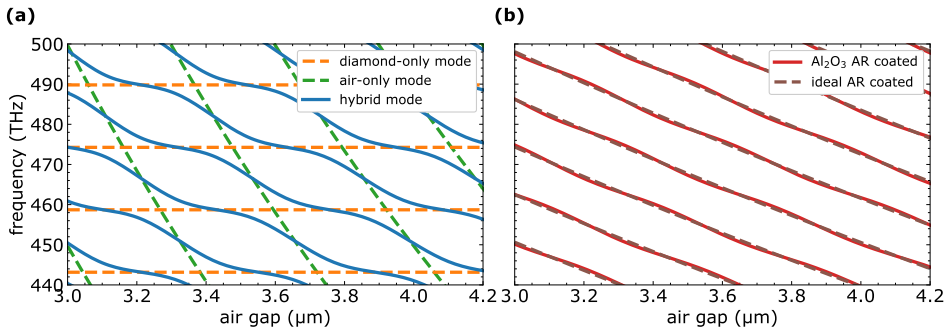

Figure 4.6: (a) The diamond-only and air-only resonances follow resonance conditions given by $\nu_d = (2m_d - 1)c/(4n_d t_d)$, and $\nu_a = m_a c/(2t_a)$ with integer m_d and m_a respectively. The frequencies of the resonances of the hybrid cavity are given by eq. 4.26. (b) With an ideal AR coating with $n_{AR} = \sqrt{n_d}$ the hybrid mode behavior disappears (). An experimental AR coating with Al_2O_3 with refractive index $n_{Al_2O_3} = 1.77$ leads to resonance frequencies given by eq. 4.35 (red solid lines).
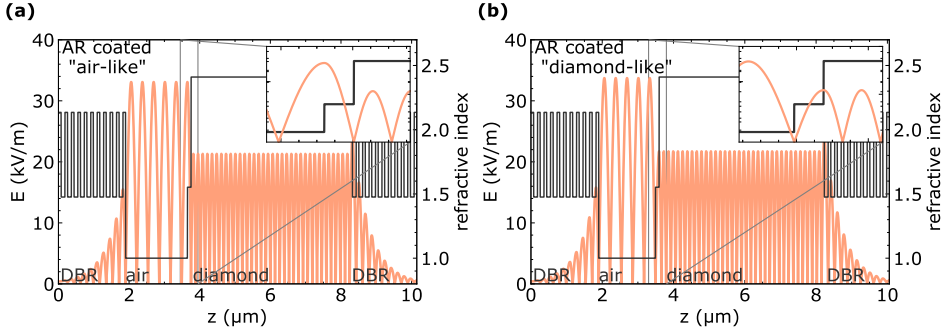
(a)

(b)

Figure 4.7: The electric field distribution for a hybrid cavity with an AR-coated diamond membrane for what would have been (a) an air-like mode (b) a diamond-like mode if there were no AR coating. With this AR coating, the electric field intensity in the diamond and air parts are equal ($E_{max,a}^2 = n_d E_{max,d}^2$).

4.6.3. SCATTERING AT A PARTIALLY REFLECTIVE INTERFACE

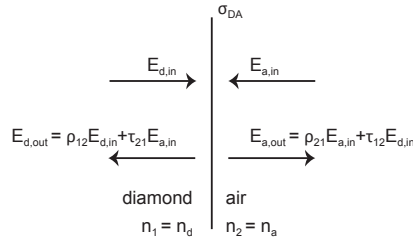This section describes how to find the scattering strength for a partially reflective interface.

Figure 4.8: The losses for a field incident on the diamond air interface are described the difference between the incoming field and the outgoing field for each side of the interface individually, as in eq. 4.41. The effective total losses in a diamond-air cavity are given by the losses from each side, multiplied by the relative intensity: $\mathcal{L}_{S,eff} = \mathcal{L}_{DA} + n_a E_{max,a}^2 / (n_d E_{max,d}^2) \mathcal{L}_{AD}$

Firstly, we define the problem by drawing the schematic in Fig. 4.8. We are going to evaluate the losses upon incidence from the left-hand side and right-hand side individually. Upon incidence, the field can be reflected or transmitted. This can be described

by a matching matrix, that is given by [20, 30, 33–35]:

$$\begin{pmatrix} E_{1,in} \\ E_{1,out} \end{pmatrix} = \frac{1}{\tau'_{12}} \begin{pmatrix} 1 & -\rho'_{21} \\ \rho'_{12} & \tau'_{12}\tau'_{21} - \rho'_{12}\rho'_{21} \end{pmatrix} \begin{pmatrix} E_{2,out} \\ E_{2,in} \end{pmatrix};$$ (4.36)

$$\rho'_{ij} = \rho_{ij} e^{-2\left(\frac{2\pi\sigma n_i}{\lambda_0}\right)^2} \approx \rho_{ij}\left(1 - 2\left(\frac{2\pi\sigma n_i}{\lambda_0}\right)^2\right);$$

$$\tau'_{ij} = \tau_{ij} e^{-1/2\left(\frac{2\pi\sigma(n_j - n_i)}{\lambda_0}\right)^2} \approx \tau_{ij}\left(1 - 1/2\left(\frac{2\pi\sigma(n_j - n_i)}{\lambda_0}\right)^2\right);$$ (4.37)

$$\rho_{ij} = \frac{n_i - n_j}{n_i + n_j};$$ (4.38)

$$\tau_{ij} = \frac{2n_i}{n_i + n_j}.$$

Here $E_{1(2),in}$ and $E_{1(2),out}$ are the incoming and outgoing fields on the left-hand side (right-hand side) of the interface, where the refractive index is $n_1(n_2)$. For the diamond-air interface, we identify $E_{1(2)} = E_{d(a)}$ and $n_1 = n_d$, $n_2 = n_d$. ρ_{ij} and τ_{ij} are the Fresnel reflection and transmission coefficients, that are extended to ρ'_{ij} and τ'_{ij} to include scattering at and interface with rms roughness of σ_{ij}. We use a Taylor expansion to approximate them, keeping only terms up to $O\left(\left(\frac{2\pi\sigma}{\lambda_0}\right)^2\right)$. Using this formalism, we can write the outgoing fields in terms of the incoming fields as:

$$E_{1,out} = \rho'_{12} E_{1,in} + \tau'_{21} E_{2,in};$$ (4.39)

$$E_{2,out} = \rho'_{21} E_{2,in} + \tau'_{12} E_{1,in}.$$ (4.40)

The losses from the left side of the interface are described by as the normalised difference between the incoming and outgoing field:

$$\mathscr{L}_{S,12} = \frac{n_1|E_{1,in}|^2 - n_1|E_{1,out}|^2}{n_1|E_{1,in}|^2}$$ (4.41)

$$= 1 - \frac{|\rho'_{12}E_{1,in} + \tau'_{21}E_{2,in}|^2}{|E_{1,in}|^2},$$ (4.42)

and a similar formulation holds for the right hand side, replacing $1 \leftrightarrow 2$. We see that here the interference between the reflected and transmitted fields plays a role. To evaluate the interference term, we need an expression for $E_{1,in}$ and $E_{2,in}$ in the cavity. To this end we use our knowledge that the cavity field has a node at the DBR on both sides of the cavity. The fields are thus given by:

$$E_{d,in} = |E_{d,in,max}|\left(\sin\left(\frac{2\pi n_d t_d}{\lambda_0}\right) + i\cos\left(\frac{2\pi n_d t_d}{\lambda_0}\right)\right)$$ (4.43)

$$E_{a,in} = |E_{a,in,max}|\left(-\sin\left(\frac{2\pi n_a t_a}{\lambda_0}\right) - i\cos\left(\frac{2\pi n_a t_a}{\lambda_0}\right)\right),$$ (4.44)

where the field in air travelling to the left has a π phase flip compared to the field in diamond travelling to the right resulting from reflection off the mirror. $E_{d,in,max}$ and

$E_{a,in,max}$ are the maxima of the incoming field in the diamond and air part respectively. They are related by eq. 4.10:

$$|E_{a,in,max}| = \sqrt{\frac{n_d}{n_a}} \sqrt{I_{rel}} |E_{d,in,max}|; \tag{4.45}$$

$$I_{rel} \equiv \frac{n_a}{n_d} \sin^2\left(\frac{2\pi n_d t_d}{\lambda_0}\right) + \frac{n_d}{n_a} \cos^2\left(\frac{2\pi n_d t_d}{\lambda_0}\right)$$

where we have defined the relative intensity as I_{rel} to simplify the notation in further calculations.

Further, we know that the air gap width on-resonance is related to t_d as given by eq. 4.33:

$$\frac{2\pi n_a t_a}{\lambda_0} = \arctan\left(-\frac{n_a}{n_d} \tan\left(\frac{2\pi n_d t_d}{\lambda_0}\right)\right), \tag{4.46}$$

where we keep $n_a = 1$ in the expression. such that:

$$\sin\left(\frac{2\pi n_a t_a}{\lambda_0}\right) = -\sqrt{\frac{1}{I_{rel}}} \sqrt{\frac{n_a}{n_d}} \sin\left(\frac{2\pi n_d t_d}{\lambda_0}\right); \tag{4.47}$$

$$\cos\left(\frac{2\pi n_a t_a}{\lambda_0}\right) = \sqrt{\frac{1}{I_{rel}}} \sqrt{\frac{n_d}{n_a}} \cos\left(\frac{2\pi n_d t_d}{\lambda_0}\right). \tag{4.48}$$

With eqs. 4.45, 4.47 and 4.48, we can rewrite the field in the air-part in terms of $|E_{d,in,max}|$ and t_d:

$$E_{a,in} = |E_{d,in,max}| \left(\sin\left(\frac{2\pi n_d t_d}{\lambda_0}\right) - i\frac{n_d}{n_a} \cos\left(\frac{2\pi n_d t_d}{\lambda_0}\right)\right). \tag{4.49}$$

We now have all the ingredients we need to evaluate the losses per cavity round trip. For that, we add the losses from the diamond side ($n_1 = n_d$) and from the air side ($n_2 = n_a$), weighting the last one by the factor comparing the relative intensities, as we have done before for the mirror losses. Using the expressions we found above, we arrive at the

resulting expression:

$$\mathcal{L}_{S,\text{eff}} = \mathcal{L}_{S,DA} + \frac{n_a E_{max,a}^2}{n_d E_{max,d}^2} \mathcal{L}_{S,AD} \tag{4.50}$$

$$= 1 - \frac{|\rho'_{12} E_{d,in} + \tau'_{21} E_{a,in}|^2}{|E_{d,in}|^2} + I_{rel}\left(1 - \frac{|\rho'_{21} E_{a,in} + \tau'_{12} E_{d,in}|^2}{|E_{a,in}|^2}\right) \tag{4.51}$$

$$= 1 + I_{rel} - \frac{|\rho'_{12} E_{d,in} + \tau'_{21} E_{a,in}|^2 + \frac{n_a}{n_d}|\rho'_{21} E_{a,in} + \tau'_{12} E_{d,in}|^2}{|E_{d,in}|^2} \tag{4.52}$$

$$= 1 + I_{rel} - \left(\rho'^2_{12} + I_{rel}\frac{n_d}{n_a}\tau'^2_{21} + \frac{n_a}{n_d}I_{rel}\frac{n_d}{n_a}\rho'^2_{21} + \frac{n_a}{n_d}\tau'^2_{12}\right) \tag{4.53}$$

$$- \left(\rho'_{12}\tau'_{21} + \frac{n_a}{n_d}\rho'_{21}\tau'_{12}\right)\frac{E_{a,in}E^\star_{d,in} + E_{d,in}E^\star_{a,in}}{|E_{d,in}|^2} \tag{4.54}$$

$$\approx n_1 \frac{(n_1 - n_2)^2}{n_1 + n_2}\left(\frac{4\pi\sigma_{DA}}{\lambda_0}\right)^2 + I_{rel}n_2\frac{(n_1 - n_2)^2}{n_1 + n_2}\left(\frac{4\pi\sigma_{DA}}{\lambda_0}\right)^2 \tag{4.55}$$

$$+ n_2\frac{(n_1 - n_2)^2}{n_1 + n_2}\left(\frac{4\pi\sigma_{DA}}{\lambda_0}\right)^2\left(2\sin^2\left(\frac{2\pi n_d t_d}{\lambda_0}\right) - 2\frac{n_1}{n_2}\cos^2\left(\frac{2\pi n_d t_d}{\lambda_0}\right)\right) \tag{4.56}$$

$$= \sin^2\left(\frac{2\pi n_d t_d}{\lambda_0}\right)\frac{(n_2 + n_1)}{n_1}(n_2 - n_1)^2\left(\frac{4\pi\sigma_{DA}}{\lambda_0}\right)^2. \tag{4.57}$$

From this expression we find that the effective losses are proportional to $\sin^2(2\pi n_d t_d/\lambda_0)$, which is the field intensity at the interface. The losses will thus be 0 for an air-like mode, and maximal for a diamond-like mode.

4.6.4. Analytic solution of a coupled Gaussian beams model

This section describes the derivation of the analytic solution to a coupled Gaussian beams model as presented in Sec. 4.2. We here outline the model and corresponding boundary conditions, and provide an analytic solution. We assume the diamond surface to be planar in the first part of this section, which is close to a realistic situation. In the second part of this section we provide an analytic solution for a curved diamond surface, in which that mode volume may be decreased compared to the planar situation.

We employ the standard notation for a Gaussian beam [52]:

$$U(\boldsymbol{r}) = \frac{A_1}{q(z)} \exp\left(-ik\frac{\rho^2}{2q(z)}\right) \exp(-ikz) \tag{4.58}$$

$$= A_0 \frac{w_0}{W(z)} \exp\left(-\frac{\rho^2}{W^2(z)}\right) \exp\left(-ikz - ik\frac{\rho^2}{2R(z)} + i\zeta(z)\right); \tag{4.59}$$

$$W(z) = w_0 \sqrt{1 + \left(\frac{z}{z_0}\right)^2}; \tag{4.60}$$

$$R(z) = z\left(1 + \left(\frac{z_0}{z}\right)^2\right); \tag{4.61}$$

$$\zeta(z) = \arctan\frac{z}{z_0}; \tag{4.62}$$

$$w_0 = \sqrt{\frac{\lambda_0 z_0}{n\pi}}. \tag{4.63}$$

where the complex beam parameter $q(z) = z + iz_0$ has been written as

$$\frac{1}{q(z)} = \frac{1}{R(z)} - i\frac{\lambda_0}{\pi n W^2(z)}, \tag{4.64}$$

to make the beam width $W(z)$ and the wave front curvature $R(z)$ explicit in the formulation. $\zeta(z)$ is the Guoy phase shift that occurs as a result of the deviation of the Gaussian beam from a planar wave, and we use $A_0 = A_1/(iz_0)$. Further, ρ is the radial coordination, z the coordinate along the beam and $k = \frac{2\pi}{\lambda_0}$ the wavenumber. The Gaussian beam is a solution for a bare plane-concave cavity, but to describe the field in a hybrid diamond-air cavity the two regions with different refractive-index regions have to be treated separately. This is evident when considering that the relation between the Gaussian beam parameters w_0 and z_0 is dependent on the refractive index in which the Gaussian beam lives (see eq. 4.63). The wave front curvature R and beam widths W of these separate beams in diamond and air are described as [20]:

$$R_d(z) = z\left(1 + \left(\frac{z_{0,d}}{z}\right)^2\right); \tag{4.65}$$

$$R_a(z) = (z - \Delta z_a)\left(1 + \left(\frac{z_{0,a}}{z - \Delta z_a}\right)^2\right); \tag{4.66}$$

$$W_d(z) = w_{0,d}\sqrt{1 + \left(\frac{z}{z_{0,d}}\right)^2}; \tag{4.67}$$

$$W_a(z) = w_{0,a}\sqrt{1 + \left(\frac{z - \Delta z_a}{z_{0,a}}\right)^2}. \tag{4.68}$$

The subscript a (d) is used for the Gaussian beam in air (diamond). The beam waist of the diamond beam is fixed to be on the plane mirror in the considered geometry, and the air beam waist is at distance Δz_a from the plane mirror. This distance, together with the Rayleigh lengths of the diamond and air beams ($z_{0,a}$ and $z_{0,d}$) fix the full description

of the Gaussian beams in the cavity. They follow from the boundary conditions imposed by the cavity dimensions. These boundary conditions can be found by considering the 'ABCD-matrix' that transforms the Gaussian beam parameters going from air (with $n = n_a$) to diamond (with $n = n_d$) [52]:

$$\begin{pmatrix} A & B \\ C & D \end{pmatrix} = \begin{pmatrix} 1 & 0 \\ 0 & n_a/n_d \end{pmatrix}. \tag{4.69}$$

Following the corresponding ABCD law for Gaussian beams we then find that the complex beam parameters in diamond and air (q_d and q_a) are related by:

$$q_d = \frac{Aq_a + B}{Cq_a + D} = \frac{q_a}{n_a/n_d}. \tag{4.70}$$

This leads to the following conditions on the beam curvature and beam width at the interface:

$$n_d R_a(t_d) = n_a R_d(t_d); \tag{4.71}$$
$$W_a(t_d) = W_d(t_d), \tag{4.72}$$

that can be solved analytically to give [53]:

$$w_{0,a} = w_{0,d}, \qquad (\rightarrow z_{0,a}/n_a = z_{0,d}/n_d). \tag{4.73}$$
$$\Delta z_a = t_d \left(1 - \frac{n_a}{n_d} \right). \tag{4.74}$$

Together with the boundary condition that the beam front curvature follows the radius of curvature of the fiber dimple:

$$R_a(t_a + t_d) = ROC, \tag{4.75}$$

this gives an expression for the beam waist of the Gaussian beam:

$$w_{0,d} = w_{0,a} = \sqrt{\frac{\lambda_0}{\pi n_a} \left(\left(t_a + \frac{t_d}{n_d} \right) \left(ROC - \left(t_a + \frac{t_d}{n_d} \right) \right) \right)^{1/4}}. \tag{4.76}$$

In this expression we recognize the standard expression for the beam waist [19], with the cavity length replaced by:

$$L' \equiv t_a + \frac{t_d}{n_d} \quad (= t_a + t_d - \Delta z_a). \tag{4.77}$$

The numerically and analytically obtained results to the model are both shown in Fig. 4.9. We see that the stability condition for the cavity changes from the condition for a bare cavity. The stability condition of a cavity is found by requiring that the Rayleigh length satisfies $z_0^2 > 0$. For a bare cavity of length L this gives, in combination with the boundary condition $R(L) = ROC$, the requirement $L < ROC$. The maximum cavity length is thus given by the radius of curvature of the concave mirror. But, for the hybrid cavity

we see in Fig. 4.9 that the cavity is stable beyond $t_d + t_a = ROC$, where $t_a = 16\ \mu$m. For the hybrid cavity the beam waist of the air mode can be disconnected from the plane mirror such that we expect the cavity stability region to be given by $t_a + t_d - \Delta z_a$. Indeed, requiring $z_{0,a}^2 > 0$ in eq. 4.76 we find that the stability condition is:
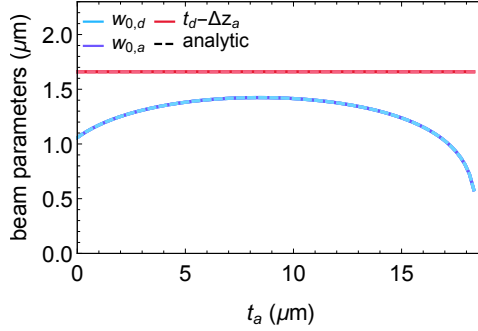
$$t_a + \frac{t_d}{n_d} \lesssim ROC \tag{4.78}$$

Figure 4.9: The numerically calculated beam parameters (solid lines) versus the air gap of a diamond-air cavity with $t_d = 4\ \mu$m and $ROC = 20\ \mu$m. Analytically obtained results (eqs. 4.73, 4.74 and 4.76) are shown as dashed lines. The analytical values for $w_{0,a}$ and $w_{0,d}$ overlap.

Analytic solution for a curved diamond surface

We here derive the analytic solutions to the coupled Gaussian beams model if the diamond surface were curved, fixing the diamond surface radius of curvature to match the beam front curvature. While the diamond-air interface is more accurately described by a plane interface, the beam waist for a curved surface can be decreased for a curved diamond surface. This may produce a cavity with a smaller mode volume.

The ABCD matrix for this situation is given by:

$$\begin{pmatrix} A & B \\ C & D \end{pmatrix} = \begin{pmatrix} 1 & 0 \\ -\frac{(n_d - n_a)}{n_d R_{DA}} & n_a/n_d \end{pmatrix}, \tag{4.79}$$

where R_{DA} is the radius of curvature of the diamond surface, that we assume to match the diamond and air Gaussian beam radius of curvature at that position: $R_a(t_d) = R_d(t_d) = -R_{DA}$. Following the ABCD-law, the complex beam parameters are related as:

$$q_d = \frac{Aq_a + B}{Cq_a + D} = \frac{q_a}{-\frac{(n_d - n_a)}{n_d R_{DA}}q_a - n_a/n_d}. \tag{4.80}$$

The boundary conditions that this leads to are:

$$R_a(t_d) = R_d(t_d); \tag{4.81}$$

$$W_a(t_d) = W_d(t_d), \tag{4.82}$$

that can be solved analytically to give:

$$z_{0,a} = \frac{n_d n_a (1 + t_d^2 / z_{0,d}^2)}{n_d^2 + n_a^2 t_d^2 / z_{0,d}^2} z_{0,d} \approx \frac{n_a}{n_d} z_{0,d}, \quad (\rightarrow w_{0,a} \approx w_{0,d}). \tag{4.83}$$

$$\Delta z_a = t_d \left(1 - \frac{n_d^2 (1 + t_d^2 / z_{0,d}^2)}{n_d^2 + n_a^2 t_d^2 / z_{0,d}^2} \right) \approx t_d \left(1 - n_a^2 n_d^2 \right), \tag{4.84}$$

where the approximation holds in the case $t_d \ll z_{0,d}$, which holds in the case that $ROC \gg t_d$, as will be justified below. We find that the 'effective cavity length' that determines the beam waist for the case with such a curved surface is $L'_{curv} \approx t_a + t_d / n_d^2$. This length is shorter than for a plane diamond surface, since the surface curvature creates a lensing effect, shifting the effective waist position of the Gaussian beam in air towards the diamond-air interface. The shorter effective length gives a narrower beam waist compared to the plane diamond.

Derivation of $t_d \ll z_{0,d}$ for $ROC \gg t_d$ In this paragraph we show that if we assume $ROC \gg t_d$, than it follows that $t_d \ll z_{0,d}$. First we assure ourselves that if $ROC \gg t_d$ holds, $R_{DA} \gg t_d$ also holds, where R_{DA} is the beam curvature at the diamond-air interface. We can deduce this by finding the conditions for which $R_{DA} = ROC$, and then deducing that $R_{DA} > ROC$ for at least all cavities with $2t_d + t_a < ROC$. We do this as follows: first we find the two solutions of $R_a(z) = ROC$:

$$z - \Delta z_a = \frac{ROC}{2} \pm \frac{\sqrt{ROC^2 - 4z_{0,a}^2}}{2}$$

If $R_{DA} = ROC$, one of these solutions must correspond to $z = t_d$, while the other should correspond to $z = t_a + t_d$. We thus conclude that $t_a = \sqrt{ROC^2 - 4z_{0,a}^2}$. If we use this in the solution for $z = t_d$ we find: $t_d - \Delta z_a = ROC/2 - t_a/2$. This is the limiting case: to have $R_{DA} < ROC$ we require $t_d + t_a/2 - \Delta z_a < ROC/2$, or at least $2t_d + t_a < ROC$. This condition is almost always satisfied for cavities with $t_d \ll ROC$ since in that case the condition reduces to $t_a \lesssim ROC$ which holds for all stable cavities.

We then use the constraint $t_d \ll R_{DA}$ to find constraints on $z_{0,d}$ and $z_{0,a}$. To this end we write R_{DA} as $R_d(t_d)$ and $R_a(t_d)$ using eq. 4.65. $t_d \ll R_{DA}$ with $R_{DA} = R_d(t_d)$ respectively, gives:

$$t_d \ll t_d \left(1 + \frac{z_{0,d}}{t_d} \right)^2 ; \tag{4.85}$$

using $(t_d - \Delta z_a) < t_d \ll R_{DA}$ for the second equation. From this we find:

$$z_{0,d} \gg t_d; \tag{4.86}$$

4.6.5. QUANTITATIVE ESTIMATES OF A MINIMUM AIR GAP WIDTH

The minimum air gap in a diamond-air cavity is civen by the geometry of the dimple. We here give a detailed description of the relevant parameters.

Independent of the fabrication procedure, the dimple depth z_d is fixed by the radius of curvature and the useful dimple diameter D_d as $z_d \approx D_d^2/(8ROC)$ [19]. For dimples with radii of curvature as considered in this manuscript ($\approx 15 - 35 \ \mu$m) and a diameter large enough to prevent clipping losses (see Sec. 4.3.2), $D_d \approx 8 \ \mu$m), the dimple depth is $z_d \approx 0.2 - 0.5 \ \mu$m. An extra air gap z_f is introduced when there is an angle θ between optical fiber or plate in which the dimple is created and the flat substrate. If the extent beyond the dimple centre is $D_f/2$, the extra air gap is $z_f = \frac{D_f}{2} \sin(\theta) \approx \frac{D_f}{2}\theta$. For setups with an optical fiber on a tip-tilt stage [21], we estimate that the maximum angle the fiber tip makes with the flat substrate is $\theta_{max} \approx 70$ mrad (≈ 20 mrad from the tip-tilt stage and ≈ 50 mrad from tilt due to mounting of the fiber). In combination with a typical fiber diameter of $D_f = 125 \ \mu$m, this leads to $z_{f,max} \approx 4.4 \ \mu$m. This effect if thus dominant over the dimple depth. To reduce the minimal air gap in fiber-based cavities, the most important approach to lowering the mode volume is thus by shaping the fiber tip [40]. For cavities employing silica plates the large extent of the plates demands careful parallel mounting of the mirror substrates.

4.6.6. MODELLING THE EFFECT OF VIBRATIONS ON THE ZPL EMISSION

This section describes how the effect of vibrations is included in the model that describes the emission into the ZPL. First, we find the cavity resonance frequencies for length detuning dt_a, and use these to calculate the corresponding spectral overlap with the NV center emission frequency via

$$\xi_s(dt_a) = \frac{1}{1 + 4Q^2 \left(\frac{\lambda_{\text{ZPL}}}{\lambda_{\text{cav}}(dt_a)} - 1 \right)^2}, \tag{4.87}$$

where λ_{ZPL} is the NV emission frequency and $\lambda_{\text{cav}}(dt_a)$ the cavity frequency for length detuning dta. $Q = \nu/\delta\nu$ is the cavity quality factor, that is calculated using the analytic methods presented in Sec. 4.2. We next multiply the Purcell factor found for the on-resonance case by the spectral overlap and calculate the resulting emission into the ZPL for each length detuning. Finally an average branching ratio β_{vib} is obtained by assuming that the cavity length is normally distributed around the resonant length with a standard deviation σ_{vib}, and integrating over all air gaps around the resonance:

$$\beta_{\text{vib}} = \int \frac{\beta_0 \xi_s(dt_a) F_p}{\beta_0 \xi_s(dt_a) F_p + 1} \frac{1}{\sqrt{2\pi\sigma_{\text{vib}}^2}} e^{-\frac{dt_a^2}{2\sigma_{\text{vib}}^2}} d(dt_a) \tag{4.88}$$

This integral is integrated numerically, to obtain the average branching ratio into the ZPL.

4.6.7. COUPLING EFFICIENCY OF A FIBER-BASED MICROCAVITY

In this section we describe the collection efficiency of the cavity mode, for a fiber-based microcavity. To that end we focus on how well the cavity mode can be matched to the
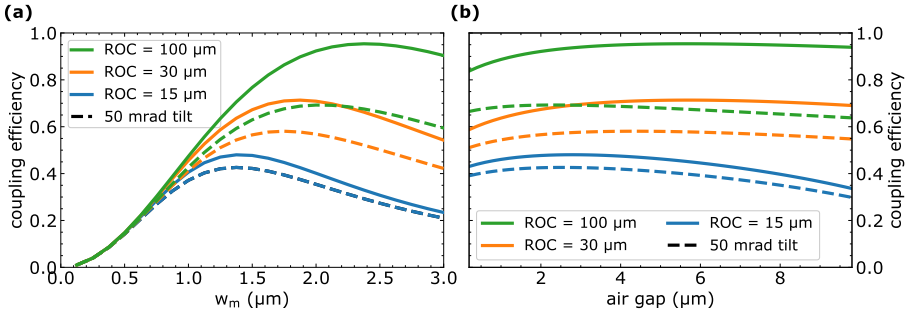
Figure 4.10: (a) The mode matching efficiency into the dimpled fiber approaches unity for an ROC of 100 μm, if the beam width on the mirror approaches unity for an ROC of 100 μm, if the beam width on the mirror approached the beam width in the fiber (w_f = 2.5 μm). A fiber tilt of 50 mrad (dashed lines) decreases the maximally achievable coupling efficiency. (b) For t_d = 4 μm the air gap width should be $\gtrsim$ 2 μm to maximize the coupling efficiency.

detection mode. In our setup we have two possible detection routes: directly into the laser-machined fiber, or via the free-space path. On the side of the free space path the cavity mode can be overlapped with the mode of the collection path using free space elements. By optimal positioning of the optical elements the coupling can in principle have unit efficiency. On the fiber-side of the cavity path such flexibility is not present. The mode-matching efficiency is determined by the power transmittivity τ given by the overlap between the Gaussian beams in the fiber and the cavity mode [19, 42]:

$$\tau = \int U_f^*(\vec{r})U_c(\vec{r})d\vec{r}. \tag{4.89}$$

The Gaussian beams $U(\vec{r})$ are given by eq. 4.59 in the fiber and cavity, at $z = t_a + t_d$. The integral is over the radial direction. The relevant parameters are thus the beam widths and curvatures in the fiber (w_f, R_f) and cavity ($w_m, R_m = ROC$), as well as the spatial overlap of the beams given by the potential misalignment of the fiber due to an off-centred dimple and fiber tilt.

The resulting coupling efficiency (solid lines in Fig. 4.10(a)) approaches unity for a large dimple radius of curvature if the beam width on the fiber mirror w_m matches the beam radius in the fiber, w_f = 2.5 μm, providing the best overlap between the Gaussian beams. With the analytic model described in Secs. 4.3 and 4.6.4 above, we can determine w_m from the radius of curvature, size of the air gap and diamond thickness through eqs. 4.68, 4.73 and 4.76. Using this we determine what coupling parameter is achievable for our cavity parameters. Fig. 4.10(b) shows that to achieve a coupling efficiency of > 0.75 an ROC > 35 μm in combination with an air gap > 2 μm is needed.

In addition spatial misalignment due to fiber tilt may significantly influence the coupling efficiency. If the fiber tilt is θ = 50 mrad (Fig. 4.10, dashed lines), a coupling efficiency > 0.75 can only be achieved for ROC > 100 μm. The influence of an off-centred dimple of dx < 0.5 μm is negligible.

The decrease of the coupling efficiency for smaller radius of curvature and air gap is in direct conflict with the maximalisation of the Purcell factor. To avoid having to trade-

off these quantities, detection via the free space path is beneficial. A stability-argument can however be made for detection through the fiber: vibrations of the cavity as a whole with respect to the optical table, as resulting from passive vibration isolation used to minimize intra-cavity vibrations [21], might hinder free-space detection. Detection and (low-power, resonant) excitation through the fiber would remove the need to actively stabilize these vibrations.

4

REFERENCES

[1] S. B. van Dam, M. Ruf and R. Hanson, *Optimal design of diamond-air microcavities for quantum networks using an analytical approach,* New J. Phys. **20**, 115004 (2018).

[2] A. Reiserer and G. Rempe, *Cavity-based quantum networks with single atoms and optical photons,* Rev. Mod. Phys. **87**, 1379 (2014).

[3] H. Bernien, B. Hensen, W. Pfaff, G. Koolstra, M. S. Blok, L. Robledo, T. Taminiau, M. Markham, D. J. Twitchen, L. Childress and R. Hanson, *Heralded entanglement between solid-state qubits separated by three metres.* Nature **497**, 86 (2013).

[4] W. B. Gao, A. Imamoglu, H. Bernien and R. Hanson, *Coherent manipulation, measurement and entanglement of individual solid-state spins using optical fields,* Nat. Photonics **9**, 363 (2015).

[5] S. Kolkowitz, Q. P. Unterreithmeier, S. D. Bennett and M. D. Lukin, *Sensing distant nuclear spins with a single electron spin,* Phys. Rev. Lett. **109**, 137601 (2012).

[6] T. H. Taminiau, J. J. T. Wagenaar, T. Van Der Sar, F. Jelezko, V. V. Dobrovitski and R. Hanson, *Detection and control of individual nuclear spins using a weakly coupled electron spin,* Phys. Rev. Lett. **109**, 137602 (2012).

[7] N. Zhao, J. Honert, B. Schmid, M. Klas, J. Isoya, M. Markham, D. Twitchen, F. Jelezko, R. B. Liu, H. Fedder and J. Wrachtrup, *Sensing single remote nuclear spins,* Nat. Nanotech. **7**, 657 (2012).

[8] N. Kalb, A. A. Reiserer, P. C. Humphreys, J. J. W. Bakermans, S. J. Kamerling, N. H. Nickerson, S. C. Benjamin, D. J. Twitchen, M. Markham and R. Hanson, *Entanglement Distillation between Solid-State Quantum Network Nodes,* Science **356**, 928 (2017).

[9] P. C. Humphreys, N. Kalb, J. P. J. Morits, R. N. Schouten, R. F. L. Vermeulen, D. J. Twitchen, M. Markham and R. Hanson, *Deterministic delivery of remote entanglement on a quantum network,* Nature **558**, 268 (2018).

[10] D. Riedel, I. Söllner, B. J. Shields, S. Starosielec, P. Appel, E. Neu, P. Maletinsky and R. J. Warburton, *Deterministic enhancement of coherent photon generation from a nitrogen-vacancy center in ultrapure diamond,* Phys. Rev. X **7**, 031040 (2017).

[11] E. M. Purcell, *Spontaneous Emission Probabilities at Radio Frequencies,* Phys. Rev. **69**, 681 (1946).

[12] A. Faraon, P. E. Barclay, C. Santori, K.-M. C. Fu and R. G. Beausoleil, *Resonant enhancement of the zero-phonon emission from a colour centre in a diamond cavity,* Nat. Photonics **5**, 301 (2011).

[13] P. E. Barclay, K. M. C. Fu, C. Santori, A. Faraon and R. G. Beausoleil, *Hybrid nanocavity resonant enhancement of color center emission in diamond,* Phys. Rev. X **1**, 011007 (2011).

4

[14] A. Faraon, C. Santori, Z. Huang, V. M. Acosta and R. G. Beausoleil, *Coupling of nitrogen-vacancy centers to photonic crystal cavities in monocrystalline diamond,* Phys. Rev. Lett. **109**, 2 (2012).

[15] B. J. M. Hausmann *et al.*, *Coupling of NV centers to photonic crystal nanobeams in diamond,* Nano Lett. **13,** 5791 (2013).

[16] L. Li *et al.*, *Coherent spin control of a nanocavity-enhanced qubit in diamond.* Nat. Commun. **6**, 6173 (2015).

[17] J. Riedrich-Möller, S. Pezzagna, J. Meijer, C. Pauly, F. Mücklich, M. Markham, A. M. Edmonds and C. Becher, *Nanoimplantation and Purcell enhancement of single nitrogen-vacancy centers in photonic crystal cavities in diamond,* Appl. Phys. Lett. **106**, 221103 (2015).

[18] S. Johnson, P. R. Dolan, T. Grange, A. A. P. Trichet, G. Hornecker, Y. C. Chen, L. Weng, G. M. Hughes, A. A. R. Watt, A. Auffèves and J. M. Smith, *Tunable cavity coupling of the zero phonon line of a nitrogen-vacancy defect in diamond,* New J. Phys. **17,** 122003 (2015).

[19] D. Hunger, T. Steinmetz, Y. Colombe, C. Deutsch, T. W. Hänsch and J. Reichel, *A fiber Fabry–Perot cavity with high finesse,* New J. Phys. **12,** 065038 (2010).

[20] E. Janitz, M. Ruf, M. Dimock, A. Bourassa, J. Sankey and L. Childress, *A Fabry-Perot microcavity for diamond-based photonics,* Phys. Rev. A **92**, 043844 (2015).

[21] S. Bogdanović, S. B. van Dam, C. Bonato, L. C. Coenen, A. M. J. Zwerver, B. Hensen, M. S. Liddy, T. Fink, A. Reiserer, M. Lončar and R. Hanson, *Design and low-temperature characterization of a tunable microcavity for diamond-based quantum networks,* Appl. Phys. Lett. **110**, 171103 (2017).

[22] J. Gallego, S. Ghosh, S. K. Alavi, W. Alt, M. Martinez-Dorantes, D. Meschede and L. Ratschbacher, *High-finesse fiber Fabry–Perot cavities: stabilization and mode matching analysis,* Appl. Phys. B Lasers Opt. **122,** 47 (2016).

[23] J. F. S. Brachmann, H. Kaupp, T. W. Hänsch and D. Hunger, *Photothermal effects in ultra-precisely stabilized tunable microcavities,* Opt. Expr. **24**, 21205 (2016).

[24] M. Khudaverdyan, W. Alt, I. Dotsenko, T. Kampschulte, K. Lenhard, A. Rauschenbeutel, S. Reick, K. Schörner, A. Widera and D. Meschede, *Controlled insertion and retrieval of atoms coupled to a high-finesse optical resonator,* New J. Phys. **10,** 073023 (2008).

[25] E. Janitz, M. Ruf, Y. Fontana, J. Sankey and L. Childress, *A High-Mechanical Bandwidth Fabry-Perot Fiber Cavity,* Opt. Express **25**, 20392 (2017).

[26] M. Fox, *Quantum Optics: an introduction* (Oxford University Press, 2006).

[27] J.-M. Gérard, *Solid-state cavity-quantum electrodynamics with self-assembled quantum dots,* in *Single Quantum Dots,* edited by P. Michler (Springer, 2003) pp. 269–314.

[28] L. Greuter, S. Starosielec, D. Najer, A. Ludwig, L. Duempelmann, D. Rohner and R. J. Warburton, *A small mode volume tunable microcavity: Development and characterization,* Appl. Phys. Lett. **105**, 121105 (2014).

[29] C. Sauvan, J. P. Hugonin, I. S. Maksymov and P. Lalanne, *Theory of the Spontaneous Optical Emission of Nanosize Photonic and Plasmon Resonators,* Phys. Rev. Lett. **110**, 237401 (2013).

[30] S. J. Orfanidis, *Electromagnetic Waves and Antennas* (Rutgers University, Piscataway, NJ, 2002).

[31] J. N. Dodd, *Atoms and Light: Interactions* (Springer US, Boston, MA, 1991).

[32] We are happy to provide the code on request.

[33] I. Filiński, *The effects of sample imperfections on optical spectra,* Phys. Status Solidi B **49**, 577 (1972).

[34] J. Szczyrbwoski and A. Czapla, *Optical absorption in D.C. sputtered InAd Films,* Thin Solid Films **46**, 127 (1977).

[35] C. C. Katsidis and D. I. Siapkas, *General transfer-matrix method for optical multilayer systems with coherent, partially coherent, and incoherent interference,* Appl. Opt. **41**, 3978 (2002).

[36] P. R. Dolan, G. M. Hughes, F. Grazioso, B. R. Patton and J. M. Smith, *Femtoliter tunable optical cavity arrays,* Opt. Lett. **35**, 3556 (2010).

[37] R. J. Barbour, P. A. Dalgarno, A. Curran, K. M. Nowak, H. J. Baker, D. R. Hall, N. G. Stoltz, P. M. Petroff and R. J. Warburton, *A tunable microcavity,* J. Appl. Phys. **110**, 053107 (2011).

[38] A. A. P. Trichet, P. R. Dolan, D. M. Coles, G. M. Hughes and J. M. Smith, *Topographic control of open-access microcavities at the nanometer scale,* Opt. Express **23**, 17205 (2015).

[39] D. Najer, M. Renggli, D. Riedel, S. Starosielec and R. J. Warburton, *Fabrication of mirror templates in silica with micron-sized radii of curvature,* Appl. Phys. Lett. **110**, 1 (2017).

[40] H. Kaupp, T. Hümmer, M. Mader, B. Schlederer, J. Benedikter, P. Haeusser, H. C. Chang, H. Fedder, T. W. Hänsch and D. Hunger, *Purcell-Enhanced Single-Photon Emission from Nitrogen-Vacancy Centers Coupled to a Tunable Microcavity,* Phys. Rev. Appl. **6**, 054010 (2016).

[41] J. Benedikter, T. Hümmer, M. Mader, B. Schlederer, J. Reichel, T. W. Hänsch and D. Hunger, *Transverse-mode coupling and diffraction loss in tunable Fabry–Pérot microcavities,* New J. Phys. **17**, 053051 (2015).

[42] W. B. Joyce and B. C. DeLoach, *Alignment of Gaussian beams,* Appl. Opt. **23**, 4187 (1984).

4

[43] P. Appel, E. Neu, M. Ganzhorn, A. Barfuss, M. Batzer, M. Gratz, A. Tschï¿½pe and P. Maletinsky, *Fabrication of all diamond scanning probes for nanoscale magnetometry,* Rev. Sci. Instrum. **87**, 063703 (2016).

[44] S. Bogdanović, M. S. Z. Liddy, S. B. van Dam, L. C. Coenen, T. Fink, M. Lončar and R. Hanson, *Robust nano-fabrication of an integrated platform for spin control in a tunable microcavity,* APL Photonics **2**, 126101 (2017).

[45] M. Hanks, M. Trupke, J. Schmiedmayer, W. J. Munro and K. Nemoto, *High-fidelity spin measurement on the nitrogen-vacancy center,* New J. Phys. **19**, 103002 (2017).

[46] B. Hensen *et al.*, *Loophole-free Bell inequality violation using electron spins separated by 1.3 kilometres,* Nature **526**, 682 (2015).

[47] L. Robledo, L. Childress, H. Bernien, B. Hensen, P. F. A. Alkemade and R. Hanson, *High-fidelity projective read-out of a solid-state spin quantum register,* Nature **477**, 574 (2011).

[48] M. Bock, P. Eich, S. Kucera, M. Kreis, A. Lenhard, C. Becher and J. Eschner, *High-fidelity entanglement between a trapped ion and a telecom photon via quantum frequency conversion,* Nat. Commun. **9**, 1998 (2018).

[49] A. Dréau, A. Tcheborateva, A. E. Mahdaoui, C. Bonato and R. Hanson, *Quantum frequency conversion to telecom of single photons from a nitrogen-vacancy center in diamond,* Phys. Rev. Appl. **9**, 064031 (2018).

[50] T. K. Yeung, D. Le Sage, L. M. Pham, P. L. Stanwix and R. L. Walsworth, *Anti-reflection coating for nitrogen-vacancy optical measurements in diamond,* Appl. Phys. Lett. **100**, 251111 (2012).

[51] W. Pfaff, B. Hensen, H. Bernien, S. B. van Dam, M. S. Blok, T. H. Taminiau, M. J. Tiggelman, R. N. Schouten, M. Markham, D. J. Twitchen and R. Hanson, *Unconditional quantum teleportation between distant solid-state quantum bits,* Science **345**, 532 (2014).

[52] B. Saleh and M. Teich, *Fundamentals of Photonics*, Wiley Series in Pure and Applied Optics (Wiley, 2007).

[53] S. Nemoto, *Waist shift of a Gaussian beam by plane dielectric interfaces.* Appl. Opt. **27**, 1833 (1988).

5

OPTICALLY COHERENT NITROGEN-VACANCY CENTERS IN μm-THIN ETCHED DIAMOND MEMBRANES

Maximilian Ruf*, Mark IJspeert*, Suzanne van Dam, Nick de Jong, Hans van den Berg, Guus Evers, and Ronald Hanson

Diamond membrane devices containing optically coherent nitrogen-vacancy (NV) centers are key to enable novel cryogenic experiments such as optical ground-state cooling of hybrid spin-mechanical systems and efficient entanglement distribution in quantum networks. Here, we report on the fabrication of a (3.4 ± 0.2) μm thin, smooth (surface roughness r_q < 0.4 nm over an area of 20 μm by 30 μm) diamond membrane containing individually resolvable, narrow linewidth (< 100 MHz) NV centers. We fabricate this sample via a combination of high energy electron irradiation, high temperature annealing, and an optimized etching sequence found via a systematic study of the diamond surface evolution on the microscopic level in different etch chemistries. While our particular device dimensions are optimized for cavity-enhanced entanglement generation between distant NV centers in open, tuneable micro-cavities, our results have implications for a broad range of quantum experiments that require the combination of narrow optical transitions and μm-scale device geometry.

* These authors contributed equally to this work

5.1. Introduction

The negative nitrogen-vacancy (NV) center is a point defect center in diamond [2, 3] that is used in a wide range of experiments, including quantum sensing [4–8], quantum computation algorithms [9, 10], and quantum communication [11–13]. In addition to second-long spin coherence times [14] and spin-conserving optical transitions [15], NV centers feature coupling to nearby nuclear spins that can act as memory quantum bits [12, 16, 17]. Many NV-based experiments require a combination of good optical and spin properties in nano-fabricated structures; these experiments include Purcell enhancement of the optical zero-phonon line (ZPL) transitions in a diamond microcavity [18–31] for entanglement generation speed-up, optical ground state cooling of a hybrid NV-cantilever spin-mechanical system [32–37], and resonant optical readout of NV centers in sensing applications [15]. While good spin coherence has been demonstrated for surface-proximal NVs (depth of ∼ 50 nm) [38–40], the incorporation of optically coherent NV centers in μm-scale devices remains an outstanding challenge.

The optically excited state of the NV center is sensitive to electric fields and crystal strain [41]. Therefore, high-frequency electric field noise can lead to dephasing in the excited state, while on longer timescales the transitions can be effectively widened by slow spectral diffusion originating from a changing charge state distribution in the environment [42, 43]. Although the latter effect can be mitigated by actively tracking the transition frequencies and adding feedback [11], it comes at the cost of reduced experimental repetition rates. Dephasing poses a more fundamental challenge: in hybrid-mechanical systems, effective optical ground state cooling requires operation in the sideband resolved regime [32, 35]. Dephasing also determines the resolvable magnetic field changes in sensing experiments, and limits the two-photon quantum interference contrast that translates into state fidelity for entanglement protocols [44, 45]. For all discussed applications of NV centers in membranes, spectral diffusion widths < 250 MHz and dephasing widths < 100 MHz are in practice desired (see Suppl. 5.7.8). However, reported spectral diffusion widths in thin (∼ 1 μm) nanofabricated structures are ∼ 1 GHz [31] for NV centers formed via nitrogen implantation [46]. Improvements in fabrication and preparation methods are therefore necessary to produce devices with linewidths sufficiently narrow for the experiments discussed above.

For our desired application of embedding a diamond membrane in an open, tuneable Fabry-Perot microcavity to increase entanglement generation rates between distant NV centers [29–31, 47, 48], we target a final membrane thickness of ∼ 4 μm. This choice is a compromise between low cavity mode volume needed for high Purcell enhancement and sufficient thickness to avoid frequent breaking of membranes during sample handling, whilst being able to embed NVs as deep in the diamond lattice as possible to avoid surface-induced noise. We furthermore require smooth samples (r_q < 0.3 nm over the ∼ 4 μm^2 large area of the cavity beam waist) to limit losses due to scattering at the diamond-air interface (scaling with r_q squared) [47, 49].

Here, we report on a full fabrication procedure that combines high energy electron irradiation, high temperature annealing, and an optimized etching sequence, to yield a diamond device that meets all the above requirements. We verify the desired NV center optical properties using an extensive study on linewidths following different etching steps.
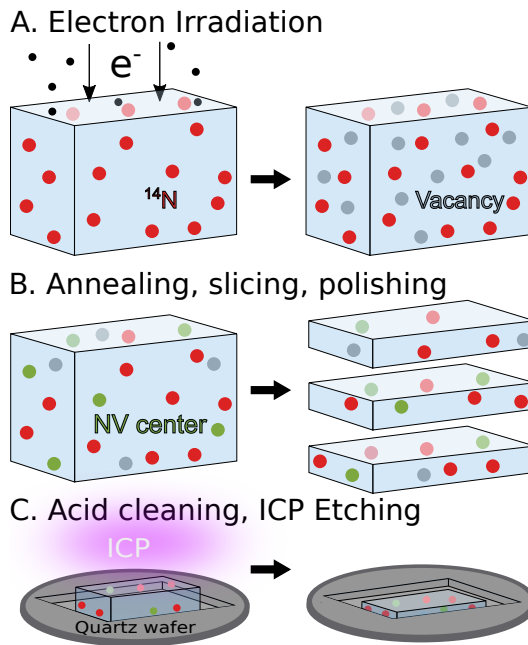
Figure 5.1: Schematic of the diamond fabrication process flow. (A) A CVD grown diamond is irradiated with electrons to form vacancies in the diamond lattice (see Suppl. 5.7.2). (B) After a tri-acid clean, a high temperature annealing process in high vacuum combines the holes with naturally occurring nitrogen in the sample to form NV centers (see Suppl. 5.7.2). The sample is then sliced into three 50 μm thick slabs that are each polished to a surface roughness of typically $r_q < 1$ nm. (C) After an acid clean to remove remaining contamination that could lead to masking during etching, the sample is etched in a ICP-RIE.

5.2. NV CENTER CREATION VIA ELECTRON IRRADIATION

We start from ultrapure, CVD grown diamond that contains only a few NV centers (see Suppl. 5.7.2), and thus requires their density to be increased. NV centers created from implanted nitrogen atoms were recently found to predominately feature broad optical lines, likely due to associated diamond lattice damage [50]. Instead, we use high energy electron irradiation to create vacancies throughout the whole diamond that can form NV centers with native nitrogen [51] (see Fig. 5.1 (A)). After tri-acid cleaning, a high temperature and high vacuum annealing sequence — consisting of three temperature steps — ensures the recombination of vacancies with naturally occurring nitrogen in the diamond to form NV centers, and anneals out vacancy chains [52, 53] (see Fig. 5.1 (B)). The resulting density of NV centers thus depends on the nitrogen distribution resulting from diamond growth, and the number of vacancies created during electron irradiation (see Suppl. 5.7.2). The diamonds are subsequently sliced and polished into three membranes of ~ 50 μm thickness each. This value is a trade-off between ease of handling of the membranes in further processing steps, and the amount of material that needs to be removed in a subsequent reactive ion etching (RIE) step using an Inductively Coupled Plasma (ICP) (see Fig. 5.1 (C)).
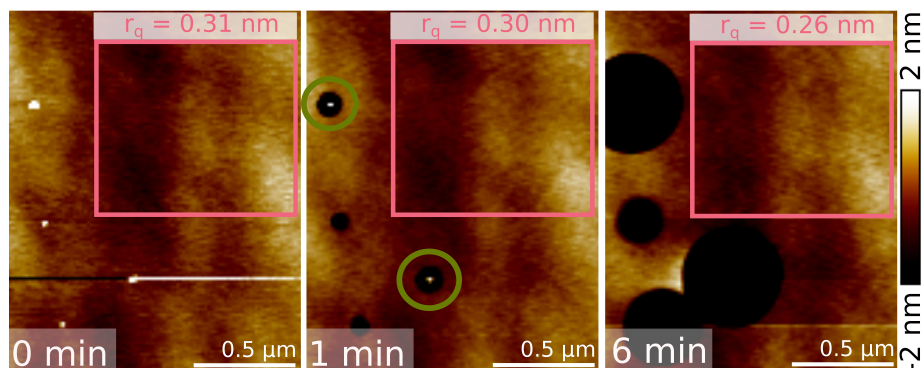
Figure 5.2: Evolution of a diamond surface during ICP-RIE with O_2 for different etching times (indicated in the bottom left corner of each AFM image for an identical area). The data demonstrates that debris on the diamond surface leads to micro-masking during etching, resulting in the formation of nanopillars (visible in the green encircled parts after 1 minute of etching). These pillars are subsequently removed via an isotropic etch component. Pink rectangles show a comparison of surface roughness r_q for a 1 μm by 1 μm wide area that excludes etch-induced holes (error 0.03 nm). Note that the black / white trace in the AFM image before etching is a data acquisition artifact.

5.3. DEVELOPMENT OF AN ETCH PROCEDURE FOR DIAMOND MEMBRANES

To find an etch recipe that leads to smooth, thin diamonds, we investigate the effect of different etch chemistries on the diamond surface roughness on the microscopic level. It is advantageous to employ an oxygen-based ICP-RIE, due to reported high diamond etch rates (> 200 nm/min [54]), and an oxygen-rich surface termination of the diamond, which is beneficial for the charge state stability of the NV⁻ center [55]. However, it has been speculated that particles, e.g. those introduced during diamond polishing, wet-processing or sample handling (see Suppl. 5.7.1), can lead to hole formation during etching with O_2 [56, 57].

5.3.1. ORIGIN OF PILLAR FORMATION DURING OXYGEN ETCHING

By overlaying Atomic Force Microscope (AFM) surface images of identical diamond areas before and after O_2 etching, we find that each of the observed circular pits originates from a particle that was initially present at that location. Fig. 5.2 shows the evolution of one such area before etching, and after 1 and 6 minutes of etching with O_2 (see Suppl. 5.7.1). The data demonstrates that the underlying mechanism of hole formation is micro-masking: the particle etch rate is lower than that of the bulk diamond surface. This leads to the formation of diamond nanopillars on the surface that deflect the impinging plasma, which enhances the etch rate locally and thus creates a hole around the pillar [54] (see the green encircled areas in Fig. 5.2 after 1 minute of etching). Due to an isotropic etch component, the pillars are eventually etched away, leaving behind a hole. These holes then remain, and widen as the etching continues. Importantly, we also find that the membrane surface roughness can be maintained during O_2 etching if particle-induced holes are excluded (see the pink rectangles in Fig. 5.2). Even after extended O_2
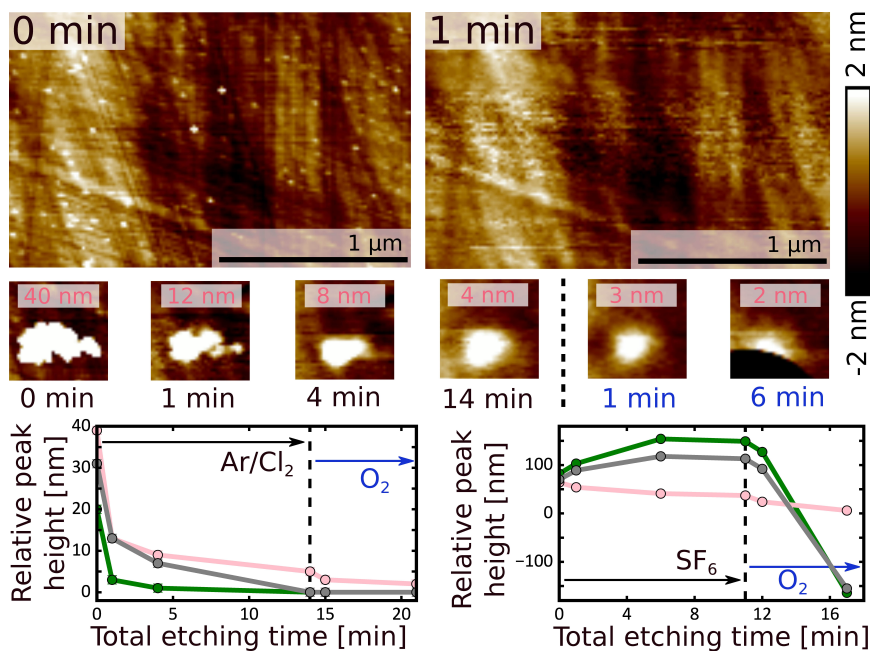
Figure 5.3: Evolution of particles and surface roughness during etching with Ar/Cl$_2$ of a diamond surface and relative particle height vs. etching time for SF$_6$ and Ar/Cl$_2$ etching. Top row of AFM images demonstrates that one minute of Ar/Cl$_2$ etching effectively removes small particles. Middle row of AFM images (1 μm by 1 μm) shows the evolution of the relative peak height of an initially large particle w.r.t. the mean surface height as a function of etching time during etching with Ar/Cl$_2$ (black time indication) and subsequent with O$_2$ (blue indication), respectively. Note that the big hole after six minutes of etching with O$_2$ results from etch-induced widening of an initially present hole on the diamond surface, caused by a low-quality diamond growth and polishing process (see Suppl. 5.7.1). Bottom graphs compare relative peak height (or hole depth) evolution under ArCl$_2$ (left graph) and SF$_6$ (right graph) pre-etching, followed by O$_2$ etching for different selected particles (see Suppl. 5.7.1 for the full underlying dataset).

etches, one thus expects to maintain the intitial diamond surface roughness if particles can be effectively removed before this step.

5.3.2. SURFACE CLEANING ETCH

To reduce the number of particles on the diamond surface to levels lower than after acid cleaning alone (see Suppl. 5.7.1), common strategies are to etch under Ar/Cl$_2$ [58] or SF$_6$ [59]. However, Ar/Cl$_2$ etching induces Cl contamination on the diamond surface [60], which is suspected to have a detrimental influence on the optical and spin properties of NV centers. Therefore, Ar/Cl$_2$ is often combined with O$_2$ etching [8, 31, 53, 59, 61, 62]. Fig. 5.3 confirms that Ar/Cl$_2$ is indeed highly effective in removing particles, and that it can be followed by O$_2$ etching without forming holes on the surface. By comparing the evolution of the relative peak height of particles w.r.t. the mean of the surrounding diamond surface (see Fig. 5.3, bottom graphs), we find that Ar/Cl$_2$ is more efficient in removing particles from the diamond surface than SF$_6$ (see Suppl. 5.7.1): while

Ar/Cl$_2$ removes small particles within the first minute of etching and continues to reduce the relative peak height of large debris for longer etching times, it takes longer for small particles to be removed in SF$_6$, and the relative peak height of some larger remaining structures increases during etching in this chemistry, leading to the formation of holes.

5.4. Fabrication of a μm-thin diamond membrane

Using the above etch recipe, we fabricate a sample following the steps in Fig. 5.1. For microwave delivery and repeated identification of the measurement area, the sample is bonded via Van der Waals forces to a super-polished mirror patterned with golden striplines and unique position markers before etching [63]. We have observed that the exposure of mirror material to the plasma leads to severe micromasking on the diamond as etched mirror material is re-deposited on the diamond surface. This results in the formation of holes on the diamond following the same mechanism as discussed above. To mitigate this effect, we use a fused quartz mask for partial exposure of the diamond [62] (see Fig. 5.4 (Top left)). We thin the sample in three etching steps, each consisting of an Ar/Cl$_2$ pre-etch, followed by a single O$_2$ step, for a total etch duration of 86 minutes of Ar/Cl$_2$ and 206 minutes of O$_2$ etching. Fig. 5.4 (Bottom) shows a confocal microscope image and stylus profilometer height trace of the bonded membrane after the full etching sequence. The geometry of the mask restricts the solid angle of incidence and leads to a position-dependent etch rate. Therefore, the sample height profile shows a curvature in the exposed region, with a thinnest membrane thickness of (3.4 ± 0.2) μm. The red dot indicates the (3.8 ± 0.2) μm thick area within which the AFM image in Fig. 5.4 (Top right) was taken after the full etch. This image confirms a smooth diamond surface ($r_q = 0.38$ nm over a 20 μm by 30 μm area) even after this prolonged etch sequence.

5.5. Photoluminescence excitation measurements

We characterize the optical properties of NV centers in between etch steps in a confocal microscopy setup < 10 K by using a largely automatized measurement sequence to determine their linewidths via photo-luminescence excitation (PLE) scans of the ZPL transitions (see Suppl. 5.7.3). After roughly localizing an NV transition in frequency space, we scan a tuneable laser around this frequency, while detecting photons emitted from the NV in the phonon side band (PSB). We repeatedly apply a sequence of a short green laser pulse (to ensure spin and charge state initialization), followed by a red frequency sweep through the expected transition frequency (to map out the specific ZPL transition under dephasing). We do this while constantly applying microwaves to avoid pumping in an optically dark spin state. By performing many scans of this kind, we probe both the effects of spectral diffusion (via a fit to the averaged counts of all scans), as well as the average dephasing width (by fitting each scan individually, and calculating the weighted mean for all fitted linewidths).

Fig. 5.5 shows the results of spectral diffusion and dephasing widths as a function of distance from the mirror interface for a total of 155 NV center transitions, stemming from 110 distinguishable NV centers. This data has been acquired at four different steps during membrane thinning and thus membrane thicknesses t_m in the measurement region. While we are not able to track identical NV centers throughout the different etch steps,
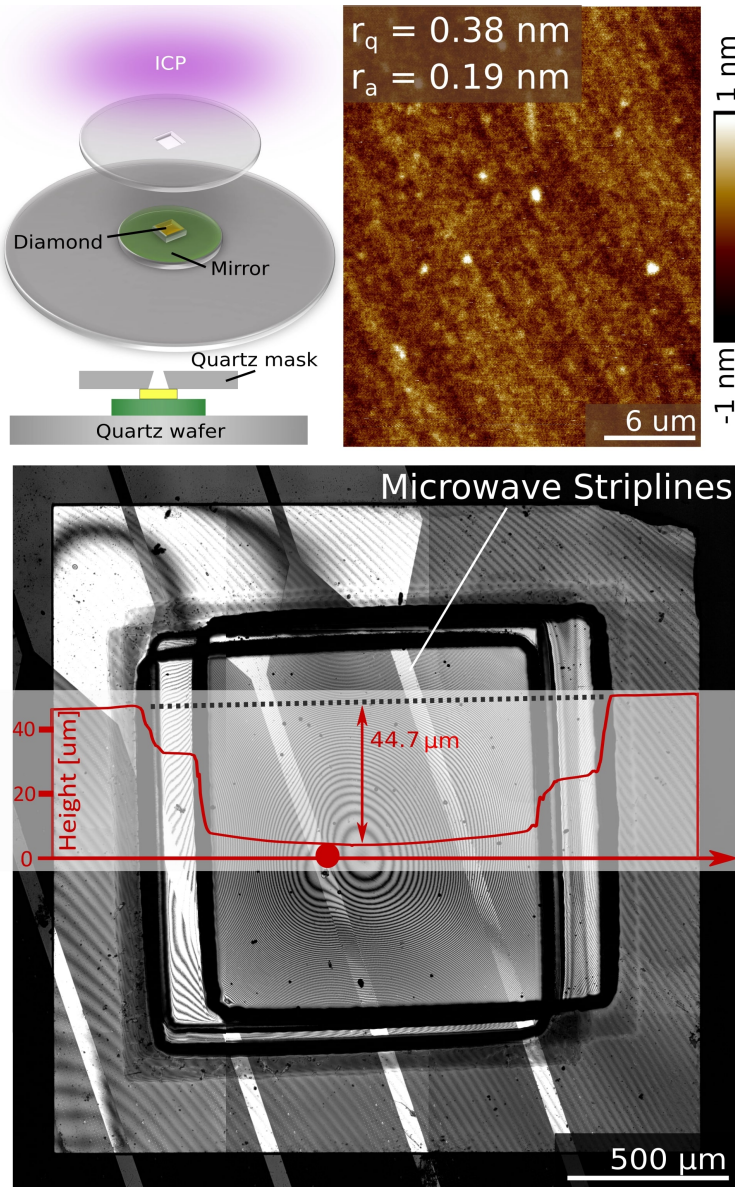
Figure 5.4: Schematic of the diamond etching setup and resulting membrane profile. (Top left) Setup used for bonded diamond etching. A diamond membrane is bonded to a mirror patterned with gold position markers and striplines, positioned on a fused quartz carrier wafer, and masked from the top with a fused quartz substrate that has a rectangular opening [62] (see Suppl. 5.7.2). (Bottom) Confocal microscope image of an etched diamond membrane, with three clearly visible offset recesses that result from repeated and shifted partial exposure. The red arrow indicates the profilometer path along which a height profile (red) was taken. It reveals a diamond wedge of 0.14° (angle of dotted line w.r.t. horizontal axis) resulting from the diamond slicing and polishing process, and a maximum etch depth of (44.7 ± 0.2) µm in the middle region. The red circle corresponds to the region within which most of the data in this paper was taken, with a final thickness of (3.8 ± 0.2) µm. The fringe spacing corresponds to a height change of 84 nm. (Top right) AFM image of the region indicated with a red circle in the middle image, showing a low surface roughness of $r_q = 0.38$ nm over an area of 20 µm by 30 µm.
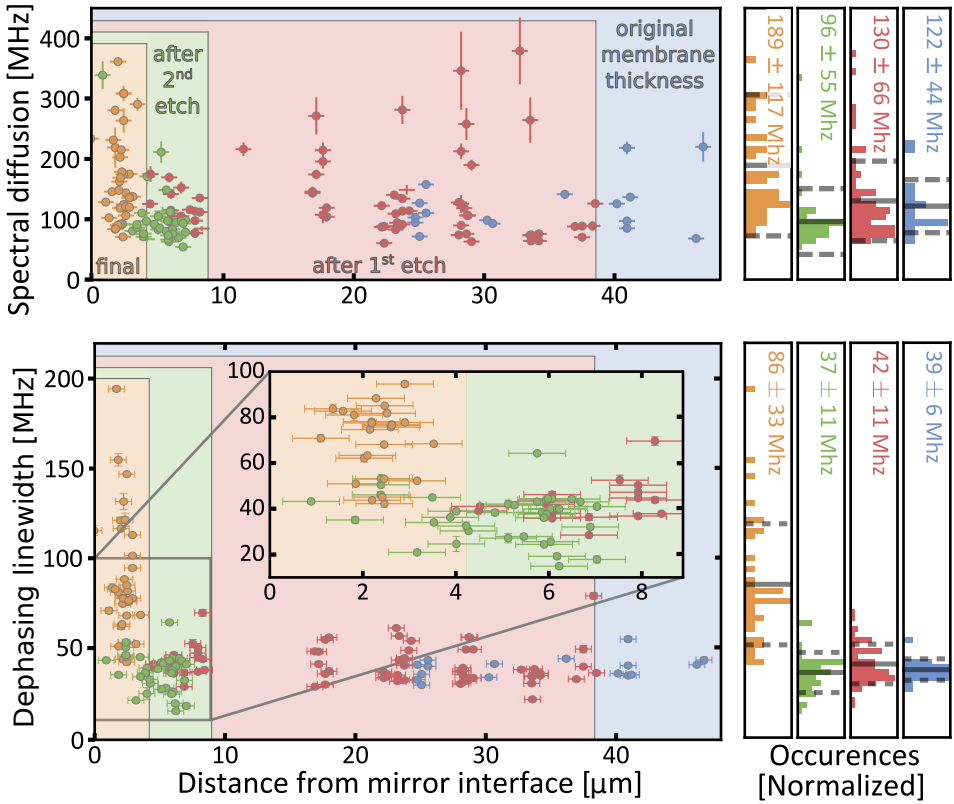
Figure 5.5: Overview of spectral diffusion (top left panel) and dephasing linewidth (bottom left panel) of NV centers at various distances from the mirror interface for different membrane thicknesses. Right hand side shows normalized histograms of the data on the left, with the black solid (dashed) lines visualizing the mean (standard deviation) of the data for a given membrane thickness, and the colored numbers indicating these values. (Blue) Data before any etching, membrane thickness in measurement region $t_m = (47.8 \pm 0.2)$ μm. (Red) Data after first etching of 26 mins Ar/Cl$_2$, followed by 45 mins of O$_2$, $t_m = (37.7 \pm 0.2)$ μm. (Green) Data after an additional 30 mins Ar/Cl$_2$ and 138 mins O$_2$ etching, $t_m = (10.1 \pm 0.2)$ μm. (Yellow) Data after an additional 30 mins Ar/Cl$_2$ and 23 mins O$_2$ etching, $t_m = (3.8 \pm 0.2)$ μm. The horizontal clustering of points is a data acquisition artifact.

we make sure to look at the same 20 μm by 20 μm area of diamond for all measurements, apart from the data for the thinnest membrane, for which we additionally included a second region ∼ 200 μm from the main measurement area for increased statistics. Confocal scans performed after each etching step show no evidence of strong variations in NV center density.

The data shows the potential of electron irradiation as a reliable way of introducing coherent NV centers throughout the membrane: for the unetched case, we find an average dephasing width of (39 ± 6) MHz, and an average spectral diffusion width of (122 ± 44) MHz. We suspect that laser-power induced linewidth broadening prevents us from resolving lifetime limited values for the dephasing linewidths (see Suppl. 5.7.4). Importantly, for membranes etched down to $t_m = (37.7 \pm 0.2)$ μm and to $t_m = (10.1 \pm 0.2)$ μm,

we observe that all linewidth averages overlap within statistical uncertainties.

We find roughly two times broader linewidths when characterizing NVs at the final membrane thickness of t_m = (3.8 ± 0.2) μm in the measurement region; the spectral diffusion width averages to (189 ± 117) MHz, while the dephasing width averages to (86 ± 33) MHz. Yet, even for this thickness, we find that 22 out of 37 measured NV centers fulfill our pre-set criteria of dephasing linewidth < 100 MHz and spectral diffusion linewidth < 250 MHz. Possible mechanisms that could explain this linewidth broadening after the last etching step include additional dephasing due to Cl residue left behind on the diamond surface after the proportionally longer etching under Ar/Cl_2 for this final etch step, as well as lattice damage induced by reflection of ions from the diamond-mirror interface.

The NV ZPL transitions shift with crystal strain: while axial strain results in an overall resonance frequency shift, transverse strain splits the E_x and E_y optical transitions [2]. To determine whether strain in the diamond influences the observed linewidth broadening, we extract the transverse and axial strain from a subset of NV centers via a reconstruction of the NV center Hamiltonian (see Suppl. 5.7.7). Although the average axial and transverse strain increase with decreasing NV distance from the mirror interface, the data does not show a dependency of the measured spectral diffusion and dephasing linewidths on strain (see Suppl. 5.7.7), suggesting that there is no direct causal relation between the two. Possible causes of increased strain found for NVs after the last etching step include a stressed layer that remains after the membrane polishing process [64–66], effects due to bonding of the diamond to the mirror (including stress resulting from the difference in thermal expansion coefficients for the diamond and mirror), and lattice-damage induced by reflected ions as discussed above. Future systematic studies beyond the current work are required to pinpoint the origin unambiguously.

5.6. CONCLUSIONS

In conclusion, we have demonstrated the fabrication of a diamond sample with a high density of NV centers, introduced through electron irradiation and subsequent high temperature annealing. The surface roughness (r_q < 0.4 nm for a 20 μm by 30 μm area), thickness (~ 4 μm) and NV linewidths (< 100 MHz) of this sample allow for enhanced entanglement generation rates via the Purcell effect in an open, tuneable microcavity setup. Given these sample properties and vibration levels of 0.1 nm rms under pulse-tube operation [48], we expect an emission of ZPL photons coupled into the fiber mode of 35% [49], which translates into an entanglement rate enhancement of two orders of magnitude. This would allow one to form a quantum repeater beating direct transmission [67–69], signaling the surpassing of a fundamental milestone on the route to building a quantum network.

5.7. Supplementary information

5.7.1. Diamond surface evolution under ICP-RIE etching with SF_6 and Ar/Cl_2

This section describes the systematic study of the evolution of diamond surfaces on the microscopic level under reactive ion etching (RIE) using an inductively coupled plasma (ICP). All measurements were performed on high pressure, high temperature (HPHT) grown, ⟨100⟩ oriented type Ib diamonds (Element Six, $3 \times 3 \times 0.3$ mm). These diamonds contain many surface and sub-surface defects resulting from the growth and polishing process. When excluding these defect areas intrinsic to HPHT samples, this material can still be used to extract quantitative surface data when comparing different processing steps (see sections below).

Sample preparation

Before etching, as-received HPHT diamonds are cleaned in HNO_3 (99%) for 10 minutes. The samples are then rinsed for 10 minutes in de-ionized (DI) water, cleaned in acetone in an ultrasonic bath for 5 minutes, rinsed for one minute in isopropyle alcohol (IPA), and blow-dried with nitrogen.

During this research, we have compared the effect of different pre-etch wet cleaning methods on the diamond surface quality after etching. While we have not compared the number of particles after different wet cleaning methods quantitatively, we find that the HNO_3 cleaning described above yields a similar surface roughness after etching in comparison with commonly used, yet time-consuming techniques such as tri-acid and hydrofluoric acid (HF).

Diamond etching methods

Etch procedures were carried out using ICP-RIE (Oxford Plasmalab 100). Many holes are formed during etching of diamond surfaces when using etch holders made out of Si or Al_2O_3, as the respective material is etched and re-deposited. Following the same mechanism as reported in the main text, this leads to hole formation in the diamond surface. To avoid this process, we use a 4 inch fused quartz carrier wafer during etching, that shows minimal material re-deposition on the diamond surface. To avoid charging during etching (which prevents the release of the carrier wafer from a mechanically clamped wafer holder after etching), we apply a ~ 15 nm thick Ti layer on the backside of this wafer via sputter deposition (Alliance Concept AC450), and clamp the wafer in the etcher with a metal ring. A summary of all etch parameters and measured etch rates (diamond sample and fused quartz carrier wafer) can be found in Table 5.1.

	O_2	Ar/Cl_2	SF_6
ICP / RF power (W)	1100 / 90	500 / 200	500 / 50
Gas flow (sccm)	50 O_2	10 Ar / 20 Cl_2	30 SF_6
Pressure (μbar)	10	10	13
Carrier wafer temperature (°C)	20	30	30
Diamond etch rate (masked, nm/min)	210 ± 10	42 ± 2	n. m.
Diamond etch rate (not masked, nm/min)	350 ± 20	39 ± 2	44 ± 2
Fused quartz etch rate (nm/min)	11 ± 1	80 ± 5	113 ± 6

Table 5.1: Summary of etch parameters and diamond sample and fused quartz carrier wafer etch rates found in this work. N. m. not measured.

ATOMIC FORCE MICROSCOPY ANALYSIS

The Atomic Force Microscope (AFM, Bruker FastScan) data underlying the evolution of the height of a particle w.r.t. the mean diamond surface height for identical areas and different etch times as displayed in Fig. 3 of the main text can be seen in Fig. 5.6 for the SF_6 based etching sequence, and in Fig. 5.7 for the Ar/Cl_2 based etching sequence. We infer the particle heights and errorbars by plotting a histogram of surface height around a particle, and taking the mean and standard deviation of the distribution after employing a cut-off above the mean sample surface height.

ORIGIN OF PARTICLES ON DIAMOND SURFACE

During etch recipe development, we have gathered evidence that some particles left behind on the diamond surface after wet cleaning are diamond material (which can be inferred from the particle etch rate, and leads to a smoothened pillar, similar to the feature observed in the pink encircled particle in Fig. 5.6 below). Other particles adhere to the surface and remain after wet-processing (we have unsuccessfully experimented with using ultra-high grade isopropyl alcohol as a last solvent before sample drying, as well as megasonic nozzle cleaning to remove wet-cleaning induced particles), or are introduced during handling of the samples, even if this is done under ISO7 cleanroom conditions (see the AFM image after 14 minutes of etching with O_2 in Fig. 5.7 below). These mechanisms vary between diamond handling events.

We have used X-ray photoelectron spectroscopy (XPS) in an attempt to characterize the origin of particles on several samples. However, the results have been inconclusive: As our smallest XPS beam covers an area of 300 um by 700 um, it is hard to measure the chemical composition of a small amount of particles, as the signal is obscured by the large contribution of C and O elements, as well as by charging of the diamond surface, leading to a line shift that makes it hard to quantify measurement results. On the other hand, energy-dispersive X-ray (EDX) measurements of individual particles on a diamond after wet-cleaning show that most material in drying strains consists of C+O+Na+Cl, with a small number of particles also showing C+O+Ni. The fact that these particles act as "good" masks during etching with O_2 supports the hypothesis that this material contains oxides.
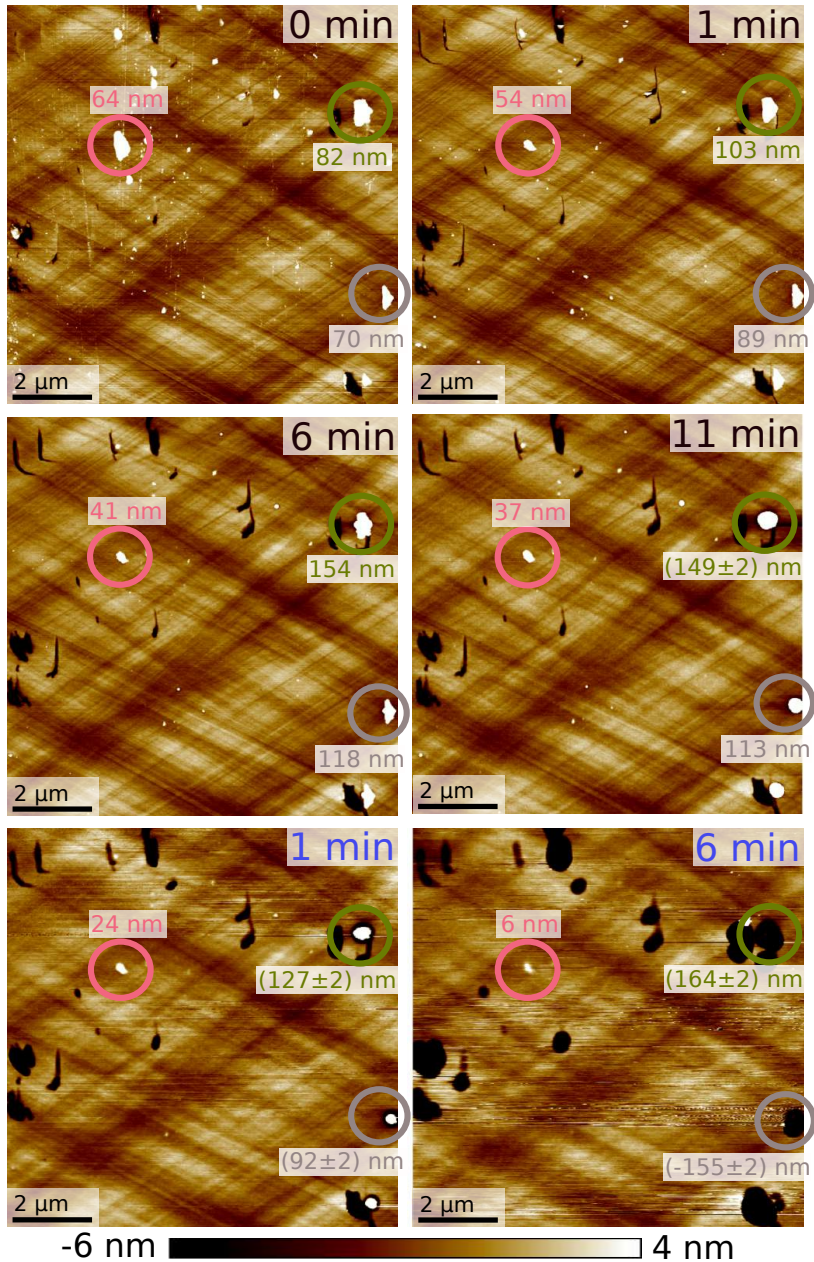
Figure 5.6: Evolution of an identical HPHT diamond surface area during ICP-RIE with SF_6 (black time indication), followed by etching with O_2 (blue time indication), for different etching times (indicated in the top right of each AFM trace). This sample shows many surface defects, resulting from the diamond growth and polishing process. Colored circles indicate the relative height of particles w.r.t. the mean diamond surface height for a specific etch time, with an errorbar of ±1 nm unless otherwise indicated. This data underlies Figure 3 of the main text.
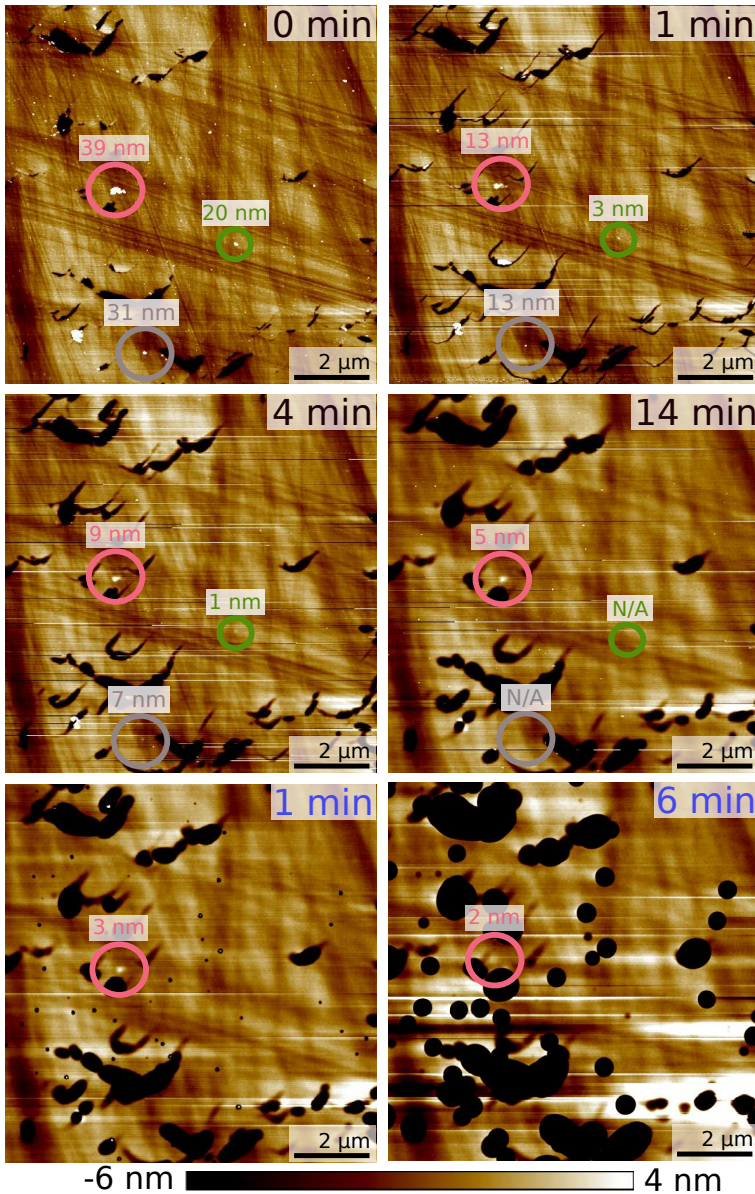
Figure 5.7: Evolution of an identical HPHT diamond surface area during ICP-RIE for different etching times (indicated in the top right of each AFM trace) with Ar/Cl_2 (black time indication), followed by etching with O_2 (blue time indication). This sample shows many surface defects, resulting from the diamond growth and polishing process. Colored circles indicate the relative height of particles w.r.t. the mean diamond surface height for a specific etch time, with an errorbar of ± 1 nm. Note that for this particular etch sequence, many particles are introduced by handling the diamond in between etch steps (e.g. visible by comparing the images after 1 min and 14 min of Ar/Cl_2 etching). This explains the formation of many small holes after 1 min of O_2 etching, that can be avoided when etching directly after the Ar/Cl_2 etch (i.e. without unloading the diamond from the etcher). This data underlies Figure 3 of the main text.

5.7.2. FABRICATION OF A THIN DIAMOND PLATELET

This section describes the full process-flow employed to fabricate the (3.4 ± 0.2) μm thick diamond plate discussed in the main text.

We start fabrication by irradiating as-received, commercially available type IIa CVD grown diamonds (Element Six, $2 \times 2 \times 0.5$ mm, company specified nitrogen density $<$ 885 μm^{-3}, $\langle 100 \rangle$ crystal orientation) with electrons (electron energy 2 MeV, fluence 1 or 5×10^{13} e$^-$/cm^{2}s) at the Reactor Institute in Delft. As described in the main text, this forms vacancies in the diamond lattice (~ 30 or 150 μm^{-3}). On samples that underwent the same procedure as the one described here, we find typical natural NV density values of < 0.005 μm^{-3} (compared to company specified values of < 5 μm^{-3}). To reduce potential diamond surface contamination with metals resulting from the diamond polishing process [70, 71] that could lead to contamination of the annealing chamber, we immerse the samples in a mixture of 1:1:1 H_2SO_4(97%):HNO_3(60%):$HClO_4$(60%) at 120 °C for one hour in a re-flux configuration. We then rinse the sample for 10 minutes in de-ionized (DI) water, clean it for 5 minutes in acetone in an ultrasonic bath, rinse it for one minute in isopropyl alcohol (IPA), and blow-dry the sample with nitrogen.

Next, we anneal the sample in a three step high temperature annealing process under high vacuum ($< 10^{-6}$ mbar) to combine vacancies with naturally occurring nitrogen in the sample to form NV centers, and to anneal out defects such as di-vacancies [53]. We ramp the temperature from room temperature to 400 °C in 4 hours, hold the temperature constant for 8 hours, increase the temperature to 800 °C over a 12 hour time-span, hold this temperature for 8 hours, increase the temperature to 1100 °C in 12 hours, hold it constant for a period of 10 hours, and then switch off the oven to cool to room temperature. All temperature increases are ramped linearly at a slow rate to maintain a high vacuum in the annealing chamber that is needed to avoid surface graphitization of the diamond [53]. This treatment results in typical NV densities of $(0.01 - 0.1)$ μm^{-3}.

After slicing of a sample into three membranes of ~ 50 μm each, the membranes are polished to a surface roughness of typically $r_q < 1$ nm (Delaware Diamond Knives). We then clean the membranes in HNO_3 (99%) for 10 minutes, followed by the same after-acid cleaning and drying procedure as described above. Subsequently, we bond the sample via Van der Waals forces to a mirror patterned with golden markers and strip lines to allow for repeated localization of the same area in subsequent NV characterization steps, and for application of microwaves to NV centers [63].

As discussed in the main text, the exposure of mirror material to the plasma leads to severe micromasking on the diamond. We therefore mask the diamond and mirror from the top with a fused quartz wafer (thickness 500 μm) that has a laser-cut square opening

	Ar/Cl$_2$ time (min)	O$_2$ time (min)	Thickness t$_m$ (μm)
Before any etching	–	–	47.8 ± 0.2
First etching step	26	45	37.7 ± 0.2
Second etching step	30	138	10.1 ± 0.2
Third etching step	30	23	3.8 ± 0.2

Table 5.2: Summary of etching times under Ar/Cl$_2$, followed by O$_2$, and corresponding thickness in NV measurement region t$_m$ after each etching step, measured with a stylus profilometer.

(Lasertec BV) (1.4 mm side length on the side facing the diamond, narrowing towards the top at an angle of 30 ° to reduce etch-induced trenching effects [72], see Fig. 4 of the main text for mask geometry). This prevents exposure of mirror material to the etching plasma. We then etch the diamond in different ICP-RIE steps as described in the main text and summarized in Table 5.2, using the plasma parameters summarized in Table 5.1. Note that once bonded, we do not wet-clean the sample in between etch steps.

5.7.3. NV characterization methods

Experimental setup
To measure the optical properties of NV centers, we use a home-built confocal microscope operated at low temperature (< 10 K) inside a closed-cycle cryostat (Montana Instruments s50) with optical access. A microscope objective (Olympus MPLFLN-100X) is mounted on an xyz scanner (Physik Instrumente P-615K011). To extract the NV transition linewidths, we lock a 637 nm external cavity laser (New Focus Velocity TLB-6700) to a wavemeter (High finesse WS-6) via a PC controlled PID loop acting on the laser control. We then sweep the setpoint of the lock, and detect fluorescent photons from the NV emitted in the phonon side band (PSB) on an APD (Laser Components Count-20C-FC), while recording the corresponding laser frequency value. The PSB is spectrally separated from the zero phonon line by a dichroic mirror (Semrock L2NL-0016) with a custom made razor edge at ~ 637 nm. We use off-resonant green laser excitation (532 nm, Cobolt Samba 100) to initialize the NV in the negative charge state and $m_s = 0$ spin state. The laser pulses are created via acousto-optic modulators (Gooch and Housego). To further suppress unwanted residual light from the green laser, we introduce an additional PC-controlled home-built shutter in the beam path after the second round of measurements of Fig. 5 in the main text (i.e. starting from measurements after the second membrane etch). To rotate the NV electron spin, we generate microwave signals via an arbitrary waveform generator (AWG) and a microwave source (Rhode und Schwarz SMBV100A) that are amplified (Amplifier Research 40S1G4) before delivery to the striplines on the mirror.

Data acquisition sequence
We have developed a largely automized software sequence that allows us to measure the spectral diffusion and dephasing linewidths of many NV centers. An overview of the decision tree followed is displayed in Fig. 5.8 (Left).

NV localization   After performing a confocal microscope scan ($\lambda = 532$ nm, see Fig. 5.9 (A) for an example), potential NV center locations are selected via manual input. If one dimensional off-resonant scans ($\lambda = 532$ nm) along both the x- and y- directions show a fluorescence profile with a Gaussian profile within certain width bounds after a maximum of 3 optimizations each, the protocol continues by optimizing the signal to noise ratio of a scan along the x-direction for different z positions of the objective. This method allows to determine the optimal focal distance, as it does not take into account background fluorescence originating from defects in the mirror substrate. We then measure a continuous wave (CW) optically detected magnetic resonance spectrum (ODMR) around the NV zero field splitting (≈ 2.88 GHz, see Fig. 5.9 (B)). As the quality of the mi-
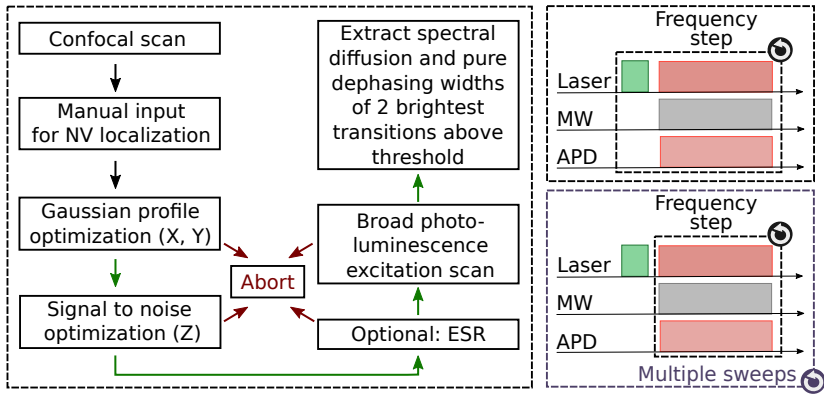
Figure 5.8: Sketches of automated data acquisition sequence and employed laser scans. (Left) Decision tree employed during automated data acquisition. Black arrows indicate that no software decision is made, green arrows represent continuation after a positive previous step, and red arrows indicate that the previous step failed, the routine is aborted, and the software starts over with a Gaussian profile optimization at potential NV center locations (see text for detailed description of each step). (Right, top) Schematic of the pulse sequence used during a broad PLE scan. Green laser pulses (10 μW, 10 μs) are continuously interleaved with red laser pulses (20 nW, 100 μs, with a wait time of 10 μs in between pulses), while sweeping the red laser's frequency with a resolution of 10 MHz, and integrating for a total time of 25 ms per frequency point. (Right, bottom) Schematic of the pulse sequence used to characterize an individual NV center ZPL line. In contrast to the sequence employed in (right, top), we only apply one green pulse (10 μW, 1s) at the beginning of each red frequency sweep. We then sweep the red laser's frequency (8 nW) with a resolution of 4 MHz, and integrate for 10 ms per point.

crowave striplines deteriorates after prolonged etching, ODMR scans are only performed for the first two sets of data. If a dip in the fluorescence signal (corresponding to the m_s = 0 to m_s = 1 spin transition) falls below one standard deviation from the data mean, we mark the spot as a potential NV center and continue with characterization of the optical transition frequencies. For all subsequent measurements, we use either the microwave frequency found by fitting the CW-ODMR spectra, or the zero field splitting frequency of 2.88 GHz (starting from the third set of data, from which on reduced microwave stripline quality does not allow us to detect CW-ODMR signals).

Optical characterization　　We proceed with scanning a tuneable laser around the expected ZPL transition wavelength, while detecting photons emitted from the NV in the phonon side band (PSB, see Fig. 5.9 (C)). To detect all six allowed spin-conserving ZPL transitions, we constantly apply microwaves to mix the NV spin levels, while interleaving pulses of the tuneable red laser with green laser pulses to ensure the NV is in the negative charge state via optical off-resonant pumping, see Fig. 5.8 (Right, top). The software then selects the brightest peaks above a certain threshold (maximum of 2 peaks) for a narrow linescan. In this case, it repeatedly applies a sequence of a short green laser pulse (to ensure spin and charge state initialization), followed by a red frequency sweep through the expected transition frequency (to map out the specific ZPL transition under dephasing). This is done while constantly applying microwaves to avoid pumping in an optically dark spin state, see Fig. 5.8 (Right, bottom). Fig. 5.9 (D) shows an example of 20 subsequent
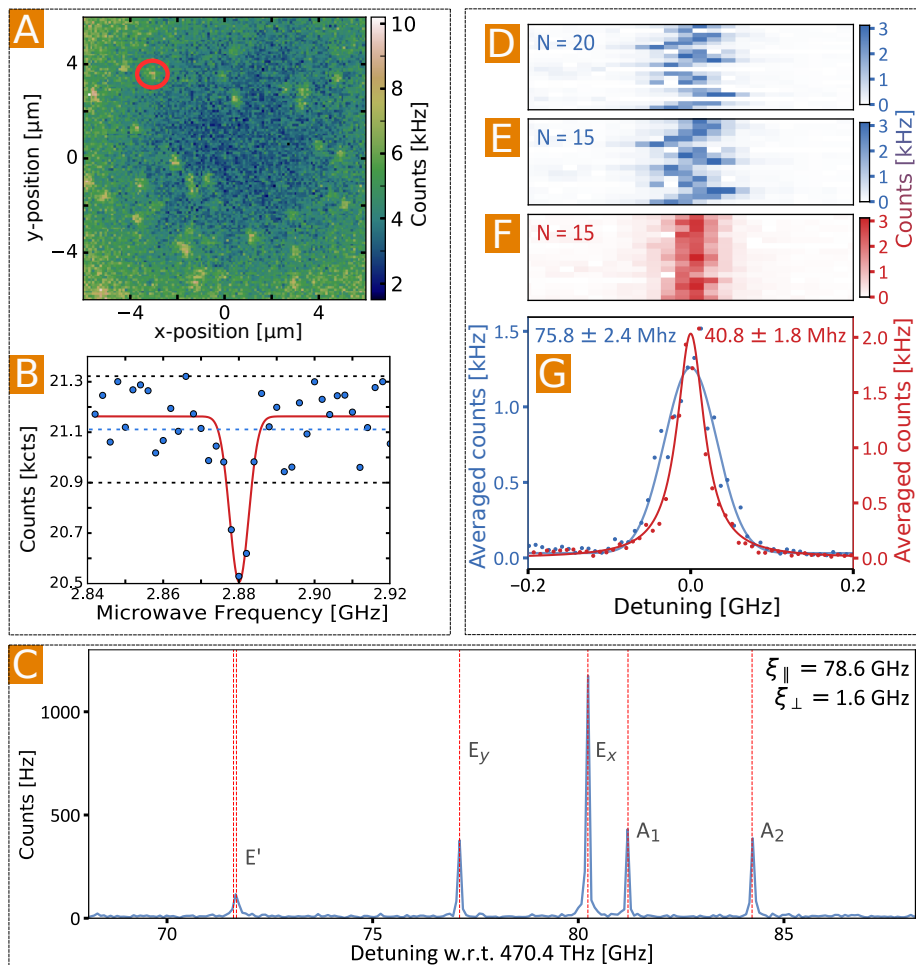
Figure 5.9: Examples of measurement results during data acquisition for one NV center. (A) Confocal microscope scan under green excitation ($\lambda = 532$ nm), with the NV measured throughout this figure encircled in red. (B) Optically detected magnetic resonance of the NV center ($\lambda = 532$ nm) under no external magnetic field, with the mean of the datapoints and one standard deviation from the mean labeled in red and blue, respectively. Since a dip in the fitted ESR spectrum corresponding to the $m_s= 0$ to $m_s= \pm 1$ spin transitions deviates more than one standard deviation from the mean, the routine continues with a PLE scan at this position. (C) PLE of the ZPL lines, showing six lines associated with the allowed optical transitions of the NV center from the ground to the excited state. Note that the E_1 and E_2 transitions overlap and are labeled as E'. Red lines correspond to transition energies calculated from the NV Hamiltonian, using the $m_s= 0$ transition frequencies (E_x and E_y) as inputs to the model. (D) Series of 20 PLE scans of the E_x transition displayed in (C), binned into 8 MHz frequency steps. Spectral jumps due to green repump pulses and empty traces due to NV center ionization are visible. (E) Remaining 15 PLE traces of the data displayed in (D) after removal of ionized traces, giving an indication of the spectral diffusion width of the individual ZPL transition. (F) Data displayed in (E), with fitted lorentzian center frequencies of individual traces used to align frequency axes to each other, to reveal the dephasing linewidth of the ZPL transition. (G) (Blue) Averaged and gaussian fitted data of (E), revealing a Gaussian spectral diffusion linewidth of (75.8 ± 2.4) MHz. (Red) Averaged and Lorentzian fitted data of (F), yielding a dephasing linewidth of (40.8 ± 1.8) MHz.

scans conducted in this manner, with spectral jumps resulting from a changing charge state distribution in the NV vicinity and empty traces due to photo-ionization visible. We then remove photo-ionized traces, and obtain the NV linewidth under spectral diffusion (via a gaussian fit to the averaged counts of all scans, see Fig. 5.9 (E)), as well as the full width at half maximum (FWHM) of the average dephasing linewidth. To extract all dephasing linewidth data shown in this manuscript, we fit each line profile individually, and calculate the weighted average, γ, for all scans of a certain transition via

$$\gamma = \frac{\sum_i \gamma_i \sigma_i^{-2}}{\sum_i \sigma_i^{-2}}, \tag{5.1}$$

where γ_i is the FWHM of an individual lorentzian shaped trace, and σ_i the corresponding standard error of the fit. The errorbar of the average dephasing linewidth, σ_γ, is then given by

$$\sigma_\gamma = \sqrt{\frac{1}{\sum_i \sigma_i^{-2}}}. \tag{5.2}$$

Fig. 5.9 (F) shows the results of the 15 remaining scans displayed in Fig. 5.9 (E) after aligning the center frequency of each fitted trace, to show the effect of dephasing. Fig. 5.9 (G) shows the averaged counts of the traces in Figs. 5.9 (E) and (F) in blue and red, respectively. The solid blue and red lines indicate a Guassian and Lorentzian fit to this data, respectively. Note that the way of extracting the dephasing linewidth in this figure by fitting one lorentzian to the averaged data is different from the approach described above and used in the rest of this paper, which is based on fitting all linescans individually, and calculating their weighted mean. Fitting the averaged data is chosen here for ease of visualization.

5.7.4. Laser-power induced linewidth broadening

To quantify the contribution of laser-power induced linewidth broadening to the measured dephasing linewidths, we model each ZPL transition as an ideal two-level system [73, 74]. Following this model, we fit the theoretically expected curve of form $\sqrt{\gamma_i^2 + \Omega^2}$ to our data, where γ_i is the natural linewidth of the NV transition, and $\Omega^2 = b \times P$ the squared Rabi frequency, where P is the applied laser power and b is a constant. We scan a laser twenty times over a pre-localized NV transition (using the pulse sequence described above and depicted in Fig. 5.8 (Right, bottom)), and extract the weighted average dephasing linewidth (as described above). We repeat this measurement for different powers of the red laser beam. Fig. 5.10 shows the result of the fit. We extract a natural dephasing linewidth of $(18.3 ^{+5.7}_{-8.7})$ MHz, compared to an extracted FWHM of (48.7 ± 0.7) MHz when using 8 nW of red power, as used throughout this paper. This means that the transition is power broadened, potentially explaining why we do not observe lifetime-limited linewidths throughout this paper.

5.7.5. Objective depth conversion factor

The high refractive index of diamond leads to a shift in the observed focal point position w.r.t. that in vacuum. We determine the resulting conversion factor between distance
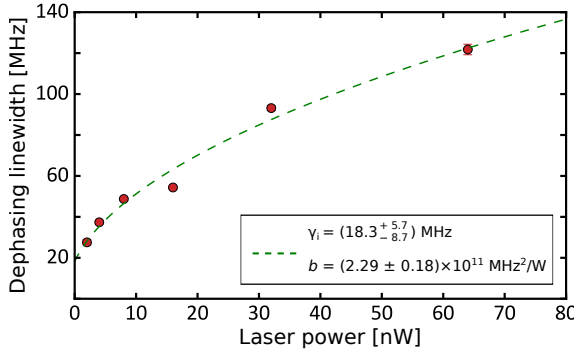
Figure 5.10: Dephasing linewidth as a function of laser power (solid red datapoints), and corresponding fit (green dashed line, see text for description). Throughout this paper, 8 nW of red power were used to measure the dephasing linewidths of NV centers, resulting in operation in the power broadening regime.

travelled by the microscope objective and distance travelled by the focal point in diamond in the following way: we first measure the distance t_f which we need to shift our microscope objective to move the laser focus from one diamond surface to the other, i.e. from the air-diamond to the diamond-mirror interface. We then determine the inverse ratio of this value and the actual diamond thickness as measured by a stylus profilometer. Table 5.3 displays the data obtained in this way. By evaluating the propagation of the uncertainties on the individual values, we obtain an average conversion factor of $2.64^{+0.11}_{-0.09}$ for our dataset. Throughout this paper, we use this conversion factor to determine the depth of NV centers w.r.t. the mirror interface. This is the reason for the discrepancy of the thicknesses indicated by the color shading in Fig. 5 of the main text compared to the directly reported values of diamond thicknesses in the measurement region that have been directly obtained by stylus profilometer measurements.

5.7.6. CONFOCAL NV DEPTH ERROR ANALYSIS AND DUPLICATE REMOVAL
In order to estimate the error on the depth of an NV center as determined by the method described above, we plot a histogram of the frequency difference between all measured NV center peaks, as displayed in Fig. 5.11 (Top, left). A peak around a frequency difference of zero, that results from scanning a given NV center twice, is visible. This can

	Diamond thickness t_m (µm)	Objective travel distance t_f (µm)	Conversion factor
Before etching	47.8 ± 0.2	18.2 ± 0.2	$2.63^{+0.04}_{-0.04}$
1st etching step	37.7 ± 0.2	14.6 ± 0.2	$2.58^{+0.05}_{-0.05}$
2nd etching step	10.1 ± 0.2	3.4 ± 0.2	$2.97^{+0.25}_{-0.22}$
3rd etching step	3.8 ± 0.2	1.6 ± 0.2	$2.38^{+0.48}_{-0.38}$

Table 5.3: Summary of diamond membrane thicknesses as measured with a stylus profilometer, corresponding objective travel distance, measured by determining the separation between focusing on the two diamond surfaces (i.e. the air-diamond and diamond-mirror interfaces), and resulting calculated conversion factors.
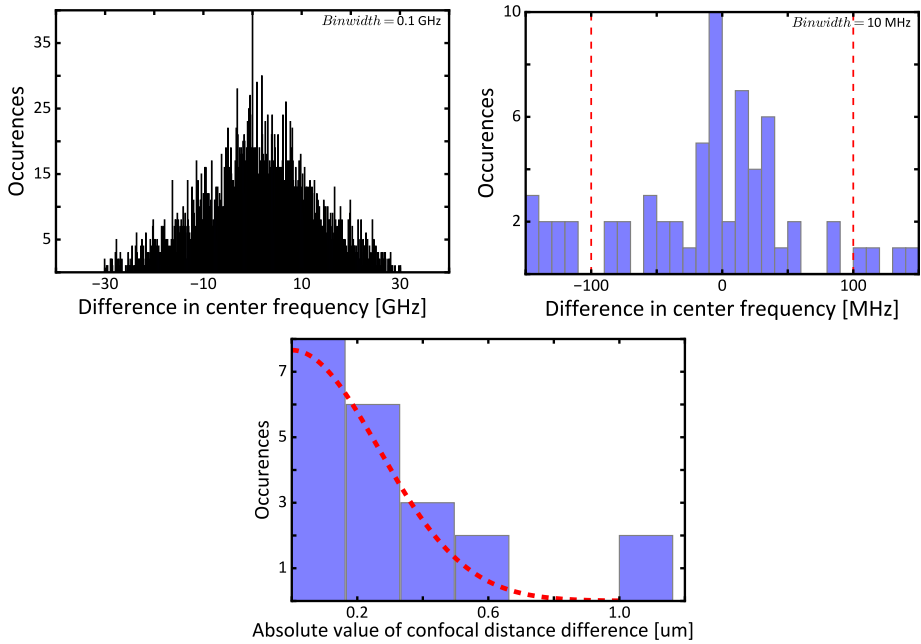
Figure 5.11: Estimation of confocal NV depth errorbar. (Top, left) Histogram of difference between center frequencies of all measured NV center peaks, binned into 0.1 GHz bins. A peak around zero frequency difference that we attribute to repeated scanning of identical blobs is visible. (Top, right) Histogram of difference between center frequencies of all measured NV center peaks, binned into 10 MHz bins, zoomed in to a range from -150 MHz to 150 MHz. Dotted red vertical lines denote used frequency bounds for (Bottom) Histogram showing absolute values of confocal distance difference of blobs that are likely identical. Red dotted line denotes fit result to a Gaussian function (see text for functional form). The datapoints are found using the frequency criterion displayed in (B), and the requirement that the Euclidean distance between NVs that this frequency difference results from is less than $(4 \, \mu m)^3$.

happen for our scans, as the focal depth in our setup broadens with increasing distance from the diamond surface (see section 5.7.5). As a consequence, the bright fluorescence profile of a single NV center can appear at various objective positions. Additionally, some NV centers are close to each other, which triggers the position optimization algorithm to select the same NV center in different scans. We use this information about blobs likely to be the same to remove double entries: if the peak frequencies of two seperately measured NV centers differ by less than 100 MHz (see Fig. 5.11 (Top, right)), and if the Euclidean distance between those NV centers is less than $(4 \, \mu m)^3$, we consider these NVs to be the same, and only keep the data for one of them in our analysis. We also use this criterion to extract the depth error from multiple measurements on identical NV centers: the first step is to consider the absolute difference Z in confocal depth for both of such measurements. This difference can be defined as $Z := X_1 - X_2$, where the first and second measurements are realizations of the independent random variables $X_1, X_2 \sim \mathcal{N}(\mu, \sigma^2)$ respectively, where $\mathcal{N}$ is the normal distribution with mean μ and standard deviation σ. The idea is to extract σ from the explicit form of the probability density function that governs the random variable $|Z|$. First note that $Z \sim \mathcal{N}(0, 2\sigma^2)$. Thus, for $x \geq 0$, the

cumulative distribution function $F_{|Z|}(x)$ can be written as:

$$F_{|Z|}(x) := P(|Z| \leq x)$$
$$= P(-x \leq Z \leq x)$$
$$= P(-x < Z \leq x)$$
$$= F_Z(x) - F_Z(-x)$$
$$= 2F_Z(x) - 1.$$

Note that $F_{|Z|}(x) = 0$ for $x < 0$, such that the probability density function $f_{|Z|}(x)$ now equals:

$$f_{|Z|}(x) := \frac{\partial}{\partial x} F_{|Z|}(x)$$
$$= 2 f_Z(x) \mathbb{1}_{(0,\infty)}(x)$$
$$= \frac{1}{\sigma \sqrt{\pi}} \exp\left(-\frac{x^2}{4\sigma^2}\right) \mathbb{1}_{(0,\infty)}(x),$$

where $\mathbb{1}_{(0,\infty)}$ is the Heaviside step function. Fitting this functional form to the data displayed in Fig. 5.11, we extract an errorbar of 0.18 µm for our dataset. Assuming this error to be independent from the error we determined for the conversion factor (see Sec. 5.7.5), we calculate the root sum of squared uncertainties to determine the overall uncertainty of the distance of an NV center from the diamond-mirror interface for all datapoints in this paper.

5.7.7. Correlations of NV center strain and linewidth

As discussed in the main text, we are interested to see whether strain regime and measured linewidths are correlated. To this end, we overlay measured broad resonant excitation spectra with simulations of the ZPL transition frequencies calculated from the Hamiltonian of the NV center to determine the local strain environment for individual NVs [41, 75], using the parameters reported in Refs. [2] and [76]: we first fit the position of all peaks in the broad frequency spectrum. We then use two of them as inputs for the E_x and E_y transitions in our model. We then calculate the ground and excited state energies, and compute the allowed transition frequencies between them. We then permute through all combinations of two peaks in the fitted broad spectrum as input for E_x and E_y, and use the combination that matches best to the measured spectrum to extract the axial NV strain $\xi_\parallel = (E_x + E_y)/2$ and the transverse NV strain $\xi_\perp = (E_x - E_y)/2$. Fig. 5.9 (C) shows an example of how we determine the strain regime for an NV center in this way. Out of the 110 distinguishable NV centers studied in this paper, a total of 58 NV centers allowed us to extract a unique strain regime using the method described above. For 24 of these NV centers we characterized the linewidths of two ZPL transitions with a narrow linescan, whereas for the rest of them, only one transition was measured.

As visualized in Fig. 5.12, we qualitatively find a correlation between axial and transverse strain, and between each of these two strain values and the mirror interface distance. Fig. 5.13 shows the spectral diffusion (left panels) and dephasing linewidths (right panels) as a function of difference between axial strain of individual NVs and the mean of
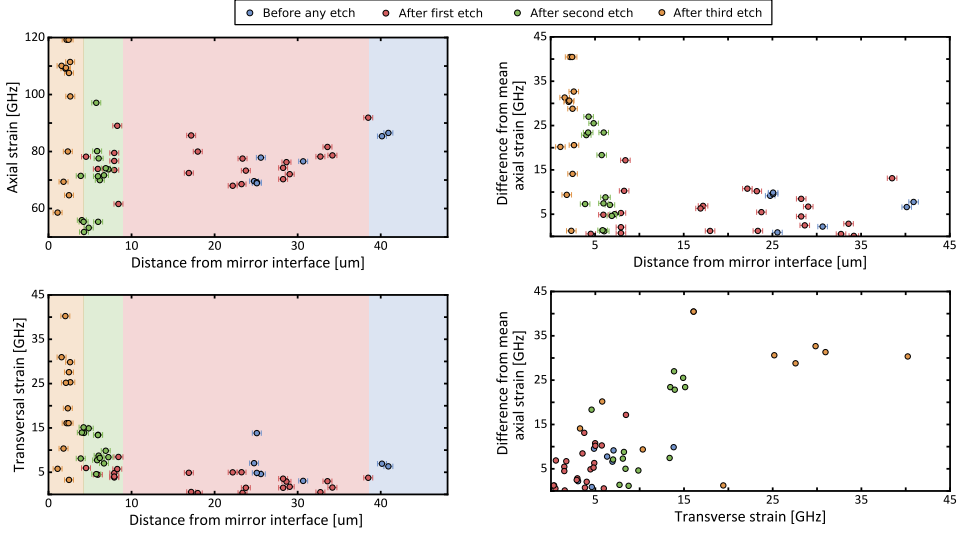
Figure 5.12: Dependence of axial and transverse strain on the NV distance from the diamond-mirror inter-face and dependence of axial on transverse strain for these NVs. (Left, top) Dependence of total axial strain (w.r.t. 470.4 THz) on the mirror interface distance. (Left, bottom) Transverse strain as a function of mirror in-terface distance. (Right, top) Dependence of the difference of axial strain of individual NVs and the mean of axial strains of the whole dataset on the mirror interface distance. (Right, bottom) Dependence of the differ-ence of axial strain of an individual NV and the mean of axial strains of the whole dataset on transverse strain. (Blue) Data before any etching, membrane thickness in measurement region $t_m = (47.8 \pm 0.2)$ μm. (Red) data after first etching of 26 mins Ar/Cl$_2$ and 45 mins O$_2$, $t_m = (37.7 \pm 0.2)$ μm. (Green) Data after an additional 30 mins Ar/Cl$_2$ and 138 mins O$_2$ etching, $t_m = (10.1 \pm 0.2)$ μm. (Yellow) Data after an additional 30 mins Ar/Cl$_2$ and 23 mins O$_2$ etching, $t_m = (3.8 \pm 0.2)$ μm. The horizontal clustering of points is a data acquisition artifact.

axial strains of the whole dataset (top panels), axial strain w.r.t. 470.4 GHz (middle pan-els) and transverse strain (bottom panels). These graphs imply that we cannot explain the observed broadening of linewidths for the final membrane thickness of $t_m = (3.8 \pm 0.2)$ with strain-induced effects.

5.7.8. DEPHASING LINEWIDTH TARGET VALUE

Entanglement generation between two remote NV centers requires frequency indistin-guishability between their emitted photons. We consider optical transitions with fre-quency uncertainty of $2\pi \times \gamma$ that are broadened beyond the lifetime-limited value due to dephasing. In this case, indistinguishability can still be achieved if the time resolution of the detector dt is good enough to erase the frequency information (i.e. if $2\pi \times \gamma \ll 1/dt$, see Refs. [77, 78]). To arrive at a quantitative target, we set this condition to be $2\pi \times \gamma < 1/10 \times 1/dt$. For a typical silicon APD with 300 ps timing jitter, this leads to the require-ment $\gamma < 50$ MHz, and therefore to a full-with half maximum linewidth < 100 MHz. Note that frequency erasure requires filtering on photon detection time difference [77], and hence narrower lines will require less filtering and thus yield a higher entangling rate.
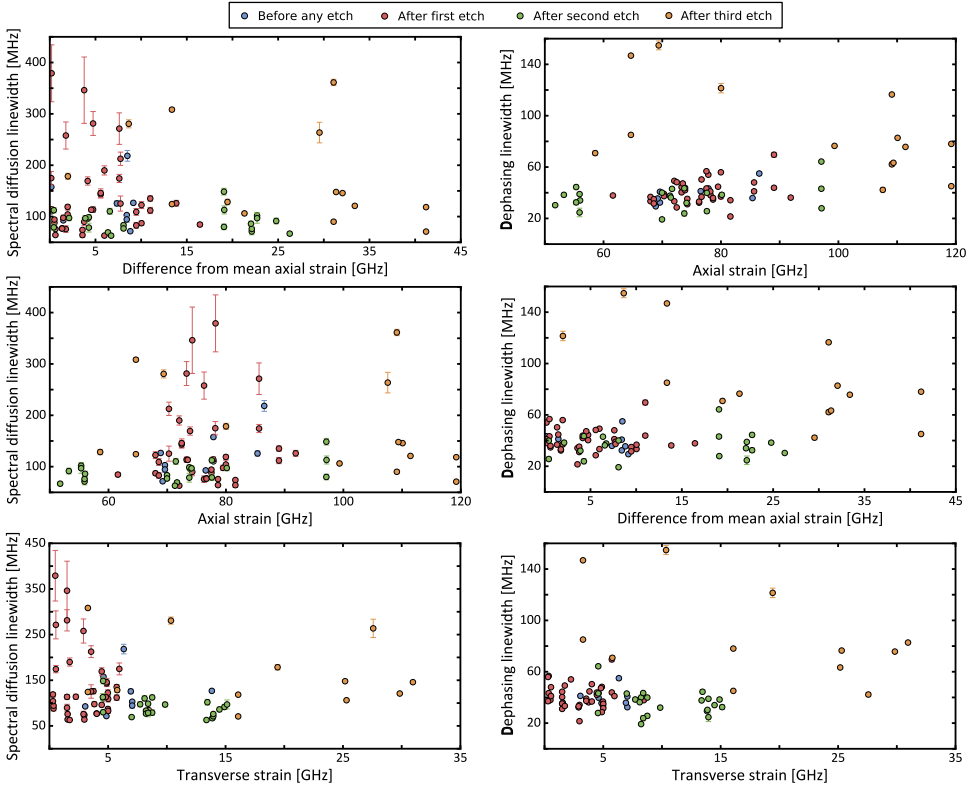
Figure 5.13: Spectral diffusion linewidth (left panels) and dephasing linewidths (right panels) of NV centers as a function of transverse and axial strain for different membrane thicknesses. (Top panels) Linewidths as a function of the difference of axial strain of an individual NV from the mean of axial strains of the whole dataset. (Middle panels) Linewidths as a function of axial strain (w.r.t. 470.4 THz). (Bottom panels) Linewidths as a function of transverse strain. The data shows that there is no significant correlation between strain and measured linewidths for our sample. (Blue) Data before any etching, membrane thickness in measurement region $t_m = (47.8 \pm 0.2)$ μm. (Red) data after first etching of 26 mins Ar/Cl$_2$ and 45 mins O$_2$, $t_m = (37.7 \pm 0.2)$ μm. (Green) Data after an additional 30 mins Ar/Cl$_2$ and 138 mins O$_2$ etching, $t_m = (10.1 \pm 0.2)$ μm. (Yellow) Data after an additional 30 mins Ar/Cl$_2$ and 23 mins O$_2$ etching, $t_m = (3.8 \pm 0.2)$ μm.

REFERENCES

[1] M. Ruf, M. Ijspeert, S. Van Dam, N. De Jong, H. Van Den Berg, G. Evers and R. Hanson, *Optically Coherent Nitrogen-Vacancy Centers in Micrometer-Thin Etched Diamond Membranes,* Nano Letters **19,** 3987 (2019).

[2] M. W. Doherty, N. B. Manson, P. Delaney, F. Jelezko, J. Wrachtrup and L. C. L. Hollenberg, *The nitrogen-vacancy colour centre in diamond,* Physics Reports **528,** 1 (2013).

[3] M. Atatüre, D. Englund, N. Vamivakas, S. Y. Lee and J. Wrachtrup, *Material platforms for spin-based photonic quantum technologies,* Nature Reviews Materials **3,** 38 (2018).

[4] C. L. Degen, *Scanning magnetic field microscope with a diamond single-spin sensor,* Applied Physics Letters **92,** 243111 (2008).

[5] J. R. Maze *et al.*, *Nanoscale magnetic sensing with an individual electronic spin in diamond,* Nature **455,** 644 (2008).

[6] G. Balasubramanian *et al.*, *Nanoscale imaging magnetometry with diamond spins under ambient conditions,* Nature **455,** 648 (2008).

[7] M. S. Grinolds, P. Maletinsky, S. Hong, M. D. Lukin, R. L. Walsworth and A. Yacoby, *Quantum control of proximal spins using nanoscale magnetic resonance imaging,* Nature Physics **7,** 687 (2011).

[8] P. Maletinsky, S. Hong, M. S. Grinolds, B. Hausmann, M. D. Lukin, R. L. Walsworth, M. Loncar and A. Yacoby, *A robust scanning diamond sensor for nanoscale imaging with single nitrogen-vacancy centres.* Nature Nanotechnology **7,** 320 (2012).

[9] G. Waldherr, Y. Wang, S. Zaiser, M. Jamali, T. Schulte-Herbrüggen, H. Abe, T. Ohshima, J. Isoya, J. F. Du, P. Neumann and J. Wrachtrup, *Quantum error correction in a solid-state hybrid spin register,* Nature **506,** 204 (2014).

[10] J. Cramer, N. Kalb, M. A. Rol, B. Hensen, M. S. Blok, M. Markham, D. J. Twitchen, R. Hanson and T. H. Taminiau, *Repeated quantum error correction on a continuously encoded qubit by real-time feedback,* Nature Communications **7,** 1 (2016).

[11] B. Hensen *et al.*, *Loophole-free Bell inequality violation using electron spins separated by 1.3 kilometres,* Nature **526,** 682 (2015).

[12] N. Kalb, A. A. Reiserer, P. C. Humphreys, J. J. Bakermans, S. J. Kamerling, N. H. Nickerson, S. C. Benjamin, D. J. Twitchen, M. Markham and R. Hanson, *Entanglement distillation between solid-state quantum network nodes,* Science **356,** 928 (2017).

[13] P. C. Humphreys, N. Kalb, J. P. Morits, R. N. Schouten, R. F. Vermeulen, D. J. Twitchen, M. Markham and R. Hanson, *Deterministic delivery of remote entanglement on a quantum network,* Nature **558,** 268 (2018).

[14] M. H. Abobeih, J. Cramer, M. A. Bakker, N. Kalb, M. Markham, D. J. Twitchen and T. H. Taminiau, *One-second coherence for a single electron spin coupled to a multi-qubit nuclear-spin environment,* Nature Communications **9**, 1 (2018).

[15] L. Robledo, L. Childress, H. Bernien, B. Hensen, P. F. A. Alkemade and R. Hanson, *High-fidelity projective read-out of a solid-state spin quantum register,* Nature **477**, 574 (2011).

[16] P. C. Maurer *et al., Room-Temperature Quantum Bit Memory Exceeding One Second,* Science **336**, 1283 (2012).

[17] T. H. Taminiau, J. Cramer, T. Van Der Sar, V. V. Dobrovitski and R. Hanson, *Universal control and error correction in multi-qubit spin registers in diamond,* Nature Nanotechnology **9**, 171 (2014).

[18] D. Englund, B. Shields, K. Rivoire, F. Hatami, J. Vučković, H. Park and M. D. Lukin, *Deterministic coupling of a single nitrogen vacancy center to a photonic crystal cavity,* Nano Letters **10**, 3922 (2010).

[19] J. Wolters, A. W. Schell, G. Kewes, N. Nüsse, M. Schoengen, H. Döscher, T. Hannappel, B. Löchel, M. Barth and O. Benson, *Enhancement of the zero phonon line emission from a single nitrogen vacancy center in a nanodiamond via coupling to a photonic crystal cavity,* Applied Physics Letters **97**, 141108 (2010).

[20] T. Van Der Sar, J. Hagemeier, W. Pfaff, E. C. Heeres, S. M. Thon, H. Kim, P. M. Petroff, T. H. Oosterkamp, D. Bouwmeester and R. Hanson, *Deterministic nanoassembly of a coupled quantum emitter-photonic crystal cavity system,* Applied Physics Letters **98**, 1 (2011).

[21] A. Faraon, C. Santori, Z. Huang, V. M. Acosta and R. G. Beausoleil, *Coupling of nitrogen-vacancy centers to photonic crystal cavities in monocrystalline diamond,* Physical Review Letters **109**, 2 (2012).

[22] B. J. Hausmann *et al., Coupling of NV centers to photonic crystal nanobeams in diamond,* Nano Letters **13**, 5791 (2013).

[23] J. C. Lee *et al., Deterministic coupling of delta-doped nitrogen vacancy centers to a nanobeam photonic crystal cavity,* Applied Physics Letters **105**, 261101 (2014).

[24] L. Li *et al., Coherent spin control of a nanocavity-enhanced qubit in diamond,* Nature Communications **6**, 6173 (2015).

[25] J. Riedrich-Möller, S. Pezzagna, J. Meijer, C. Pauly, F. Mücklich, M. Markham, A. M. Edmonds and C. Becher, *Nanoimplantation and Purcell enhancement of single nitrogen-vacancy centers in photonic crystal cavities in diamond,* Applied Physics Letters **106**, 2 (2015).

[26] A. Faraon, P. E. Barclay, C. Santori, K. M. C. Fu and R. G. Beausoleil, *Resonant enhancement of the zero-phonon emission from a colour centre in a diamond cavity,* Nature Photonics **5**, 301 (2011).

5

[27] P. E. Barclay, K. M. C. Fu, C. Santori, A. Faraon and R. G. Beausoleil, *Hybrid nanocavity resonant enhancement of color center emission in diamond,* Physical Review X **1**, 1 (2011).

[28] M. Gould, E. R. Schmidgall, S. Dadgostar, F. Hatami and K. M. C. Fu, *Efficient Extraction of Zero-Phonon-Line Photons from Single Nitrogen-Vacancy Centers in an Integrated GaP-on-Diamond Platform,* Physical Review Applied **6**, 2 (2016).

[29] H. Kaupp, C. Deutsch, H. C. Chang, J. Reichel, T. W. Hänsch and D. Hunger, *Scaling laws of the cavity enhancement for nitrogen-vacancy centers in diamond,* Physical Review A **88**, 1 (2013).

[30] S. Johnson, P. R. Dolan, T. Grange, A. A. P. Trichet, G. Hornecker, Y. C. Chen, L. Weng, G. M. Hughes, A. A. R. Watt, A. Auffèves and J. M. Smith, *Tunable cavity coupling of the zero phonon line of a nitrogen-vacancy defect in diamond,* New Journal of Physics **17**, 122003 (2015).

[31] D. Riedel, I. Söllner, B. J. Shields, S. Starosielec, P. Appel, E. Neu, P. Maletinsky and R. J. Warburton, *Deterministic enhancement of coherent photon generation from a nitrogen-vacancy center in ultrapure diamond,* Physical Review X **7**, 1 (2017).

[32] P. Rabl, S. J. Kolkowitz, F. H. Koppens, J. G. Harris, P. Zoller and M. D. Lukin, *A quantum spin transducer based on nanoelectromechanical resonator arrays,* Nature Physics **6**, 602 (2010).

[33] O. Arcizet, V. Jacques, A. Siria, P. Poncharal, P. Vincent and S. Seidelin, *A single nitrogen-vacancy defect coupled to a nanomechanical oscillator,* Nature Physics **7**, 879 (2011).

[34] S. Kolkowitz, A. C. B. Jayich, Q. P. Unterreithmeier, S. D. Bennett, P. Rabl, J. G. E. Harris and M. D. Lukin, *Coherent Sensing of a Mechanical Resonator with a Single-Spin,* Science **335**, 1603 (2012).

[35] K. V. Kepesidis, S. D. Bennett, S. Portolan, M. D. Lukin and P. Rabl, *Phonon cooling and lasing with nitrogen-vacancy centers in diamond,* Physical Review B - Condensed Matter and Materials Physics **88**, 1 (2013).

[36] D. A. Golter, T. Oo, M. Amezcua, K. A. Stewart and H. Wang, *Optomechanical Quantum Control of a Nitrogen-Vacancy Center in Diamond,* Physical Review Letters **116**, 1 (2016).

[37] D. Lee, K. W. Lee, J. V. Cady, P. Ovartchaiyapong and A. C. B. Jayich, *Topical review: spins and mechanics in diamond,* Journal of Optics **19**, 033001 (2017).

[38] K. Ohno, F. Joseph Heremans, L. C. Bassett, B. A. Myers, D. M. Toyli, A. C. Bleszynski Jayich, C. J. Palmstrøm and D. D. Awschalom, *Engineering shallow spins in diamond with nitrogen delta-doping,* Applied Physics Letters **101**, 082413 (2012).

[39] E. Kim, V. M. Acosta, E. Bauch, D. Budker and P. R. Hemmer, *Electron spin resonance shift and linewidth broadening of nitrogen-vacancy centers in diamond as a function of electron irradiation dose*, Applied Physics Letters **101**, 082410 (2012).

[40] C. A. McLellan, B. A. Myers, S. Kraemer, K. Ohno, D. D. Awschalom and A. C. Bleszynski Jayich, *Patterned Formation of Highly Coherent Nitrogen-Vacancy Centers Using a Focused Electron Irradiation Technique*, Nano Letters **16**, 2450 (2016).

[41] M. W. Doherty, N. B. Manson, P. Delaney and L. C. L. Hollenberg, *The negatively charged nitrogen-vacancy centre in diamond: The electronic solution*, New Journal of Physics **13** (2011).

[42] K. M. C. Fu, C. Santori, P. E. Barclay, L. J. Rogers, N. B. Manson and R. G. Beausoleil, *Observation of the dynamic Jahn-Teller effect in the excited states of nitrogen-vacancy centers in diamond*, Physical Review Letters **103**, 1 (2009).

[43] P. Siyushev, H. Pinto, M. Vörös, A. Gali, F. Jelezko and J. Wrachtrup, *Optically controlled switching of the charge state of a single nitrogen-vacancy center in diamond at cryogenic temperatures*, Physical Review Letters **110**, 1 (2013).

[44] H. Bernien, L. Childress, L. Robledo, M. Markham, D. Twitchen and R. Hanson, *Two-Photon Quantum Interference from Separate Nitrogen Vacancy Centers in Diamond*, Physical Review Letters **108**, 043604 (2012).

[45] H. Bernien, B. Hensen, W. Pfaff, G. Koolstra, M. S. Blok, L. Robledo, T. H. Taminiau, M. Markham, D. J. Twitchen, L. Childress and R. Hanson, *Heralded entanglement between solid-state qubits separated by three metres*, Nature **497**, 86 (2013).

[46] S. Pezzagna, D. Rogalla, D. Wildanger, J. Meijer and A. Zaitsev, *Creation and nature of optical centres in diamond for single-photon emission—overview and critical remarks*, New Journal of Physics **13**, 035024 (2011).

[47] E. Janitz, M. Ruf, M. Dimock, A. Bourassa, J. Sankey and L. Childress, *Fabry-Perot microcavity for diamond-based photonics*, Physical Review A **92**, 1 (2015).

[48] S. Bogdanović, S. B. van Dam, C. Bonato, L. C. Coenen, A.-M. J. Zwerver, B. Hensen, M. S. Z. Liddy, T. Fink, A. Reiserer, M. Lončar and R. Hanson, *Design and low-temperature characterization of a tunable microcavity for diamond-based quantum networks*, Applied Physics Letters **110**, 171103 (2017).

[49] S. B. van Dam, M. Ruf and R. Hanson, *Optimal design of diamond-air microcavities for quantum networks using an analytical approach*, New Journal of Physics **20**, 115004 (2018).

[50] S. B. van Dam, M. Walsh, M. J. Degen, E. Bersin, S. L. Mouradian, A. Galiullin, M. Ruf, M. IJspeert, T. H. Taminiau, R. Hanson and D. R. Englund, *Optical coherence of diamond nitrogen-vacancy centers formed by ion implantation and annealing*, Physical Review B **99**, 161203 (2019).

5

[51] B. Campbell and A. Mainwood, *Radiation Damage of Diamond by Electron and Gamma Irradiation,* physica status solidi (a) **181**, 99 (2000).

[52] J. O. Orwa *et al., Engineering of nitrogen-vacancy color centers in high purity diamond by ion implantation and annealing,* Journal of Applied Physics **109**, 083530 (2011).

[53] Y. Chu *et al., Coherent optical transitions in implanted nitrogen vacancy centers,* Nano Letters **14**, 1982 (2014).

[54] B. J. M. Hausmann, M. Khan, Y. Zhang, T. M. Babinec, K. Martinick, M. McCutcheon, P. R. Hemmer and M. Loncar, *Fabrication of diamond nanowires for quantum information processing applications,* Diamond & Related Materials **19**, 621 (2010).

[55] V. Petráková, A. Taylor, I. Kratochvílová, F. Fendrych, J. Vacík, J. Kučka, J. Štursa, P. Cígler, M. Ledvina, A. Fišerová, P. Kneppo and M. Nesládek, *Luminescence of nanodiamond driven by atomic functionalization: Towards novel detection principles,* Advanced Functional Materials **22**, 812 (2012).

[56] S. E. Grillo and J. E. Field, *The polishing of diamond,* Journal of Physics D: Applied Physics **30**, 202 (1997).

[57] H. A. Atikian, A. Eftekharian, A. Jafari Salim, M. J. Burek, J. T. Choy, A. Hamed Majedi and M. Lončar, *Superconducting nanowire single photon detector on diamond,* Applied Physics Letters **104**, 122602 (2014).

[58] C. L. Lee, E. Gu, M. D. Dawson, I. Friel and G. A. Scarsbrook, *Etching and micro-optics fabrication in diamond using chlorine-based inductively-coupled plasma,* Diamond and Related Materials **17**, 1292 (2008).

[59] M. Challier, S. Sonusen, A. Barfuss, D. Rohner, D. Riedel, J. Koelbl, M. Ganzhorn, P. Appel, P. Maletinsky and E. Neu, *Advanced fabrication of single-crystal diamond membranes for quantum technologies,* Micromachines **9**, 1 (2018).

[60] Y. Tao, J. M. Boss, B. A. Moores and C. L. Degen, *Single-crystal diamond nanomechanical resonators with quality factors exceeding one million,* Nature Communications **5**, 1 (2014).

[61] D. Riedel, D. Rohner, M. Ganzhorn, T. Kaldewey, P. Appel, E. Neu, R. J. Warburton and P. Maletinsky, *Low-loss broadband antenna for efficient photon collection from a coherent spin in diamond,* Physical Review Applied **2**, 1 (2014).

[62] P. Appel, E. Neu, M. Ganzhorn, A. Barfuss, M. Batzer, M. Gratz, A. Tschöpe and P. Maletinsky, *Fabrication of all diamond scanning probes for nanoscale magnetometry,* Review of Scientific Instruments **87**, 063703 (2016).

[63] S. Bogdanović, M. S. Z. Liddy, S. B. van Dam, L. C. Coenen, T. Fink, M. Lončar and R. Hanson, *Robust nano-fabrication of an integrated platform for spin control in a tunable microcavity,* APL Photonics **2**, 126101 (2017).

[64] P. Volpe, P. Muret, F. Omnes, J. Achard, F. Silva, O. Brinza and A. Gicquel, *Diamond & Related Materials Defect analysis and excitons diffusion in undoped homoepitaxial diamond fi lms after polishing and oxygen plasma etching,* Diamond & Related Materials **18**, 1205 (2009).

[65] I. Friel, S. L. Clewes, H. K. Dhillon, N. Perkins, D. J. Twitchen and G. A. Scarsbrook, *Diamond & Related Materials Control of surface and bulk crystalline quality in single crystal diamond grown by chemical vapour deposition,* Diamond & Related Materials **18**, 808 (2009).

[66] M. Naamoun, A. Tallaire, F. Silva, J. Achard, P. Doppelt and A. Gicquel, *Etch-pit formation mechanism induced on HPHT and CVD diamond single crystals by H 2/O 2 plasma etching treatment: Part of topical section on fundamentals and applications of diamond,* Physica Status Solidi (A) Applications and Materials Science **209**, 1715 (2012).

[67] H.-J. Briegel, W. Dür, J. I. Cirac and P. Zoller, *Quantum Repeaters: The Role of Imperfect Local Operations in Quantum Communication,* Physical Review Letters **81**, 5932 (1998).

[68] F. Rozpędek, K. Goodenough, J. Ribeiro, N. Kalb, V. C. Vivoli, A. Reiserer, R. Hanson, S. Wehner and D. Elkouss, *Parameter regimes for a single sequential quantum repeater,* Quantum Science and Technology **3**, 034002 (2018).

[69] F. Rozpędek, R. Yehia, K. Goodenough, M. Ruf, P. C. Humphreys, R. Hanson, S. Wehner and D. Elkouss, *Near-term quantum-repeater experiments with nitrogen-vacancy centers: Overcoming the limitations of direct transmission,* Physical Review A **99**, 052330 (2019).

[70] J. R. Hird and J. E. Field, *Diamond Polishing,* Proceedings of the Royal Society A: Mathematical, Physical and Engineering Sciences **460**, 3547 (2004).

[71] T. Schuelke and T. A. Grotjohn, *Diamond polishing,* Diamond and Related Materials **32**, 17 (2013).

[72] P. Appel, E. Neu, M. Ganzhorn, A. Barfuss, M. Batzer, M. Gratz, A. Tschöpe and P. Maletinsky, *Fabrication of all diamond scanning probes for nanoscale magnetometry,* Review of Scientific Instruments **87** (2016).

[73] M. L. Citron, H. R. Gray, C. W. Gabel and C. R. Stroud, *Experimental study of power broadening in a two-level atom,* Physical Review A **16**, 1507 (1977).

[74] G. Grynberg, A. Aspect, C. Fabre and C. Cohen-Tannoudji, *Introduction to Quantum Optics* (Cambridge University Press, Cambridge, 2010).

[75] J. R. Maze, A. Gali, E. Togan, Y. Chu, A. Trifonov, E. Kaxiras and M. D. Lukin, *Properties of nitrogen-vacancy centers in diamond: The group theoretic approach,* New Journal of Physics **13** (2011).

5

[76] L. C. Bassett, F. J. Heremans, D. J. Christle, C. G. Yale, G. Burkard, B. B. Buckley and
      D. D. Awschalom, *Ultrafast optical control of orbital and spin dynamics in a solid-
      state defect,* Science **345,** 1333 (2014).

[77] T. Legero, T. Wilk, A. Kuhn and G. Rempe, *Time-resolved two-photon quantum in-
      terference,* Applied Physics B **77,** 797 (2003).

[78] T. Legero, T. Wilk, A. Kuhn and G. Rempe, *Characterization of Single Photons Using
      Two-Photon Interference,* Advances in Atomic, Molecular and Optical Physics **53,**
      253 (2006).

5

6

RESONANT EXCITATION AND PURCELL ENHANCEMENT OF COHERENT NITROGEN-VACANCY CENTERS COUPLED TO A FABRY-PÉROT MICROCAVITY

Maximilian Ruf*, Matthew Weaver*, Suzanne van Dam, and Ronald Hanson

The nitrogen-vacancy (NV) center in diamond has been established as a prime building block for quantum networks. However, scaling beyond a few network nodes is currently limited by low spin-photon entanglement rates, resulting from the NV center's low probability of coherent photon emission and collection. Integration into a cavity can boost both values via the Purcell effect, but poor optical coherence of near-surface NV centers has so far prevented their resonant optical control, as would be required for entanglement generation. Here, we overcome this challenge, and demonstrate resonant addressing of individual, fiber-cavity-coupled NV centers, and collection of their Purcell-enhanced coherent photon emission. Utilizing off-resonant and resonant addressing protocols, we extract an enhancement of the zero-phonon line emission by a factor of up to 4, consistent with a detailed theoretical model. This model predicts that the probability of coherent photon detection per optical excitation can be increased to 10% for realistic parameters - an improvement over state-of-the art solid immersion lens collection systems by two orders of magnitude. The resonant operation of an improved optical interface for single coherent quantum emitters in a closed-cycle cryogenic system at T ~ 4 K is an important result towards extensive quantum networks with long coherence.

6.1. INTRODUCTION

Future large-scale quantum networks sharing entanglement between their nodes may enable a suite of new applications, such as secure communication, distributed quantum computation, and quantum enhanced sensing [2–6]. These networks require nodes with both access to long-lived memory qubit registers that can be operated with high fidelity, and bright spin selective optical transitions with good coherence [3]. Promising node candidates include group IV defects in diamond [7–9], defects in SiC [10–12], rare earth ions in solid state hosts [13–15], quantum dots [16, 17], neutral atoms [18, 19], and trapped ions [20, 21].

The nitrogen-vacancy (NV) center in diamond combines optical transitions suitable for remote entanglement generation under moderate cryogenic conditions with outstanding electron spin coherence ($T_2 > 1$ s) and extensive control capabilities over local ^{13}C memory atoms [22, 23]; these features have enabled pioneering quantum network experiments [24, 25] and fundamental tests of physics [26]. However, entanglement generation rates are limited by the relatively low photon emission into the zero-phonon line (ZPL), as well as low collection efficiency from diamond, hindering scaling beyond a few nodes. Both values can be significantly increased by embedding the NV center inside an optical cavity, making use of the Purcell effect. Cavity-coupling of NV centers at low temperature has been demonstrated for different cavity implementations, including photonic crystals [27–32], microdisk resonators [33], and open microcavities [34, 35].

Entanglement generation between nodes requires coherent photon detection after resonant excitation of the optical transitions of individual NV centers [22]. However, poor optical coherence (~ GHz linewidths), resulting from surface noise effects and/or implantation-induced damage, has so far prevented resonant optical addressing of Purcell-enhanced NV centers [27, 30, 32, 34, 36, 37]. This has presented a critical roadblock on the path towards remote entanglement generation.

In this work, we demonstrate resonant optical addressing of Purcell-enhanced NV centers coupled to a fiber-based cavity, capitalizing on recent breakthroughs in diamond membrane fabrication [38] and diamond-based open microcavities [34, 39–44]. We outline the experimental system in Sec. 6.2, and begin experiments by verifying Purcell enhancement under off-resonant excitation in Sec. 6.3. Next, we develop and demonstrate a resonant excitation protocol for NV centers in the cavity. We use the resonant addressing to measure optical coherence (Sec. 6.4) and Purcell enhancement (Sec. 6.5). Finally, in Sec. 6.6, we quantify the Purcell-enhanced photon emission and the collection efficiency from a single quantum emitter. We conclude with an outlook including future prospects and new avenues opened up by this work.

6.2. EXPERIMENTAL SETUP

An overview of the experimental setup used in this work can be seen in Fig. 6.1(a). At the heart of the experiment is an open, fiber-based Fabry-Pérot microcavity (design finesse 6200), formed from a flat, super-polished mirror, and a laser ablated fiber mirror [45]; this finesse value is chosen as it maximises the outcoupled fraction of photons emitted into the zero-phonon line (ZPL) for the vibrations present in the cavity [46] (~ [0.1 - 0.2] nm root mean squared amplitude, for a detailed discussion, see App. 6.8.5). The fiber
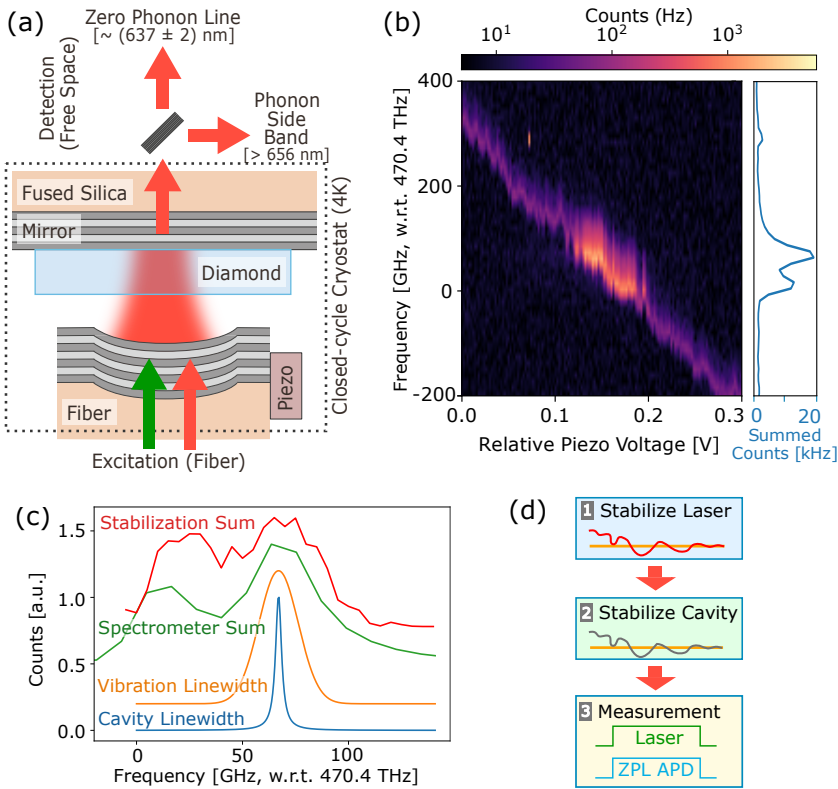
Figure 6.1: Experimental setup, NV-cavity characterization measurements, and measurement sequence. (a) Overview of the experimental setup. A tunable fiber-based microcavity with embedded diamond membrane is formed inside a closed-cycle cryostat operated at a temperature of 4 K. (b) Fluorescence counts for different applied piezo voltages (and thus cavity lengths) under off-resonant excitation, detected with a spectrometer in a ± 2 nm window around the NV center zero-phonon line (ZPL) of ∼ 637 nm (integration time 5 s per point). Right panel shows data on the left, summed over all piezo voltages. (c) From bottom to top, measurements of intrinsic cavity linewidth, inferred vibrations-broadened cavity linewidth, spectrometer peaks (same data as right panel of (b)), and stabilization curve, using the continuous off-resonant excitation and ZPL detection measurement sequence displayed in (d). (d) General measurement sequence used throughout this paper. A ∼ 637 nm laser is frequency stabilized to a wavemeter (1), and serves as a reference for the cavity length (2). Measurement blocks that are repeated multiple times are interleaved between stabilization rounds (3).

sits on top of a piezo positioning stage, which enables in situ tuning of the cavity position and length under operation in a closed-cycle cryostat ($T \sim 4$ K for all measurements in this paper). Excitation light is delivered to the cavity via the fiber mirror, while all detection in this work takes place in free space through the flat mirror of the cavity. Unbalanced mirror coatings set the design finesse almost entirely by transmission through this flat cavity mirror; for a full overview of the experimental setup, please see App. 6.8.1. An electron irradiated and annealed diamond membrane is bonded to the flat cavity mirror [41], and etched down to a final thickness of ∼ 5.8 µm in the cavity region, following the process flow developed in Ref. [38]. Importantly, this recipe has been shown to preserve the optical coherence of NV centers needed for entanglement generation, even

for few-µm thin diamond samples.

We start characterizing the coupled system of the membrane and fiber-cavity by recording cavity spectra under illumination with a broadband light source for different cavity lengths. From fits to a transfer matrix model [39], we infer a membrane thickness of ∼ 5.8 µm, and an air gap of ∼ 7 µm (see App. 6.8.2). This air gap could not be reduced further, likely due to a piece of dust on, or an angled mounting of, the fiber. This limits the cavity finesse to ∼ 2000 ($Q \sim 1.3 \times 10^5$) due to operation in the clipping loss regime of the fiber mirror [45, 46]. The cavity quantum electrodynamics parameters (NV center optical transition linewidth [38], NV-cavity coupling rate, and cavity decay rate $\{\gamma, g, \kappa\}$ ∼ $2\pi \times \{18$ MHz, 35 MHz, 3.5 GHz$\}$) place the system in the weak coupling regime, which is favorable for photon collection (App. 6.8.2).

We find NV centers by scanning a fundamental cavity mode over the ZPL transition frequencies (∼ 470.4 THz), while constantly illuminating with off-resonant (∼ 515 nm) laser light. At this laser wavelength, the optical excitation keeps the NV center predominantly in the negative charge and $m_s = 0$ spin state. Fig. 6.1(b) shows the fluorescence counts in a window of ± 2 nm around the expected ZPL frequency on a spectrometer, for different piezo voltages (and thus cavity lengths). Background light in the cavity serves as an internal light source [47], revealing the expected decrease in cavity frequency with increasing voltage. As the cavity mode is tuned through the ZPL transition frequencies of a small ensemble of NV centers, additional NV center fluorescence is collected. Summing the spectrometer fluorescence counts per frequency over all cavity lengths reveals two peaks (right panel of Fig. 6.1(b)), which are likely due to the E_x and E_y transitions (see Sec. 6.4 below). Each peak is significantly wider than the intrinsic cavity linewidth.

To investigate the origin of the observed width of the NV center emission peaks, we compare the intrinsic cavity linewidth (blue trace in Fig. 6.1(c)) - measured on a timescale much faster than the vibrations in the cavity (App. 6.8.2) - to the "vibration linewidth", calculated by convolving the measured vibration value with the intrinsic cavity linewidth (orange trace in Fig. 6.1(c)). The resulting curve, which is an estimate for the linewidth averaged over during the full spectrometer run, explains most of the width of the peaks in the summed spectrometer data (green trace in Fig. 6.1(c)); the additional width is attributed to a frequency distribution of NV centers in the cavity (see Sec. 6.4 below).

For more refined cavity control, we design a measurement protocol which we use throughout the remainder of this paper (see Fig. 6.1(d)). The sequence starts by stabilizing a ∼ 637 nm laser to a given setpoint using a wavemeter. We then stabilize the cavity to this laser frequency, after which we start a measurement sequence. By repeating this procedure, we can take out slow drifts between measurements. We test this measurement protocol by stabilizing the cavity to different laser setpoints and taking fluorescence data in the ZPL under off-resonant excitation (red trace in Fig. 6.1(c)). The resulting data is consistent with the lineshape found via the spectrometer measurement.

6.3. OFF-RESONANT EXCITATION

Entanglement generation rates in quantum networks scale with the collection of coherent photon emission. A cavity acts as a spectral filter, only allowing resonant emission to exit, and opens up an additional decay channel for the excited state of any coupled
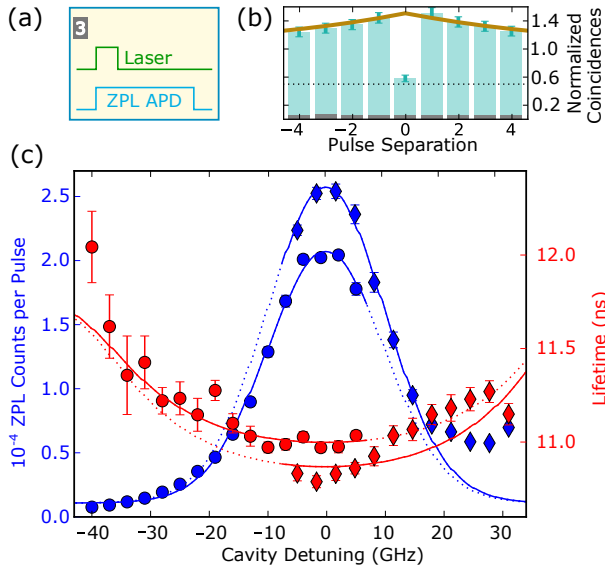
Figure 6.2: Purcell enhancement of NV centers under off-resonant excitation. (a) Measurement block for pulsed off-resonant excitation and detection in the ZPL. (b) Normalized pulsed autocorrelation measurement of NV center fluorescence from the cavity on two ZPL detectors. Dark boxes on the bottom are background fluorescence between the pulses. We fit the data to a simple bunching model based on probabilistic state initialization into a bright state (solid line), see App. 6.8.4. (c) Detuning sweep of the cavity with respect to the NV centers with measured ZPL fluorescence counts (blue) and lifetime (red). The data is taken on different days (circles and diamonds). We perform a joint fit of our model to both curves (solid lines), see App. 6.8.4. (b) and (c) were measured at different locations on the sample, which are also different from Fig. 6.1.

NV centers, which in turn decreases their lifetime. Thus, when the cavity is resonant with an NV center optical transition, more ZPL light should be emitted with a reduced lifetime, as has been observed in different cryogenic systems [27–34]. Importantly, this additional decay is also funneled into the cavity mode which can be readily collected, as opposed to free space systems, in which the ZPL light is emitted in all directions. From the reduced lifetime, one can (following the definition of Refs. [27–30]) extract the Purcell enhancement induced by the cavity, F_P^{ZPL}, as

$$F_P^{ZPL} = \frac{1}{\beta_0}\left(\frac{\tau_0}{\tau'} - 1\right), \tag{6.1}$$

where β_0 is the Debye-Waller factor, recently estimated to be 2.55% [34], τ_0 is the lifetime without the influence of the cavity, and τ' is the reduced NV center lifetime (see App. 6.8.3 for a derivation). In this paper, we choose the definition of the Purcell factor as the increased emission into the zero-phonon line (ZPL) in the cavity only - rather than the increase in total emission - because it better reflects the coherent ZPL light which can be used for entanglement. A subset of the ZPL light, $F_P^{ZPL}\beta_0/(F_P^{ZPL}\beta_0 + 1)$, is collectable via the cavity mode; this definition means that $F_P^{ZPL} = 0$ without Purcell enhancement from the cavity.

To measure lifetime and fluorescence from NV centers in the cavity under off-resonant

excitation, we replace the measurement block in Fig. 6.1(d) with pulsed green excitation, pictured in Fig. 6.2(a). The cavity is again stabilized with a red laser and the excitation is provided by a ∼ 532 nm picosecond pulsed laser input through the fiber. We collect the resulting fluorescence in the ZPL path on an avalanche photodiode (APD), and extract counts per pulse and lifetime as we sweep the detuning of the cavity. For further experimental details please see App. 6.8.4.

Fig. 6.2(c) shows one such detuning sweep, in which the fluorescence counts and lifetime vary with cavity detuning. The highest fluorescence counts and lowest NV center lifetime coincide, demonstrating Purcell-enhanced NV center emission induced by coupling to the cavity. The widths of the fluorescence peak and of the lifetime reduction curve are several times broader than the cavity linewidth. To understand the quantitative behavior of the detuning sweep, we introduce a model which includes vibrations of the cavity and a spectral distribution of NV center transition frequencies (see App. 6.8.3). By fitting this model to the data, we can extract the emission into the ZPL in the cavity, $F_P^{ZPL}\beta_0/(F_P^{ZPL}\beta_0 + 1) = (7.9 \pm 2.2)\%$, and the off-resonant lifetime, $\tau_0 = (11.8 \pm 0.2)$ ns, which is consistent with the lifetime of NV centers reported for bulk diamond [48, 49]. This data was taken on two different days, leading to two different curves in Fig. 6.2(c) (circles and diamonds) that can be explained by drifts, which we account for in our modeling (App. 6.8.4).

We investigate whether the emission is produced by a single emitter using an auto-correlation ($g^{(2)}$) measurement. At most locations, there is little or no drop in coincidence counts at zero pulse separation. Therefore, we conclude that we are addressing several emitters within the cavity mode volume, likely because the high density of NV centers in our sample lowers the chance of single center addressing with off-resonant excitation. Fig. 6.2(b) displays the most significant drop in coincidences observed, which falls to (0.58 ± 0.05) at zero time delay ([0.54 ± 0.05] with background correction). We observe significant bunching behavior for small pulse separations, which we attribute to probabilistic state initialization into a bright state (App. 6.8.4). The enhancement of the ZPL by a factor of 3.9 ± 0.9 (assuming the same β_0 as in Ref. [34]) is a lower bound for the largest enhancement of single centers at this spot, because there are multiple NV centers within the cavity mode volume.

6.4. CONTINUOUS RESONANT EXCITATION

Entanglement generation in quantum networking protocols requires coherent addressing of individual zero-phonon line (ZPL) transitions with linewidths close to their lifetime-limited value [22]. To determine the suitability of our device for such tasks, we now move on to photoluminescence excitation (PLE) scans.

The measurement protocol for these scans is displayed in Fig. 6.3(a, inset): short green pulses used for initialization of the NV center in the negative charge and $m_s = 0$ spin state are interleaved with red measurement pulses. Fluorescence counts collected in the phonon-sideband (PSB) during the red pulses are then correlated with simultaneously recorded wavemeter readings. This scheme thus allows predominant detection of the two $m_s = 0$ spin-conserving optical transitions per NV center; these transitions connect the ground state to the two optically excited states typically labeled as E_x and E_y. For further details about this measurement sequence, please see App. 6.8.4.
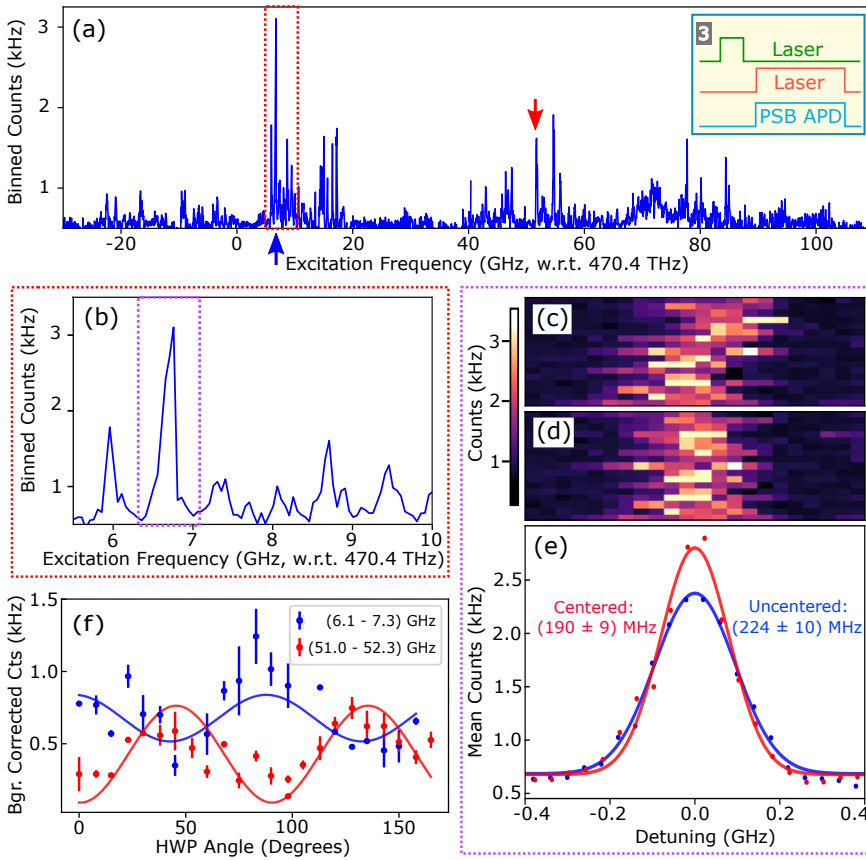
Figure 6.3: Photoluminescence excitation (PLE) scans. (a) Broad PLE scan (cavity resonant with excitation laser, binned into 50 MHz bins), revealing multiple bright lines per cavity position. Blue and red arrows indicate the center position of polarization angle scans displayed in (f). (Inset, a) Measurement block used during PLE scans. (b) Zoom-in of the red dashed frequency region in (a). (c) Series of 17 consecutive PLE scans (measurement time ~ 15 min per trace) for the purple shaded frequency region in (b). (d) Same data as in (c), but center position of Gaussian fit to each individual trace used to correct for slow drift during the measurement. (e) Averaged and Gaussian fitted data of (c, blue) and (d, red), showing spectral diffusion limited linewidths of (224 ± 10) MHz and (190 ± 9) MHz, respectively. (f) Background corrected mean fluorescence counts during PLE scans for a frequency region of (6.1 - 7.3) GHz (blue) and (51. - 52.3) GHz (red, each w.r.t. 470.4 THz) as a function of excitation laser half wave plate (HWP) angle, showing that individual transitions are polarized. Solid lines are sinusoidal fits.

A resulting PLE scan can be seen in Fig. 6.3(a). We observe a multitude of narrow lines per cavity spot, confirming our interpretation that there are multiple NV centers present per cavity mode volume. Fig. 6.3(b) shows a zoom-in into the red dashed region of Fig. 6.3(a); note that each binned point is comprised of many underlying individual datapoints. Importantly, the individual transition peaks can be spectrally distinguished, which is a pre-requisite for single resonant NV center addressing, as probed below.

To test the spectral stability of the transition peaks, we repeatedly scan the excitation

laser over a NV center ZPL transition. Fig. 6.3(c) shows a series of 17 consecutive scans over the frequency region dashed in purple in Fig. 6.3(b). To correct for slow drifts in this measurement (likely due to temperature fluctuations in the cryostat), we fit a Gaussian lineshape to each individual PLE trace, and shift the lines to a common center frequency, displayed in Fig. 6.3(d); the resulting data is representative of the average spectral diffusion experienced on the timescale of one single frequency scan (largely induced by the continuous off-resonant repumping [38]). Fig. 6.3(e) shows the averaged data of the original and centered scans in blue and red, respectively. From Gaussian fits to this data (solid lines), we extract full width at half maximum linewidths of (224 ± 10) MHz and (190 ± 9) MHz for the original and centered case, respectively. We probed the linewidths of 14 NV center transitions during the course of this study, for a total of 4 different cavity positions. Tab. 6.1 in App. 6.8.4 shows the individual linewidths of each NV center transition, which average to (204 ± 59) MHz and (168 ± 49) MHz, for the un-centered and centered case, respectively. Thus, the linewidths in our sample are comparable to the ones measured in bulk diamond samples with similar protocols; close-to transform limited lines have been achieved without continuous green repumping in both bulk diamonds and in microns-thin membranes as used here [38, 50]. Importantly, NV centers with this level of optical coherence have enabled previous entanglement generation experiments by exploiting resonant excitation for charge state and frequency preselection [22].

We next investigate the polarization behaviour of NV center transitions in the cavity by scanning the polarization angle of the excitation laser with a half wave plate (HWP), and observe a dependence of the background corrected fluorescence counts on this HWP angle, see Fig. 6.3(f); polarization can be used to suppress resonant excitation pulses in a cross-polarization detection scheme [22], as demonstrated below. Interestingly, the NV centers in the two studied frequency clusters around 470.407 THz and 470.452 THz show a different polarization behaviour. A possible origin of this effect is a strain-induced splitting in transition frequencies for E_x and E_y polarized lines, as observed in Ref. [38]; future investigation is required to conclusively determine the origin.

6.5. PULSED RESONANT EXCITATION

Now that we can resolve individual NV centers spectrally, we characterize their Purcell enhancement with a detuning sweep similar to that of Sec. 6.3. The measurement block replaces off-resonant pulses with single frequency resonant pulses (Fig. 6.4(a)). The sequence consists of a green repump pulse to initialize the NV center predominantly in the negative charge and $m_s = 0$ spin state, followed by a series of short (~ 2 ns) red pulses at the frequency of the NV center transition. We record the fluorescence counts in the phonon-sideband (PSB) path after each pulse, and extract the NV center lifetime. For further details about the measurement sequence, please see App. 6.8.4.

First, we perform a pulsed autocorrelation measurement with two detectors in the PSB path to confirm that the individual peaks measured during photoluminescence excitation scans are indeed from single NV centers. Fig. 6.4(b) displays the normalized g(2) value of (0.19 ± 0.09) ($[0.16 \pm 0.07]$ with background correction) for zero pulse separation. Unlike the off-resonant case, the value at zero pulse difference clearly falls below 0.5 in all three NV centers we tested, indicating that we are observing single quantum emitters.
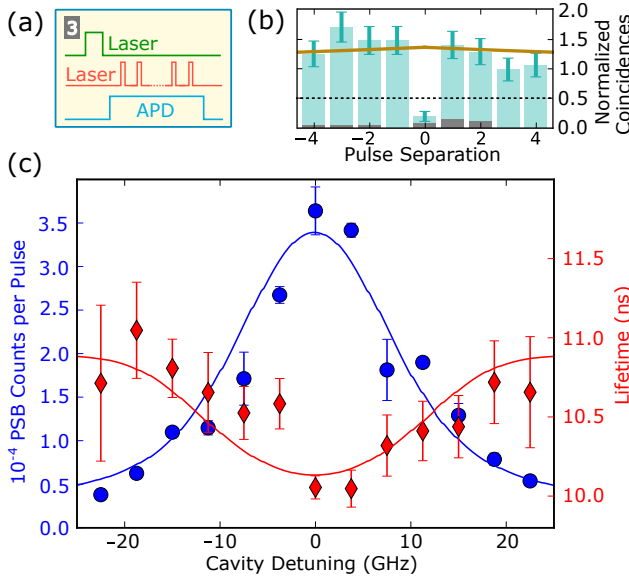
Figure 6.4: Purcell enhancement of NV centers probed with resonant excitation. (a) Measurement block used for pulsed resonant excitation and detection in the PSB / ZPL. (b) Normalized pulsed autocorrelation measurement of NV center fluorescence from the cavity on two PSB detectors. Dark boxes on the bottom are background fluorescence measured with the excitation detuned by 5 GHz. The fit accounts for bunching effects due to probabilistic state initialization into a bright state and the finite pulse train we apply (solid line), see App. 6.8.4. (c) Detuning sweep of the cavity with respect to the NV center with measured PSB fluorescence (blue) and lifetime (red). We perform a joint fit of both curves to a model (solid lines) with four free parameters (App. 6.8.4). (b) and (c) were measured on the same NV center as Fig. 6.3(c-e), which is a different emitter than the ones studied in Fig. 6.2(a-b).

For the same NV center measured in Fig. 6.3(c-e), we sweep the detuning of the cavity from the NV center transition while keeping the excitation pulses resonant with the latter to measure the Purcell enhancement. The collection efficiency of PSB emission is independent of the cavity length. However, the probability of exciting the NV center depends on the overlap between the excitation laser frequency and the cavity resonance, so the PSB intensity should vary with detuning for fixed excitation power (see App. 6.8.3). In the measurement (Fig. 6.4(c)), the fluorescence counts increase and the lifetime decreases when the cavity is on resonance with the NV center, demonstrating that we observe Purcell-enhanced NV center emission. We fit our model to both curves and extract the fraction of ZPL emission into the collectable cavity mode, $F_P^{ZPL}\beta_0/(F_P^{ZPL}\beta_0+1) = (7.0 \pm 3.4)\%$ (see definition in Sec. 6.3), the off-resonant lifetime, $\tau_0 = (10.9 \pm 0.2)$ ns, and the root mean squared cavity vibrations, $\sigma_{vib} = (0.18 \pm 0.02)$ nm (see App. 6.8.4). This Purcell factor corresponds to a cooperativity, C, of 0.08 ± 0.04 (see App. 6.8.3). The enhancement of this NV center is consistent with the enhancement we found for NV centers under off-resonant excitation.

6.6. ZPL COLLECTION AND FUTURE IMPROVEMENTS

So far, we have only studied light emitted into the phonon-sideband (PSB) after exci-
tation with resonant light pulses. For quantum information applications, however, it is
important to extract the emitted zero-phonon line (ZPL) photons with high efficiency.
In the current configuration, the excitation light is directly transmitted to the detector.
Therefore, we separate out the ZPL photons from the bright excitation pulse with cross-
polarization and time-bin filtering [22, 26], and shorten the excitation pulse further by
introducing an additional electro-optic modulator (see App. 6.8.1 for details).

To be able to detect ZPL photons after a resonant excitation pulse, cross-polarization
detection is especially important, because state of the art photodetectors have a dead
time longer than the lifetime of the NV center; if a photon from the excitation pulse
hits the detector, the dead time prevents detection of a ZPL photon, effectively reducing
detection efficiency. Unfortunately, cross polarization only reduces the pulse power by
a factor of 4 in our setup, which is likely due to vibrations of the freely hanging single
mode fiber in the cryostat. We additionally insert a 8.6 dB attenuation neutral-density
(ND) filter into the ZPL path so that the efficiency of the detector remains high.

Fig. 6.5(a) displays the fluorescence counts after a resonant excitation pulse, recorded
simultaneously in the PSB and ZPL collection paths. The fluorescence in the ZPL path
decays with a lifetime that agrees to within error with the lifetime of the NV center in the
PSB path (App. 6.8.4). Thus, our technique enables us to see ZPL light from an NV center
in a cavity under resonant excitation.

Summing the fluorescence counts from the NV center in the ZPL path gives us a
benchmark for the performance of our system as a collection enhancement tool. The
excitation pulse obscures the initial counts, so we extrapolate a fit to the lifetime to ex-
tract the total NV center counts in the ZPL and correct for the ND filter. We find $(9.3 \pm 0.2) \times 10^{-5}$ photons per pulse in the ZPL path and $(4.6 \pm 0.1) \times 10^{-4}$ in the PSB path. Due
to low available laser power, we operate with both low initialization probability into the
$m_s = 0$ state and low excitation probability to the excited state (see App. 6.8.6).

To better compare the cavity with other collection enhancement systems, and to un-
derstand current limitations and possible improvements in a future system, we break
the loss of coherent photons down into its main contributions, see Fig. 6.5(b) (App. 6.8.6
contains a detailed derivation and full discussion of these values). For the current cavity
system, ~ 14 dB of losses are associated with our limited probability of exciting the NV
center to its excited state from one resonant laser pulse, ~ 15 dB of losses result during
photon collection, and ~ 12 dB of losses result from the NV center emitting a photon in
the PSB, rather than the ZPL.

Importantly, correcting for the excitation probability alone already raises the ZPL de-
tection probability to $\sim 2.0 \times 10^{-3}$, which is comparable to the collection of coherent ZPL
photons achieved for a NV center in a solid immersion lens ($\sim 5 \times 10^{-4}$) [25, 26]. Thus, de-
spite the relatively low collection efficiency from our current cavity, limited in large parts
due to operation in the clipping regime of the fiber mirror, our system already produces
ZPL photons at a level comparable to state of the art non-cavity systems (see App. 6.8.6).

There are a number of changes which could improve ZPL collection under resonant
excitation; we focus on three main developments which have already been achieved in
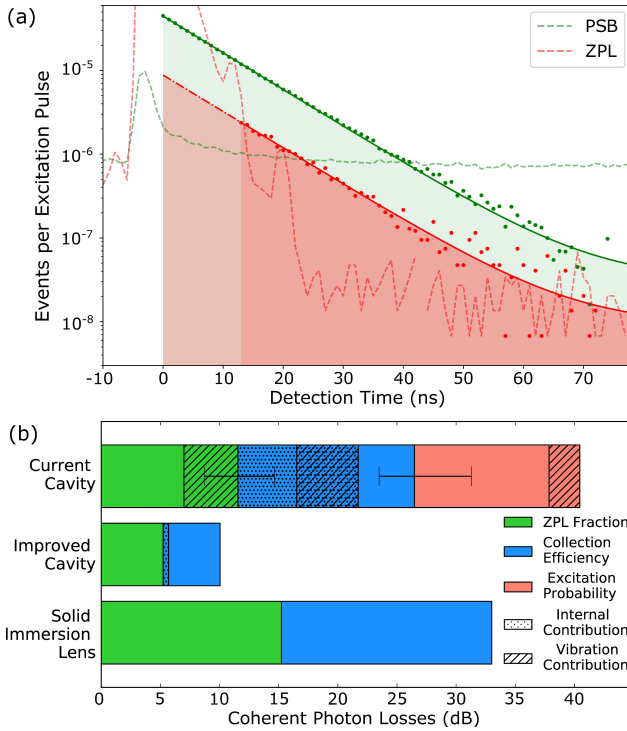other systems. First, introducing microwaves and a spin pumping laser is a standard

Figure 6.5: Zero-phonon line (ZPL) and phonon-sideband (PSB) fluorescence counts after resonant excitation and estimation of current and future ZPL count loss sources. (a) Background corrected PSB (green) and ZPL (red) fluorescence per excitation pulse (points), recorded at the same time. Background from the bright excitation pulse is shown with dashed lines (App. 6.8.4). The parallel decay of an exponential fit to both curves (solid lines) indicates emission from the same NV center. Shaded regions indicate areas for which fluorescence counts are summed to extract counts per excitation pulse (for the ZPL we include the extrapolated region shaded in light red), see App. 6.8.4. (b) Schematic of the sources of loss of coherent ZPL photons for the current cavity, the proposed improved cavity and a state-of-the art solid immersion lens (SIL) collection system. We breakdown the loss contributions into ZPL fraction, collection efficiency and excitation probability and separate the losses into vibration induced losses (stripes) and internal cavity losses (dotted) (see App. 6.8.6).

technique for initializing and controlling the NV$^-$ charge and m$_s$ = 0 spin state with high fidelity in bulk samples. The narrow spectral diffusion linewidths demonstrated in this work should make this possible in our system as well. Together with upgraded laser excitation pulse power, this should allow for near unity excitation per pulse, as is common for bulk diamond samples [51]. By increasing the polarization extinction by a factor of at least 100 by either fixing the fiber in the cryostat or switching to polarization maintaining fiber, the excitation pulse can be suppressed sufficiently even for these higher excitation powers. Second, reducing the vibrations by a factor of 20 (from ~ 0.2 nm to ~ 0.01 nm), as demonstrated in Refs. [15, 52–55], would increase the ZPL detection fraction by a factor of ~ 16. Our current data already shows evidence for this potential improvement: by correlating the lifetime and the PSB fluorescence counts per resonant excitation pulse with the vibration level in the cryostat, we observe a reduction in lifetime (increase in

fluorescence counts) from (10.02 ± 0.12) ns ($[2.5 \pm 0.1] \times 10^{-4}$) to (9.77 ± 0.08) ns ($[5.8 \pm 0.2] \times 10^{-4}$) for data collected during high and low vibration time periods of the cryostat, respectively. We explore this correlation in detail in App. 6.8.5. Finally, by working with a different fiber that is not clipping-loss limited, we expect to improve collection by a factor of 3. A further advantage of the last two improvements is that the required laser power and polarization extinction are reduced by a factor of 5 and 25, respectively (see App. 6.8.6). Together, these three improvements would raise the joint probability of producing and detecting a ZPL photon after short pulsed excitation to ~ 10%.

6.7. CONCLUSION

We demonstrate resonant excitation of cavity-coupled NV centers with narrow optical transitions; the observed enhancement of collected coherent photons is in excellent agreement with our theoretical model. Using mutually non-exclusive numbers that have already each been achieved in several systems, we predict that we can increase the collected ZPL photons per excitation pulse to ~ 10% in a future NV-cavity system operated in a closed-cycle cryostat. The demonstration of resonant excitation of an NV center in a cavity represents a critical step on the path towards Purcell-enhanced remote entanglement generation.

Building on the previous success of NV centers in entanglement generation and other network protocols [22, 24, 25], a cavity enhanced NV-photon interface could dramatically improve entanglement rates and fidelity; single click and double click protocols would speed up by a factor of 100 and 10000 respectively. This opens the door to experiments such as device independent quantum key distribution and quantum repeaters [56, 57]. In the longer run, we expect that the realization of fully coherent quantum emitters embedded in optical fiber-based cavities will enable more extensive quantum networks with long coherence times, a crucial step towards a quantum internet.

6.8. APPENDIX

6.8.1. EXPERIMENTAL SETUP

Fig. 6.6 shows an overview of the experimental setup used in this work. The control electronics block (Fig. 6.6(a)) consists of a real-time controller (Jaeger Adwin Pro II), an arbi-
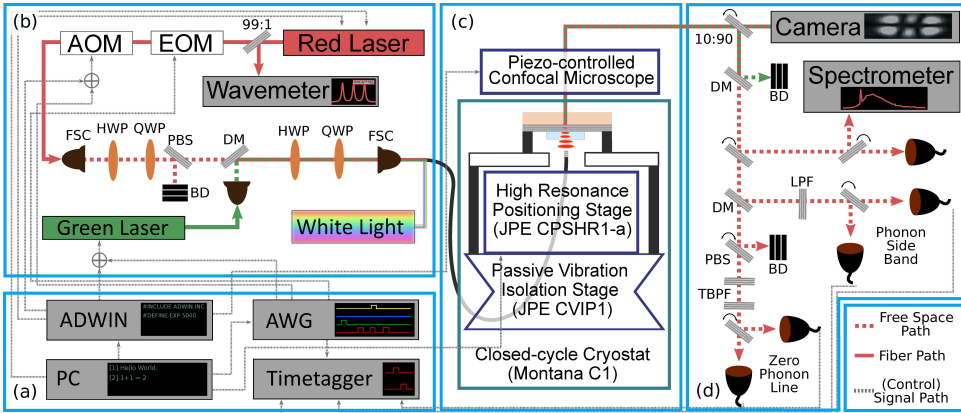
Figure 6.6: Schematic of the experimental setup. (a) Control electronics block. (b) Excitation path. Free space coupler (FSC), half- (HWP) and quarter- (QWP) wave plate, polarizing beamsplitter (PBS), dichroic mirror (DM), beam dump (BD). (c) Cavity setup. (d) Detection path. Long-pass filter (LPF), tuneable band pass filter (TBPF).

trary waveform generator (AWG, Tektronix 5014), a time resolved photon counting module (Timetagger, Picoquant HydraHarp 400), and a PC, from which all measurements are controlled.

In the excitation path (Fig. 6.6(b)), ~ 637 nm pulses with nanosecond time resolution are carved out of a red tuneable laser (Newfocus Velocity TLB-6300-LN) that is continuously monitored on a wavemter (High Finesse WS6) using an amplitude-electro-optic- (EOM, Jenoptik AM635) and an acousto-optic- (AOM, Gooch and Housego) modulator. After free space launching of the beam, a polarizing beamsplitter (PBS, Thorlabs) maps polarization angle fluctuations into amplitude fluctuations. The red path is combined with directly modulated green laser light (~ 515 nm, Cobolt MLD515) using a dichroic mirror (Semrock FF560-FDi01), before the combined path is fiber coupled to the cavity. Half- (HWP) and quarter- (QWP) wave-plates before and after the dichroic mirror correct for slow drift in polarization, and rotate the polarization of the resonant excitation light, respectively. For cavity linewidth measurements, we replace the amplitude modulating EOM with a phase modulating EOM (Jenoptik PM635, driven by a Rohde and Schwarz SGS100A signal generator), and connect it directly to the cavity fiber (IVG CU600). For measurements of the bandstructure of the cavity, we instead use a broadband "white light source" (NKT SuperK Compact) to illuminate the cavity fiber.

The position of the cavity fiber mirror can be tuned in-situ via a high resonance frequency piezo positioning stage (JPE CPSHR1-a), mounted on top of a vibration isolator (JPE CVIP1) inside a closed cycle cryostat operated at $T \sim 4$ K (Montana C2), see Fig. 6.6(c). Light is collected from the cavity through a piezo-controlled (PI P-622/625) microscope objective (Mitutoyo Plan Apo 50X, numerical aperature (NA) 0.55). We choose the flat mirror side to collect light from the cavity as it enables in principle unity coupling efficiency; the mode-match between the beam in the fiber and the Gaussian mode in the cavity at the position of the fiber mirror leads to a finite coupling efficiency when collecting from the fiber side.

In the detection path (Fig. 6.6(d)), a 10:90 mirror mounted on a flip mount reflects
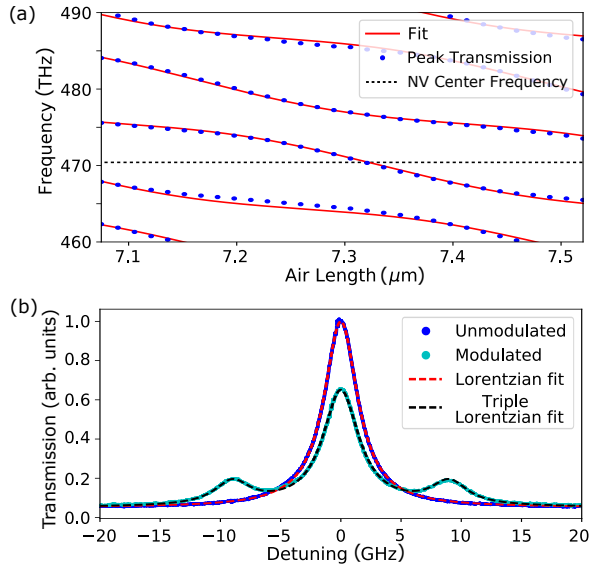
Figure 6.7: Example data traces of cavity dispersion and finesse. (a) Cavity dispersion for the coupled membrane-air fiber-cavity system. The length of the cavity is swept and transmission is recorded on a spectrometer. From fits of the fundamental modes to a transfer matrix model, we can determine the diamond and air thicknesses to be 5.8 µm and 7.3 µm, respectively. (b) Finesse measurement. We scan the cavity quickly over a transmission peak to extract the cavity linewidth ($\kappa/2\pi$ = [3.5 ± 0.2] GHz) from fits to the data; the laser exciting the cavity is modulated with sidebands of 9 GHz with an EOM, serving as frequency calibration reference.

light to a camera for visualization of the cavity modes. A dichroic mirror (Semrock DI 02-R365, pass edge at ~ 656 nm) filters out green excitation light, before another flip mirror couples transmitted cavity light to a spectrometer (Princeton Instruments SP-2500i, used for bandstructure and rough NV center frequency estimation measurements) or an APD (Thorlabs APD130A2, used to measure the cavity linewidth). A dichroic mirror (Semrock DI 02-R365, pass edge at ~ 656 nm) then transmitts the NV center ZPL light, while reflecting the PSB light. The PSB light then gets filtered (Semrock LP02-647RU-25) from any residual green excitation light, before being collected on APDs (LaserComponents or PicoQuant, detection with a multimode fiber, 50 µm core diameter, 0.22 NA). A PBS (Thorlabs) in the ZPL filter path on a flip mirror filters out resonant excitation pulses. Before being collected (LaserComponents or PicoQuant, detection with a multimode fiber, 10 µm core diameter, 0.1 NA), the ZPL light is filtered with two tuneable bandpass filters (TBPF, Semrock TBP 01-700/13, window [637 ± 2] nm) to suppress background fluorescence.

6.8.2. CAVITY CHARACTERIZATION MEASUREMENTS

To characterize the cavity, we first input white light through the fiber, and measure the cavity transmission on a spectrometer for different cavity lengths. Fig. 6.7(a) displays the resulting dispersion diagram with avoided crossings between air and diamond modes [39, 40]. From a fit to this data, we infer that we operate in an air-like mode with a dia-

mond thickness of 5.8 µm and a typical air gap between 5 µm and 7.5 µm (7.3 µm in the measurement shown) [39]. This gap cannot be reduced further, likely due to an angled mounting of, or dirt on, the fiber. To measure the cavity linewidth, we then scan the cavity length through a resonance and measure the corresponding transmission peak after the cavity with a photodiode (sub-ms timescale to minimize vibration contributions to the linewidth). We apply sidebands to the laser to calibrate the frequency of this scan. In the measurement displayed in Fig. 6.7(b), the linewidth of the cavity is $\kappa/2\pi = (3.5 \pm 0.2)$ GHz, and the finesse is (2200 ± 100). Over the course of this work, we operated with a finesse between 1000 and 2500, dependent on the cavity position.

Based on the measured parameters of the cavity and a complete transfer matrix method described in Ref. [46], we can estimate the maximum possible Purcell enhancement in our cavity ($F_P^{ZPL} \approx 6$), which corresponds to a coupling between NV centers and the cavity of $g/2\pi \approx 50$ MHz. This estimate holds for an NV center at the optimal depth location, which is a cavity standing wave antinode, and the optimal xy position for maximum overlap with the Gaussian mode of the cavity. We describe the mismatch with the ideal position with a parameter, ξ, which we measure via the Purcell enhancement in the main text. The coupling is also reduced by vibrations as discussed in App. 6.8.3. The transition linewidth of the NV center was measured to be $\gamma/2\pi \approx 18.3^{+5.7}_{-8.3}$ MHz in similar devices fabricated with the same method when accounting for power broadening [38]. In Sec. 6.3 and Sec. 6.5, we measured the Purcell enhancement under off-resonant and resonant excitation and determined $F_P^{ZPL} \approx 3$ and thus $g/2\pi \approx 35$ MHz (see eq. 6.4 and 6.5). The relative values of g, κ and γ, put us in the weak coupling Purcell regime ($\gamma < g < \kappa$), which is a favorable parameter range for collecting photons from an emitter [58].

6.8.3. Theoretical model

Purcell enhancement

NV centers exhibit limited emission into the zero-phonon line (ZPL), β_0, given by the Debye-Waller factor. Some states also couple to a non-radiative transition through an intersystem crossing [59]. Without interaction with a cavity, we can model the decay from the NV center excited state, γ_0, with a radiative decay rate, γ_{rad}, and non-radiative decay rate, γ_{dark}, as:

$$\gamma_0 = \beta_0\gamma_{rad} + (1 - \beta_0)\gamma_{rad} + \gamma_{dark}. \tag{6.2}$$

Coupling to the mode of the cavity opens up another decay channel for the NV center, which we characterize with the cooperativity, C, and the Purcell factor, F_P^{ZPL}. The decay rate from the NV excited state, modified by the cavity, γ', is then given as

$$\gamma' = F_P^{ZPL}\beta_0\gamma_{rad} + \beta_0\gamma_{rad} + (1 - \beta_0)\gamma_{rad} + \gamma_{dark}, \tag{6.3}$$

with

$$C = \frac{4g^2}{\kappa\gamma}, \tag{6.4}$$

$$F_P^{ZPL} = \frac{C}{\beta_0}, \tag{6.5}$$

where $g/2\pi$ is the NV-cavity coupling, $\kappa/2\pi$ is the cavity linewidth, and $\gamma/2\pi$ is the previously measured optical transition linewidth of the NV center [38, 60]. We choose the definition of the Purcell factor as the enhancement of the ZPL — rather than the enhancement of the total emission from the NV center — because it better reflects the increase in coherent light.

In this work, we primarily investigate transitions with linear polarization, and we preferentially initialize into the $m_s = 0$ ground state with green excitation. The transitions in the $m_s = 0$ manifold are E_x and E_y, for which γ_{dark} is much smaller than γ_{rad} in bulk diamond [49, 61]: In Sec. 6.5, we measure a reduced lifetime when the cavity is off resonance of (10.9 ± 0.2) ns, compared to the ~ 12 ns typically found in bulk diamond [49, 61]; from this, we estimate that $\gamma_{dark}/\gamma_{rad} \approx 0.1$, so we assume $\gamma_{rad} \gg \gamma_{dark}$, and simplify eqs. 6.2 and 6.3 to

$$\frac{\gamma'}{\gamma_0} = \frac{\tau_0}{\tau'} = 1 + F_P^{ZPL}\beta_0\frac{\gamma_{rad}}{\gamma_{rad}+\gamma_{dark}} \qquad (6.6)$$
$$\approx 1 + F_P^{ZPL}\beta_0,$$

where τ_0 is the NV center lifetime without the cavity and τ' is the modified lifetime. The fraction emitted into the ZPL in the cavity mode is $F_P^{ZPL}\beta_0/(F_P^{ZPL}\beta_0 + 1)$. If the assumption that γ_{dark} is negligible is incorrect, then $F_P^{ZPL}\beta_0$ is increased by a factor of $(\gamma_{rad} + \gamma_{dark})/\gamma_{rad}$. A simple rearrangement then gives us eq. 6.1.

The rates of detected photons in the ZPL path, C_{ZPL}, and the phonon-sideband (PSB) path, C_{PSB}, are

$$C_{zpl}(t) = p_{ex}\frac{F_P^{ZPL}\beta_0}{F_P^{ZPL}\beta_0 + 1}\eta_{zpl}\gamma' e^{-\gamma' t} \qquad (6.7)$$
$$= p_{ex}F_P^{ZPL}\beta_0\eta_{zpl}\gamma_0 e^{-\gamma' t}$$

and

$$C_{psb}(t) = p_{ex}\frac{1-\beta_0}{F_P^{ZPL}\beta_0 + 1}\eta_{psb}\gamma' e^{-\gamma' t} \qquad (6.8)$$
$$= p_{ex}(1-\beta_0)\eta_{psb}\gamma_0 e^{-\gamma' t},$$

where p_{ex} is the probability that a pulse excites the NV center to its excited state, and η_{zpl} (η_{psb}) is the detection efficiency for ZPL (PSB) photons from the cavity. As will be discussed in App. 6.8.6, it is helpful to break the ZPL detection efficiency down into internal and external efficiencies with $\eta_{zpl} = \eta_{int}\eta_{ext}$. A number of these parameters depend on the normalized intra-cavity power, P, which itself depends on the detuning between the cavity and the transition, Δ:

$$P(\Delta) = \frac{\kappa^2/4}{\kappa^2/4 + \Delta^2}. \qquad (6.9)$$

This modifies F_P^{ZPL} and η_{zpl} to

$$F_P^{ZPL}(\Delta) = F_P^{ZPL}(0)P(\Delta) \qquad (6.10)$$
$$\eta_{zpl}(\Delta) = \eta_{ext}\eta_{int}(0)P(\Delta) \qquad (6.11)$$

The PSB collection is not resonant with the cavity, and its spectral distribution lies mostly outside of the stopband of the mirror, so there should be minimal changes from small variations in cavity detuning. For the same reason, green excitation light is also independent of the cavity detuning. However, resonant red excitation depends strongly on cavity detuning, and the corresponding power in the cavity. The Rabi frequency is proportional to the square root of the intra-cavity power which scales with $P(\Delta)$. Therefore, in the resonant excitation case:

$$p_{ex}(\Delta) = \sin\left(\phi_p(0)\sqrt{P(\Delta)}/2\right) \tag{6.12}$$

Here $\phi_p(0)$ is the Rabi rotation angle induced by the pulse on resonance (e.g. π for a complete population of the excited state). In the weak excitation limit explored in this work, this can be approximated as $\phi_p(0)\sqrt{P(\Delta)}/2$.

Vibration Model

The above simple model does not take into account the vibrations in the cavity length. We extend the model of Ref. [46] to build a complete numerical transfer matrix model for the cavity. We assume a Gaussian distribution of cavity lengths, f_{vib}, given as

$$f_{vib}(dL) = \frac{1}{\sqrt{2\pi\sigma^2}}e^{-\frac{dL^2}{2\sigma^2}}, \tag{6.13}$$

where σ is the width of the length distribution, and dL the length flucutations around a certain cavity length, as induced from vibrations. We then find the Purcell-enhanced fraction of emission into the ZPL ($F_p(dL)\beta_0$) for each dL.

Off-resonant Excitation   Under off-resonant excitation, the probability of exciting the NV center does not depend on the length of the cavity. For each frequency detuning, Δ, we find the equivalent cavity detuning length, L_{det}, using our complete model of the cavity dispersion relationship. We integrate eq. 6.7 over the length distribution in eq. 6.13 to determine the emitted counts in the ZPL:

$$
\begin{aligned}
C_{zpl}(t, L_{det}) &= p_{ex}\gamma_0 \int dL\, f_{vib}(dL)g_{nv}(L_{det}+dL)\beta_0 F_P^{ZPL}(L_{det}+dL)\\
&\quad \times \eta_{zpl}(L_{det}+dL)\exp\left[-\gamma'(L_{det}+dL)t\right]\\
&= p_{ex}\beta_0 F_P^{ZPL}(0)\eta_{ext}\eta_{int}(0)\gamma_0 \int dL\, f_{vib}(dL)g_{nv}(L_{det}+dL)\\
&\quad \times P(L_{det}+dL)^2 \exp\left[-(1+\beta_0 F_P^{ZPL}(L_{det}+dL))\gamma_0 t\right].
\end{aligned} \tag{6.14}
$$

We then numerically integrate and fit the function $C(t)$ to an exponential decay to determine the measured lifetime $\tau(\Delta)$. We also sum over t to find total counts $C_{tot}(\Delta)$. For the case of multiple NV centers we also introduce an extra Gaussian broadening term, g_{nv}, inside the integral. The exact form of g_{nv} depends on the (unknown) distribution of NV centers, but we find that the Purcell factor we extract is relatively insensitive to the shape we pick.

Resonant Excitation   Under resonant excitation the probability of exciting the NV center depends strongly on the excitation laser detuning from the cavity. This modifies the function for counts from the cavity slightly. We integrate the counts curves in the same way as in the case of off-resonant excitation to determine the total counts. For collection from the ZPL and the PSB, respectively, we get

$$
\begin{aligned}
C_{zpl}(t, L_{det}) = {} & \frac{p_{in}\phi_p(0)}{2}\beta_0 F_P^{ZPL}(0)\eta_{ext}\eta_{int}(0)\gamma_0 \\
& \times \int dL\, f_{vib}(dL)P(L_{det}+dL)^{5/2} \\
& \times \exp\left[-(1+\beta_0 F_P^{ZPL}(L_{det}+dL))\gamma_0 t\right],
\end{aligned}
\tag{6.15}
$$

$$
\begin{aligned}
C_{psb}(t, L_{det}) = {} & \frac{p_{in}\phi_p(0)}{2}(1-\beta_0)\eta_{psb}\gamma_0 \\
& \times \int dL\, f_{vib}(dL)\sqrt{P(L_{det}+dL)} \\
& \times \exp\left[-(1+\beta_0 F_P^{ZPL}(L_{det}+dL))\gamma_0 t\right].
\end{aligned}
\tag{6.16}
$$

p_{in} is the probability of initializing in the m_s=0 state. We do not include g_{nv} because we only excite single NV centers in the case of resonant excitation. Counts and lifetime are then calculated in the same manner as for the off-resonant case.

6.8.4. MEASUREMENT TECHNIQUES AND DATA ANALYSIS

OFF-RESONANT EXCITATION

Protocol and timings   For the off-resonant excitation measurements described in Sec. 6.3, a measurement sequence starts by stabilizing a red excitation laser to a wavemeter, followed by stabilization of the cavity on transmission to that frequency. We excite the cavity with a ~ 65 picosecond pulsed green laser (Onefive Katana / Advanced Laser Diode Systems PiLas, ~ 532 nm, repetition rate 1 MHz, continuous output power measured after the cavity ~ 1mW), and collect resulting fluorescence in the zero-phonon line (ZPL) with an avalanche photodiode (APD) and a time resolved photon counting module (see Fig. 6.2(a)). Due to a favourable signal to noise ratio, we choose to collect light in the ZPL, rather than in the PSB, as off-resonant excitation results in increased background in our sample. We stabilize the cavity on a certain detuning frequency point (always on NV center resonance in case of a $g^{(2)}$ measurement) every ~ 10 seconds to mitigate slow drifts during the measurement.

We first take a background trace for a detuning of ~ 100 GHz below the NV center resonance frequency, so that we can be sure to not record any NV center light; as the background is spectrally flat in the case of off-resonant excitation, we can then use this data to correct for background fluorescence in the subsequent measurement sequence (background lifetime [6.6 ± 0.6] ns). We then start a measurement, which consists of 16 (14) repeated scans over the full detuning in the case of the diamond-shape (circular-shape) marked data in Fig. 6.2(c), each of which is comprised of 12 (16) frequency steps that take ~ 6 minutes each. This data was taken on two different days, with slight drifts in cavity position (and thus NV-cavity coupling) in between. Because the cavity filters out the signal off resonance, there is a limit to how far we can detune and accurately measure a lifetime, so we do not include data beyond that point. For Fig. 6.2(c), we include data
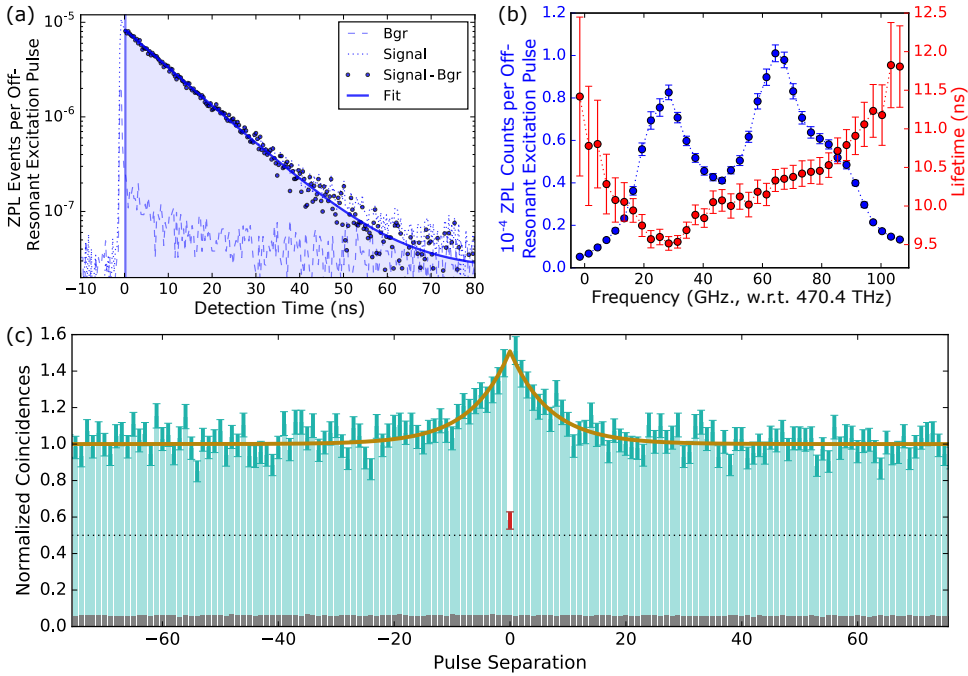
Figure 6.8: Example off-resonant excitation time trace, additional detuning sweep, and full photon autocorrelation data. (a) Example trace of the data taken during off-resonant excitation. From a fit to the background corrected data, we extract a lifetime of (10.71 ± 0.08) ns, and (2.6 ± 0.1) ×10⁻⁴ ZPL detection events per off-resonant excitation pulse (blue shaded area). (b) Detuning sweep of the cavity with respect to the NV centers with extracted ZPL fluorescence counts (blue) and lifetime (red). This measurement is analogous to the one displayed in Fig. 6.2(c), but taken at a different cavity position. (c) Full data for the pulsed photon autocorrelation measurement displayed in Fig. 6.2(b), with a total measurement time of ∼ 65 minutes. Grey bars represent background counts between the pulses, green bars represent integrated counts per pulse, and red point represents the extracted value for zero pulse separation between detector clicks. Solid brown line is a fit to a simple bunching model based on probabilistic state initialization into a bright state. Dashed black line at 0.5 normalized coincidences represents the theoretical boundary for single emitter emission.

with a signal to noise ratio of ∼ 20 (cavity on resonance with the NV center) down to ∼ 5 (point of largest detuning between cavity and NV frequency).

Detuning sweep analysis and additional data   An example time trace, corresponding to the underlying data for the frequency detuning point of 2 GHz from the NV center frequency (diamond-shaped data, Fig. 6.2(c)) can be seen in Fig. 6.8(a). To fit the full data of Fig. 6.2(c) to our theoretical model (eq. 6.14), we proceed in the following way: We first perform a joint fit with five parameters (NV center frequency, on-resonance counts, root mean squared vibrations level, off-resonance NV center lifetime, and mismatch with the cavity) to all data. A sixth parameter, the Gaussian distribution of NV center transition frequencies (as we are looking at multiple NV centers per cavity spot) is kept fixed, as it is interchangeable with vibration level; we choose a value that is consistent with typical photoluminescence excitation results (we also interchanged this width parameter to a

square rather than a Gaussian distribution, leading to similar results). We then extract the Purcell enhancement and lifetime parameters reported in the main text from this overall fit. In a second step, we fix the NV center frequency, vibrations level and off-resonant lifetime, and re-fit the two traces (taken on several days) individually, allowing different on-resonance counts and cavity mismatch values. We use the results of these fits to plot the solid lines displayed in Fig. 6.2(c).

An additional detuning sweep, measured on a different cavity position, can be seen in Fig. 6.8(b). The shape of the lifetime and count curves indicates that while the NV centers are clustered around two frequency values, there are potentially many more NV center frequencies around those two values, making it hard to fit our full model to the data. The location of the two peaks is consistent with the data reported in Fig. 6.1(d, green and red curves). Since the green off-resonant laser both excites the NV centers and initializes them predominantly in the negative charge and $m_s = 0$ spin state, we expect the measured counts to be dominated from $m_s = 0$ spin-conserving optical transitions, typically labeled as E_x and E_y. A slight strain in the sample, as also observed in Ref. [38], seems to be a likely cause for the origin of the splitting between the peaks. Future investigation beyond the current work is required to confirm the mechanism behind this effect.

Photon autocorrelation analysis   The data underlying the photon autocorrelation measurement displayed in Fig. 6.2(b) can be seen in Fig. 6.8(c). We compute the time differences between ZPL clicks after splitting the signal and measuring with two photodetectors, and integrate the counts for the time differences corresponding to a certain pulse separation number. We then fit a simple bunching model based on a 3-level-system to the resulting data [62], as the green laser leads to a finite state initialization into a bright state. We find a steady-state initialization probability of (0.66 ± 0.06), which is consistent with literature [63, 64]. From this fit, we can extract that the normalized autocorrelation falls to (0.58 ± 0.05) for zero pulse separation, or (0.54 ± 0.05) with background correction. The $g^{(2)}$ data displayed here represents the deepest dip we found. We therefore conclude that the NV center emission is predominantly from multiple NV centers per cavity spot in the off-resonant excitation case.

PHOTOLUMINESCENCE EXCITATION SCANS
Protocol and timings   For the photoluminescence excitation (PLE) scans described in Sec. 6.4, a measurement sequence starts by stabilizing a red excitation laser to a wavemeter, followed by stabilization of the cavity on transmission to that frequency. The measurement block, depicted in Fig. 6.3(a, inset), then consists of short green pulses (5 μs, 60 μW) used for initialization of the NV center in the negative charge and $m_s = 0$ spin state, that are interleaved with red measurement pulses (75 μs, 20 nW); counts collected in the phonon-sideband (PSB) during these red pulses are then correlated with simultaneously recorded wavemeter readings. To prevent background from building up, we introduce a wait time between a green and red pulse of 0.5 ms, and break the red pulse down into 250 equal pulses of 300 ns each, with a wait time of 6.5 μs in between red pulses. We sweep the excitation laser frequency after 250 green pulse repetitions in steps of ~ 2 MHz, and stabilize the cavity every ~ 20 seconds to the excitation laser.

Transition Number	Cavity Area Number	Center Position (GHz, w.r.t. 470.4 THz)	Gaussian Linewidth (MHz)	Centered Linewidth (MHz)
1	1	16.3	105 ± 9	100 ± 6
2	1	17.6	154 ± 11	125 ± 6
3	1	20.0	146 ± 5	131 ± 8
4	1	24.7	161 ± 11	110 ± 6
5	2	18.6	187 ± 18	192 ± 22
6	3	12.3	175 ± 16	175 ± 16
7	4	6.7	224 ± 10	190 ± 9
8	4	8.2	264 ± 11	251 ± 13
9	4	17.8	273 ± 41	161 ± 17
10	4	19.3	207 ± 25	136 ± 26
11	4	47.8	194 ± 18	143 ± 7
12	4	48.6	217 ± 19	175 ± 9
13	4	50.9	210 ± 16	201 ± 12
14	4	69.4	333 ± 56	257 ± 54
Mean			204 ± 59	168 ± 49

Table 6.1: Spectral stability data for all measured NV center transitions. We extract an average Gaussian linewidth of (204 ± 59) MHz, and a Centered Linewidth of (168 ± 49) MHz. For a definition of these quantities, please see the text. Transition 7 corresponds to the transition probed in Figs. 6.3(c-e).

6

Additional spectral stability data   The spectral stability of all tested NV center transitions is displayed in Tab. 6.1. We extract the data following two different approaches: the first is to directly average the counts from all PLE scan repetitions on a certain transition, leading to a value that includes slow drifts (several minutes - hours timescale), which we refer to as the "Gaussian linewidth". In a second method, we take out small drifts over the course of the measurement (possibly induced by temperature fluctuations in the cryostat leading to slight variation in membrane strain [and thus resonance position]). We do this by fitting each individual scan first, re-shifting all scans corresponding to a certain transition with respect to a common mean frequency, and then extracting the "centered linewidth" from a fit to the averaged shifted data (minutes timescale). The second value still includes spectral diffusion and thus follows a Gaussian distribution, as we constantly interleave green pulses that re-shuffle the NV center charge environment with red measurement pulses. The Gaussian linewidth averages to (204 ± 59) MHz, while the centered linewidth averages to (168 ± 49) MHz over all NV center transitions investigated in this study; these values are consistent with previous findings on a sample fabricated using the same process flow [38]. Importantly, they are also consistent with values extracted for bulk diamond samples under off-resonant repumping, and NV centers with similar optical coherence have been used in previous entanglement generation protocols [22].

Protocol and timings   For the resonant excitation measurements described in Sec. 6.5 and Sec. 6.6, a measurement sequence starts by stabilizing a red excitation laser to a

wavemeter, followed by stabilization of the cavity on transmission to that frequency. This sets the cavity length to a certain detuning point from a NV center transition frequency that we pre-characterize using photoluminescence excitation scans. The red excitation laser is then stabilized to this NV center transition frequency using the wavemeter a second time. The measurement block, which starts next and is depicted in Fig. 6.3(a, inset), consists of short green pulses (10 μs, 60 μW) used for initialization of the NV center in the negative charge and $m_s = 0$ spin state, that are interleaved with short red measurement pulses (nominal time 2 ns, generated by a cascade of two electro-optic modulators and one accousto-optic modulator and an AWG, see App. 6.8.1); counts collected in the PSB / ZPL in a time window around these resonant excitation pulses are then recorded with a time resolved photon counting module. To prevent background from building up, we introduce a wait time between a green and a red pulse of 1.8 ms, and break the red pulse down into 500 equal pulses, with a wait time of 6.5 μs in between red pulses. The cavity is stabilized every ~ 20 seconds to the desired cavity detuning point, after which the laser is stabilized to the NV center transition frequency again, and a new measurement block is started. We repeat measurements for a certain cavity detuning point for ~ 15 minutes, before we move on to measure a background file for the same amount of time. For the background measurement block, we subtract a certain frequency value from both the cavity stabilization frequency and the NV center excitation frequency, for which we check independently that no NV center transition is close by. Before starting a measurement on the next detuning point, we interleave several PLE scans, and extract the current NV center transition frequency in an automated fashion, to account for slow drifts.

Data analysis   An example time trace, corresponding to the underlying data of Fig. 6.5(a), can be seen in Fig. 6.9(a) for the ZPL data after resonant excitation, and in Fig. 6.9(b) for the PSB data after resonant excitation. This data was taken while keeping the detuning between the cavity and NV center transition frequency at zero, and is an average over 16 experimental repetitions (~ 4 hours of data). As discussed in Sec. 6.6, cross-polarization only suppresses the pulse by a factor of ~ 4 in our system, likely due to vibrations of the freely hanging single mode fiber in the cryostat causing polarization fluctuations. Therefore, we opted to use a 8.6 dB neutral density filter in the ZPL path to reduce detector blinding.

From exponential fits to the ZPL and PSB data, we extract a lifetime of (9.97 ± 0.22) ns and (9.87 ± 0.02) ns, respectively. Since the data is taken simultaneously in the ZPL and PSB, and agrees within errorbars, we conclude that our technique enables us to resolve resonant, coherent NV center photons after a resonant excitation pulse. By integrating the counts in the red and green shaded areas in Figs. 6.9(a,b), we extract a photon collection of $(9.3 \pm 0.2) \times 10^{-5}$ ZPL photons and $(4.6 \pm 0.1) \times 10^{-4}$ PSB photons per excitation pulse, respectively.

To fit the full data of Fig. 6.4(c) to our theoretical model (eq. 6.16), we proceed in the following way: We first fit the curve of PSB counts per resonant excitation pulse with the maximum counts and root mean squared vibration level as free parameters. We use the vibration level determined from this first fit as a fixed value for a second fit, in which we fit the lifetime curve with the NV-cavity mismatch and NV off-resonant lifetime as free
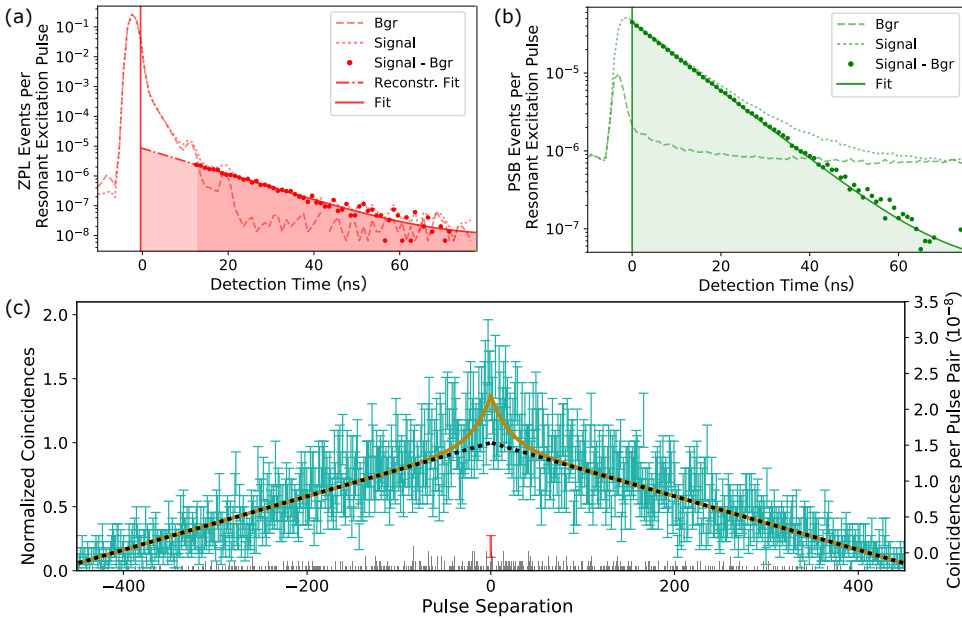
Figure 6.9: Resonant excitation example data traces and full photon autocorrelation data. Example trace of ZPL (a) and PSB (b) detection events after a resonant excitation pulse, overlaid with a fit to the data. This data is the same data as in Fig. 6.5(a). The shaded area indicates the regions used to extract total counts per excitation pulse values. (c) Full data for the pulsed photon autocorrelation measurement displayed in Fig. 6.4(b), with a total measurement time of ~ 6 hours. Grey bars represent background counts extracted from independent measurements (see text), green bars represent integrated and normalized counts per pulse, and red point represents the extracted value for zero pulse separation. Solid brown line is a fit to a simple bunching model based on probabilistic state initialization into a bright state. Dashed black line represents the normalization line extracted from a fit that is a sloped line due to a finite number of excitation pulses per pulse train (see text).

parameters. From the results of this fit, we then calculate the Purcell enhancement, and plot the model displayed in the solid lines of Fig. 6.4(c).

Photon autocorrelation analysis The data underling the photon autocorrelation measurement for the case of resonant excitation, displayed in Fig. 6.4(b), can be seen in Fig. 6.9(c). We compute the time differences between PSB clicks after splitting the signal and measuring with two photodetectors, and integrate the counts for the time differences for a narrow time window that avoids detector after-pulsing effects. We then fit a simple bunching model to the resulting data, as the green laser leads to a finite state initialization into a bright state (as is the case for off-resonant excitation measurements). Due to a finite number of 500 red pulses per measurement pulse sequence (see above), the normalization line in this data is not straight but sloped. By calculating the normalized coincidences at zero pulse separation (normalized to the point of the sloped line at zero pulse separation), we can then extract that the autocorrelation falls to (0.19 ± 0.09), or (0.16 ± 0.07) when correcting for background counts. This is well below the threshold of 0.5, signalling that we are looking at emission from a single quantum emitter. All three resonant excitation photon autocorrelation measurements of NV centers in this
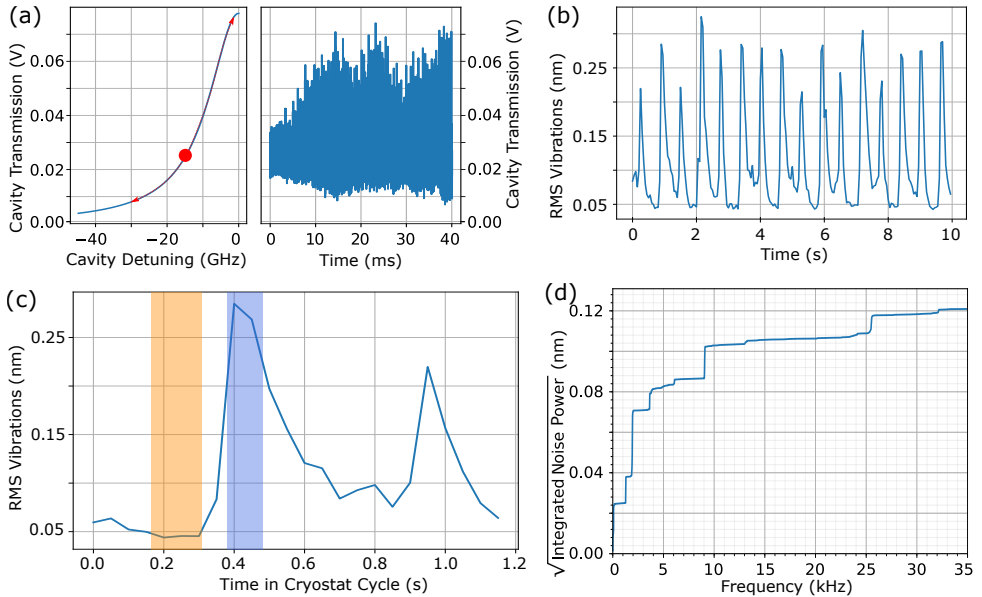
Figure 6.10: Characterization of vibrations in the closed-cycle cryostat at 4 K. (a) Measurement principle. The laser is operated on the flank of the cavity transmission (indicated with a red dot), such that vibration induced shifts in cavity frequency cause a change in cavity transmission. (b) Root mean squared (rms) vibrations over a ten second measurement cycle, binned into 50 ms time bins. (c) Using a synchronization signal of the cryostat marking the beginning of a new coldhead cycle, the same data as in (b) is averaged with respect to time in the cryostat cycle. Blue and orange shaded regions indicate time periods assigned as having low and high vibration values for data analysis similar to the one in Fig. 6.11. (d) Square root of integrated noise power vs cavity frequency, showing the frequency contents of the observed vibrations.

study fell well below 0.5, thus confirming that the emission peaks in photoluminescence excitation scans are originating from single quantum emitters.

6.8.5. CAVITY VIBRATIONS AND THEIR INFLUENCE ON COUNTS AND LIFE-TIMES

All measurements in this paper were taken in a closed-cycle cryostat operated at $T \sim 4$ K. Such a cryogenic system has intrinsic vibrations due to moving parts. Nevertheless, we chose a closed-cycle system - as opposed to an essentially vibrations free liquid helium bath cryostat - because of its ease of operation, and the possibility of uninterrupted measurement cycles on a timescale of several months without any human intervention; this is an important operational consideration for a future quantum network, with nodes distributed over distant locations, as it removes the cost and labour associated with a helium infrastructure.

CHARACTERIZATION OF ROOT MEAN SQUARED CAVITY VIBRATIONS

To characterize the cavity length fluctuations induced by the cryostat, we follow the measurement principle schematically depicted in Fig. 6.10(a). We operate the red excitation laser on the flank of the cavity transmission, which allows us to map vibration induced
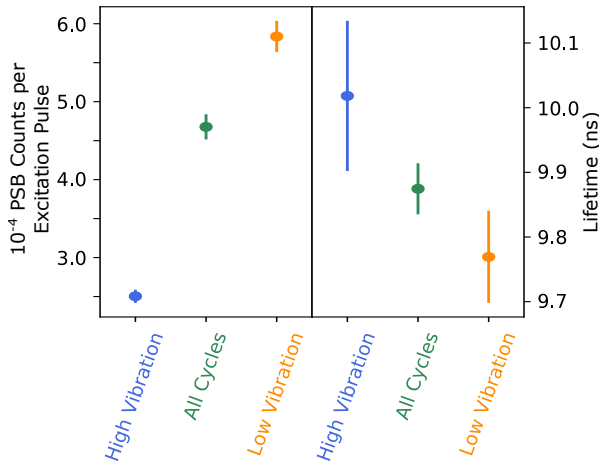
Figure 6.11: Influence of the cavity vibrations on PSB counts per excitation pulse (left side) and lifetime (right side) for the case of resonant NV center excitation. The cavity is kept on resonance with the NV center transition frequency. This data was taken for a different cooldown and thus vibration level assignment than the one depicted schematically in Fig. 6.10(c).

shifts in cavity frequency to cavity transmission changes. We lower the cavity finesse by retracting the fiber, which increases the beam diameter at the position of the fiber mirror to a value where the light mode in the cavity clips at the finite diameter of the ablated mirror region, introducing additional cavity losses. This broadens the Lorentzian cavity transmission to a width where the change in cavity length induced by vibrations in the cryostat is fully contained within one flank of the cavity transmission peak (indicated in red in Fig. 6.10(a)). By measuring the Lorentzian cavity transmission function independently, we can then map changes in cavity transmission to changes in cavity detuning and thus cavity length.

The root mean square (rms) vibrations for a measurement time of 10 seconds, binned into 50 ms time bins, are displayed in Fig. 6.10(b). We observe a (5 - 6) fold change in vibration value over the course of the measurement. Utilizing a synchronization signal from the cryostat coldhead signalling the beginning of a new coldhead movement period, we can average this data with respect to time in the cryostat cycle, see Fig. 6.10(c). The square root of the integrated noise power for the full dataset is plotted in Fig. 6.10(d). There are several frequencies up to ~ 26 kHz that contribute significantly to the observed vibrations. The multitude of peaks above the resonance frequency of our cavity piezos (~ [2 - 4] kHz) make active cavity stabilization hard in practice. We therefore operate the cavity free-running during all measurements, only correcting for slow drift by stabilizing the cavity to the excitation laser every ~ (10 - 20) seconds.

INFLUENCE ON FLUORESCENCE COUNTS AND LIFETIMES

As discussed in App. 6.8.3, cavity length fluctuations influence the collected counts and detected lifetime from an NV center. In the case of resonant excitation and PSB detection, both the excitation probability, and the Purcell enhancement, depend on the cavity detuning at a given time. To probe this dependence, we utilize a synchronization sig-

nal from the cryostat coldhead that marks the beginning of a new period, and use it to record the time in the cryostat period that a NV center photon is detected. We assign NV center photon arrival timestamps to periods in the cryostat with low (orange shaded area in Fig. 6.10(c)) and high vibration values (blue shaded area in Fig. 6.10(c)). We can then extract the vibration influence on counts and corresponding excited state lifetime, see Fig. 6.11. During the cryostat times with low vibrations, we extract a NV center lifetime (counts per excitation pulse) of (9.77 ± 0.08) ns ($[5.8 \pm 0.2] \times 10^{-4}$), compared to (10.02 ± 0.12) ns ($[2.5 \pm 0.1] \times 10^{-4}$) during high vibration times. In comparison, the lifetime (counts) over all cryostat times is (9.87 ± 0.04) ns ($[4.7 \pm 0.2] \times 10^{-4}$). This serves as a further proof that it is indeed Purcell enhancement through coupling to a cavity that leads to a lifetime reduction and increase in counts of the NV center when the cavity frequency is tuned to the NV center transition frequency. Additionally, it also shows that reducing the vibrations in a future system increases Purcell enhancement, as discussed in App. 6.8.6 below. We average over all cryostat period times in the measurements in this study, except if stated otherwise.

6.8.6. Current challenges and future improvements

In Sec. 6.6, we measured the absolute counts from an NV center in the cavity in both the PSB and the ZPL under resonant excitation. It is helpful to understand the loss contributions which prevent perfect PSB and ZPL detection. In this way, we can project what improvements may be possible with future upgrades to the setup. The investigations in this section underlie the loss plot in Fig. 6.5(b).

Vibrations

First, we estimate the effect of vibrations on cavity coupling and enhancement. In our model in App. 6.8.3, the vibrations reduce three parameters: the excitation probability of the NV center, the ZPL fraction emitted into the cavity, and the collection efficiency of the cavity. These effects are correlated, because the vibrations are slow (~ ms timescale) compared to the excitation and emission timescales of the NV center (~ ns timescale). Only the excitation probability of the NV center has a notable contribution to the PSB counts, as the fraction into the PSB is only slightly decreased for our cavity, and the PSB is not collected resonantly with the cavity.

From the data in Fig. 6.4(b) and Fig. 6.5(a), we determine that $(7.0 \pm 3.4)\%$ of the emission goes into the ZPL path, and we excite and detect ZPL photons with a probability of $(9.3 \pm 0.2) \times 10^{-5}$. If we set the vibration level to zero in our model, we find that 17% is emitted into the ZPL, and 1.7×10^{-3} ZPL photons are collected. Thus, the total reduction of ZPL collection and excitation due to vibrations is 13 dB. Because these reductions are correlated, we distribute the vibration contributions to the losses in Fig. 6.5(b) according to the relative contribution to the $P^{5/2}$ term in eq. 6.15.

Collection efficiency

We divide the ZPL collection efficiency into two parts: internal collection efficiency and external collection efficiency ($\eta_{zpl} = \eta_{int}\eta_{ext}$). The external collection efficiency is the coupling between the mode exiting the cavity and the detector, and is determined by the classical optics in between. Internal collection efficiency is the probability that a photon escapes the cavity and couples into the free space mode.

The internal efficiency, η_{int}, can be estimated using the measured transmission rate of the free space mirror, κ_{FS}, as $\eta_{int} = \kappa_{FS}/\kappa$. We design κ_{FS} to be significantly larger than the fiber transmission and scattering loss rates. However, the angle of the fiber forced us to operate in a regime where diffraction losses contributed significantly to the cavity finesse (which can be readily overcome with a new fiber). Therefore, in this work we operated with η_{int} in the range of 0.05 - 0.17, which also includes a factor of ∼ 1/3 from vibrations.

To measure the external collection efficiency, we send classical light through the fiber, and estimate the losses at each section between the fiber input and the detector. The loss to and from the cavity, probed in the fiber in reflection, is approximately -12.4 dB, including the fiber connector and fiber splice twice, and the reflection off the cavity once. Based on the depth of the reflection dip from the cavity, we estimate that we have a 2.8% incoupling efficiency. Based on the design values of our mirrors, we expect 2.5% incoupling from the fiber side, which is in reasonable agreement, and suggests that there is not a large mode mismatch between the cavity and the fiber. For a measurement of the transmitted light, we filter the input laser beam with a 20 dB filter and measure counts on an APD in the ZPL path. Subtracting out the light lost in the excitation path, we estimate that the total collection efficiency is 4%. This is likely divided into ∼ 11% internal collection efficiency and ∼ 32% external collection efficiency, but the precise contributions are not known. The external efficiency is determined by classical optics and the detector efficiency, so we expect that the external efficiency can also be improved in future experiments with better coatings and superconducting nanowire detectors.

We can also estimate the collection efficiency of the PSB path to make full use of the direct comparison in counts between PSB and ZPL. This efficiency is relatively low in our setup, because we have a long working distance objective with a numerical aperture of 0.55 (App. 6.8.1 contains a full description of the optics path). Depending on the angle of the NV center dipole emission axis in our <100> sample, the collection is between 0.9% and 2.5%. There is likely a bias towards NV centers with a better coupled dipole, because they produce more collectable PSB counts, and thus are easier to spot when searching for NV centers. The top collecting mirror has a narrow stop band, which by design allows 83% of the PSB light through. We estimate 83% transmission through the path and 70% APD detection efficiency, but the exact values are unknown. Altogether we expect between 0.4% and 1.2% collection efficiency in the PSB.

Benchmarking with excitation probability correction

We can benchmark our system against other diamond collection optics such as solid immersion lenses. However, the state of the art in these systems is near perfect initialization and excitation of the NV center. Higher initialization can be achieved with an additional spin pumping laser and microwaves [22]. In our system we initialize with a green laser, which only has a limited probability of initializing into the $m_s = 0$ spin state. Furthermore, we do not saturate the initialization with green or the excitation with red, due to limited laser power, so it is hard to estimate the probability of excitation. One might expect a lower laser power requirement than for non-cavity NV systems, because the NV driving is enhanced by a factor of the finesse (∼ 2000). However, this is offset by losses in the fiber (∼ 0.24) and the low coupling efficiency into the cavity through the fiber mirror (∼ 0.025). The extended mode area in the fiber cavity compared to the mode

Improvement	Achieved in Refs.	Enhance-ment Factor	ZPL% Collec-tion	C	Excitation Power
Spin Pump / Reso-nant Repump	[22, 48]	20	0.2	0.08	1
20x Vibration Re-duction	[15, 52–54]	16	3	0.21	0.55
Finesse limited by mirror coatings (6000)	[40, 43]	3	9	0.64	0.18
Higher Finesse (11000)	[40, 43]	1.2	10	1.0	0.1
Diamond-like Mode	[40, 43, 44]	2	20	1.5	0.06

Table 6.2: Summary of suggested improvements to current diamond fiber-cavity. The first three upgrades represent improvements that have already been achieved in other systems, as indicated in the second column. Finesse would be limited by the mirror if achieved losses limit the finesse to significantly greater than 6000. The last two items have been achieved but not simultaneously with the other requirements. We give the resulting enhancement of the ZPL collected, the absolute fraction collected in the ZPL, the cooperativity and the relative decrease in the excitation power required.

6

of a high numerical aperture objective also reduces the driving (~ 0.01). In total, we require approximately a factor of 10 more power, which is consistent with the probability of excitation we observe. Therefore, the counts we observe are not directly comparable to state of the art.

We can instead use our calculations of the collection efficiencies to estimate the excitation probability based on the total counts we observe from the NV center in the PSB and the ZPL. First we use the ZPL counts; we expect that with perfect initialization the counts in the ZPL should be $F_P^{ZPL}\beta_0/(F_P^{ZPL}\beta_0+1) \times \eta_{int} \times \eta_{ext}$ or approximately 2.6×10^{-3} based on the results of Sec. 6.5 and Sec. 6.6. This corresponds to an excitation probability of 3%. For comparison, the PSB counts should be $(1-\beta_0)/(F_P^{ZPL}\beta_0+1)\eta_{psb}$. The estimated collection efficiency and measured counts give us an excitation probability between and 14% and 4% (with a bias towards the latter). This corresponds to between 0.6 and 2×10^{-3} counts in the ZPL with perfect initialization. The estimates show reasonable agreement, and exact determination of the different losses is left for future work. Even with the limited collection efficiency in this work, the ZPL counts we collect are comparable to state of the art when correcting for initialization and excitation probability.

Improvements

Based on the current challenges and our modelling, we suggest three improvements which should be possible in the short term, as summarized in Tab. 6.2. We constrain
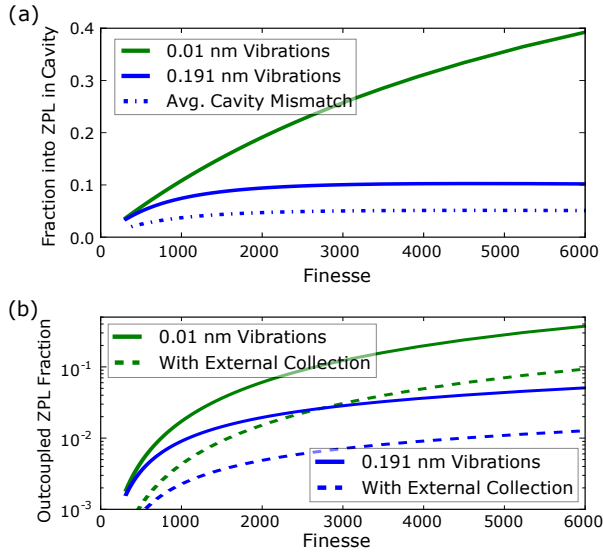
Figure 6.12: Projections for ZPL emission and collection fraction. We fix the design parameters of the mirrors to match our current system (Finesse 6200). Fraction emitted into the ZPL (a) and outcoupled fraction of photons in the ZPL (b) for the current (blue) and improved (green) vibration levels, as a function of achieved cavity finesse. These simulations are based on the model from Ref. [46].

ourselves to performances that have already been achieved in other systems. The first improvement is to implement microwave control of the ground state NV center spin, which will allow spin pumping and also yellow resonant repumping for higher initialization and even lower spectral diffusion. Using these techniques, it should be possible to achieve near unity excitation as has been shown in bulk diamond [22, 48].

The second improvement is to reduce vibrations; a number of research groups have achieved considerably lower vibrations of comparable fiber-based microcavities [15, 52–54]. In Fig. 6.12, we simulate the dependence of ZPL emission fraction and collection fraction on the finesse for different vibration levels. We project that a factor of 20 vibration levels reduction gains a factor of 16 in total ZPL collection.

The third improvement is increasing the finesse; our current finesse is limited by diffraction losses, but with a better fiber it should be limited by the mirror coatings, gaining another factor of 3. As indicated in Tab. 6.2, the laser power required to saturate the excitation of NV centers in the cavity should reduce by a factor of 5 after these improvements. Furthermore, the ZPL emission fraction is expected to increase by a factor 5, reducing the required polarization extinction by a factor of 25. Although it has not yet been achieved simultaneously, a diamond fiber-cavity with finesse 11000 diamond-like modes would further increase ZPL collection by approximately a factor of 2. Altogether we expect that about 10% ZPL collection should be possible with already achieved parameters and 20% with combining the best results from different setups. The improvements in the Purcell factor also correspond to an increase in the cooperativity, C, and there is a route to exceeding $C = 1$ with this approach.

REFERENCES

[1] M. Ruf, M. Weaver, S. van Dam and R. Hanson, *Resonant Excitation and Purcell Enhancement of Coherent Nitrogen-Vacancy Centers Coupled to a Fabry-Perot Microcavity,* Physical Review Applied **15,** 024049 (2021).

[2] H. J. Kimble, *The quantum internet,* Nature **453,** 1023 (2008).

[3] S. Wehner, D. Elkouss and R. Hanson, *Quantum internet : A vision for the road ahead,* Science **362,** 303 (2018).

[4] A. Ekert and R. Renner, *The ultimate physical limits of privacy,* Nature **507,** 443 (2014).

[5] N. H. Nickerson, J. F. Fitzsimons and S. C. Benjamin, *Freely scalable quantum technologies using cells of 5-to-50 qubits with very lossy and noisy photonic links,* Physical Review X **4,** 1 (2014).

[6] D. Gottesman, T. Jennewein and S. Croke, *Longer-baseline telescopes using quantum repeaters,* Physical Review Letters **109,** 1 (2012).

[7] C. T. Nguyen, D. D. Sukachev, M. K. Bhaskar, B. Machielse, D. S. Levonian, E. N. Knall, P. Stroganov, R. Riedinger, H. Park, M. Lončar and M. D. Lukin, *Quantum Network Nodes Based on Diamond Qubits with an Efficient Nanophotonic Interface,* Physical Review Letters **123,** 1 (2019).

[8] M. K. Bhaskar, R. Riedinger, B. Machielse, D. S. Levonian, C. T. Nguyen, E. N. Knall, H. Park, D. Englund, M. Lončar, D. D. Sukachev and M. D. Lukin, *Experimental demonstration of memory-enhanced quantum communication,* Nature **580,** 60 (2020).

[9] M. E. Trusheim *et al.*, *Transform-Limited Photons from a Coherent Tin-Vacancy Spin in Diamond,* Physical Review Letters **124,** 1 (2020).

[10] D. J. Christle *et al.*, *Isolated Spin Qubits in SiC with a High-Fidelity Infrared Spin-to-Photon Interface,* Physical Review X **7,** 021046 (2017).

[11] R. Nagy *et al.*, *High-fidelity spin and optical control of single silicon-vacancy centres in silicon carbide,* Nature Communications **10,** 1954 (2019).

[12] A. Bourassa, C. P. Anderson, K. C. Miao, M. Onizhuk, H. Ma, A. L. Crook, H. Abe, J. Ul-Hassan, T. Ohshima, N. T. Son, G. Galli and D. D. Awschalom, *Entanglement and control of single nuclear spins in isotopically engineered silicon carbide,* Nature Materials **19,** 1319 (2020).

[13] M. Raha, S. Chen, C. M. Phenicie, S. Ourari, A. M. Dibos and J. D. Thompson, *Optical quantum nondemolition measurement of a single rare earth ion qubit,* Nature Communications **11,** 1 (2020).

[14] J. M. Kindem, A. Ruskuc, J. G. Bartholomew, J. Rochman, Y. Q. Huan and A. Faraon, *Control and single-shot readout of an ion embedded in a nanophotonic cavity,* Nature **580**, 201 (2020).

[15] B. Merkel, A. Ulanowski and A. Reiserer, *Coherent and Purcell-Enhanced Emission from Erbium Dopants in a Cryogenic High-Q Resonator,* Physical Review X **10**, 041025 (2020).

[16] A. Delteil, Z. Sun, W. B. Gao, E. Togan, S. Faelt and A. Imamoglu, *Generation of heralded entanglement between distant hole spins,* Nature Physics **12**, 218 (2016).

[17] R. Stockill, M. J. Stanley, L. Huthmacher, E. Clarke, M. Hugues, A. J. Miller, C. Matthiesen, C. Le Gall and M. Atatüre, *Phase-Tuned Entangled State Generation between Distant Spin Qubits,* Physical Review Letters **119**, 1 (2017).

[18] S. Ritter, C. Nölleke, C. Hahn, A. Reiserer, A. Neuzner, M. Uphoff, M. Mücke, E. Figueroa, J. Bochmann and G. Rempe, *An elementary quantum network of single atoms in optical cavities,* Nature **484**, 195 (2012).

[19] J. Hofmann, M. Krug, N. Ortegel, L. Gérard, M. Weber, W. Rosenfeld and H. Weinfurter, *Heralded Entanglement Between Widely Separated Atoms,* Science **337**, 72 (2012).

[20] D. Hucul, I. V. Inlek, G. Vittorini, C. Crocker, S. Debnath, S. M. Clark and C. Monroe, *Modular entanglement of atomic qubits using photons and phonons,* Nature Physics **11**, 37 (2015).

[21] L. J. Stephenson, D. P. Nadlinger, B. C. Nichol, S. An, P. Drmota, T. G. Ballance, K. Thirumalai, J. F. Goodwin, D. M. Lucas and C. J. Ballance, *High-Rate, High-Fidelity Entanglement of Qubits Across an Elementary Quantum Network,* Physical Review Letters **124**, 1 (2020).

[22] H. Bernien, B. Hensen, W. Pfaff, G. Koolstra, M. S. Blok, L. Robledo, T. H. Taminiau, M. Markham, D. J. Twitchen, L. Childress and R. Hanson, *Heralded entanglement between solid-state qubits separated by three metres,* Nature **497**, 86 (2013).

[23] C. E. Bradley, J. Randall, M. H. Abobeih, R. C. Berrevoets, M. J. Degen, M. A. Bakker, M. Markham, D. J. Twitchen and T. H. Taminiau, *A Ten-Qubit Solid-State Spin Register with Quantum Memory up to One Minute,* Physical Review X **9**, 31045 (2019).

[24] N. Kalb, A. A. Reiserer, P. C. Humphreys, J. J. Bakermans, S. J. Kamerling, N. H. Nickerson, S. C. Benjamin, D. J. Twitchen, M. Markham and R. Hanson, *Entanglement distillation between solid-state quantum network nodes,* Science **356**, 928 (2017).

[25] P. C. Humphreys, N. Kalb, J. P. Morits, R. N. Schouten, R. F. Vermeulen, D. J. Twitchen, M. Markham and R. Hanson, *Deterministic delivery of remote entanglement on a quantum network,* Nature **558**, 268 (2018).

[26] B. Hensen *et al.*, *Loophole-free Bell inequality violation using electron spins separated by 1.3 kilometres,* Nature **526**, 682 (2015).

6

[27] A. Faraon, C. Santori, Z. Huang, V. M. Acosta and R. G. Beausoleil, *Coupling of nitrogen-vacancy centers to photonic crystal cavities in monocrystalline diamond,* Physical Review Letters **109**, 2 (2012).

[28] B. J. Hausmann *et al.*, *Coupling of NV centers to photonic crystal nanobeams in diamond,* Nano Letters **13**, 5791 (2013).

[29] L. Li *et al.*, *Coherent spin control of a nanocavity-enhanced qubit in diamond,* Nature Communications **6**, 6173 (2015).

[30] J. Riedrich-Möller, S. Pezzagna, J. Meijer, C. Pauly, F. Mücklich, M. Markham, A. M. Edmonds and C. Becher, *Nanoimplantation and Purcell enhancement of single nitrogen-vacancy centers in photonic crystal cavities in diamond,* Applied Physics Letters **106**, 2 (2015).

[31] T. Schröder, M. Walsh, J. Zheng, S. Mouradian, L. Li, G. Malladi, H. Bakhru, M. Lu, A. Stein, M. Heuck and D. Englund, *Scalable fabrication of coupled NV center - photonic crystal cavity systems by self-aligned N ion implantation,* Optical Materials Express **7**, 1514 (2017).

[32] T. Jung, J. Görlitz, B. Kambs, C. Pauly, N. Raatz, R. Nelz, E. Neu, A. M. Edmonds, M. Markham, F. Mücklich, J. Meijer and C. Becher, *Spin measurements of NV centers coupled to a photonic crystal cavity,* APL Photonics **4**, 120803 (2019).

[33] A. Faraon, P. E. Barclay, C. Santori, K. M. C. Fu and R. G. Beausoleil, *Resonant enhancement of the zero-phonon emission from a colour centre in a diamond cavity,* Nature Photonics **5**, 301 (2011).

[34] D. Riedel, I. Söllner, B. J. Shields, S. Starosielec, P. Appel, E. Neu, P. Maletinsky and R. J. Warburton, *Deterministic enhancement of coherent photon generation from a nitrogen-vacancy center in ultrapure diamond,* Physical Review X **7**, 1 (2017).

[35] S. Johnson, P. R. Dolan, T. Grange, A. A. P. Trichet, G. Hornecker, Y. C. Chen, L. Weng, G. M. Hughes, A. A. R. Watt, A. Auffèves and J. M. Smith, *Tunable cavity coupling of the zero phonon line of a nitrogen-vacancy defect in diamond,* New Journal of Physics **17**, 122003 (2015).

[36] S. B. Van Dam, M. Walsh, M. J. Degen, E. Bersin, S. L. Mouradian, A. Galiullin, M. Ruf, M. Ijspeert, T. H. Taminiau, R. Hanson and D. R. Englund, *Optical coherence of diamond nitrogen-vacancy centers formed by ion implantation and annealing,* Physical Review B **99**, 161203 (2019).

[37] M. Kasperczyk, J. A. Zuber, A. Barfuss, J. Kölbl, V. Yurgens, S. Flågan, T. Jakubczyk, B. Shields, R. J. Warburton and P. Maletinsky, *Statistically modeling optical linewidths of nitrogen vacancy centers in microstructures,* Physical Review B **102**, 075312 (2020).

[38] M. Ruf, M. IJspeert, S. Van Dam, N. De Jong, H. Van Den Berg, G. Evers and R. Hanson, *Optically Coherent Nitrogen-Vacancy Centers in Micrometer-Thin Etched Diamond Membranes,* Nano Letters **19**, 3987 (2019).

6

[39] E. Janitz, M. Ruf, M. Dimock, A. Bourassa, J. Sankey and L. Childress, *Fabry-Perot microcavity for diamond-based photonics,* Physical Review A **92**, 1 (2015).

[40] S. Bogdanović, S. B. van Dam, C. Bonato, L. C. Coenen, A.-M. J. Zwerver, B. Hensen, M. S. Z. Liddy, T. Fink, A. Reiserer, M. Lončar and R. Hanson, *Design and low-temperature characterization of a tunable microcavity for diamond-based quantum networks,* Applied Physics Letters **110**, 171103 (2017).

[41] S. Bogdanović, M. S. Z. Liddy, S. B. van Dam, L. C. Coenen, T. Fink, M. Lončar and R. Hanson, *Robust nano-fabrication of an integrated platform for spin control in a tunable microcavity,* APL Photonics **2**, 126101 (2017).

[42] S. Häußler, J. Benedikter, K. Bray, B. Regan, A. Dietrich, J. Twamley, I. Aharonovich, D. Hunger and A. Kubanek, *Diamond photonics platform based on silicon vacancy centers in a single-crystal diamond membrane and a fiber cavity,* Physical Review B **99**, 1 (2019).

[43] R. Høy Jensen, E. Janitz, Y. Fontana, Y. He, O. Gobron, I. P. Radko, M. Bhaskar, R. Evans, C. D. Rodríguez Rosenblueth, L. Childress, A. Huck and U. Lund Andersen, *Cavity-Enhanced Photon Emission from a Single Germanium-Vacancy Center in a Diamond Membrane,* Physical Review Applied **13**, 064016 (2020).

[44] M. Salz, Y. Herrmann, A. Nadarajah, A. Stahl, M. Hettrich, A. Stacey, S. Prawer, D. Hunger and F. Schmidt-Kaler, *Cryogenic platform for coupling color centers in diamond membranes to a fiber-based microcavity,* Applied Physics B **126**, 131 (2020).

[45] D. Hunger, T. Steinmetz, Y. Colombe, C. Deutsch, T. W. Hänsch and J. Reichel, *A fiber Fabry–Perot cavity with high finesse,* New Journal of Physics **12**, 065038 (2010).

[46] S. B. van Dam, M. Ruf and R. Hanson, *Optimal design of diamond-air microcavities for quantum networks using an analytical approach,* New Journal of Physics **20**, 115004 (2018).

[47] D. Riedel, S. Flågan, P. Maletinsky and R. J. Warburton, *Cavity-Enhanced Raman Scattering for in situ Alignment and Characterization of Solid-State Microcavities,* Physical Review Applied **13**, 1 (2020).

[48] L. Robledo, L. Childress, H. Bernien, B. Hensen, P. F. A. Alkemade and R. Hanson, *High-fidelity projective read-out of a solid-state spin quantum register,* Nature **477**, 574 (2011).

[49] N. Kalb, P. C. Humphreys, J. J. Slim and R. Hanson, *Dephasing mechanisms of diamond-based nuclear-spin memories for quantum networks,* Physical Review A **97**, 1 (2018).

[50] H. Bernien, L. Childress, L. Robledo, M. Markham, D. Twitchen and R. Hanson, *Two-Photon Quantum Interference from Separate Nitrogen Vacancy Centers in Diamond,* Physical Review Letters **108**, 043604 (2012).

6

[51] L. Robledo, H. Bernien, I. Van Weperen and R. Hanson, *Control and coherence of the optical transition of single nitrogen vacancy centers in diamond,* Physical Review Letters **105**, 1 (2010).

[52] B. Casabone, C. Deshmukh, S. Liu, D. Serrano, A. Ferrier, T. Hümmer, P. Goldner, D. Hunger and H. de Riedmatten, *Dynamic control of Purcell enhanced emission of erbium ions in nanoparticles,* Nature Communications **12**, 1 (2021).

[53] L. Greuter, S. Starosielec, D. Najer, A. Ludwig, L. Duempelmann, D. Rohner and R. J. Warburton, *A small mode volume tunable microcavity: Development and characterization,* Applied Physics Letters **105**, 121105 (2014).

[54] J. F. S. Brachmann, H. Kaupp, T. W. Hänsch and D. Hunger, *Photothermal effects in ultra-precisely stabilized tunable microcavities,* Optics Express **24**, 21205 (2016).

[55] E. Janitz, M. Ruf, Y. Fontana, J. Sankey and L. Childress, *High mechanical bandwidth fiber-coupled Fabry-Perot cavity,* Optics Express **25**, 20932 (2017).

[56] G. Murta, S. B. van Dam, J. Ribeiro, R. Hanson and S. Wehner, *Towards a realization of device-independent quantum key distribution,* Quantum Science and Technology **4**, 035011 (2019).

[57] F. Rozpędek, R. Yehia, K. Goodenough, M. Ruf, P. C. Humphreys, R. Hanson, S. Wehner and D. Elkouss, *Near-term quantum-repeater experiments with nitrogen-vacancy centers: Overcoming the limitations of direct transmission,* Physical Review A **99**, 052330 (2019).

[58] A. Reiserer and G. Rempe, *Cavity-based quantum networks with single atoms and optical photons,* Reviews of Modern Physics **87**, 1379 (2015).

[59] M. W. Doherty, N. B. Manson, P. Delaney, F. Jelezko, J. Wrachtrup and L. C. L. Hollenberg, *The nitrogen-vacancy colour centre in diamond,* Physics Reports **528**, 1 (2013).

[60] J. Borregaard, A. S. Sørensen and P. Lodahl, *Quantum Networks with Deterministic Spin–Photon Interfaces,* Advanced Quantum Technologies **2**, 1800091 (2019).

[61] M. L. Goldman, A. Sipahigil, M. W. Doherty, N. Y. Yao, S. D. Bennett, M. Markham, D. J. Twitchen, N. B. Manson, A. Kubanek and M. D. Lukin, *Phonon-Induced Population Dynamics and Intersystem Crossing in Nitrogen-Vacancy Centers,* Physical Review Letters **114**, 145502 (2015).

[62] C. Kurtsiefer, S. Mayer, P. Zarda and H. Weinfurter, *Stable solid-state source of single photons,* Physical Review Letters **85**, 290 (2000).

[63] G. Waldherr, J. Beck, M. Steiner, P. Neumann, A. Gali, T. H. Frauenheim, F. Jelezko and J. Wrachtrup, *Dark states of single nitrogen-vacancy centers in diamond unraveled by single shot NMR,* Physical Review Letters **106**, 1 (2011).

[64] N. Aslam, G. Waldherr, P. Neumann, F. Jelezko and J. Wrachtrup, *Photo-induced ionization dynamics of the nitrogen vacancy defect in diamond investigated by single-shot charge state detection,* New Journal of Physics **15**, 013064 (2013).

7

DESIGN AND OPTIMIZATION OF PHOTONIC CRYSTAL CAVITIES

Future quantum networks require nodes that feature a combination of excellent spin coherence properties and an efficient spin-photon interface with good optical coherence. The first order insensitivity of group-IV color centers in diamond to electric fields makes these defect centers suitable for integration into nanophotonic cavities, with a potential for reaching high coherent cooperativities of the emitter-cavity system. Here, we give a brief introduction to the different properties of group-IV color centers and NV centers, to the state of the art of group-IV based quantum networks, and to the theory behind employed photonic crystal cavities. We present a workflow that optimizes structures numerically for highest Purcell enhancement, and discuss the robustness of optimized photonic crystal cavity designs to real-world fabrication imperfections. Finally, we outline a method to efficiently couple to nanophotonic structures using tapered optical fibers and waveguides. Coherent quantum emitters in nanofabricated structures could be a key building block of scalable quantum networks.

7.1. INTRODUCTION

A promising way to improve the spin-photon interface of color centers in diamond is to embed them into optical cavities with high quality factor to mode volume ratio; this allows to reach large coherent cooperativities, potentially enabling near-deterministic spin-photon gates (see Ch. 3). Group-IV color centers in diamond are particular suitable for these tasks, as their first order insensitivity to electric field fluctuations results in close-to-lifetime limited optical transition linewidths of the color center even when close to surfaces [2–4]. In this chapter, we discuss the differences between group-IV color centers and NV centers, the state of the art of group-IV color center based quantum networks, and the design and optimization of all-diamond photonic crystal cavities.

This chapter is organized as follows: Sec. 7.2 gives an introduction to the optical and spin properties of color centers in diamond, focusing in particular on group-IV color centers. In Sec. 7.3, we introduce the state of the art of group-IV color center based quantum networks, highlighting the potential of a strong coupling of the color center to a nanophotonic cavity or waveguide. Sec. 7.4 then introduces the fundamental working principles behind photonic crystal cavities, before a routine to optimize photonic crystal cavities for large color center - cavity cooperativities is discussed in Sec. 7.5. Sec. 7.5 also shows the effects of real-world fabrication imperfections on the designed structures. Finally, a strategy to efficiently couple to nanophotonic cavities is presented in Sec. 7.6.

7.2. OPTICAL AND SPIN PROPERTIES OF COLOR CENTERS IN DIAMOND*

Nitrogen-vacancy and group-IV color centers in diamond feature different structural symmetries, which result in different properties of their spin-photon interface. Here, we briefly introduce the most important differences between those color centers in diamond, to the point necessary to understand why the recent emergence of group-IV color centers has revived the field of integration of color centers in all-diamond cavities; we refer the reader to the many excellent articles that cover the physics of these color centers in great detail [5–7]. Here, we consider all color centers to be in the negative charge state, except where indicated differently; this negative charge state is the one most commonly studied and used in experiments geared towards entanglement generation.

Fig. 7.1 shows the difference in atomic structure of nitrogen-vacancy (NV) centers and group-IV color centers (consisting of silicon-vacancy (SiV) [8–10], germanium-vacancy (GeV) [11], tin-vacancy (SnV) [12, 13] and lead-vacancy (PbV) [14] centers). As discussed in Ch. 2, an NV center is formed by a nitrogen atom replacing a carbon atom of the diamond lattice, next to a lattice vacancy, giving rise to a C_{3v} symmetry [Fig. 7.1(a)]. The NV center possesses a permanent electric dipole moment, making the optical transition frequencies sensitive to charge fluctuations in its environment [5]. This sensitivity to electric fields has been used as a resource to tune different NV centers onto resonance [15], counteracting local strain inhomogeneities in the host diamond crystal which shift the transition frequencies of color centers. However, it has also hindered the nanophotonic integration of NV centers due to degradation of their optical properties near surfaces [16, 17], as discussed in detail in Ch. 3.

For group-IV color centers, the group-IV atom takes an interstitial lattice site be-
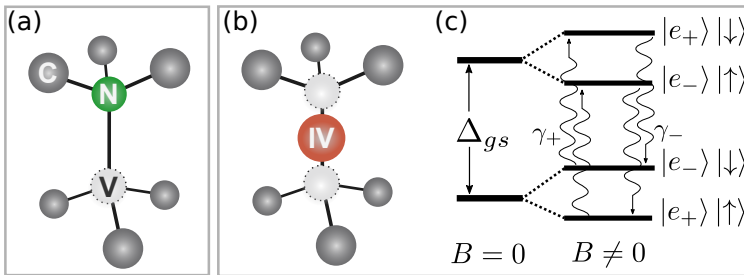
Figure 7.1: Schematic atomic structure of NV (a) and group-IV (b) color centers in diamond and ground state level structure of group-IV color centers (c). The inversion symmetry of group-IV color centers leads to a vanishing permanent electric dipole moment, making those defect centers suitable for integration in nanophotonic structures. This structure also results in orbital and spin double degeneracies in the ground and excited state (c, only ground state shown for simplicity) that are lifted by (mostly) spin-orbit coupling (Δ_{gs}) and by application of an external magnetic field (B), respectively. Phonon-induced transitions (γ_+ / γ_-) between orbital states limit (communication) qubit coherence times (see text).

tween two lattice vacancies. The resulting inversion-symmetric D_{3_d} structure of the defect [Fig. 7.1(b)] results in no permanent electric dipole and thus a first-order insensitivity to electric field fluctuations. As a consequence, tuning optical transition frequencies of group-IV color centers by electric fields is relatively inefficient [18, 19], potentially necessitating other techniques. On the other hand, the vanishing permanent electric dipole makes these color centers excellent candidates for integration into photonic nanostructures (discussed in Sec. 7.3 below).

Group-IV emitters also feature a different level structure than the NV center: both optical ground and excited states are formed by doubly-degenerate orbital states, which are each split into pairs by spin-orbit interaction and the Jahn-Teller effect. Under an external magnetic field, the double spin degeneracy in each pair ($S = 1/2$) is lifted [6, 8, 20]. The qubit subspace can then for example be defined over the two opposing spin sublevels of the optical ground state's lower orbital branch [see Fig. 7.1(c)]. This, however, means that direct microwave driving of the qubit levels is forbidden in first order, as one would need to flip both spin and orbital quantum numbers. Typically, this complication is overcome by working with emitters with transversal strain $\sim \Delta_{gs}$, which mixes the orbital levels, such that the qubit state can be effectively described by the spin only and thus be driven with higher efficiency [10]. Coherent microwave control of group-IV color centers has recently been demonstrated for SiV centers [10, 21], with infidelities on the percent level [21]. For other group-IV color centers, only incoherent microwave driving of spin transitions has been achieved so far [11, 13]. The reported infidelities for coherent SiV control are a result of qubit dephasing during microwave pulses, as relatively low Rabi frequencies ($\sim$ 10 MHz) are used to limit heating-induced decoherence. It is expected that the use of superconducting waveguides [22] will further improve microwave pulse fidelities (as a result of potentially significantly reduced ohmic heating) for all color centers.

Spin dephasing in the group-IV qubit subspace is dominated by phonon-assisted transitions to the upper ground state orbital branch, which leads to the acquisition of a random phase: while the phonon transitions are in principle spin-conserving, the

Vacancy	ZPL WL [nm]	Quantum efficiency [%]	Debye-Waller factor	Radiative Lifetime [ns]	Ground state splitting [GHz]	T_{oper} [K]
SiV	737 [23]	(1 − 10) [2, 24] 60 [26]	(0.65 − 0.9) [27, 28]	1.7 [2, 25]	50 [8, 9, 25]	0.1
GeV	602 [29]	(12 − 25) [30, 31]	∼ 0.6 [11]	(1.4 − 6) [3, 29]	170 [11]	0.4
SnV	620 [13]	∼ 80 [12]	0.57 [32]	(4.5 − 7) [13, 33, 34]	850 [12, 13]	1.8
PbV	520 [14] / 555 [35–37]	not known	not known	> 3 [14] / 3.5 [35–37]	5700 [14] / 3900 [37]	9.8 / 7.0
NV	637 [5]	> 85 [38]	0.03 [39, 40]	(11 − 13) [39, 41, 42]	n. a.	n. a.

Table 7.1: Overview of optical and orbital properties of group-IV (SiV, GeV, SnV, PbV) and NV defect centers in diamond. All listed numbers are approximate values. We consider all defects to be in the negative charge state. The Debye-Waller Factor characterizes the fraction of radiative emission into the ZPL, while we define the quantum efficiency as the ratio of radiative to all decay. Ground state splitting denotes splitting between orbital states in the optical ground state of group-IV color centers (see Fig. 7.1(c) and text). T_{oper} is the calculated operation temperature below which the expected orbital lifetime is above 100 ms. We estimate this temperature by calculating the phonon transition rate $\gamma_+ \propto \Delta_{gs}^3/(e^{(\Delta_{gs/k_b T)}} − 1)$ [see Fig. 7.1(c)], where Δ_{gs} is the orbital ground state splitting, T is the temperature, and k_B the Boltzmann constant (as $\gamma_- > \gamma_+$, γ_+ determines the qubit coherence times), as in Refs. [12, 13]. We then find the proportionality factor to map this to a concrete temperature by using the measured values of Ref. [9]. We note that there are currently different findings about the exact parameters for the lead vacancy center in diamond. We therefore include two pairs of values with their respective references.

7

detuning between the spin states varies depending on which orbital state is occupied, see Fig. 7.1(c) [43, 44]. In Tab. 7.1, we map reported ground state splittings into a concrete performance metric by extrapolating the temperatures T_{oper} below which we expect an orbital coherence time > 100 ms due to low phonon occupation. From this, we see that a larger ground state splitting (associated with stronger spin-orbit coupling strengths for heavier ions) is beneficial for maintaining long qubit coherence. However, this requires higher microwave driving powers for similar off-axis strain values, as the strain-induced orbital mixing is related to the spin-orbit coupling strength, and thus the overlap between orbital states is reduced [10]. All-optical spin control schemes represent an alternative to microwave driving, as demonstrated e.g. for SiV [25, 45, 46] and GeV [11] centers. For SnV centers, spin initialization by optical pumping has been observed [13]. Another way of defining and driving a qubit could be to mix the (mostly) orthogonal spin components via an off-axis magnetic field, and use surface acoustic waves to drive phonon transitions between the orbital levels, with demonstrated Rabi frequencies ∼ 30 MHz [47]. Such an off-axis magnetic field, however, is at odds with achieving the high spin cyclicity needed for single shot spin state readout and high fidelity entanglement generation, necessitating a careful tradeoff [10]. For magnetic fields aligned with the color center's symmetry axis, readout fidelities above 99.99% have been achieved [21, 48].

Tab. 7.1 also shows a comparison of the most important optical properties for both group-IV color centers and nitrogen-vacancy centers in diamond. To generate entanglement, only the fraction of coherent photons emitted in the zero-phonon-line (ZPL, for which no lattice vibrations assist the transition [5]) can be used [49]. Importantly,

all quantified zero-phonon-line emission fractions for group-IV color centers are significantly larger than for the NV center, as the inversion symmetry of these emitters causes their excited states to have greater overlap with the optical ground state [20], resulting in a higher fraction of direct photon transitions [50, 51]. While most recent quantum memory experiments with SiV centers have operated in dilution refrigerators (see below) in order to suppress thermal phonon population [21, 46], the SnV center with relatively high expected operating temperature requirements might be particularly promising for use as quantum network node. We note that the neutral charge state variants of group-IV color centers are also promising, as they potentially combine the favorable spin-photon interface of negative group-IV color centers with the excellent spin coherence times and easy qubit manipulation of negative nitrogen vacancy centers [20, 52–55]. We do not discuss it extensively here due to its early stage of study.

7.3. State of the art of group-IV color center based quantum networks*

The first-order electric field insensitivity of group-IV color centers in diamond [4, 13, 14, 20, 29, 33, 56–58] has enabled the demonstration of close-to-lifetime limited optical transitions even in heavily fabricated nanophotonic structures [2–4, 10, 57, 59]. To date, photonic crystal cavity coupling of group-IV color centers in diamond at low temperatures has been demonstrated for SiV [2, 10, 23, 48, 60] and SnV centers [34], with demonstrated $C_{coh} > 100$ for the case of the SiV center [23].

Fig. 7.2(a) shows a schematic of a SiV center embedded in a photonic crystal cavity. Spin-photon entanglement with fidelity $\geq$ 94 % has been generated in this system using cavity quantum electrodynamics (cQED) reflection-based schemes, in which photons impinging on the cavity containing the communication qubit are reflected or transmitted depending on the spin-state of the communication qubit [48]. This also enables high fidelity single shot spin state readout with demonstrated fidelities > 99.9% [see Fig. 7.2(b,c)].

While entanglement between distant SiV centers has not yet been demonstrated, strong collective interactions between two SiV centers [60] in the same cavity and probabilistic entanglement generation between two SiVs [2, 61] in one waveguide have been observed. In addition, photon outcoupling efficiencies from the emitter-cavity system into fiber > 0.9 have enabled the demonstration of memory-enhanced quantum communication [23]. This experiment sets the state of the art for quantum repeater experiments.

Additionally, recent experiments have demonstrated key quantum network node capabilities, including dynamical decoupling of the SiV spin from the bath with coherence times above 1 ms [21, 62], ^{13}C nuclear spin initialization, control, and readout via the central SiV electron spin [10, 63], and frequency control of SiV centers via strain tuning [59, 61, 64]. Combined with recent efforts to fabricate SiV centers in nanophotonic waveguides at a large scale and their integration in photonic circuits [59], these results show the potential of silicon-vacancy centers and other closely related group-IV color centers as nodes for a quantum network.
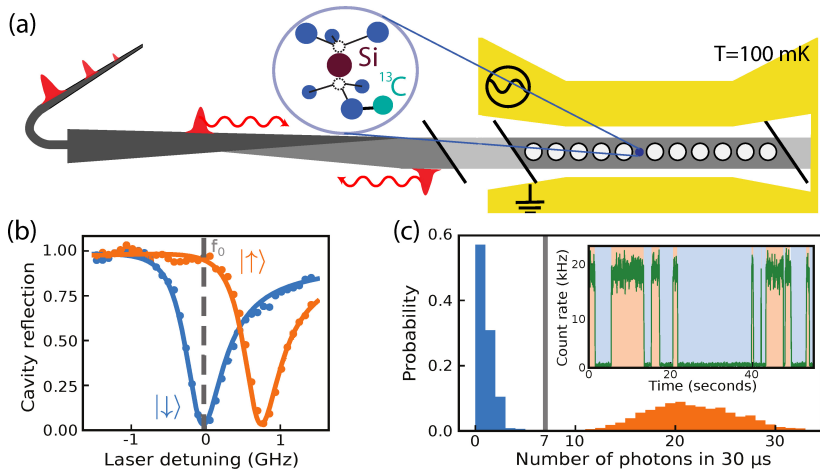
Figure 7.2: State-of-the-art research showing the potential of group-IV color centers in diamond as quantum network nodes. (a) Schematic of a silicon-vacancy (SiV) center (blue circle) embedded in a fiber-coupled (dark grey) all-diamond photonic crystal cavity (light grey area with holes). Coherent emitter-cavity cooperativities ~ 100 have enabled high-fidelity reflection-based spin-photon entanglement generation [23], and control of individual ^{13}C nuclear spins via microwave pulses applied to the electron spin of the silicon vacancy spin qubit (yellow electrodes) has been demonstrated [48]. Figure adapted with permission from Ref. [48]. Copyright (2019) by the American Physical Society. (b) Spin-state dependent reflection spectrum of a SiV center in a critically coupled photonic crystal cavity with C_{coh} ~ 100. The spin-state dependent photon reflection with high collection efficiency enables spin-state readout with fidelity > 99.9 % in a single shot (c), and has recently enabled the first demonstration of memory-enhanced quantum communication [23]. Figures (b) and (c) are adapted with permission from Ref. [23].

7

7.4. PHOTONIC CRYSTAL CAVITY DESIGN

Having discussed the state of the art of group-IV color center based quantum networks, which are in large parts enabled by strong coupling of the emitter to a photonic crystal cavity, we now move on to introduce the working principles behind such cavities.

In a photonic crystal, the propagation of electromagnetic waves is altered from propagation through a homogeneous bulk dielectric material by a periodic dielectric material variation. For periodic variations on the scale of the wavelength of the electromagnetic waves, this can lead to destructive interference for certain frequencies. These wavelength ranges are called bandgaps, and can serve as a mirror for light, in complete analogy to the macroscopic Bragg mirrors employed in Ch. 6. In this chapter, we will design structures that confine a single allowed optical mode in between two bandgap generating regions, forming an optical cavity with wavelength-scale mode volume. Here, we will only give a brief, high-level introduction, as necessary to understand the most important aspects. For this, we follow the excellent discussions in Refs. [65, 66]. For a detailed introduction to the topic of photonic crystals, including a full mathematical treatment, see Refs. [67, 68].

7.4.1. BANDSTRUCTURE ENGINEERING VIA UNIT CELL DESIGN

According to Bloch's theorem, the solutions to Maxwell's equations that govern the propagation of electromagnetic waves are given as a plane wave modified by a periodic function, given the dielectric material these waves propagate in is periodic; such a material is called a photonic crystal. Assuming an infinite extension of a photonic crystal, one can restrict to solving Maxwell's equation for a single unit cell of this crystal only. Here, a unit cell is the smallest building block of the material that can describe the full structure when using symmetries. The solutions then describe all electromagnetic wave propagation. In this work, we solve this using an iterative minimization algorithm implemented in COMSOL®.

Let us take the concrete example of a rectangular photonic crystal (unit cell displayed in Fig. 7.3(a)), made from diamond (refractive index $n \sim 2.4$ at visible wavelengths) and surrounded by vacuum ($n = 1$). Holes that are placed periodically in the middle of the beam introduce a periodic modulation of the refractive index along the axis of the beam (which we assume along the x direction for the rest of this chapter).

The numerically computed band structure for parts of the irreducible unit cell for this structure can be seen in Fig. 7.3(b), with the simulation parameters listed in Tab. 7.2. Far away from the nanobeam, the allowed modes should be free space plane waves, which follow the dispersion relation $\omega = c|\mathbf{k}|$. Since the beam is only periodic in one direction, $\mathbf{k}$ is only bound for propagation *along* the beam ($k_{||}$ is conserved), while the perpendicular components of $\mathbf{k}$ can take any value. This effect gives rise to a continuum of modes above the light line, for which $\omega = ck_x$. These modes are called "radiation modes" and represent modes carrying energy away from the beam.

While the nanobeam in our example only shows translational periodicity along the x direction, a one dimensional nanobeam can still confine light along off-axial directions. At the interface between the diamond and air, conservation of ω and k_x (effectively Snell's law from ray optics) leads to the localization of modes in the diamond. These modes lie below the light line, due to the higher refractive index material of diamond compared to air. However, the perpendicular component of $\mathbf{k}$ is imaginary, which corresponds to modes that do not propagate in air but instead decay exponentially away from the nanobeam. These modes are called "index guided modes", and are localized modes along directions that do not feature translational symmetry of the unit cell. A non-zero coupling between guided and light cone modes means that for a structure with periodicity along one dimension only, no true bandgap exists.

In the case of Fig. 7.3(b), the red solid and blue dashed lines correspond to the allowed frequencies in the structure, which feature different reflection symmetries w.r.t. y and z planes in the middle of the beam. Bands of transverse electric modes (TE, even vector symmetry w.r.t. z reflection, no electric field along propagation direction) and transverse magnetic modes (TM, odd vector symmetry w.r.t. z reflection, no magnetic field along propagation direction) emerge. For the rectangular nanobeam considered in this work, a bandgap opens up between the two lowest lying TE modes (orange shaded region). Figs. 7.3(d,e) show the normalized electric field distribution in the unit cell along the propagation direction for $k_{||} = \pi/a$ for the lower and upper TE mode at the bandgap. One can see that the field is localized in the high index material for the lowest TE mode, which allows for maximal electric field overlap with the dipole of an emitter (e.g. a SnV
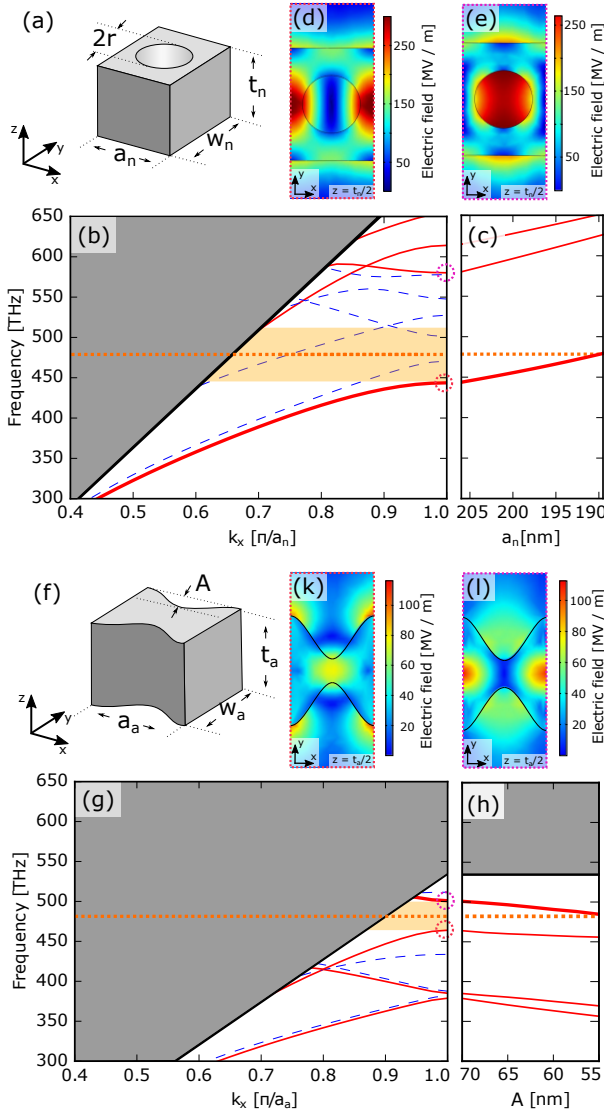
Figure 7.3: Photonic crystal nanobeam unit cell and corresponding bandstructure simulations. (a) Unit cell of a rectangular photonic crystal nanobeam in diamond, parametrized by hole radius, r, beam thickness, t_n, lattice period, a_n, and beam width, w_n. (b) Numerically obtained bandstructure for the irreducible Brillouin zone of the structure in (a) for light propagation along the x direction. The light line (black) divides the plot into a continuum of unguided modes (gray area), and a region in which discrete guided modes exist. These consist of transverse electric TE modes (red solid lines, no electric field along propagation direction) and transverse magnetic TM modes (blue dashed lines, no magnetic field along propagation direction). Orange shaded region highlights the fundamental bandgap of TE modes, for which no TE modes exist. (c) Lowest frequency TE mode in (b) as a function of lattice constant, a_n, at $k_x = \pi/a_n$, while keeping all other unit cell parameters constant. Reducing the lattice constant allows to raise the mode's frequency into the bandgap. Orange dashed line corresponds to targeted cavity frequency, matching the zero-phonon line emission frequency of tin vacancy defects in diamond. (d, e) Distribution of normalized electric field in the unit cell for the first TE (d) and second TE (e) modes at $k_x = \pi/a_n$. (f-l) show corresponding plots to (a-e), for an "alligator" style unit cell displayed in (f), parametrized by sinusoidal amplitude, A, beam thickness, t_a, lattice period, a_a, and beam width, w_a.

center) located in the diamond nanobeam (assuming perfect emitter placement and dipole direction).

To localize the fundamental TE mode in the bandgap (which offers highest electric field localization at the intended location of the emitter in the center of the beam), we introduce a perturbation in the lattice constant, which we explore in detail in Sec. 7.4.2. For now, we observe that by reducing the lattice constant, the lowest TE band shifts up in frequency at $k_{||} = \pi/a$, see Fig. 7.3(c). This can be understood intuitively from the fact

	Rectangular Nanobeam				Alligator Nanobeam			
Parameter	a_n	r	w_n	t_n	a_a	A	w_a	t_a
Value [nm]	206	71	275	230	280	70	185	230

Table 7.2: Unit cell parameter values used to simulate the rectangular and alligator nanobeam bandstructures displayed in Fig. 7.3. See Fig. 7.3 for a definition of parameters.

that a unit cell with reduced lattice constant features less high refractive index material. Thus, by introducing a perturbation in the middle of the bandgap generating structure, we can localize a single frequency mode in the photonic bandgap.

To show the universality of these concepts, Fig. 7.3(f) displays the unit cell design for an *alligator* photonic crystal structure, as studied in Refs. [69–71]. Instead of periodically placing a hole in the nanobeam, we modulate its outer dimensions with a sinusoidal form. This is motivated from the idea that such a structure should potentially be easier to fabricate as the small hole diameters in rectangular nanobeams limit etch rate uniformity throughout nanobeams. Additionally, dipole emitters can in principle be further removed from surfaces, which have been speculated to have a detrimental effect on the optical emission properties of inversion symmetric color centers in diamond [4, 10, 61]. As can be seen in Fig. 7.3(g), this structure can lead to the emergence of a band gap for TE like modes between the third and fourth lowest lying modes. From plots of the normalized electric field distribution in the unit cell displayed in Figs. 7.3(k,l), we see that we are interested in localizing the upper frequency band for maximal overlap with a dipole emitter. Fig. 7.3(h) shows that we can lower the frequency of the upper bandgap mode by adding high refractive index material in the form of reducing the amplitude of the sinusoidal modulation.

7.4.2. CAVITY DESIGN

In the previous section, we have seen that one can introduce a mode into the bandgap by slightly changing the unit cell such that it allows a guided mode in the original bandgap. In principle, one could deform a single unit cell only. In practice, however, one strives to introduce the defect in a smooth way, to minimize coupling to radiation modes: if one breaks the discrete translational symmetry of the lattice, k_x is no longer conserved, leading to coupling of guided modes to radiation modes, resulting in an additional loss channel [65, 72].

Here, we use a functional form for the lattice constant introduced in Ref. [65], and used throughout various photonic crystal cavity systems [10, 73]:

$$a(x) = a_n \times \left[1 - d \left(2x^3 - 3x^2 + 1 \right) \right], \tag{7.1}$$

where d is a parameter characterizing the fractional maximal deviation from the nominal unit cell value a_n, $x = \frac{j}{N}$ describes the position of the unit cell with N the number of unit cells used to introduce the lattice defect, $j \in [0, N] \subset \mathbb{N}_0$, and $j = 0$ the middle of the beam. As we use a symmetric well function w.r.t. the middle of the beam, we here only define the positive half of the well and apply symmetries in simulation. x follows the
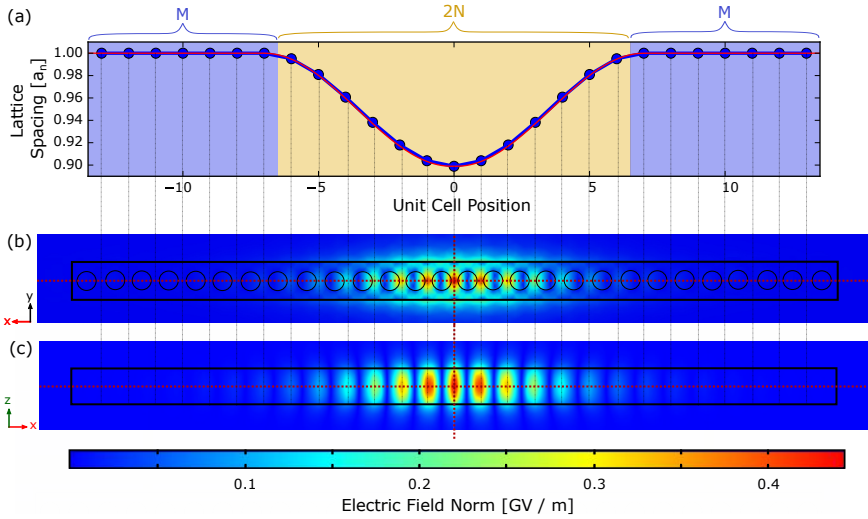
Figure 7.4: Lattice spacing variation and resulting normalized electric field mode profile for a high quality factor photonic crystal nanobeam. (a) Variation of the lattice spacing from the bandgap generating value, a_n, (shaded in blue) to a value of $a(0) = (1 - d) \times a_n$ at $x = 0$ (unit cell position 0 w.r.t. the center of the nanobeam), for which the fundamental TE mode frequency corresponds to the target cavity frequency value. Blue and yellow areas correspond to bandgap and cavity generating areas, respectively. Cavity generating values are $N = 7$, $d = 0.10$, and $\eta = 1.05$ (b, c) Normalized electric fields along different nanobeam orientations for a nanobeam optimized from the lattice spacing variation in (a), and the unit cell simulation parameters as listed in Tab. 7.2. These parameters result in a simulated quality factor $Q \sim 1.1 \times 10^6$, and an optical mode volume $V \sim 0.46(\lambda/n)^3$. Dashed red lines correspond to symmetry axes of the beam.

map

$$x \rightarrow y(x) = \begin{cases} \frac{1}{2}(2x)^\eta & \text{if } x \le 0.5, \\ 1 - \frac{1}{2}(2(1-x))^\eta & \text{if } x > 0.5, \end{cases} \tag{7.2}$$

with η describing the slope of the well function. In particular, this functional form guarantees that

$$\left.\frac{da(x)}{dx}\right|_{x=0,1} = 0. \tag{7.3}$$

An example of a lattice spacing variation following eq. 7.1 can be seen in Fig. 7.4(a). Here, we use $N = 7$, and set the number of unit cells with a lattice spacing of a_n, M, equal to $M = 7$. As we only define the positive half of the structure here and apply symmetries in simulation, this effectively defines a nanobeam with 28 total holes. As can be seen from the normalized electric field profiles in Figs. 7.4(b,c), this structure localizes a mode in the middle of a beam, with a simulated mode volume of $V \sim 0.46(\lambda/n)^3$, and a quality factor of $Q \sim 1.1 \times 10^6$. Note that it suffices to simulate one eighth of the full nanobeam structure when constraining our mode of interest to be a TE mode using appropriate boundary conditions, and taking advantage of the symmetry of the nanobeam.

7.5. PHOTONIC CRYSTAL CAVITY OPTIMIZATION

In the previous section, we have introduced the principles behind a photonic crystal nanobeam, and shown the electric field distribution in a rectangular nanobeam with high Q / V ratio. Here, we will explain the simulation process flow followed to obtain these results (based on the workflow presented in Ref. [65]), and investigate the robustness of these structures to real-world fabrication imperfections. While the methods described are of general nature, we will focus on the particular case of the rectangular photonic crystal nanobeam introduced in Fig. 7.3(a) and Fig. 7.4(b).

7.5.1. OPTIMIZATION PROCESS FLOW

An overview of the process flow followed to optimize a nanobeam photonic crystal cavity can be seen in Fig. 7.5. We start by simulating the bandstructure for an infinitely repeated unit cell, see Sec. 7.4.1. To utilise reasonable starting values, we use the parameters of Ref. [74], verify that the modes of interest have an electric field maximum inside the high index material, and optimize the bandgap[1].

Having simulated a bandgap generating structure, and a lattice defect that allows to localize a mode in the bandgap at the target frequency, we move on to fix a functional form that introduces the defect in the lattice, see Sec. 7.4. In the case of the rectangular cavity, a nanobeam is characterized by the set of parameters a_n, d, r, t_n, w_n, η, M and N. In our simulations, we fix M and N, as well as t_n (as we can tune the thickness in our fabrication process very precisely and iteratively by tuning the undercut etch time, see Ch. 8). We furthermore use a_n as a parameter that we rescale to keep the resonant wavelength, λ, of the structure in a small interval around the target frequency; this leaves us with an optimization problem over four parameters: d, r, w_n, η.

Maximal Purcell enhancement can be obtained for minimal V / Q, as discussed in Ch. 3. As we do not have knowledge about the functional form describing the optimization problem, we use a direct search method embedded in Matlab that makes use of the Nelder-Mead Simplex Algorithm with bounds on parameters (*fminsearchbnd* [76, 77]), and use a Matlab interface to Comsol to start individual Comsol simulations. To make sure the algorithm does not converge to local minima, we then use this fminsearchbnd algorithm in a re-seeded fashion: We form arrays of the optimization parameters, with a variation of ~ 25 % from the values we find via bandstructure simulations (and around $\eta = 1$), and draw random starting values for the optimization algorithm from these arrays. The algorithm then minimizes the ratio V / Q from these starting values, before we re-seed the algorithm with new values from our parameter arrays.

To allow for meaningful simulation results, we expand the fminsearch algorithm with a check that the current parameters allow for a physical geometry (e.g. avoiding hole diameters that are bigger than the nanobeam width), and a routine that keeps the structure resonant within a small interval Δ_λ around the target wavelength λ_{tar} by adjusting a_n. We furthermore cap unreasonably small or high quality factors, which indicate that no good mode has been found, or which are way beyond what can be expected in experiments, respectively. In this way, simulations can be terminated when stuck in a local

---

[1] We note that Ref. [75], e.g., gives an introduction on how to find reasonable ab-initio design parameters, and that one can make use of the scale invariance of photonic crystals to find a straightforward map between unit cell designs that are optimized for different wavelengths [68].
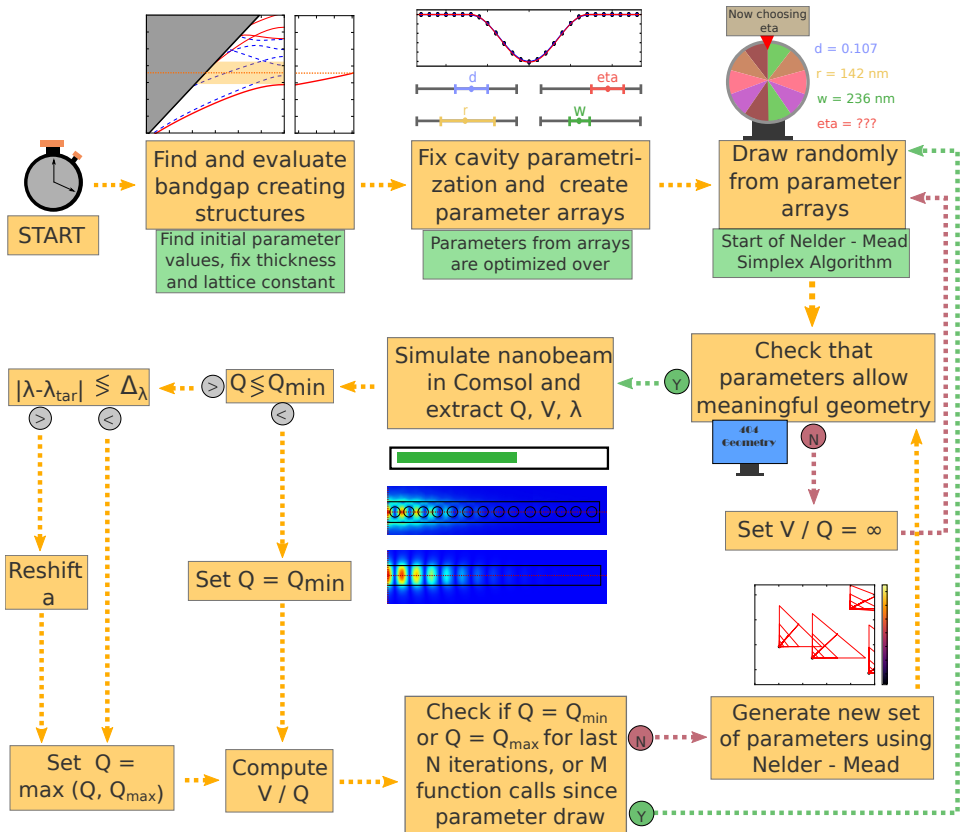
Figure 7.5: Flowchart of the process of arriving at a high (quality factor / mode volume) cavity design. Q, Q_{min} and Q_{max} simulated, minimal allowable and maximal allowable cavity quality factor, V mode volume of the cavity field, λ and λ_{tar} simulated and targeted cavity resonance wavelength, Δ_λ maximum allowed wavelength deviation. See the main text for a discussion of this simulation process.

minimum / maximum thus saving computation time.

7.5.2. NANOBEAM OPTIMIZATION RESULTS AND THEIR ROBUSTNESS

Having designed a nanobeam optimization routine, we now move on to perform such an optimization, and analyze its results. Without loss of generality, we focus on the case of a rectangular photonic crystal nanobeam, and optimize its quality factor to mode volume ratio, using the process flow of the previous section; Fig. 7.6 shows the results of one such optimization run, following the simulation process flow of Fig. 7.5.

Fig. 7.6(a) displays the results of two optimization run re-seeds, i.e. the optimization results for the wavelength and quality factor of the mode with highest quality factor of a rectangular nanobeam, for optimization from two starting parameter values. Convergence of the quality factor, as well as the mode's resonance wavelength towards the zero-phonon line wavelength of tin-vacancy centers ($\sim$ 620 nm) are visible.
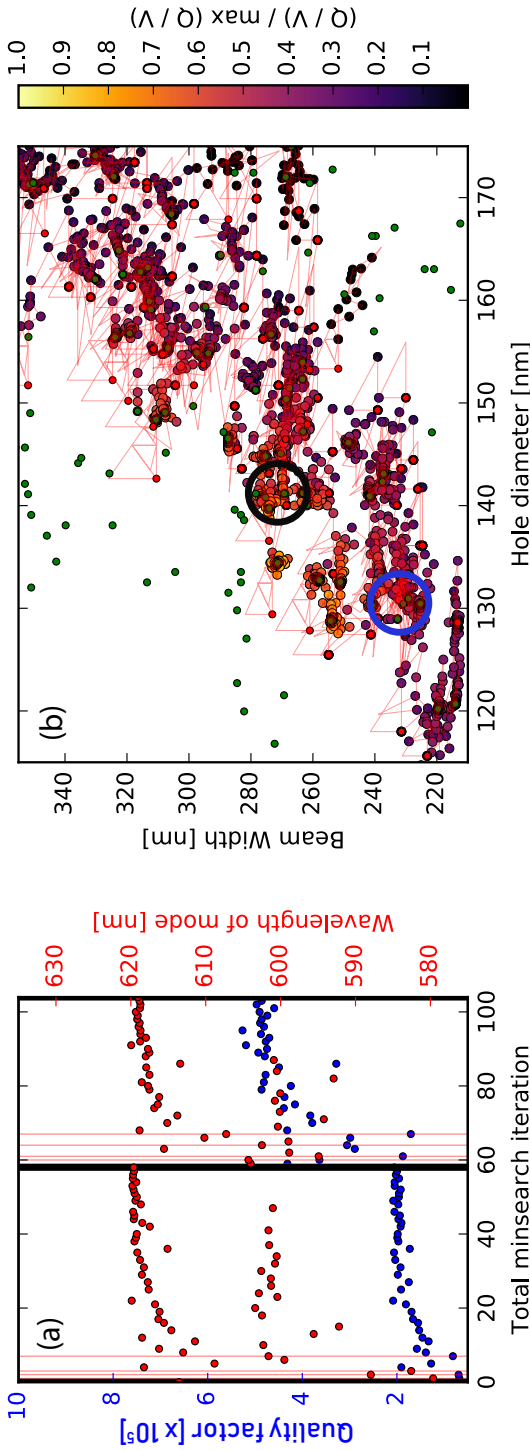
Figure 7.6: Nanobeam simulation optimization results. (a) Quality factor and wavelength of the highest quality factor resonance of a rectangular photonic crystal cavity structure as a function of total minsearch iteration. Red vertical lines indicates a re-shift of the nominal lattice constant (effective for the next iteration), used to bring the resonance frequency close to the targeted value, while black vertical lines indicate a re-seed of the optimization algorithm (see text). (b) Two-dimensional slice of the optimization parameter space, plotting the ratio of quality factor, Q, to mode volume, V, as a function of hole diameter and beam width of a rectangular photonic crystal nanobeam. Green and red small circles indicate the start and finish of an individual minsearch routine [i.e. a simulation sequence without algorithm re-seed, corresponding to the iterations between black vertical lines in (a)]. Red solid lines indicate the optimization path (only simulation results for which the quality factor is bigger than a minimal value of 1000 are plotted in this figure). Blue and black big circles correspond to simulation points in Fig. 7.7.

7
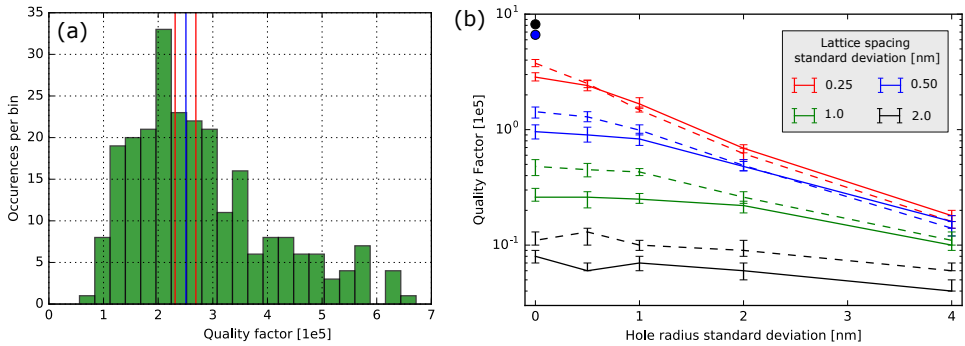
Figure 7.7: Robustness of nanobeam simulation results. Nanobeam hole positions and hole radii are defined following a Gaussian distribution with mean of the actual intended position / radius, and a certain standard deviation. (a) Histogram of 250 consecutive simulations using simulation parameters corresponding to the blue encircled point in Fig. 7.6(b), but using a hole position standard deviation of 0.25 nm, and a hole radius standard deviation of 0.5 nm. Blue and red vertical lines indicate the median and 95 % confidence interval of the median, respectively. (b) Median of the quality factor as a function of hole radius standard deviation for different hole position standard deviations; each datapoint is comprised of 250 individual simulations as in (a), with errorbars corresponding to the 95 % confidence interval of the median. Solid and dashed lines correspond to the black and blue encircled points in Fig. 7.6(b), with their original simulated quality factor for perfect hole positioning and radius indicated with circles.

Fig. 7.6(b) shows a two-dimensional parameter slice of the results of a full nanobeam optimization routine, comprised of 129 minsearch algorithm re-seeds (two of which are highlighted in Fig. 7.6(a)). This simulation takes about 48 hours of computation time on a regular office computer. We plot the ratio of quality factor, Q, to mode volume, V, normalized to its maximum ratio, as a function of hole diameter, $2 \times r$, and nanobeam width, w_n, and note that this only comprises two of the four parameters that we optimize over, with the fractional maximal deviation from the nominal lattice constant, d, and the lattice well functional form parameter, η, being the remaining two free optimization parameters (as discussed in Sec. 7.5.1). While maximal Q / V is limited to a small region in parameters, there is a broad range of parameters that allow to reach $[Q / V] / \max (Q / V) > 0.7$. This can potentially be exploited to design nanobeams with parameter values that are more robust to fabrication imperfections (e.g. by using larger hole radii), but feature resonances with slightly lower expected Q / V. Yet, the reliability of the process might be higher, allowing to achieve higher Q / V in the actual fabricated structures.

To evaluate the robustness of our designs to real-world fabrication imperfections, and to get a sense of the level of control needed to be achieved in fabrication, we take two example data points from the optimization routine (marked with blue and black circles in Fig. 7.6(b)), and slightly introduce disorder in the simulations, see Fig. 7.7: instead of placing holes at the exact desired location, we instead sample the position of each hole from a Gaussian distribution, with the mean of the distribution the intended hole position, and a standard deviation that we vary throughout simulations. Additionally, we sample the radius of each hole from a Gaussian distribution formed in the same manner. Note that disturbing these two parameters influences four design parameters, as the hole position is determined by a combination of d, η, and a_n. All other parameters can in
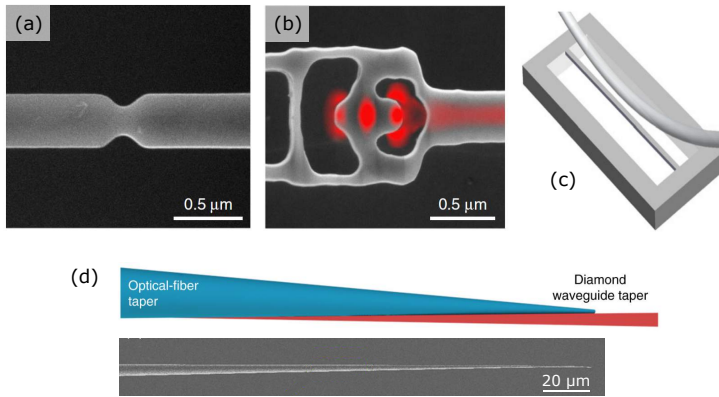
Figure 7.8: Overview of structures used to couple light to photonic crystal cavities and waveguides in diamond. Free-space coupling via notch (a) or inverse designed couplers (b). (a), (b), adapted from Ref. [78], in accordance with creative commons attribution 4.0 international license. (c) Double-sided tapered single mode fiber (adapted from Ref. [79], in accordance with creative commons attribution 3.0 license). (d) Single-sided single mode fiber (adapted with permission from Ref. [80], copyrighted (2017) by the American Physical Society. For a description of these methods and achieved efficiencies, see the main text.

principle be tuned in a deterministic fashion by slightly scaling the whole geometry (see Ch. 8).

Fig. 7.7(a) shows the results of 250 simulation repetitions, using simulation parameters corresponding to the blue encircled point in Fig. 7.6(b), and a lattice position / hole radius standard deviation of 0.25 nm and 0.5 nm, respectively. We observe a large spread in quality factors, ranging from $\sim 7 \times 10^4$ to $\sim 6.7 \times 10^5$. Fig. 7.7(b) shows the median and 95 % confidence bounds on the median of the quality factor as a function of hole radius standard deviation, for different lattice position standard deviations, and for two different parameter starting values, corresponding to the blue and black encircled points in Fig. 7.6(b); thus, a histogram as shown in Fig. 7.7(a) underlies each datapoint. As expected, already slight deviations from perfect hole placement and radii have a significant effect on the quality factor. Although the two starting points are drawn from different positions in parameter space, the simulations of Fig. 7.7(b) indicate that different points behave similar when including imperfections. This suggests that it is advantageous to fabricate structures with parameters for which simulations yield highest Q / V, and that it is not necessary to probe each point for its robustness to imperfections.

7.6. COUPLING TO PHOTONIC CRYSTAL CAVITIES

For fast, high fidelity photon-mediated entanglement generation protocols with color centers in diamond, high photon collection efficiency is crucial. To date, different strategies of coupling to color centers embedded in nanostructured photonic environments such as waveguides and photonic crystal cavities have been employed; Fig. 7.8 shows an overview of these structures.

A relatively straightforward way of coupling to nanophotonic structures is via so-called notch couplers that work by slightly breaking the symmetry of the nanophotonic

structure via a small geometric disturbance, see Fig. 7.8(a); this allows coupling to fo-
cused free-space optical beams. While easy to realize, these structures have limited effi-
ciencies ~ 1% [2]. Recently, coupling efficiencies of symmetry-breaking free space cou-
plers in diamond have been increased to ~ 25 % using more complex geometries found
via inverse-design methods [4, 78] that take fabrication imperfections into account, and
use advanced computational methods, see Fig. 7.8(b) [81]. Other demonstrated free-
space coupling systems in diamond relying on the same working principle include grat-
ing couplers, with demonstrated efficiencies up to 30 % [82, 83].

To date, highest coupling efficiencies to diamond nanophotonic structures (> 90 %)
have been demonstrated using double-side [79, 84, 85] (Fig. 7.8(c)) and single-side ta-
pered single mode fibers (Fig. 7.8(d)) [10, 23, 80, 86, 87], both relying on evanescent field
coupling of the fiber mode to the diamond nanophotonic structure. Double-side tapered
fibers are most commonly fabricated by heating and simultaneously pulling on an opti-
cal fiber, until parts of the fiber reach diameters < 1μm [88]. At this point, single-sided
tapered fibers are most commonly used, since they are easier to align to the nanopho-
tonic structures, and have proven to be more stable under cryogenic conditions, due to
a reduced length compared to the double-sided tapered fibers [89]. These tapered fibers
are typically fabricated via wet-etching (using hydrofluoric acid) a cleaved optical fiber
that has been stripped of its cladding; tight control over the fiber shape can be employed
via the speed at which the fiber is pulled out of the acid [80]. This method allows to re-
alize tapering angles, ta_a, as low as one degree. These fibers are then contacted with a
tapered waveguide (yellow part in Fig. 7.9, with a minimal taper width w_t), such that the
light is adiabatically transferred from the fiber mode via the formed collective mode of
the fiber and waveguide taper, and into the waveguide mode (green part in Fig. 7.9) [84].
We plan on employing single-sided tapered optical fibers in the future, with simulated
coupling efficiencies in excess of 90 %. Apart from allowing close-to-unity coupling effi-
ciencies, fiber-based couplers have another critical advantage over free space versions:
As discussed in Sec. 7.2, achieving long spin coherence for all established inversion sym-
metric color centers in diamond requires dilution refrigerator temperatures. However,
such cryogenic systems have high intrinsic vibrations and limited optical access. There-
fore, a robust, essentially monolithic coupling technique (as the tapered fibers and ta-
pered waveguides hold together via van der Waals forces once contacted) with limited
optical access (to avoid radiation-induced heating) is advantageous.

To couple from the diamond waveguide to the photonic crystal nanobeam, holes
are typically removed from one side of the bandgap generating region, reducing the re-
flectivity on one side of the cavity and thus leading to finite coupling to the waveguide
that is terminated in that mirror; the coupling rate of the cavity can then be tuned by
adding or removing holes [10, 80]. This in turn would mean, however, that only discrete
coupling values are accessible. This issue can be overcome by varying the mirror hole
radii and / or lattice spacings, however such designs have been found to be relatively
sensitive to fabrication errors. Therefore, we opt for a different approach in this the-
sis: instead of changing the waveguide into the mirror region, we terminate the waveg-
uide with a bandgap generating region, and place it next to the nanophotonic cavity, see
Fig. 7.9 [84, 90, 91]. Instead of abruptly changing the geometry from the waveguide to
mirror generating region, we continually change the hole radius from no hole to the mir-
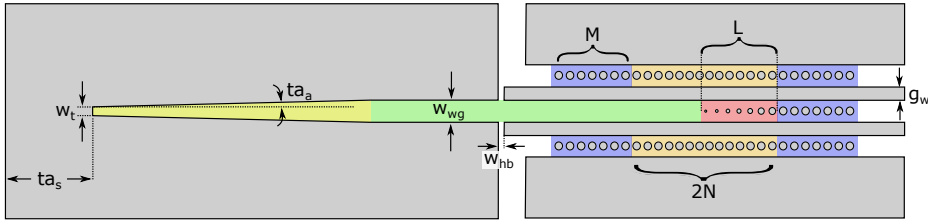
Figure 7.9: Final device geometry, containing two photonic crystal cavities [mirror regions shaded in blue (formed over M unit cells), cavity regions shaded in orange (formed over $2N$ unit cells)], and one coupling waveguide (shaded in green, waveguide width w_{wg}), that can be coupled to via evanescent field coupling to a tapered optical fiber in a tapered waveguide region (yellow, tapering waveguide angle ta_a, minimum taper width w_t, spacing of fiber taper end to diamond substrate ta_s). Slight variations in cavity design parameters and / or imperfect fabrication lead to non-overlapping resonant frequencies of the two nanobeams, allowing their individual addressing. The waveguide is terminated in a mirror (blue), allowing to probe devices on reflection and transfer the waveguide field to the nanobeam cavities via evanescent field coupling (by tuning the waveguide-nanobeam distance g_w). To avoid scattering into leaky modes in the light cone, the hole radius of the waveguide gradually changes from no holes to the mirror hole size, while keeping the lattice spacing throughout the hole radius variation constant (shaded in red, changed over L unit cells). To allow for structural integrity, waveguides are anchored to the diamond frame via small holding bars with width w_{hb}.

ror hole size, to avoid scattering to leaky modes, as discussed in Sec. 7.4.2 (red region in Fig. 7.9, tapered over L unit cells). Changing the distance between the waveguide and coupler in the design of the nanophotonic chip, g_w, we can then access a continuum of waveguide-cavity couplings in experiments [91]. For structural integrity, we fix the waveguide to the diamond supporting frame via small (to reduce coupling to the substrate [92]) holding bars of width w_{hb}. Typically, we aim for a spacing between the diamond substrate and the beginning of the taper, ta_s, of $ta_s > 100$ µm, to avoid touching the diamond substrate with the tapered fiber, which would lead to unwanted losses.

ACKNOWLEDGEMENTS

REFERENCES

[1] M. Ruf, N. H. Wan, H. Choi, D. Englund and R. Hanson, *Quantum networks based on color centers in diamond,* Journal of Applied Physics **130**, 070901 (2021).

[2] A. Sipahigil *et al.*, *An integrated diamond nanophotonics platform for quantum-optical networks,* Science **354**, 847 (2016).

[3] M. K. Bhaskar *et al.*, *Quantum Nonlinear Optics with a Germanium-Vacancy Color Center in a Nanoscale Diamond Waveguide,* Physical Review Letters **118**, 223603 (2017).

[4] A. E. Rugar, C. Dory, S. Aghaeimeibodi, H. Lu, S. Sun, S. D. Mishra, Z.-X. Shen, N. A. Melosh and J. Vučković, *Narrow-Linewidth Tin-Vacancy Centers in a Diamond Waveguide,* ACS Photonics **7**, 2356 (2020).

[5] M. W. Doherty, N. B. Manson, P. Delaney, F. Jelezko, J. Wrachtrup and L. C. Hollenberg, *The nitrogen-vacancy colour centre in diamond,* Physics Reports **528**, 1 (2013).

[6] C. Hepp, *Electronic structure of the silicon vacancy color center in diamond,* Ph.D. thesis, Saarland University (2014).

[7] C. Bradac, W. Gao, J. Forneris, M. E. Trusheim and I. Aharonovich, *Quantum nanophotonics with group IV defects in diamond,* Nature Communications **10**, 5625 (2019).

[8] C. Hepp, T. Müller, V. Waselowski, J. N. Becker, B. Pingault, H. Sternschulte, D. Steinmüller-Nethl, A. Gali, J. R. Maze, M. Atatüre and C. Becher, *Electronic Structure of the Silicon Vacancy Color Center in Diamond,* Physical Review Letters **112**, 036405 (2014).

[9] B. Pingault, D. D. Jarausch, C. Hepp, L. Klintberg, J. N. Becker, M. Markham, C. Becher and M. Atatüre, *Coherent control of the silicon-vacancy spin in diamond,* Nature Communications **8**, 1 (2017).

[10] C. T. Nguyen *et al.*, *An integrated nanophotonic quantum register based on silicon-vacancy spins in diamond,* Physical Review B **100**, 1 (2019).

[11] P. Siyushev *et al.*, *Optical and microwave control of germanium-vacancy center spins in diamond,* Physical Review B **96**, 081201 (2017).

[12] T. Iwasaki, Y. Miyamoto, T. Taniguchi, P. Siyushev, M. H. Metsch, F. Jelezko and M. Hatano, *Tin-Vacancy Quantum Emitters in Diamond,* Physical Review Letters **119**, 253601 (2017).

[13] M. E. Trusheim *et al.*, *Transform-Limited Photons from a Coherent Tin-Vacancy Spin in Diamond,* Physical Review Letters **124**, 1 (2020).

[14] M. E. Trusheim *et al.*, *Lead-related quantum emitters in diamond,* Physical Review B **99**, 1 (2019).

[15] H. Bernien, L. Childress, L. Robledo, M. Markham, D. Twitchen and R. Hanson, *Two-Photon Quantum Interference from Separate Nitrogen Vacancy Centers in Diamond,* Physical Review Letters **108**, 043604 (2012).

[16] A. Faraon, C. Santori, Z. Huang, V. M. Acosta and R. G. Beausoleil, *Coupling of Nitrogen-Vacancy Centers to Photonic Crystal Cavities in Monocrystalline Diamond,* Physical Review Letters **109**, 033604 (2012).

[17] M. Ruf, M. IJspeert, S. van Dam, N. de Jong, H. van den Berg, G. Evers and R. Hanson, *Optically Coherent Nitrogen-Vacancy Centers in Micrometer-Thin Etched Diamond Membranes,* Nano Letters **19**, 3987 (2019).

[18] L. De Santis, M. Trusheim, K. Chen and D. Englund, *Investigation of the Stark Effect on a Centrosymmetric Quantum Emitter in Diamond,* arXiv preprint (2021), arXiv:2101.01322 .

[19] S. Aghaeimeibodi, D. Riedel, A. E. Rugar, C. Dory and J. Vučković, *Electrical Tuning of Tin-Vacancy Centers in Diamond,* Physical Review Applied **15**, 064010 (2021).

[20] G. Thiering and A. Gali, *Ab Initio Magneto-Optical Spectrum of Group-IV Vacancy Color Centers in Diamond,* Physical Review X **8**, 021063 (2018).

[21] D. D. Sukachev, A. Sipahigil, C. T. Nguyen, M. K. Bhaskar, R. E. Evans, F. Jelezko and M. D. Lukin, *Silicon-Vacancy Spin Qubit in Diamond: A Quantum Memory Exceeding 10 ms with Single-Shot State Readout,* Physical Review Letters **119**, 223602 (2017).

[22] A. J. Sigillito *et al.*, *Fast, low-power manipulation of spin ensembles in superconducting microresonators,* Applied Physics Letters **104**, 222407 (2014).

[23] M. K. Bhaskar, R. Riedinger, B. Machielse, D. S. Levonian, C. T. Nguyen, E. N. Knall, H. Park, D. Englund, M. Lončar, D. D. Sukachev and M. D. Lukin, *Experimental demonstration of memory-enhanced quantum communication,* Nature **580**, 60 (2020).

[24] E. Neu, M. Agio and C. Becher, *Photophysics of single silicon vacancy centers in diamond: implications for single photon emission,* Optics Express **20**, 19956 (2012).

[25] L. Rogers, K. Jahnke, T. Teraji, L. Marseglia, C. Müller, B. Naydenov, H. Schauffert, C. Kranz, J. Isoya, L. McGuinness and F. Jelezko, *Multiple intrinsically identical single-photon emitters in the solid state,* Nature Communications **5**, 4739 (2014).

[26] J. Riedrich-Möller, C. Arend, C. Pauly, F. Mücklich, M. Fischer, S. Gsell, M. Schreck and C. Becher, *Deterministic Coupling of a Single Silicon-Vacancy Color Center to a Photonic Crystal Cavity in Diamond,* Nano Letters **14**, 5281 (2014).

[27] E. Neu, D. Steinmetz, J. Riedrich-Möller, S. Gsell, M. Fischer, M. Schreck and C. Becher, *Single photon emission from silicon-vacancy colour centres in chemical vapour deposition nano-diamonds on iridium,* New Journal of Physics **13**, 0 (2011).

7

[28] A. Dietrich, K. D. Jahnke, J. M. Binder, T. Teraji, J. Isoya, L. J. Rogers and F. Jelezko, *Isotopically varying spectral features of silicon-vacancy in diamond,* New Journal of Physics **16**, 113019 (2014).

[29] T. Iwasaki *et al., Germanium-Vacancy Single Color Centers in Diamond,* Scientific Reports **5**, 1 (2015).

[30] R. Høy Jensen, E. Janitz, Y. Fontana, Y. He, O. Gobron, I. P. Radko, M. Bhaskar, R. Evans, C. D. Rodríguez Rosenblueth, L. Childress, A. Huck and U. Lund Andersen, *Cavity-Enhanced Photon Emission from a Single Germanium-Vacancy Center in a Diamond Membrane,* Physical Review Applied **13**, 064016 (2020).

[31] M. Nguyen, N. Nikolay, C. Bradac, M. Kianinia, E. A. Ekimov, N. Mendelson, O. Benson and I. Aharonovich, *Photodynamics and quantum efficiency of germanium vacancy color centers in diamond,* Advanced Photonics **1**, 1 (2019).

[32] J. Görlitz, D. Herrmann, G. Thiering, P. Fuchs, M. Gandil, T. Iwasaki, T. Taniguchi, M. Kieschnick, J. Meijer, M. Hatano, A. Gali and C. Becher, *Spectroscopic investigations of negatively charged tin-vacancy centres in diamond,* New Journal of Physics **22**, 013048 (2020).

[33] S. D. Tchernij *et al., Single-Photon-Emitting Optical Centers in Diamond Fabricated upon Sn Implantation,* ACS Photonics **4**, 2580 (2017).

[34] A. E. Rugar, S. Aghaeimeibodi, D. Riedel, C. Dory, H. Lu, P. J. McQuade, Z.-X. Shen, N. A. Melosh and J. Vučković, *Quantum Photonic Interface for Tin-Vacancy Centers in Diamond,* Physical Review X **11**, 031021 (2021).

[35] S. Ditalia Tchernij *et al., Single-Photon Emitters in Lead-Implanted Single-Crystal Diamond,* ACS Photonics **5**, 4864 (2018).

[36] J. E. Fröch, A. Bahm, M. Kianinia, Z. Mu, V. Bhatia, S. Kim, J. M. Cairney, W. Gao, C. Bradac, I. Aharonovich and M. Toth, *Versatile direct-writing of dopants in a solid state host through recoil implantation,* Nature Communications **11**, 5039 (2020).

[37] P. Wang, T. Taniguchi, Y. Miyamoto and M. Hatano, *Low-Temperature Spectroscopic Investigation of Lead-Vacancy Centers in Diamond Fabricated by High-Pressure and High- Temperature Treatment,* arXiv preprint (2021), arXiv::2106.03413 .

[38] I. P. Radko, M. Boll, N. M. Israelsen, N. Raatz, J. Meijer, F. Jelezko, U. L. Andersen and A. Huck, *Determining the internal quantum efficiency of shallow-implanted nitrogen-vacancy defects in bulk diamond,* Optics Express **24**, 27715 (2016).

[39] A. Faraon, P. E. Barclay, C. Santori, K. M. C. Fu and R. G. Beausoleil, *Resonant enhancement of the zero-phonon emission from a colour centre in a diamond cavity,* Nature Photonics **5**, 301 (2011).

[40] D. Riedel, I. Söllner, B. J. Shields, S. Starosielec, P. Appel, E. Neu, P. Maletinsky and R. J. Warburton, *Deterministic enhancement of coherent photon generation from a nitrogen-vacancy center in ultrapure diamond,* Physical Review X **7**, 1 (2017).

7

[41] N. Kalb, P. C. Humphreys, J. J. Slim and R. Hanson, *Dephasing mechanisms of diamond-based nuclear-spin memories for quantum networks,* Physical Review A **97**, 062330 (2018).

[42] M. Ruf, M. Weaver, S. van Dam and R. Hanson, *Resonant Excitation and Purcell Enhancement of Coherent Nitrogen-Vacancy Centers Coupled to a Fabry-Perot Microcavity,* Physical Review Applied **15**, 024049 (2021).

[43] K. D. Jahnke, A. Sipahigil, J. M. Binder, M. W. Doherty, M. Metsch, L. J. Rogers, N. B. Manson, M. D. Lukin and F. Jelezko, *Electron–phonon processes of the silicon-vacancy centre in diamond,* New Journal of Physics **17**, 043011 (2015).

[44] S. Meesala *et al.,* *Strain engineering of the silicon-vacancy center in diamond,* Physical Review B **97**, 1 (2018).

[45] B. Pingault, J. N. Becker, C. H. Schulte, C. Arend, C. Hepp, T. Godde, A. I. Tartakovskii, M. Markham, C. Becher and M. Atatüre, *All-Optical Formation of Coherent Dark States of Silicon-Vacancy Spins in Diamond,* Physical Review Letters **113**, 263601 (2014).

[46] J. N. Becker, B. Pingault, D. Groß, M. Gündoğan, N. Kukharchyk, M. Markham, A. Edmonds, M. Atatüre, P. Bushev and C. Becher, *All-Optical Control of the Silicon-Vacancy Spin in Diamond at Millikelvin Temperatures,* Physical Review Letters **120**, 053603 (2018).

[47] S. Maity, L. Shao, S. Bogdanović, S. Meesala, Y.-I. Sohn, N. Sinclair, B. Pingault, M. Chalupnik, C. Chia, L. Zheng, K. Lai and M. Lončar, *Coherent acoustic control of a single silicon vacancy spin in diamond,* Nature Communications **11**, 193 (2020).

[48] C. T. Nguyen, D. D. Sukachev, M. K. Bhaskar, B. MacHielse, D. S. Levonian, E. N. Knall, P. Stroganov, R. Riedinger, H. Park, M. Lončar and M. D. Lukin, *Quantum Network Nodes Based on Diamond Qubits with an Efficient Nanophotonic Interface,* Physical Review Letters **123**, 1 (2019).

[49] H. Bernien, B. Hensen, W. Pfaff, G. Koolstra, M. S. Blok, L. Robledo, T. H. Taminiau, M. Markham, D. J. Twitchen, L. Childress and R. Hanson, *Heralded entanglement between solid-state qubits separated by three metres,* Nature **497**, 86 (2013).

[50] J. Franck and E. G. Dymond, *Elementary processes of photochemical reactions,* Transactions of the Faraday Society **21**, 536 (1926).

[51] E. Condon, *A Theory of Intensity Distribution in Band Systems,* Physical Review **28**, 1182 (1926).

[52] B. L. Green, S. Mottishaw, B. G. Breeze, A. M. Edmonds, U. F. S. D'Haenens-Johansson, M. W. Doherty, S. D. Williams, D. J. Twitchen and M. E. Newton, *Neutral Silicon-Vacancy Center in Diamond: Spin Polarization and Lifetimes,* Physical Review Letters **119**, 096402 (2017).

7

[53] B. C. Rose *et al.*, *Observation of an environmentally insensitive solid-state spin defect in diamond,* Science **361**, 60 (2018).

[54] B. L. Green, M. W. Doherty, E. Nako, N. B. Manson, U. F. S. D'Haenens-Johansson, S. D. Williams, D. J. Twitchen and M. E. Newton, *Electronic structure of the neutral silicon-vacancy center in diamond,* Physical Review B **99**, 161112 (2019).

[55] Z.-H. Zhang, P. Stevenson, G. Thiering, B. C. Rose, D. Huang, A. M. Edmonds, M. L. Markham, S. A. Lyon, A. Gali and N. P. de Leon, *Optically Detected Magnetic Resonance in Neutral Silicon Vacancy Centers in Diamond via Bound Exciton States,* Physical Review Letters **125**, 237402 (2020).

[56] A. Sipahigil, K. D. Jahnke, L. J. Rogers, T. Teraji, J. Isoya, A. S. Zibrov, F. Jelezko and M. D. Lukin, *Indistinguishable Photons from Separated Silicon-Vacancy Centers in Diamond,* Physical Review Letters **113**, 113602 (2014).

[57] R. E. Evans, A. Sipahigil, D. D. Sukachev, A. S. Zibrov and M. D. Lukin, *Narrow-Linewidth Homogeneous Optical Emitters in Diamond Nanostructures via Silicon Ion Implantation,* Physical Review Applied **5**, 044010 (2016).

[58] T. Müller, C. Hepp, B. Pingault, E. Neu, S. Gsell, M. Schreck, H. Sternschulte, D. Steinmüller-Nethl, C. Becher and M. Atatüre, *Optical signatures of silicon-vacancy spins in diamond,* Nature Communications **5**, 3328 (2014).

[59] N. H. Wan, T. J. Lu, K. C. Chen, M. P. Walsh, M. E. Trusheim, L. De Santis, E. A. Bersin, I. B. Harris, S. L. Mouradian, I. R. Christen, E. S. Bielejec and D. Englund, *Large-scale integration of artificial atoms in hybrid photonic circuits,* Nature **583**, 226 (2020).

[60] R. E. Evans *et al.*, *Photon-mediated interactions between quantum emitters in a diamond nanocavity,* Science **362**, 662 (2018).

[61] B. Machielse *et al.*, *Quantum Interference of Electromechanically Stabilized Emitters in Nanophotonic Devices,* Physical Review X **9**, 1 (2019).

[62] C. T. Nguyen, D. D. Sukachev, M. K. Bhaskar, B. Machielse, D. S. Levonian, E. N. Knall, P. Stroganov, R. Riedinger, H. Park, M. Lončar and M. D. Lukin, *Quantum Network Nodes Based on Diamond Qubits with an Efficient Nanophotonic Interface,* Physical Review Letters **123**, 1 (2019).

[63] M. H. Metsch, K. Senkalla, B. Tratzmiller, J. Scheuer, M. Kern, J. Achard, A. Tallaire, M. B. Plenio, P. Siyushev and F. Jelezko, *Initialization and Readout of Nuclear Spins via a Negatively Charged Silicon-Vacancy Center in Diamond,* Physical Review Letters **122**, 190503 (2019).

[64] Y. I. Sohn *et al.*, *Controlling the coherence of a diamond spin qubit through its strain environment,* Nature Communications **9**, 17 (2018).

[65] J. Chan, *Laser cooling of an optomechanical crystal resonator to its quantum ground state of motion,* Ph.D. thesis, Caltech (2012).

[66] S. M. Meenehan, *Cavity Optomechanics at Millikelvin Temperatures,* Ph.D. thesis, Caltech (2015).

[67] K. Sakoda, *Optical Properties of Photonic Crystals* (Springer, Berlin, 2005).

[68] J. D. Joannopoulos, S. G. Johnson, J. N. Winn and R. D. Meade, *Photonic Crystals* (Princeton University Press, Princeton, 2011).

[69] S. L. Mouradian, *A Scalable Quantum Computation Platform: Solid State Quantum Memories Coupled to Photonic Integrated Circuits,* Ph.D. thesis, MIT (2018).

[70] A. Goban, C.-L. Hung, S.-P. Yu, J. Hood, J. Muniz, J. Lee, M. Martin, A. McClung, K. Choi, D. Chang, O. Painter and H. Kimble, *Atom–light interactions in photonic crystals,* Nature Communications **5**, 3808 (2014).

[71] F. Rozpędek, R. Yehia, K. Goodenough, M. Ruf, P. C. Humphreys, R. Hanson, S. Wehner and D. Elkouss, *Near-term quantum-repeater experiments with nitrogen-vacancy centers: Overcoming the limitations of direct transmission,* Physical Review A **99**, 052330 (2019).

[72] Y. Akahane, T. Asano, B. S. Song and S. Noda, *High-Q photonic nanocavity in a two-dimensional photonic crystal,* Nature **425**, 944 (2003).

[73] A. Wallucks, I. Marinković, B. Hensen, R. Stockill and S. Gröblacher, *A quantum memory at telecom wavelengths,* Nature Physics **16**, 772 (2020).

[74] S. Mouradian, N. H. Wan, T. Schröder and D. Englund, *Rectangular photonic crystal nanobeam cavities in bulk diamond,* Applied Physics Letters **111**, 021103 (2017).

[75] Q. Quan and M. Loncar, *Deterministic design of wavelength scale, ultra-high Q photonic crystal nanobeam cavities,* Optics Express **19**, 18529 (2011).

[76] J. D'Errico, *fminsearchbnd, fminsearchcon, MATLAB Central File Exchange,* Retrieved 2020-10-09 .

[77] J. A. Nelder and R. Mead, *A Simplex Method for Function Minimization,* The Computer Journal **7**, 308 (1965).

[78] C. Dory *et al.*, *Inverse-designed diamond photonics,* Nature Communications **10**, 1 (2019).

[79] B. Khanaliloo, H. Jayakumar, A. C. Hryciw, D. P. Lake, H. Kaviani and P. E. Barclay, *Single-Crystal Diamond Nanobeam Waveguide Optomechanics,* Physical Review X **5**, 041051 (2015).

[80] M. J. Burek *et al.*, *Fiber-coupled diamond quantum nanophotonic interface,* Physical Review Applied **8**, 1 (2017).

[81] A. Y. Piggott, J. Lu, T. M. Babinec, K. G. Lagoudakis, J. Petykiewicz and J. Vučković, *Inverse design and implementation of a wavelength demultiplexing grating coupler,* Scientific Reports **4**, 7210 (2015).

7

[82] T. G. Tiecke, K. P. Nayak, J. D. Thompson, T. Peyronel, N. P. de Leon, V. Vuletić and M. D. Lukin, *Efficient fiber-optical interface for nanophotonic devices,* Optica **2**, 70 (2015).

[83] P. Rath, S. Khasminskaya, C. Nebel, C. Wild and W. H. Pernice, *Grating-assisted coupling to nanophotonic circuits in microcrystalline diamond thin films,* Beilstein Journal of Nanotechnology **4**, 300 (2013).

[84] S. Gröblacher, J. T. Hill, A. H. Safavi-Naeini, J. Chan and O. Painter, *Highly efficient coupling from an optical fiber to a nanoscale silicon optomechanical cavity,* Applied Physics Letters **103**, 1 (2013).

[85] M. Mitchell, D. P. Lake and P. E. Barclay, *Realizing Q > 300 000 in diamond microdisks for optomechanics via etch optimization,* APL Photonics **4**, 016101 (2019).

[86] T. G. Tiecke, K. P. Nayak, J. D. Thompson, T. Peyronel, N. P. de Leon, V. Vuletić and M. D. Lukin, *Efficient fiber-optical interface for nanophotonic devices,* Optica **2**, 70 (2015).

[87] R. E. Evans *et al.*, *Photon-mediated interactions between quantum emitters in a diamond nanocavity,* Science **362**, 662 (2018).

[88] A. J. R. MacDonald, G. G. Popowich, B. D. Hauer, P. H. Kim, A. Fredrick, X. Rojas, P. Doolin and J. P. Davis, *Optical microscope and tapered fiber coupling apparatus for a dilution refrigerator,* Review of Scientific Instruments **86**, 013107 (2015).

[89] A. Wallucks, *Towards an Optomechanical Quantum Memory,* Ph.D. thesis, TU Delft (2020).

[90] S. Hong, R. Riedinger, I. Marinković, A. Wallucks, S. G. Hofer, R. A. Norte, M. Aspelmeyer and S. Gröblacher, *Hanbury Brown and Twiss interferometry of single phonons from an optomechanical resonator,* Science **358**, 203 (2017).

[91] I. Marinkovic, *Optomechanical devices in the quantum regime,* Ph.D. thesis, TU Delft (2019).

[92] Y. Q. Huan, *Efficient coupling of tapered optical fibers to silicon nanophotonic waveguides on rare-earth doped crystals,* Senior thesis, Caltech (2019).

7

8

FABRICATION AND CHARACTERIZATION OF PHOTONIC CRYSTAL CAVITIES IN DIAMOND

Maximilian Ruf*, Nina Codreanu*, Chris van Egmond, Richard Norte, Simon Groeblacher, and Ronald Hanson

Group-IV color centers in diamond are prime candidates for nodes of future large-scale quantum networks, due to their optically active spin, long spin coherence times at low temperatures, and first-order insensitivity to changes in the electric field. This insensitivity allows for integration of color centers in nanophotonic cavities in a way that preserves the coherence of optical transitions. Such a cavity-enhanced interface can realize high-fidelity spin-photon interactions at high rates, making use of the Purcell effect. Here, we introduce different methods to fabricate thin, free-hanging diamond structures as needed for high electric field confinement and thus large Purcell enhancement. We describe a process flow to fabricate all-diamond photonic crystal cavities and waveguides, employing a quasi-isotropic (dry) diamond etch to release structures from the bulk diamond. We discuss the quality of the resulting cavities, and present typical failure mechanisms of the fabrication process. Coupling coherent quantum emitters to photonic crystal cavities that can be integrated in photonic circuits is a key capability on the way towards extended quantum networks with long coherence.

---

*These authors contributed equally to this work

8.1. Introduction

Future large-scale quantum networks require nodes that combine excellent spin properties with efficient spin-photon interfaces. A promising way to realize such an interface is to embed color centers in diamond into an optical cavity, making use of the Purcell effect. However, the fabrication of nanophotonic cavities in diamond itself is challenging, as there is no known wet-processing technique that allows to fabricate free-hanging structures, in contrast to many nanophotonic material hosts. In this chapter, we describe a process flow to fabricate photonic crystal cavities and waveguides in diamond, using a crystal-plane dependent inductively coupled plasma (ICP) dry reactive-ion-etch (RIE) process. We furthermore discuss the quality and possible ways of improvement of the resulting structures.

In Sec. 8.2, we outline different methods to fabricate free-standing all-diamond nanophotonic structures, and motivate our fabrication process choice. In Sec. 8.3, we give an overview of the developed process flow, including a table that contains the most important fabrication parameters. In Sec. 8.4, we provide further details on a crucial choice for our process flow — a Si_3N_4 hard mask that allows to transfer the nanophotonic patterns into the diamond — and give a brief overview of pros and cons of different hard mask choices in literature that are in principle compatible with the fabrication of nanophotonic geometries. Sec. 8.5 then describes the crystal-plane dependent dry ICP-RIE etch that we use to both release devices from the bulk substrate, and to precisely tune the thickness of the resulting nanophotonic structures. We then report on final fabricated devices and their measured quality factors in Sec. 8.6, before we discuss current challenges and research directions in Sec. 8.7. We finish this chapter with an outlook on possible future improvements to the fabrication process in Sec. 8.8.

8.2. Fabrication of free-standing, all-diamond nanophotonic structures

One dimensional photonic crystal nanobeam waveguides and cavities confine the electromagnetic field by a periodic modulation of refractive index along the longitudinal direction of the beam. At the same time, off-axis light is confined due to a refractive index contrast between the nanobeam material and the lower refractive index material in the nanobeam's surroundings (see Ch. 7). To confine light at the zero-phonon line (ZPL) resonance frequencies of color centers in diamond (~ [600 - 800] nm), thin diamond films with thickness ~ (200 - 400) nm are required. Typically, such thin structures are realized using (hetero-) epitaxial growth, for which a thin film of the target material in which the photonic structure is to be defined is grown on a substrate with different material composition. After patterning the photonic structure, the substrate is then selectively removed in an etching step to release the target film (see e.g. [1, 2]).

In contrast to many other materials, however, high quality (i.e. low residual nitrogen and boron concentration, low stress, low concentration of lattice defects), μm-thin single-crystal diamond (SCD) as required for color center in diamond applications has not been grown on wafer scale using hetero-epitaxy. This is in particular due to lattice mismatches, and dislocations in grown material [3, 4]. Therefore, different ways of fabricating thin diamond structures from commercially available bulk SCD are required.

An overview of common fabrication methods used to fabricate high quality thin diamond films from bulk SCD (grown via chemical vapour deposition), can be seen in Fig. 8.1. These methods can be grouped into the following four main categories:

- **(a) Selective etching of a sacrificial graphite layer, Fig. 8.1(a)**: A layer of graphite at a depth of up to ~ 5 μm (thickness ~ 100 nm, both can be controlled via the choice of the ions and their energy) is created by ion implantation of the SCD above a critical damage threshold, and subsequent high temperature annealing. The resulting graphite layer can then be etched away using a wet etching technique, releasing a μm-thin diamond membrane [5–7]. This membrane can subsequently be flipped and mounted on a carrier wafer for further handling. Note that this carrier wafer again can be chosen from a material that offers the capability of selective undercut (wet) etching. To increase the quality of the formed diamond membrane, this process is sometimes combined with SCD overgrowth and backside etching of the thin diamond membrane to obtain highest quality thin film SCD [8–10].

- **(b) Thinning of diamond membrane, Fig. 8.1(b)**: A commercially sourced, polished, and microns-thin diamond membrane is thinned down to the target thickness using reactive ion etching. This typically involves oxygen and argon-chlorine based plasmas, see Ch. 5. After thinning, the membrane can be handled on a carrier wafer that can be undercut selectively (e.g. using a Si carrier wafer and a potassium hydroxide (KOH) etch) [11–15]).

- **(c) Angled diamond undercut etch, Fig. 8.1(c)**: Nanophtonic structures with *triangular* device cross-section can be fabricated from bulk SCD using a patterned mask (e.g. Si_3N_4 or a metallic layer) that features a high selectivity to either diamond plasma etches or focused ion beams. Using either a Faraday cage that deflects the trajectory of impinging ions of a subsequent oxygen plasma [16–19] or an angled ion etcher [20–22], the diamond nanobeam structure can then be etched at an angle. This undercuts the nanobeam or waveguide from the substrate for parts of the sample.

- **(d) Quasi-isotropic diamond undercut etch, Fig. 8.1(d)**: Nanophotonic structures with *rectangular* device cross-section can be fabricated in a way similar to the angled diamond etching process discussed above, with the difference that the sidewalls of the structure resulting from the first anisotropic diamond etch [Fig. 8.1(d,1)] are protected with an additional mask [Fig. 8.1(d,2)]. A subsequent zero bias voltage quasi-isotropic oxygen-based diamond reactive ion etch that has been shown to feature crystal-plane dependant etch rates [23–28] then allows to undercut devices with rectangular cross-sections when aligning the nanophotonic structures along specific crystallographic directions (discussed in detail in Sec. 8.5 below).

In this work, we fabricate nanophotonic structures using the quasi isotropic diamond undercut etch method [process (d)]. This process does not require sub-μm-thin membrane transfer during which the diamond film is prone to breaking as in processes
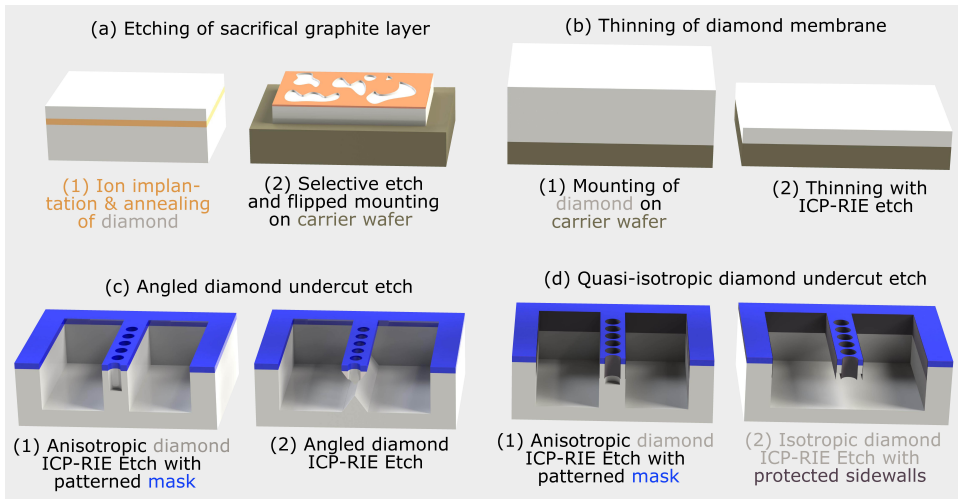
Figure 8.1: Overview of common fabrication methods used to create high quality, sub-µm-thin diamond membranes as required for high cooperativity photonic crystal applications. (a) Selective etching of a sacrificial amorphous carbon layer, introduced by ion implantation and annealing. (b) Inductively coupled plasma (ICP) reactive ion etching (RIE) of a diamond membrane. (c) Angled ICP-RIE using a mask, to fabricate diamond nanobeams with triangular cross-section. (d) Quasi-isotropic ICP-RIE using a mask and sidewall protection, to fabricate diamond nanobeams with rectangular cross-section. See main text for a description of these methods.

(a) and (b), as it instead relies on fabricating on commercially available 500 µm-thick diamond substrates. Additionally, this avoids the extra costs associated with slicing and polishing diamonds into high-quality, thin membranes. While — to the best of our knowledge — all fabrication methods achieve approximately the same quality factors of diamond photonic crystal cavities at the resonant wavelength of color centers in diamond ($Q \sim 10^4$ [11, 22, 25, 29]), it is expected that scattering losses, induced by mixing TE- and TM- like modes due to the inherently triangular device-cross section, will ultimately limit quality factors of triangular devices (c) [18, 25, 30]. Furthermore, it has been shown that for achieving high device yield, an angled plasma etcher is required for process flow (c), as the Faraday cage technique suffers from non-uniform etch rates [22]. However, such a machine is costly and not available in the cleanroom in Delft. Lastly, future large-scale quantum networks will likely be based on hybrid photonic circuits at each node, as detailed in Ch. 10; rectangular device cross-sections simplify efficient coupling and bonding of diamond-based nanophotonic structures to such circuits (see Ch. 10). Thus, the remains of this chapter will focus on the quasi-isotropic diamond undercut etch process (d) to fabricate all-diamond nanophotonic structures.

8.3. PROCESS FLOW

We now proceed to give an overview of the developed process flow, as depicted in Fig. 8.2. Here, we only give a brief discussion of the most important aspects of this process, and refer the reader to the many recent review articles discussing diamond nanofabrication

| (1) Silicon Nitride Deposition (PECVD) | (6) Electron Beam Lithography | (8) Silicon Nitride Bosch Etch (CHF_3 / O_2) |
| (4) Resist spin | (7) Development | |

(9) Resist strip (PRS)	(12) Aluminium Oxide Atomic Layer Deposition	(13) Al_2O_3 ICP-RIE etch (BCl_3/Cl_2)
(10) Piranha Clean		(14) Anisotropic Diamond ICP-RIE Etch (O_2)
(11) Anisotropic Diamond ICP-RIE Etch (O_2)		

| (15) Isotropic Diamond ICP-RIE Etch (O_2) | (15) Isotropic Diamond ICP-RIE Etch (O_2) | (16) Hydrofluoric acid clean |

Figure 8.2: Process flow used to fabricate photonic crystal cavities and waveguides in diamond. See Tab. 8.1 for a detailed overview of the parameters of each step, as well as the main text for a discussion.

in more detail [31–33]. Crucially, all important fabrication flow parameters, etch rates and selectivities can be found in Tab. 8.1. We also note that the two most important aspects of this process flow — the choice of hard mask, and the quasi-isotropic etching of diamond along crystal planes that can be exploited to fabricate free-hanging structures — will be discussed after this more general overview in detail in Secs. 8.4 and 8.5, respectively.

We start fabrication by plasma-enhanced chemical vapor deposition (PECVD) of a Si_3N_4 layer (step 1) on a commercially available, polished diamond grown via chemical-vapor-deposition (CVD) (Element Six, top surface [100]). We then spin coat a thin resist layer on top of the Si_3N_4 layer (steps 2-4), in which we pattern the desired nanophotonic structures using electron beam lithography (using a thin conducting polymer layer on top of the resist to avoid charging effects that can distort the desired pattern, steps 5 and 6). After subsequent development (step 7), we transfer this pattern into the Si_3N_4 hard mask using a fluoroform-based etch (step 8, described in detail Sec. 8.4 below). We then remove the remaining resist using a combination of a photoresist stripper (to remove most resist, step 9), and a subsequent aggressive Piranha wet clean that removes any

remaining resist residues (step 10). This additional Piranha step has proven crucial to obtain a high yield of devices, as we initially observed that resist residuals can lead to uncontrolled breaking of small diamond flakes out of the top of nanobeams in the last fabrication step.

Table 8.1

Step number and name (see also Fig. 8.2)	Parameters / Remarks
1. Si_3N_4 PECVD	8 h oxygen chamber clean before deposition, 10 min chamber conditioning, deposition rate ~ 12.5 nm / min (thickness ~ 200 nm), 20 sccm SiH_4, 20 sccm NH_3, 980 sccm N_2, alternating cycles of 20 W LF (8 s), followed by 20 W RF (12 s), 650 mtorr, 300 °C, Oxford Plasmalab 80 Plus
2. Optional O_2 ash	To increase resist adhesion, 100 W, 200 sccm O_2, 30 s, PVA Tepla 300
3. Glue diamond to Si carrier chip	Pipette drop of PMMA495A4 on Si carrier chip, spin coat at 1000 rpm to distribute evenly, slide diamond in from side using tweezers, bake 2 min at 120 °C
4. CSAR13 Spin	AR-P6200.13, 4000 rpm (~ 400 nm), bake 3 min at 150 °C
5. Elektra92 Spin	AR-PC-5090, 4000 rpm (~ 30 nm), bake 2 min at 90 °C
6. Exposure	350 µC / cm^2, beam step size 2 nm, resolution 3 nm, beam current 267 pA, aperture 200 µm, 100 keV, fracturing mode 'curved follow geometry' [34], Raith EPBG5200
7. Development	60 s de-ionized water (DI), to dissolve Elektra92, followed by N_2 dry blow; 60 s pentyl acetate, 5 s ortho-xylene, 60 s IPA, N_2 dry blow
8. Si_3N_4 etch	210 seconds, 500 W ICP, 50 W RF, 60 sccm CHF_3, 6 sccm O_2, 1×10^{-7} bar, 20 °C, etch rates ~ 100 nm / min CSAR13, ~ 100 nm / min Si_3N_4, Adixen AMS 100 I-speeder
9. Resist removal	PRS 3000^{TM}, 10 minutes, 85 °C, diamond comes loose of Si piece, rinse in DI water, then IPA & dry blow
10. Piranha clean	75 ml H_2SO_4, 25 ml H_2O_2, 80 °C, 10 minutes, rinse in DI water, then dry blow
11. 1st diamond etch	Anisotropic oxygen ICP-RIE, params see Ch.5, etch rates ~ 8 (300) nm / min for Si_3N_4 (diamond), time varied (see text), Oxford Plasmalab 100
12. Al_2O_3 atomic layer deposition	220 cycles, 105 °C, 70 sccm N_2, interleaved 15 ms pulses with 11 s purge each after H_2O and TMA pulse, ~ 15 nm in 220 cycles, Oxford Flexal

8

Table 8.1 – continued from previous page

Step number and name (see also Fig. 8.2)	Parameters / Remarks
13. Al_2O_3 ICP-RIE etch	45 sccm BCl_3, 5 sccm Cl_2, 10 W RF, 600 W ICP, 20 °C, 3 μbar, etch rate ~ 29 (10) nm / min for Al_2O_3 (Si_3N_4), Oxford Plasmalab 100
14. Optional 2nd diamond etch	Anisotropic oxygen ICP-RIE, same params as step 12, time varied (see text)
15. 3rd diamond etch	Quasi-isotropic oxygen ICP-RIE, 0 W RF, 2500 W ICP, 15 μbar, 65 °C, 50 sccm O_2, time varied (see text), Oxford Plasmalab 100
16. Hydrofluoric Acid Dip	40% Hydrofluoric Acid (HF), 10 minutes, DI water rinse, N_2 dry blow

Table 8.1: Overview of fabrication steps used to fabricate rectangular photonic crystal cavities in diamond. See Fig. 8.2 for a visualization of this process flow.

Having defined the pattern in the hard mask, we next use a first anisotropic diamond etch employing an oxygen-based chemistry to transfer this pattern into the diamond (step 11). Here, we etch ~ 3 times deeper than the intended height of the final structure, to allow for precise thickness tuning via a slow upward diamond etch rate in step 15, and to obtain a flat device bottom surface (see Sec. 8.5). We then uniformly coat the full structure with a ~ 15 nm thin layer of Al_2O_3 using an atomic layer deposition (ALD) process (step 12). By anisotropically etching this layer using a boron-chlorine and chlorine based chemistry (step 13) [35], only the vertical sidewalls of the diamond remain covered with the thin Al_2O_3 layer. Crucially, this layer serves as an excellent mask to protect the sidewalls of the nanophotonic structures during a subsequent quasi-isotropic diamond etch. This etch uses an oxygen-based chemistry without any forward (RF) power to undercut the diamond structures (step 15, discussed in detail in Sec. 8.5 below), exploiting crystal-plane dependant etch rates. Additionally, by interleaving quasi-isotropic diamond etching with scanning electron microscope (SEM) inspection steps, a contrast difference between Al_2O_3 only and a combination of Al_2O_3 and diamond can be used to thickness-tune devices (also discussed in Sec. 8.5). Prior to quasi-isotropic etching, we optionally add a second anisotropic diamond etch that deepens the pattern in the diamond. While we did not study the effect of this etch on the subsequent quasi-isotropic underetch time in detail, we noticed a reduction in undercutting times when including this additional anisotropic etch step (step 14), consistent with the observations in Ref. [36]. However, the additional step can also lead to devices breaking, thus requiring a careful tradeoff (discussed in detail in Sec. 8.7). As a final process step, a hydrofluoric acid dip removes both the Si_3N_4 hard mask and the Al_2O_3 sidewall covering, uncovering all-diamond, free-hanging nanophotonic structures. Importantly, we have observed that these devices are sufficiently strong to allow for direct nitrogen dry-blowing of the sample after a DI water rinse, avoiding more time consuming methods such as critical point drying that are typically used to overcome surface-tension induced structure

8

Hard mask material	Diamond etch rate [nm/min]	Mask etch rate [nm/min]	Resulting selectivity	Used for	Ref.
HSQ	~ 200	~ 20	~ 10	Pil/PCC	[18, 38]
Au	~ 220	~ 26	~ 8	Pil	[38]
Ti	~ 200	~ 1	~ 200	Pil	[39]
W	~ 60	~ 6	~ 10	PCC	[40]
SiO_2	n. r.	n. r.	~ 40	TFHM	[14]
Si_3N_4	~ 60	~ 1.5	~ 40	WGMR	[23]
Si_3N_4	n. r.	n. r.	~ 30	PCC	[25, 26]
Si_3N_4	~ 300	~ 8	~ 38	PCC	Here

Table 8.2: Overview of materials used as a mask to transfer different nanophotonic structures into diamond using an oxygen-dominated plasma chemistry. Reported methods are in principle compatible with the process flow presented in Fig. 8.2. Whispering gallery mode resonators (WGMR), photonic crystal cavities (PCC), parabolic reflectors / nanopillars (Pil), and photonic crystal cavities fabricated via a transferred hard mask fabrication method (THFM); n. r. not reported. See text for discussion.
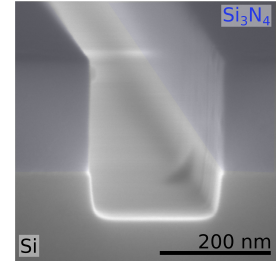
Figure 8.3: SEM image (85° tilt angle) of a nominally 200 nm wide line, transferred into a ~ 200 nm thick Si_3N_4 layer on a silicon chip via an optimized CHF_3 etch. This image corresponds to after step 8 in Fig. 8.2 / Tab. 8.2.

breaking [37].

8.4. MASK CHOICE

There are three main requirements of the mask that transfers the designed nanophotonic pattern into the diamond: a high selectivity to the diamond etch, easy and reliable patterning of the mask with nm resolution, and easy removal of the mask once nanofabrication is finished. In particular, we seek a high selectivity to the diamond etch, for two main reasons: First, a high selectivity limits mask erosion that could lead to unwanted rounding / sidewall roughness of final nanostructures. Second, this requires only a thin mask that typically leads to more uniform etch rates across small features (as a consequence of a reduced aspect ratio compared to employing a thicker mask). We here choose to decouple the mask writing and high etch selectivity to diamond requirements by using a Si_3N_4 hard mask in addition to a resist layer in the process, a choice that we will outline in this section.

Tab. 8.2 shows an overview of different mask materials that have been used to fabricate nanophotonic structures (or, to the best of our knowledge, should be compatible with such fabrication) in diamond using oxygen-based anisotropic diamond etching. This table only contains one mask that can be directly patterned (as it combines the functions of etch mask and electron beam resist): Hydrogen silsesquioxane (HSQ, chemical composition $[HSiO_{3/2}]_n$ [41]). However, HSQ features a limited selectivity to the diamond etching of ~10, challenging handling due to low shelve life and bad adhesion to the substrate. Additionally, it requires comparatively large electron doses to clear, which increases exposure times and can cause unwanted charging effects [33, 42]. We therefore refrain from using it for this process. This leaves us with hard masks that can not be directly patterned, thus requiring writing of an additional resist layer. After transferring the written pattern into this "hard mask", it then serves as a resistant mask to the subsequent diamond etch.

A reported choice of hard masks are metallic layers (e.g. Au, Ti, W), with reported selectivities of up to ~ 200 for the case of Ti [39]. However, the sidewall roughness of the diamond structures in Ref. [39] is relatively high (which was not problematic for the sidewalls of atomic force microscope tips that were fabricated in this reference), preventing us to use this material here. Additionally, metals have been suspected to be a source of detrimental scattering loss that ultimately limits quality factors. While this is likely not the main source of losses in first generation devices, it might ultimately limit device quality factors. We therefore choose to use a non-metallic material for fabrication that should allow us to overcome this potential limitation a priori. Another reported hard mask material is SiO_2 [14]. However, in Ref. [36], it was reported that depositing SiO_2 on diamond leads to stress induced cracking of SiO_2 layers, making them unsuitable for fabrication.

Instead, we here use Si_3N_4 as a hard mask, with reported selectivities to an oxygen-based diamond ICP-RIE etch of up to ~ 40. This material has been used to fabricate different nanophotonic structures, including whispering gallery mode resonators [23] and photonic crystal cavities [25, 26] in diamond. Furthermore, highly optimized etch procedures to transfer the resist pattern into the diamond were readily available in our cleanroom, using a pseudo-Bosch ICP-RIE etch employing a fluoroform-based chemistry and CSAR-6200.13 resist (see Tab. 8.1) [43]. A resulting optimized etch profile of 200 nm-wide test lines, obtained by patterning and etching a layer of Si_3N_4 on a Si wafer, breaking the resulting lines perpendicularly, and imaging them in a SEM under a 85° angle, can be seen in Fig. 8.3 (see Ref. [34] for details of this method). It shows that the resulting Si_3N_4 etch profile is smooth, straight, and shows no significant widening. While the employed CSAR-6200.13 resist [44] widens in this etch (see Ref. [45] for details), the Si_3N_4 sidewalls feature the desired close-to-vertical profile. Additional ellipsometer measurements confirm an etch selectivity of this hard mask to a subsequent diamond etch of ~ 38, in accordance with the values reported in literature [23, 25, 26]. We note that we initially used C_4F_8/SF_6 and CHF_3/Ar based chemistries to etch the Si_3N_4, however the resulting lines showed either significant widening (C_4F_8/SF_6), or a much reduced selectivity (CHF_3/Ar). For details on these etch optimizations, please see Ref. [45].

8.5. (Quasi-) isotropic ICP-RIE etching in diamond

Our process critically relies on the selective quasi-isotropic ICP-RIE etching of diamond along crystal planes, as first demonstrated in Refs. [23, 24]. This process was inspired by the single-crystal reactive etching and metallization (SCREAM) process [46], introduced in the 1990s to selectively etch single-crystal silicon along crystal planes, and is a process widely adopted in nanofabrication. The process relies on tuning the etching regime close to the transition point between physical (etch process dominated by an ion's kinetic energy) and chemical (etch process dominated by the chemical etching barrier) etching, as demonstrated in Ref. [47]: By tuning the kinetic energy of the reactive ions (achieved via changing the RF power applied to the plasma), it was shown that when lowering the oxygen ions' energy to below ~ 60 eV (corresponding to applied RF voltages of below ~ 40 W), crystallographic etching in diamond can be observed. As the applied bias is reduced, the observable etch planes change, with the {111} family of lattice planes being revealed for the case of zero applied bias as the etching is slowest along the <111> crystallographic

8
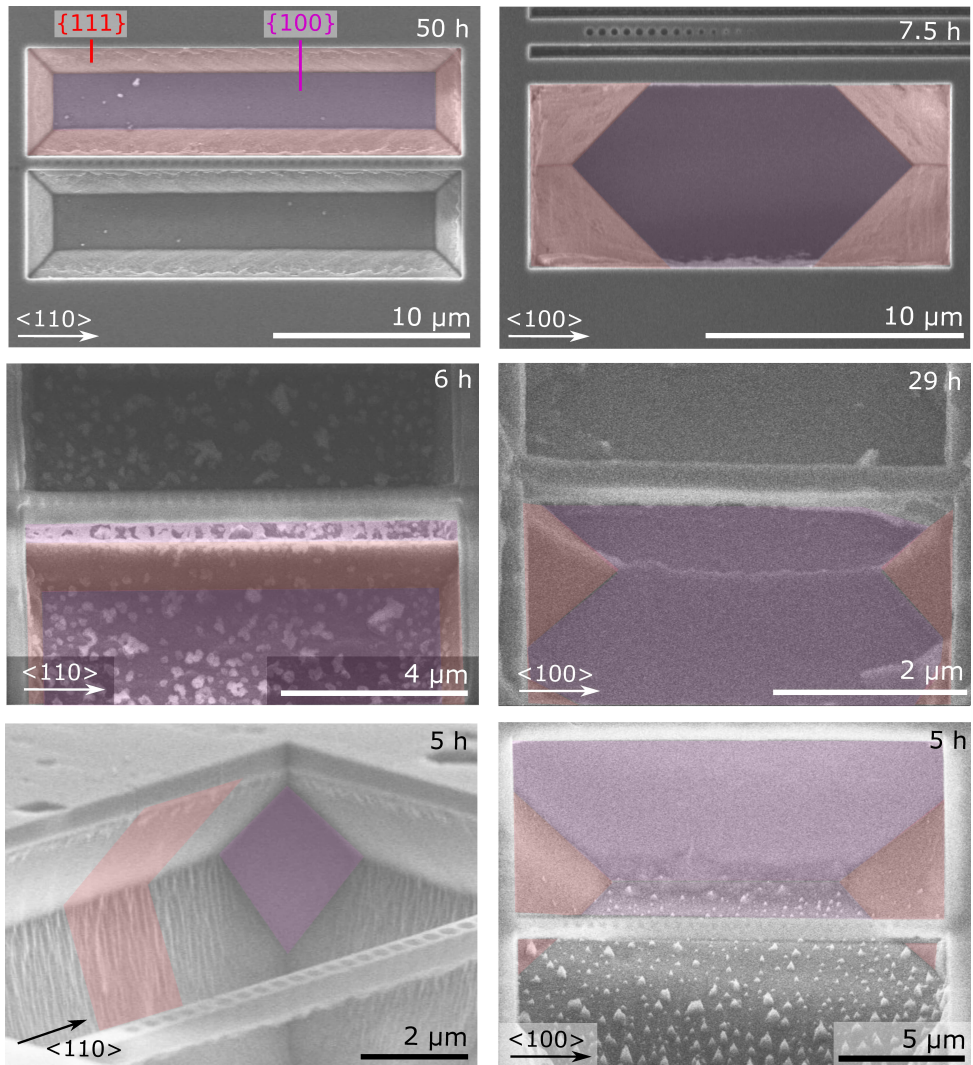
Figure 8.4: SEM images of diamond nanobeams aligned along <110> (left figures) and <100> (right figures) crystallographic directions, quasi-isotropically underetched using an oxygen-based ICP-RIE etch with no forward power (see text). (Top, middle, bottom left, bottom right) images correspond to angles in the SEM of (0°, 25°, 75°, 45°), respectively. Number in the top right corner of each image indicates the total quasi-isotropic underetch time. A balance between chemical and physical etching results in crystallographic direction dependant etch rates (see text). This leads to underetching that starts evenly along the beam (<110> aligned beams) or spreads sideways from the middle (<100> aligned beams). Note that the images in the bottom row, as well as the top right image, have been obtained for reduced quasi-isotropic oxygen etch plasma pressure (going from ~100 µbar to ~15 µbar), resulting in a larger relative contribution of physical etching, and thus deeper trenches next to nanobeams / reduced etch times.

directions. While the work employed in Ref. [47] uses a temperature of ~ 10 °C, other groups [23–25, 48] showed that a higher isotropic temperature of ~ (200 − 250) °C results in significantly reduced undercut times, as well as less deep etches into the diamond (along the <100> direction), although a detailed characterization of this dependency has not been reported in literature. Qualitatively, this effect can be understood by a higher plasma temperature (or similarly a higher plasma pressure) increasing the relative rate of chemical to physical etching. Currently, the oxygen-based chemistry ICP-RIE etcher at our processing facility (Kavli Nanolab Delft, Oxford PlasmaLab 100) only supports etch temperatures of up to 65 °C; we thus expect increased undercut etch times compared to previous work focusing on the fabrication of quasi-isotropically etched photonic crystal cavities in diamond [23–25, 48].

Fig. 8.4 shows SEM images of diamond nanobeams aligned along the <110> (left side) and <100> (right side) crystallographic directions, after the quasi-isotropic undercut etch (see images for undercut times). It can be seen that etching is slowest along the {111} family of lattice planes, and fastest along the [100] direction. Thus, by aligning nanobeams along the <110> crystallographic directions, we can ensure that the whole nanobeam is evenly undercut [see Fig. 8.4(left, middle)] before the diamond is etched upwards slowly (allowing for thickness tuning discussed below). In contrast, for beams aligned along the <100> crystallographic directions, the undercut starts from the middle of the beam and spreads sidewards, as the {111} families of planes get etched away slowly [see Fig. 8.4(right, middle)]; this can result in an uneven thickness profile of undercut structures.

For the photonic crystal nanobeams to work as intended in simulation, we rely on a rectangular device cross-section, and precise nanobeam thickness, see Ch. 7. Fig. 8.5 shows the evolution of the nanobeam device cross-section and thickness throughout the etch process. After 4 hours of isotropic etching, the {111} families of lattice planes are visible at the device bottom of <110> oriented nanobeams [Fig. 8.5(a)], before an additional 2 hours of etching flattens the bottom surface [Fig. 8.5(b)]. An additional isotropic oxygen etch (for a total of 16 hours in the case of Fig. 8.5(c), here shown for a <100> oriented device) then slowly reduces the nanobeam's thickness, starting from the bottom. Crucially, a contrast difference between areas of diamond covered with Al_2O_3, and just Al_2O_3 (where the diamond has already been etched away) allows to fine-tune the device thickness (compare Figs. 8.5(c,d) which are SEM images of the same waveguide taper before and after the hydrofluoric acid dip).

So far, challenges associated with the repeatability of the process flow (see also Sec. 8.7 below) have prevented us from quantifying the etch rates along different crystal planes, and for different etching parameters. Apart from the observation of a quadratic dependence of undercut and upwards etch rates on time [23], and the qualitative observation that higher plasma temperatures and pressures reduce the time needed to undercut and thickness tune nanobeams [36], a concise study of the etch rates and their dependence on plasma parameters for quasi-isotropic diamond etching remains elusive in literature, to the best of our knowledge. We expect that such a study could not only help to quantify the process and thus find optimal parameter regimes, but also be of significant value to determine whether the principle of fabricating free-hanging, all-diamond nanostrucutres is conceivable for diamonds cut along different crystallographic direc-

8
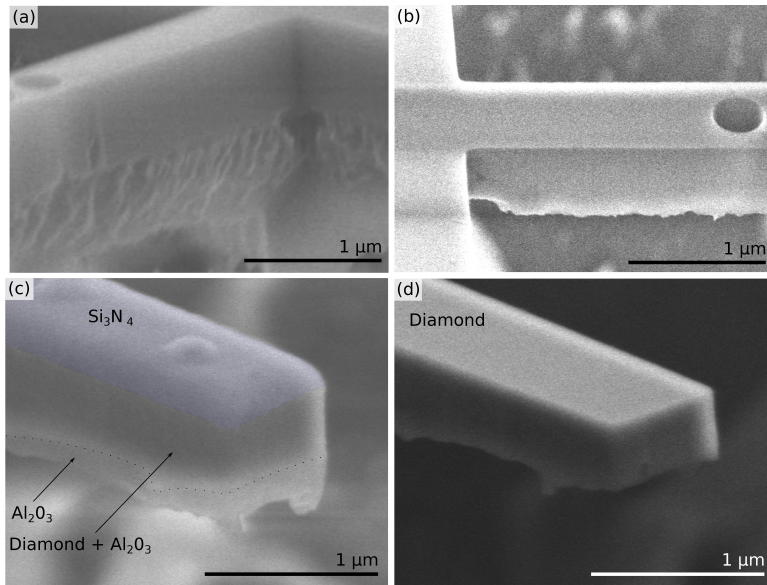
Figure 8.5: SEM images of quasi-isotropically etched diamond nanobeams oriented along <110> (a, b) and <100> crystallographic directions (c,d), for quasi-isotropic plasma exposures of 4h (a), 6h (b), and 16h (c,d). Images are taken before (c) and after (a,b,d) the hydrofluoric acid etch (final fabrication step 16 in Tab. 8.1, to remove Si_3N_4 and Al_2O_3). The crystal-plane dependant etch rates first reveal the {111} planes (a), before the slower etching along the $[\bar{1}00]$ direction flattens and thins the nanobeam from the bottom upwards. A resulting contrast in SEM images between areas of diamond covered with Al_2O_3, and just Al_2O_3 (where the diamond has already been etched away) allows to fine-tune the device thickness, as visible in SEM images showing the same waveguide edge before (c) and after (d) the hydrofluoric acid etch.

tions, as this could increase the electric field overlap of the cavity with the emitters (depending on the color center in diamond emitter and transition, dipoles are either parallel or perpendicular oriented w.r.t. <111> directions [49, 50]).

8.6. FABRICATED DEVICES AND THEIR QUALITY

Example SEM images of all-diamond photonic crystal nanobeams, oriented along <100> and <110> crystallopgrahic directions, can be seen in Fig. 8.6. These beams are designed to operate at ~1550 nm, as a setup to extract the optical quality factors of cavities resonant with this wavelength is available in Delft, while a setup for ~ 620 nm light is under construction. The images show that devices can be fabricated in parallel fashion, with the potential to fabricate hundreds of devices on a single chip. For the sample displayed in Figs. 8.6(b-d), the total quasi-isotropic etch time is 5 h, resulting in nanobeams of thickness ~ 420 nm (nanobeams along <100> crystallographic direction), and ~ 710 nm (nanobeams along <110> crystallographic direction). As expected, the combination of etching along the {100} and {111} families of lattice planes leads to a faster etching for <100> oriented nanobeams (see Sec. 8.5). Here, the <110> oriented nanobeams are thicker than what is expected from the first anisotropic diamond etch (~ 675 nm). This can explain the relatively rough bottom surface visible in Fig. 8.6(c), as the bottom
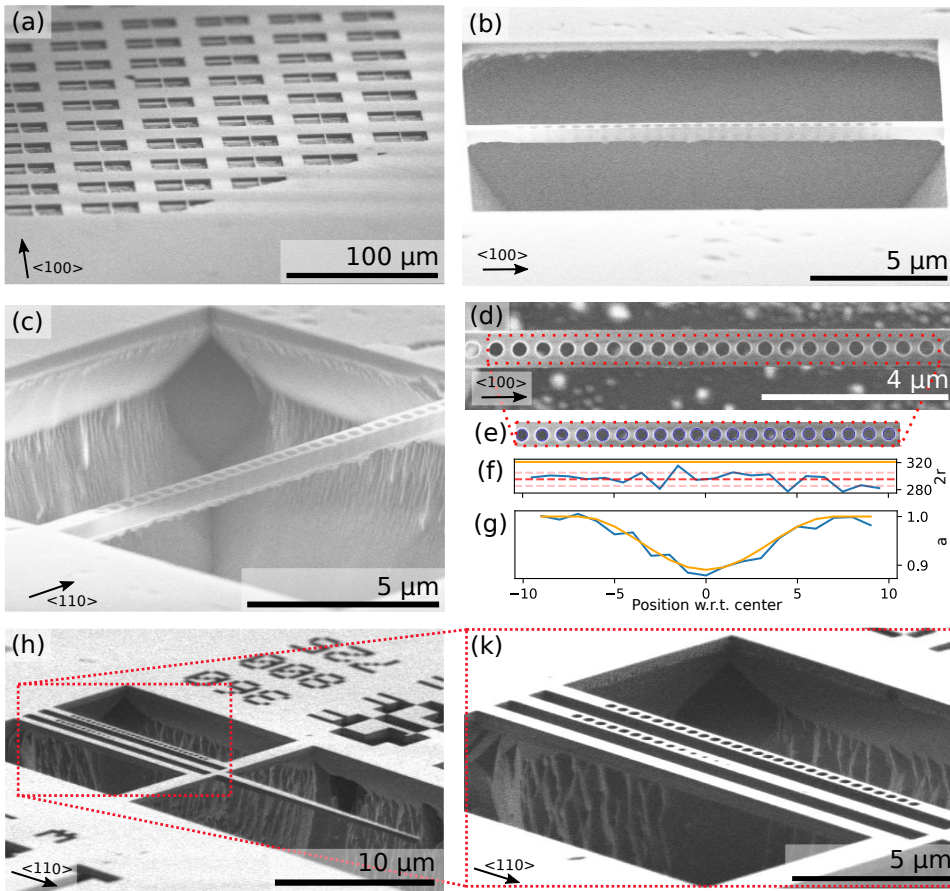
Figure 8.6: SEM images of diamond nanobeams after all processing steps (after step 16 in Tab. 8.1), for beams oriented along <100> (a, b, d), and <110> crystallographic directions, and extracted hole radius (e, f) and lattice spacing (e, g). Images (a), (b, c, d), and (h, k) correspond to samples etched with total isotropic underetch times of 4h, 5h, and 14h, respectively. (a,b,c) are recorded under 75° tilt angle and show that devices are fully undercut, while (d) is a top-view image that demonstrates that the holes used to define the photonic crystal are fully etched through, with the red dashed region showing the area used to automatically detect hole positions and diameters (e, found circles overlaid in blue). (f) and (g) show target (orange) and measured (blue) hole diameter, $2r$, and lattice spacing, a, vs. position from the nanobeam center. Bright and light red dashed lines in (f) correspond to the mean and standard deviation of the data, respectively. (h, k) photonic crystal nanobeam, tapered waveguide terminated in a mirror (to be used to couple to the photonic crystal nanobeam with an etched fiber, as discussed in Ch. 7), and a planar waveguide aligned along the <110> crystallographic direction, after all fabrication (70° tilt angle).

surface has not flattened out fully yet for this <110> oriented beam, in contrast to the structures aligned along the <100> direction [see Fig. 8.6(b)]. We attribute the macroscopic bottom roughness in Fig. 8.6(b) to uneven etching as a consequence from a non-optimized clearing of the diamond surface that leads to the formation of pillars; this is also visible in the background of Fig. 8.6(d). For further details on the surface roughness

	Original simulation	<100> PCC	<110> PCC
Width	690 nm	~ 700 nm	~ 700 nm
Hole diameter	338 nm	~ 340 nm	~ 340 nm
Thickness	568 nm	~ 420 nm	~ 720 nm
Lattice spacing	507 nm	~ 522 nm	~ 500 nm
Simulated Q	~ 1×10^6	~ 5.3×10^5	~ 9×10^5
Simulated λ_c	~ 1531 nm	~ 1501 nm	~ 1548 nm

Table 8.3: Overview of originally simulated photonic crystal cavity (PCC) parameters, and of measured PCC parameters for PCC alignment along the <100> and <110> crystallographic directions. We simulate the optical quality factor, Q, and cavity resonance wavelength λ_c corresponding to those values, assuming perfect hole placement (see Ch. 7 for details).

of nanobeams, see Sec. 8.7 below.

Fig. 8.6(d) displays a top view SEM image of a <100> oriented device, showing that the holes that modulate the effective refractive index of the diamond along the axis of light propagation are fully opened. We use a image recognition script in Matlab© to analyze SEM images regarding the width, lattice spacing, and hole diameter of the resulting structures [Fig. 8.6(e)], and to compare these values to the intended design parameters. As expected, the relative lattice spacings in Fig. 8.6(g) resemble the intended values within measurement errors. We thus here use the mean value of the nominal lattice spacings to correct the SEM scalebar. The extracted hole diameters [Fig. 8.6(f)] feature a significant tapering throughout the beam height [~ 380 nm diameter on the top as measured from SEM images and ~ (300/295) nm diameter on the bottom of the ~ 420 nm thick nanobeam in Fig. 8.6(d)] as extracted from SEM / software measurements. While the software allows us to extract a standard deviation of ~ 10 nm for the standard deviation of the holes, we note that the current resolution of SEM images (limited by charging of the non-conducting diamond during imaging) leads to measurement uncertainties on a comparable length scale. While we have not yet simulated the effect of the hole angling on the device quality, we expect it to be a non-negligible contribution reducing the device quality factors, yet also note that this effect should be less critical for the intended device thickness of ~ 230 nm associated with a resonant wavelength of ~ 620 nm (see Ch. 7).

Tab. 8.3 shows an overview of original simulation values (i.e. values obtained when maximizing structures for highest Purcell enhancement, as outlined in Ch. 7) and values extracted from SEM images similar to the one in Fig. 8.6(d), as well as corresponding simulation results. Following this results table, we opted to measure 5 devices oriented along the <100> crystallographic direction, by positioning tapered fibers [51] over the middle of the nanobeams, and measuring a peak in reflected signal when a laser's frequency (Santec TSL-530, tuning range ~ (1500-1630) nm) is scanned over the cavity resonance (for which the enhanced intra-cavity lightfield can be collected back by the fiber with low efficiency) [34]. This resulted in four devices with quality factors of around 1×10^3, with wavelengths ranging from (1520 - 1540) nm, and one device with Q = $5.8^{+0.3}_{-0.2} \times 10^3$ at ~ 1510 nm (compared to a simulation value of Q 5.3×10^5 at a wavelength of ~ 1501 nm). While the lattice spacing for these devices was varied from 482 nm - 533 nm over 10 steps, we have not observed scaling of wavelengths with this design parameter, in con-

trast to our expectations from Ch. 7. We attribute this discrepancy to a combination of device bottom roughness, angled holes, and varying hole sizes. These effects will be the subject of future investigation.

Fig. 8.6(h) shows an SEM image of all-diamond nanophotonic structures after all fabrication that features the full intended device design, discussed in Ch. 7. This design consists of two photonic crystal nanobeams, each next to a tapered waveguide terminated in a mirror, that allows for evanescent field coupling of light from the waveguide to the nanophotonic cavities. Here, we used a simplified design, for which one photonic crystal cavity was replaced by a simple rectangular waveguide. Next steps will focus on testing the fiber-coupling efficiency to the waveguides and from the waveguides to the cavities, and on measuring the quality factors of optimized photonic crystal nanobeams.

8.7. CURRENT CHALLENGES AND RESEARCH DIRECTIONS

Having discussed the current quality of fabricated photonic crystal cavities, we now move on to highlight current challenges on the way to a reliable process yielding high-quality nanophotonic structures.

8.7.1. BREAKING OF SIDEWALL PROTECTION

As introduced in Sec. 8.4, the Si_3N_4 hard mask serves to protect the nanophotonic structures from the top during the anisotropic and isotropic diamond etches. As discussed in Sec. 8.5, this allows to pattern and release nanophotonic structures from the bulk diamond material. A frequent breaking mechanism for nanobeams occurs at the interface of Si_3N_4 and diamond, which are both supposed to be protected with Al_2O_3: when the Si_3N_4 sidewall protection is etched through, the isotropic oxygen etch breaks into the diamond from this interface, as can be seen in Fig. 8.7(a). Fig. 8.7(b) gives a hint to the underlying mechanism: a large angling of the Si_3N_4 hard mask on top of the diamond can be observed. Figs. 8.7(c,d) show images of nominally 200 nm wide etch test lines of Si_3N_4 on a Si wafer after Piranha cleaning (c, step 10 in Tab. 8.1), and after a subsequent first anisotropic oxygen etch for 5 minutes (d, using the parameters of step 11 in Tab. 8.1). While the resist pattern is transferred well into the Si_3N_4 hard mask (step 8 in Tab. 8.1), the finite selectivity of the subsequent anisotropic oxygen etch leads to a mask erosion and rounding of the corners, as well as a material re-deposition of a currently unknown material[1]. For sufficiently long anisotropic diamond etches, the Si_3N_4 mask is (almost) completely etched away at the edges of the diamond. While the subsequent Al_2O_3 atomic layer deposition coats these surfaces, the subsequent Al_2O_3 etch (typically timed to over-etch the Al_2O_3 by about 25 % to guarantee uniform clearing throughout the sample) then further thins this region, to the point where the hard mask is potentially broken at the edges (especially when combined with an additional second anisotropic diamond etch afterwards). While we have varied the plasma parameters during anisotropic oxy-

---

[1]Initial tests showed that this material could not be removed in a subsequent Piranha clean. Previous work has shown that hard mask erosion can lead to unwanted particle re-deposition during anisotropic diamond etching with oxygen [52, 53]; this is often overcome by continuously interleaving oxygen etching with short bursts of an etch chemistry that can remove this redeposition (for which the mask is generally etched at a comparable rate). Thus, such processes require careful balance, and we plan on investigating this in more detail in future work.
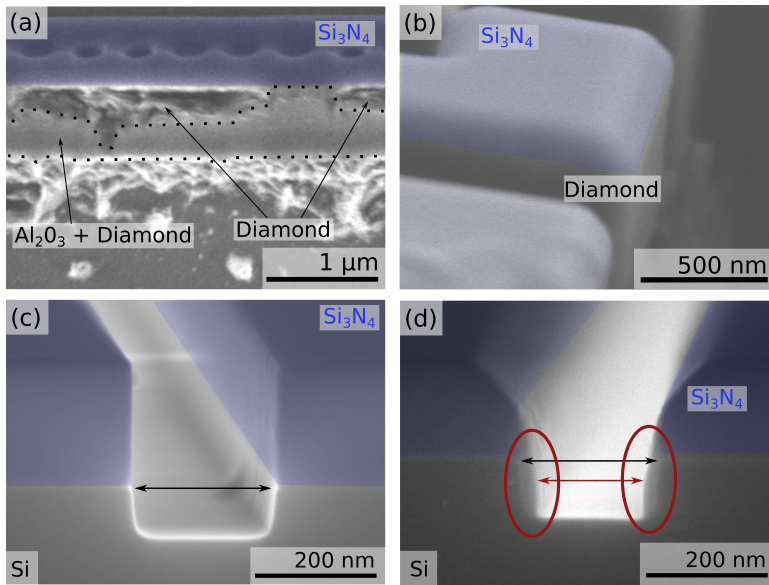
Figure 8.7: Breaking mechanism of nanobeams along the Si_3N_4 hard mask bottom, observed via SEM images after various fabrication steps. (a,b) SEM images (75° tilt) after 5h of isotropic etching (corresponding to after step 15 in Tab. 8.1), showing that the Al_2O_3 mask starts breaking from the diamond-Si_3N_4 interface (a), and that the Si_3N_4 mask is severely angled (b). (c,d) SEM images of nominally 200 nm wide test etch lines in Si_3N_4 on a Si wafer (cleaved after fabrication and inspected under a 85° tilt angle) after resist pattern transfer into the hard mask and Piranha cleaning (c, corresponding to after step 10 in Tab. 8.1), and after 5 minutes of anisotropic etching with oxygen (d, corresponding to after step 11 in Tab. 8.1). While the profile after pattern transfer and Piranha cleaning is close to the desired shape (black arrow shows a width of ~ 225 nm), subsequent oxygen etching leads to rounding of the sidewalls, as well as material redeposition (red arrow ~ 175 nm).

8

gen over a broad range [varying the ratio of ICP to RF power from our common 12:1 (see Tab. 8.1) via a ration of 10:1 [23] all the way down to 2:1 [25]], we have qualitatively observed the same mask erosion behaviour for all these parameter variations.

    One way to fabricate devices successfully is to shorten the anisotropic etching to one step (step 11 in Tab. 8.1 that defines the initial nanobeam thickness), and completely omit the second anisotropic etch step; this reduces the anisotropic etch times from ~ (5-7) min to ~ 2 min. While this increases the time needed to undercut structures (as discussed in Sec. 8.5), we have observed that omitting the second anisotropic etch limits mask erosion to the point where devices can be fabricated reliably. Additionally, the Al_2O_3 can be reliably cleared (by over-etching the Al_2O_3), without exposing the top side surfaces of nanobeams. A second method to limit mask erosion could be to optimize the deposition of Si_3N_4 (using e.g. LPCVD instead of PECVD, changing the relative gas ratios, or using rapid thermal annealing), as it has been shown that this can have a significant influence on the composition of the resulting films [54, 55]. Finally, we expect that a more systematic study of the dependence of the Si_3N_4 angling on anisotropic oxygen etch parameters could enable to find a regime where the chemical etching of the Si_3N_4 can be further reduced while keeping a high selectivity to the diamond etch and creating
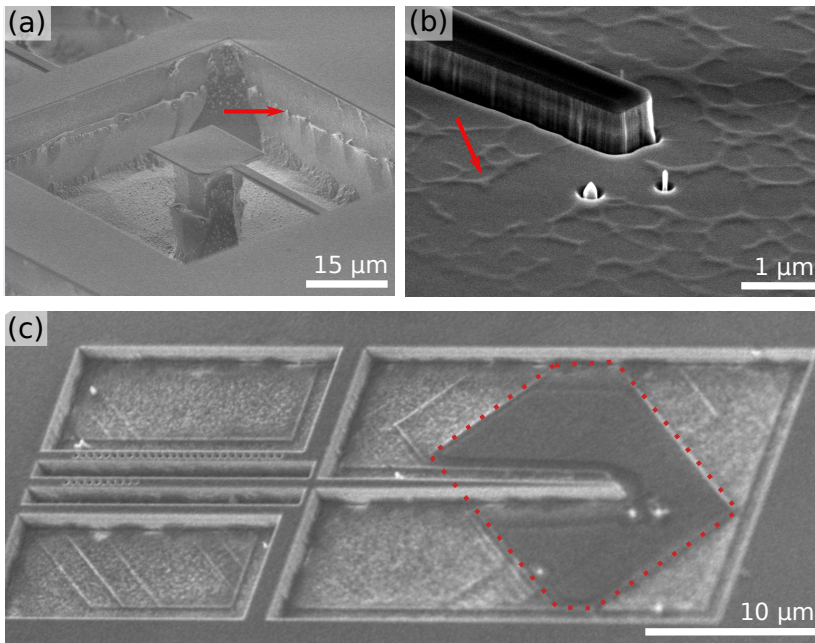
Figure 8.8: Unintended feature masking. (a) SEM image (62° tilt angle) after isotropic etching for a total of 12.5 h, performed in steps of 5 h and 7.5 h. Red arrow indicates a line of increased surface roughness coinciding with the downwards etched depth after the first isotropic etch. (b) SEM image (62° tilt angle) showing the formation of an unknown material (indicated with a red arrow) after the 1st anisotropic oxygen etch. (c) SEM image (45° tilt angle) after isotropic etching for five hours. Red dashed area corresponds to an area SEMed repeatedly before this isotropic etch.

smooth diamond surfaces [56, 57].

8.7.2. Unintended feature masking

For the fabrication process to proceed as intended and result in microscopically and macroscopically smooth surfaces, it is important to avoid unwanted masking during etching that can result in detrimental surface profiles. Fig. 8.8 shows an overview of unwanted masking observed during fabrication. Fig. 8.8(a) displays a sample after a total of 12.5 h of isotropic etching, performed in two steps. As indicated with a red arrow, a line of increased surface roughness is visible that coincides with the etched depth after the first isotropic etch. Since the sidewalls are smooth above this line, this could indicate that a thin layer that acts as a mask for subsequent etching formed after the 1st isotropic etch had finished. This layer then opened in an uncontrolled fashion during the subsequent isotropic etch, resulting in increased sidewall roughness. Another explanation for this line could be that the ratio of physical to chemical etching is increased for some time after taking the sample out of the etcher (potentially as a result of a temperature lag leading to increasing chemical etch rates over time) - this would mean that the layer could also be formed continuously during etching, but in case the chemical etch rate is the main contributor to etching, this layer might be removed fast enough to not lead

to nucleation. Fig. 8.8(b) shows an SEM image of the diamond after the 1st anisotropic diamond etch, with a red arrow indicating some thin material deposition on the surface. As there is no pillars of continuously varying height visible, this is likely formed after the sample has been taken out of the etcher. Fig. 8.8(c) shows a SEM image of a diamond sample after 5 h of isotropic etching, with a red dashed box indicating an area which had been SEMed repeatedly before the isotropic etching. Importantly, this SEMed area did not etch, indicating that a thin, unwanted layer had formed that was sufficiently strong to act as a mask during the subsequent isotropic etch. This mask is likely formed by electron-irradiation induced cross-linking of organic molecules in the SEM ("carbon deposition"), as discussed in Ref. [58]. As our process crucially relies on SEM inspection in between isotropic etch steps to fine-tune device thicknesses (see Sec. 8.5), it will be important to find a way of imaging samples without affecting subsequent processing steps, as this deposition acts as a mask during subsequent etching and thus leads to increased surface roughness, inconsistent etch rates, and sometimes even a stopping of the upward etch altogether. All other groups that have reported on the fabrication of all-diamond nanophotonic structures using the isotropic undercut etch process use a high temperature etch process, and we have confirmed with them that they do not observe this problem. This might indicate that the chemical etch rates in the low temperature plasma regime are too low to clear such formed masking layers. Future research will also focus on both ensuring low-temperature SEM sample inspection and reducing beam currents and acceleration voltages even further, as it has been observed in Ref. [58] that this can significantly reduce carbon deposition. Additionally, it has been shown that overnight sample cleaning in methanol can remove most carbon deposition [58].

8.7.3. ROUGHNESS OF DEVICE SURFACES

For optimal performance of photonic crystal nanobeams, surface-roughness-induced light scattering needs to be minimized (see also Ch. 5). Fig. 8.9 shows high resolution SEM images of photonic crystal cavities and pillars. Fig. 8.9(a) depicts the bottom and one sidewall of a nanobeam, originally aligned along the <110> crystallographic direction. After all fabrication (including a total isotropic etch time of 10 h and a subsequent HF dip), the nanobeam was broken from the diamond frame, and flipped such that the bottom surface is facing upwards. While the sidewalls show no visible surface roughness (apart from slight, localized mask breaking, highlighted with a red circle and discussed below), the bottom surface roughness is visibly increased, likely a result from not-yet flattened out {111} planes [25]. Fig. 8.9(b) shows the bottom surface of a nanobeam from the same diamond device after all fabrication, but aligned along the <100> crystallographic direction. As expected, the upward etching is faster for nanobeams aligned along this direction (see Sec. 8.5), resulting in flatter device bottom surfaces. By prolonging the upward etch time, we expect to be able to achieve even flatter bottom surfaces in the future. Future work will additionally focus on obtaining a quantitative understanding of the bottom surface roughness of nanophotonic devices and on the dependence of this roughness on etch parameters, e.g. by using atomic force microscopy. Fig. 8.9(c) shows an SEM image of the roughness of the top surface and sidewalls of a <110> oriented nanobeam cavity, photonic crystal mirror, and waveguide, after all fabrication from the same diamond device. No diamond degradation on top of the structures is visible.
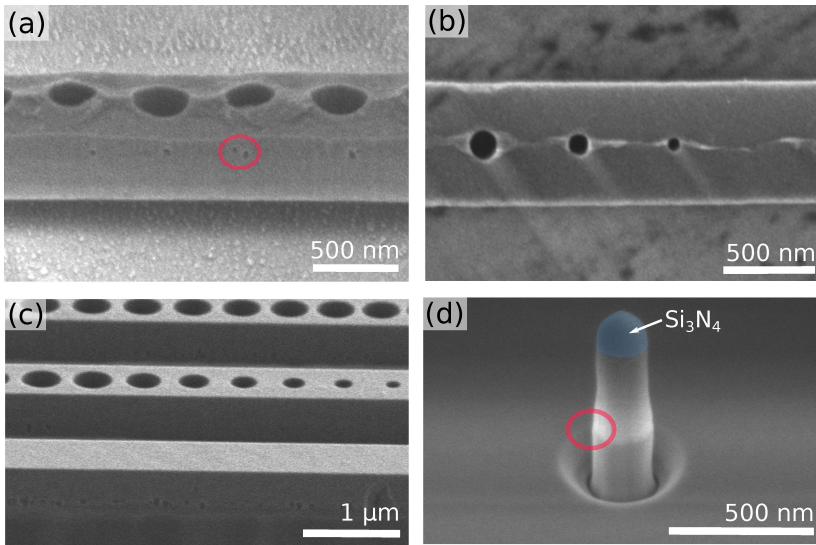
Figure 8.9: Sidewall, top and bottom roughness of photonic crystal nanobeams and pillars. SEM images (0° tilt) of the bottom surface and sidewalls of nanobeams originally aligned along the <110> (a) and <100> (b) crystallographic directions, and SEM image (62° tilt) of the top and sidewalls (c) of a nanobeam aligned along the <110> crystallographic direction, after all fabrication (total isotropic etch time 10 h). Red circle in (a) highlights an area for which the sidewall protecting mask has partially broken, leading to increased surface roughness. (d) SEM image (45° tilt) of a pillar after 1st anisotropic oxygen etch. Red circle in (d) highlights an area for which the diameter of the pillar changes. The distance of this region from the bottom of the Si_3N_4 mask roughly corresponds to the distance of the red encircled area in (a) from the top of the nanobeam.

To understand the partial breaking mechanism of device sidewalls visible in Fig. 8.9(a), Fig. 8.9(d) shows an SEM image of a nanophotonic pillar after the 1st anisotropic diamond etch. A transition in sidewall profile, highlighted with a red circle, is visible. We can exclude the possibility of this feature to be charging induced in the SEM as the shape difference and line remain visible under different SEM parameters, in particular different accelaration voltages and tilt angles. Importantly, the distance of this feature from the bottom of the Si_3N_4 hard mask is approximately the same than for the features in Fig. 8.9(a), indicating a potential link between these observations. As the diamond diameter increases in the region highlighted in red, the Al_2O_3 hard mask is (partially) etched away in this area during the anisotropic etch used to open the Al_2O_3 mask; this then translates into sidewall breaking during the subsequent isotropic diamond etch. We expect that the transition angle observed in Fig. 8.9(d) can be further reduced in the future by increasing the relative ratio of RF to ICP power during anisotropic oxygen diamond etching, as discussed in Ref. [47].

8.8. SUMMARY AND OUTLOOK

In summary, we have reported on the fabrication and characterization of all-diamond photonic crystal nanobeams in diamond with (100) top faces. Our process critically relies on the (quasi-)isotropic dry etching of diamond. We observe different quasi-isotropic

etch rates for nanobeams aligned along the the <100> and <110> crystallographic directions, in accordance with literature. Future research will focus on increasing the process reliability and throughput by further increasing the chemical etch rates during isotropic diamond etching, employing a new high temperature etcher. This might enable us to overcome challenges related to the (inconsistently observed) formation of thin (potentially carbon-based) layers in between isotropic etch steps which currently limit fabrication. Combined with further hard mask optimization to reduce isotropic etch times and increase fabrication tolerances to etch rate fluctuations, this should allow for the fabrication of high quality photonic crystal cavities with resonance wavelengths ∼ 620 nm. Single-sided tapered single mode fibers will be fabricated to couple to tapered waveguides with high efficiency. They will be used to observe tuning of photonic crystal resonance wavelengths with design parameters, a crucial step for matching the resonance wavelengths of the cavities within ∼ 10 nm from their target value. We plan on using gas tuning to fine-tune and overlap cavity resonances with the color frequency transitions [11, 19, 59]. We will study the dependence of device sidewall roughness on etch parameters, and note that it might be possible to further reduce the surface roughness of fabricated structures by a high temperature treatment followed by a tri-acid clean post fabrication; this mechanism relies on the formation and removal of graphite on the diamond surfaces [60].

Looking forward, color centers will be embedded in the photonic crystal cavities. Potential strategies include direct focused ion implantation [19, 28], or ion implantation through a photo-resist mask aligned with the nanophotonic structures [61], both after fabrication of the cavities. A third method is to fabricate nanophotonic structures around pre-localized emitters [26]. All techniques can achieve alignment accuracies of the color center in the electric field maximum of the photonic crystal cavity ∼ 20 nm. While the currently employed diamonds with (100) top face orientation feature non-optimal overlap of the color center's transition dipole with the cavity polarization, structures formed in diamond with (111) top face orientation can in principle reach unity overlap. Thus, future research will focus on extending fabrication capabilities to form photonic crystal cavities in such material [36].

In the longer run, we plan on integrating photonic crystal cavities in hybrid photonic circuits, using a pick and place technique [28]. As discussed in Ch. 10, this method has the potential to optimize the fabrication of components individually, and thus reach optimal device performance and yield. We expect the diamond micromanipulation techniques developed in Ch. 9 to be of critical importance for these tasks.

ACKNOWLEDGEMENTS

REFERENCES

[1] T. Van Der Sar, J. Hagemeier, W. Pfaff, E. C. Heeres, S. M. Thon, H. Kim, P. M. Petroff, T. H. Oosterkamp, D. Bouwmeester and R. Hanson, *Deterministic nanoassembly of a coupled quantum emitter-photonic crystal cavity system,* Applied Physics Letters **98**, 1 (2011).

[2] G. Calusine, A. Politi and D. D. Awschalom, *Silicon carbide photonic crystal cavities with integrated color centers,* Applied Physics Letters **105**, 1 (2014).

[3] M. Schreck, S. Gsell, R. Brescia and M. Fischer, *Ion bombardment induced buried lateral growth: The key mechanism for the synthesis of single crystal diamond wafers,* Scientific Reports **7**, 1 (2017).

[4] R. Nelz, J. Görlitz, D. Herrmann, A. Slablab, M. Challier, M. Radtke, M. Fischer, S. Gsell, M. Schreck, C. Becher and E. Neu, *Toward wafer-scale diamond nano- and quantum technologies,* APL Materials **7**, 011108 (2019).

[5] N. R. Parikh, J. D. Hunn, E. McGucken, M. L. Swanson, C. W. White, R. A. Rudder, D. P. Malta, J. B. Posthill and R. J. Markunas, *Single-crystal diamond plate liftoff achieved by ion implantation and subsequent annealing,* Applied Physics Letters **61**, 3124 (1992).

[6] B. A. Fairchild, P. Olivero, S. Rubanov, A. D. Greentree, F. Waldermann, R. A. Taylor, I. Walmsley, J. M. Smith, S. Huntington, B. C. Gibson, D. N. Jamieson and S. Prawer, *Fabrication of ultrathin single-crystal diamond membranes,* Advanced Materials **20**, 4793 (2008).

[7] O. Gaathon, J. S. Hodges, E. H. Chen, L. Li, S. Bakhru, H. Bakhru, D. Englund and R. M. Osgood, *Planar fabrication of arrays of ion-exfoliated single-crystal-diamond membranes with nitrogen-vacancy color centers,* Optical Materials **35**, 361 (2013).

[8] J. C. Lee *et al.*, *Deterministic coupling of delta-doped nitrogen vacancy centers to a nanobeam photonic crystal cavity,* Applied Physics Letters **105**, 261101 (2014).

[9] A. H. Piracha, K. Ganesan, D. W. M. Lau, A. Stacey, L. P. McGuinness, S. Tomljenovic-Hanic and S. Prawer, *Scalable fabrication of high-quality, ultra-thin single crystal diamond membrane windows,* Nanoscale **8**, 6860 (2016).

[10] A. H. Piracha, P. Rath, K. Ganesan, S. Kühn, W. H. Pernice and S. Prawer, *Scalable Fabrication of Integrated Nanophotonic Circuits on Arrays of Thin Single Crystal Diamond Membrane Windows,* Nano Letters **16**, 3341 (2016).

[11] A. Faraon, C. Santori, Z. Huang, V. M. Acosta and R. G. Beausoleil, *Coupling of Nitrogen-Vacancy Centers to Photonic Crystal Cavities in Monocrystalline Diamond,* Physical Review Letters **109**, 033604 (2012).

[12] B. J. M. Hausmann *et al.*, *Coupling of NV Centers to Photonic Crystal Nanobeams in Diamond,* Nano Letters **13**, 5791 (2013).

8

[13] J. Riedrich-Möller, C. Arend, C. Pauly, F. Mücklich, M. Fischer, S. Gsell, M. Schreck and C. Becher, *Deterministic Coupling of a Single Silicon-Vacancy Color Center to a Photonic Crystal Cavity in Diamond,* Nano Letters **14,** 5281 (2014).

[14] L. Li *et al.*, *Coherent spin control of a nanocavity-enhanced qubit in diamond,* Nature Communications **6,** 6173 (2015).

[15] J. V. Cady, O. Michel, K. W. Lee, R. N. Patel, C. J. Sarabalis, A. H. Safavi-Naeini and A. C. Bleszynski Jayich, *Diamond optomechanical crystals with embedded nitrogen-vacancy centers,* Quantum Science and Technology **4,** 024009 (2019).

[16] M. J. Burek, N. P. de Leon, B. J. Shields, B. J. M. Hausmann, Y. Chu, Q. Quan, A. S. Zibrov, H. Park, M. D. Lukin and M. Lončar, *Free-Standing Mechanical and Photonic Nanostructures in Single-Crystal Diamond,* Nano Letters **12,** 6084 (2012).

[17] I. Bayn *et al.*, *Fabrication of triangular nanobeam waveguide networks in bulk diamond using single-crystal silicon hard masks,* Applied Physics Letters **105,** 211101 (2014).

[18] M. J. Burek, Y. Chu, M. S. Z. Liddy, P. Patel, J. Rochman, S. Meesala, W. Hong, Q. Quan, M. D. Lukin and M. Lončar, *High quality-factor optical nanocavities in bulk single-crystal diamond,* Nature Communications **5,** 5718 (2014).

[19] A. Sipahigil *et al.*, *An integrated diamond nanophotonics platform for quantum-optical networks,* Science **354,** 847 (2016).

[20] H. A. Atikian, P. Latawiec, M. J. Burek, Y.-I. Sohn, S. Meesala, N. Gravel, A. B. Kouki and M. Lončar, *Freestanding nanostructures via reactive ion beam angled etching,* APL Photonics **2,** 051301 (2017).

[21] J. L. Zhang *et al.*, *Strongly Cavity-Enhanced Spontaneous Emission from Silicon-Vacancy Centers in Diamond,* Nano Letters **18,** 1360 (2018).

[22] C. T. Nguyen *et al.*, *An integrated nanophotonic quantum register based on silicon-vacancy spins in diamond,* Physical Review B **100,** 1 (2019).

[23] B. Khanaliloo, M. Mitchell, A. C. Hryciw and P. E. Barclay, *High-Q/V Monolithic Diamond Microdisks Fabricated with Quasi-isotropic Etching,* Nano Letters **15,** 5131 (2015).

[24] B. Khanaliloo, H. Jayakumar, A. C. Hryciw, D. P. Lake, H. Kaviani and P. E. Barclay, *Single-Crystal Diamond Nanobeam Waveguide Optomechanics,* Physical Review X **5,** 041051 (2015).

[25] S. Mouradian, N. H. Wan, T. Schröder and D. Englund, *Rectangular photonic crystal nanobeam cavities in bulk diamond,* Applied Physics Letters **111,** 021103 (2017).

[26] N. H. Wan, S. Mouradian and D. Englund, *Two-dimensional photonic crystal slab nanocavities on bulk single-crystal diamond,* Applied Physics Letters **112,** 141102 (2018).

8

[27] J. Zheng, B. Lienhard, G. Doerk, M. Cotlet, E. Bersin, H. S. Kim, Y.-C. Byun, C.-Y. Nam, J. Kim, C. T. Black and D. Englund, *Top-down fabrication of high-uniformity nanodiamonds by self-assembled block copolymer masks,* Scientific Reports **9**, 6914 (2019).

[28] N. H. Wan, T.-J. Lu, K. C. Chen, M. P. Walsh, M. E. Trusheim, L. De Santis, E. A. Bersin, I. B. Harris, S. L. Mouradian, I. R. Christen, E. S. Bielejec and D. Englund, *Large-scale integration of artificial atoms in hybrid photonic circuits,* Nature **583**, 226 (2020).

[29] M. K. Bhaskar, R. Riedinger, B. Machielse, D. S. Levonian, C. T. Nguyen, E. N. Knall, H. Park, D. Englund, M. Lončar, D. D. Sukachev and M. D. Lukin, *Experimental demonstration of memory-enhanced quantum communication,* Nature **580**, 60 (2020).

[30] I. Bayn, B. Meyler, J. Salzman and R. Kalish, *Triangular nanobeam photonic cavities in single-crystal diamond,* New Journal of Physics **13**, 025018 (2011).

[31] S. Mi, M. Kiss, T. Graziosi and N. Quack, *Integrated photonic devices in single crystal diamond,* Journal of Physics: Photonics **2**, 042001 (2020).

[32] A. Toros, M. Kiss, T. Graziosi, S. Mi, R. Berrazouane, M. Naamoun, J. Vukajlovic Plestina, P. Gallo and N. Quack, *Reactive ion etching of single crystal diamond by inductively coupled plasma: State of the art and catalog of recipes,* Diamond and Related Materials **108**, 107839 (2020).

[33] D. Rani, O. R. Opaluch and E. Neu, *Recent Advances in Single Crystal Diamond Device Fabrication for Photonics, Sensing and Nanomechanics,* Micromachines **12**, 36 (2020).

[34] J. T. Hill, *Nonlinear Optics and Wavelength Translation via Cavity-Optomechanics,* Ph.D. thesis, Caltech **2013** (2013).

[35] S.-M. Koo, D.-P. Kim, K.-T. Kim and C.-I. Kim, *The etching properties of Al2O3 thin films in N2/Cl2/BCl3 and Ar/Cl2/BCl3 gas chemistry,* Materials Science and Engineering: B **118**, 201 (2005).

[36] S. L. Mouradian, *A Scalable Quantum Computation Platform: Solid State Quantum Memories Coupled to Photonic Integrated Circuits,* Ph.D. thesis, MIT (2018).

[37] S. Castelletto, L. Rosa and B. C. Johnson, *Silicon Carbide for Novel Quantum Technology Devices,* in *Advanced Silicon Carbide Devices and Processing* (InTech, 2015).

[38] B. J. M. Hausmann, M. Khan, Y. Zhang, T. M. Babinec, K. Martinick, M. McCutcheon, P. R. Hemmer and M. Loncar, *Fabrication of diamond nanowires for quantum information processing applications,* Diamond and Related Materials **19**, 621 (2010).

[39] T. X. Zhou, R. J. Stöhr and A. Yacoby, *Scanning diamond NV center probes compatible with conventional AFM technology,* Applied Physics Letters **111**, 163106 (2017).

8

[40] B. Regan, A. Trycz, J. E. Fröch, O. C. Schaeper, S. Kim and I. Aharonovich, *Nanofab-rication of high Q , transferable diamond resonators,* Nanoscale **13**, 8848 (2021).

[41] D. B. Cordes, P. D. Lickiss and F. Rataboul, *Recent developments in the chemistry of cubic polyhedral oligosilsesquioxanes,* Chemical Reviews **110**, 2081 (2010).

[42] P. Appel, E. Neu, M. Ganzhorn, A. Barfuss, M. Batzer, M. Gratz, A. Tschöpe and P. Maletinsky, *Fabrication of all diamond scanning probes for nanoscale magnetom-etry,* Review of Scientific Instruments **87**, 063703 (2016).

[43] R. A. Norte, J. P. Moura and S. Gröblacher, *Mechanical Resonators for Quantum Optomechanics Experiments at Room Temperature,* Physical Review Letters **116**, 147202 (2016).

[44] S. Thoms and D. S. Macintyre, *Investigation of CSAR 62, a new resist for electron beam lithography,* Journal of Vacuum Science and Technology B, Nanotechnology and Microelectronics: Materials, Processing, Measurement, and Phenomena **32**, 06FJ01 (2014).

[45] C. Van Egmond, *Fabrication of Photonic Crystal Cavities in Diamond,* M.Sc. thesis, TU Delft (2020).

[46] K. A. Shaw, Z. L. Zhang and N. C. MacDonald, *SCREAM I: A single mask, single-crystal silicon, reactive ion etching process for microelectromechanical structures,* Sensors and Actuators: A. Physical **40**, 63 (1994).

[47] L. Xie, T. X. Zhou, R. J. Stöhr and A. Yacoby, *Crystallographic Orientation Dependent Reactive Ion Etching in Single Crystal Diamond,* Advanced Materials **30**, 1 (2018).

[48] A. E. Rugar, C. Dory, S. Aghaeimeibodi, H. Lu, S. Sun, S. D. Mishra, Z.-X. Shen, N. A. Melosh and J. Vučković, *Narrow-Linewidth Tin-Vacancy Centers in a Diamond Waveguide,* ACS Photonics **7**, 2356 (2020).

[49] M. W. Doherty, N. B. Manson, P. Delaney, F. Jelezko, J. Wrachtrup and L. C. Hollen-berg, *The nitrogen-vacancy colour centre in diamond,* Physics Reports **528**, 1 (2013).

[50] M. E. Trusheim *et al.*, *Transform-Limited Photons from a Coherent Tin-Vacancy Spin in Diamond,* Physical Review Letters **124**, 1 (2020).

[51] S. Gröblacher, J. T. Hill, A. H. Safavi-Naeini, J. Chan and O. Painter, *Highly efficient coupling from an optical fiber to a nanoscale silicon optomechanical cavity,* Applied Physics Letters **103**, 1 (2013).

[52] T. Yamada, H. Yoshikawa, H. Uetsuka, S. Kumaragurubaran, N. Tokuda and S.-i. Shikata, *Cycle of two-step etching process using ICP for diamond MEMS applica-tions,* Diamond and Related Materials **16**, 996 (2007).

[53] M. Challier, S. Sonusen, A. Barfuss, D. Rohner, D. Riedel, J. Koelbl, M. Ganzhorn, P. Appel, P. Maletinsky and E. Neu, *Advanced fabrication of single-crystal diamond membranes for quantum technologies,* Micromachines **9**, 1 (2018).

[54] C. Yang and J. Pham, *Characteristic Study of Silicon Nitride Films Deposited by LPCVD and PECVD,* Silicon **10**, 2561 (2018).

[55] B. Karunagaran, S. Chung, S. Velumani and E.-K. Suh, *Effect of rapid thermal annealing on the properties of PECVD SiNx thin films,* Materials Chemistry and Physics **106**, 130 (2007).

[56] H. K. Lee, K. S. Chung and J. S. Yu, *Selective Etching of Thick Si3N4, SiO2 and Si by Using CF4/O2 and C2F6 Gases with or without O2 or Ar Addition,* Journal of the Korean Physical Society **54**, 1816 (2009).

[57] N. Moldovan, R. Divan, H. Zeng and J. A. Carlisle, *Nanofabrication of sharp diamond tips by e-beam lithography and inductively coupled plasma reactive ion etching,* Journal of Vacuum Science and Technology B: Microelectronics and Nanometer Structures **27**, 3125 (2009).

[58] P. Hirsch, M. Kässens, M. Püttmann and L. Reimer, *Contamination in a scanning electron microscope and the influence of specimen cooling,* Scanning **16**, 101 (2008).

[59] S. Mosor, J. Hendrickson, B. C. Richards, J. Sweet, G. Khitrova, H. M. Gibbs, T. Yoshie, A. Scherer, O. B. Shchekin and D. G. Deppe, *Scanning a photonic crystal slab nanocavity by condensation of xenon,* Applied Physics Letters **87**, 141105 (2005).

[60] K. Chen, E. Bersin, M. Walsh, S. Mouradian and D. Englund, *Versatile Alligator Nanostructures for Quantum Networks with Solid-State Emitters,* in *Conference on Lasers and Electro-Optics* (OSA, Washington, D.C., 2020).

[61] C. T. Nguyen, D. D. Sukachev, M. K. Bhaskar, B. MacHielse, D. S. Levonian, E. N. Knall, P. Stroganov, R. Riedinger, H. Park, M. Lončar and M. D. Lukin, *Quantum Network Nodes Based on Diamond Qubits with an Efficient Nanophotonic Interface,* Physical Review Letters **123**, 1 (2019).

8

9

DIAMOND PLATELETS AS NEXT GENERATION CAVITY DEVICES

Nitrogen-vacancy centers in diamond are promising node candidates for future quantum networks, due to their excellent spin control with long coherence and the controlled access to nearby carbon nuclear spin registers. A challenge associated with the NV center is its ineffective spin-photon interface, which limits entanglement rates in current quantum networks based on this color center. Embedding a microns-thin diamond membrane containing optically coherent NV centers in an open micro-cavity can enhance the spin-photon interface due to the Purcell effect, but it is challenging to incorporate diamond samples in such cavities, and fabrication methods are limited. Here, we report on a fabrication method that can potentially generate several tens of devices from one diamond membrane and facilitate the embedding of the samples in open micro-cavities. This method combines the fabrication of microns-sized, thin diamond platelets attached to the diamond membrane frame with a break-and-place technique that breaks these devices out of the frame in a controlled fashion and positions and bonds them on the flat cavity mirror. We expect this method to be of significance for scaling up cavity-enhanced NV-based quantum networks.

9.1. MOTIVATION AND REQUIREMENTS

For the experiments reported in Chs. 5 and 6, diamond samples containing optically coherent NV centers are fabricated by Van der Waals bonding polished ~ 2 mm × 2 mm × 50 μm diamond samples to a mirror patterned with gold markers and microwave striplines [1]. These samples are then thinned down to a final thickness of ~ 3 μm in the middle of the diamond using an inductively coupled (ICP) reactive ion etch (RIE) employing argon-chlorine and oxygen based chemistries [2], while using a quartz mask to prevent exposing the mirror to the etchants. While this procedure works in principle, bonding large diamond membranes has proven hard in practice, as slight particle contamination or wedged diamond surfaces can have a significant impact on bonding quality, leading to a multitude of bonding attempts or preventing bonding altogether.

An alternative to using 2 mm × 2 mm diamond devices as a whole is to first fabricate small diamond structures (< 50 μm side length) in them, and then bond these smaller structures to a mirror with microwave striplines, in particular since the diamond surface probed by the cavity light field is only ~ 4 μm^2 [3]. Provided one can maintain a high diamond surface quality during this process, this should significantly simplify van der Waals bonding, as one only has to bond smaller structures, and thus there is a higher chance for a particle-free area. Additionally, this also facilitates bonding of wedged diamond samples. The process developed in this chapter is inspired by the recent realization of all diamond scanning probes containing NV centers [4–8], and has been successfully employed in the context of diamond-based open microcavities in Ref. [9]: The process in Ref. [9] starts with a 4 mm × 2 mm × 50 μm diamond sample containing NV centers formed by ion implantation and subsequent high temperature annealing. The sample is thinned down to ~ 1 μm for an area of 500 μm × 800 μm (using a quartz mask with corresponding opening as described in Ch. 5), and then patterned into small "platelets" (side length < 50 μm) using hydrogen silsesquioxane (HSQ) resist and oxygen etching. Approximately 500 nm wide and microns long holding bars attach the platelets to the bulk diamond material. The resulting platelets are then broken out with a needle attached to a micromanipulator, fall onto a mirror lying below the diamond, and bond via Van der Waals forces.

Apart from the ease of bonding, fabricating small diamond platelets has several other advantages:

- As discussed in Ch. 5, we have observed an increase in transverse NV center strain for thin membranes, potentially resulting from stress in the diamond material caused by different thermal expansion coefficients for the diamond and mirror. Stress in the diamond also causes birefringence, leading to a frequency splitting of cavity modes with different polarization [10, 11]. However, for generating entanglement with a cavity in the weak coupling regime, it is necessary to suppress the resonant optical pulse used to excite the NV center sufficiently from the collected photons. This is typically realized by using cross-polarization detection schemes and time filtering [3, 12]. For cavity polarization splittings much larger than the cavity linewidth, however, the cavity only supports light of one polarization, preventing such cross-polarization schemes. Thus, small diamond samples could be necessary for future entanglement generation using NV centers in open microcav-

ities, as stress that could be induced by thermal expansion coefficient mismatches should be significantly reduced..

- Many diamond platelet devices can be fabricated from one starting device, thus reducing the time overhead required for new samples.

- Due to the finite opening of the quartz mask used for thinning the diamond membrane (leading to a position dependent diamond etch rate, see Ch. 5), platelet devices of different thicknesses are fabricated during the fabrication process. This offers a straightforward way of changing the mode character in the cavity: by breaking out samples of different thicknesses, and placing them next to each other on the flat cavity mirror, one can sample different diamond thicknesses - and thus mode characters - with minimal fiber movement (see Ch. 4).

In Ch. 5, we outlined that microns-thin diamond membranes with surface roughness < 0.3 nm r_q containing NV centers with narrow optical transitions (homogeneous optical linewidth < 100 MHz) are suitable for cavity-enhanced entanglement generation based on NV centers. For platelets to replace these samples, additional requirements should be met:

- To minimize the likelihood of particles hindering bonding, the side length of diamond platelets should be constrained to < 100 μm.

- Diamond platelets have to be sufficiently attached to the diamond frame to prevent unwanted breaking, yet need to be removable with high yield using a controlled breaking mechanism.

In this chapter, we describe a method of fabricating and manipulating diamond platelets that can in principle meet these requirements.

9.2. Fabrication of diamond platelet devices

An overview of the process flow followed to fabricate diamond platelet devices can be seen in Fig. 9.1, with a detailed description of all fabrication steps and parameters in Tab. 9.1. We combine our techniques to fabricate μm-thin, etched diamond samples containing narrow linewidth NV centers described in Ch. 5 (obtained via a combination of electron irradiation, high temperature diamond annealing and diamond deep etching) with the diamond patterning techniques developed for photonic crystal fabrication in Ch. 8 (relying on a high oxygen etch selectivity of Si_3N_4 to diamond). Since most fabrication steps have been described in these chapters, we here only give a brief overview of the full fabrication process, mentioning the step number in Tab. 9.1 in brackets[1].

As described in Ch. 5, fabrication begins with tri-acid cleaning (1) of a 2 × 2 × 0.5 (mm)^3 electronic grade, [100] oriented and CVD grown type IIa diamond (Element Six). Subsequent electron irradiation creates vacancies throughout the diamond (2), before a high temperature annealing step recombines those vacancies with naturally occurring

---

[1]Note that the platelet devices in this work were fabricated with not yet optimal Si_3N_4 patterning parameters, explaining the discrepancies with the parameters in Ch. 8. We expect to obtain even smoother platelet sidewalls using these optimized parameters in the future.
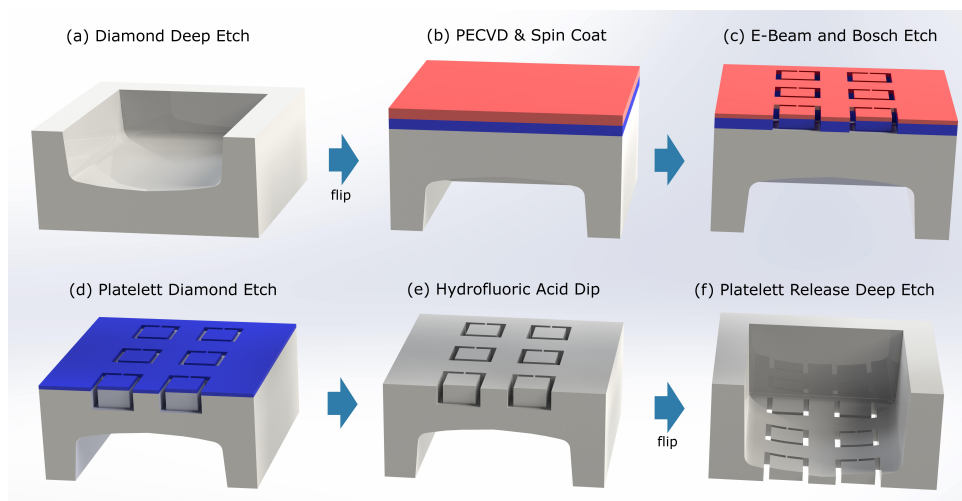
Figure 9.1: Overview of the process flow followed to fabricate diamond platelet devices. For details about these fabrication steps and corresponding parameters, see table 9.1 and the text. Note that step (a) is optional.

nitrogen in the sample (3), forming NV centers. The diamond is then sent for slicing into three slices of ~ 50 µm each, and polished to a typical surface roughness of $r_q <$ 1 nm (Delaware Diamond Knives or Almax Easylab) (4). The diamond membranes are cleaned in fuming nitric acid to remove any residual diamond surface contamination remaining from polishing (5), before they are mounted on a quartz wafer for a subsequent etch (6) to remove the top ~ 10 µm of the sample. This is necessary as the surface quality of the diamond membranes might be comprised after polishing due to formation of sub-surface defects (which can cause pits due to micro-masking during etching [2]) and extensive strain might be present (we have occasionally observed NV centers in the top layers of as-received polished membranes with transverse strains > 500 GHz, in accordance with previous observations [2, 13–15]).

To make sure the whole diamond surface stays flat as required for high quality spin coating later in the process, we do not clamp parts of the diamond with a quartz mask from the top as in Ch. 5. Instead, we fix it on a four inch quartz wafer with a drop of PMMA495 resist on the back of the diamond, acting as a glue that can easily be removed in acetone. Importantly, PMMA495 resist residues next to the diamond do not compromise the surface quality of the diamond if it gets exposed to the plasma (i.e. we observe no PMMA-induced micro-masking). We first pipette a tiny drop of PMMA495 in the middle of the quartz wafer, spread it out with tweezers, and place the diamond on the side. We then push the diamond slowly from the side on the PMMA layer, while making sure that the PMMA does not touch the top side of the diamond. We then place the wafer with the diamond on a hotplate for 2 minutes at 120 °C to bake the resist. After a subsequent etch (6), the diamond is removed from the quartz wafer with acetone, and cleaned in fuming nitric acid to remove all PMMA residue (7), before it is clamped on the quartz wafer with a quartz mask with an opening for a subsequent first diamond deep etch (Fig. 9.1(a), 8).

Step Name	Parameters / Remarks	Step in Fig. 9.1
1. Tri-Acid Clean	See Ch.5	
2. Electron Irradiation	2 MeV, dose 1 / 5 × 10^{12} e^- / cm^2	
3. Annealing	See Ch.5	
4. Slicing and Polishing	See Ch.5	
5. Fuming Nitric Acid Clean	10 min, HNO_3 (99%)	
6. Surface Cleaning Etch	Diamond mounted with PMMA495 on quartz carrier, no quartz mask on top, 30 min Ar/Cl_2, 30 min O_2, params see Ch.5	
7. Fuming Nitric Acid Clean	See Ch.5	
8. Diamond Deep etch	Diamond clamped with quartz mask (1.4 mm side opening, 300 μm thickness), 30 min Ar/Cl_2, O_2 for desired thickness (here 113 min), params see Ch.5	(a)
9. Si_3N_4 PECVD	200 nm, see Ch. 8	
10. Spin Coating	Diamond mounted on Si piece with PMMA495, resist CSAR09, 2000 rpm (thickness 280 nm), bake 3 min at 150°C	(b)
11. Gold Sputtering	Thickness 4 nm, for conduction during exposure	
12. Exposure	400 μC / cm^2, for other beam parameters see Ch. 8	
13. Development	30 s KI solution (4 g KI : 1 g I_2 : 40 ml de-ionized water (DI), to dissolve Gold), 2 × 30 s DI, 90 s AR 600-546, 30 s AR600-60	
14. Si_3N_4 Bosch etch	75 seconds, 1200 W ICP, RF2 50 RF, 40 sccm C_4F_8, 20 sccm SF_6, 0.01 mbar, etch rates ~ 110 nm / min CSAR09, ~ 200 nm / min Si_3N_4	(c)
15. Resist removal	AR600-72, 1 minute, diamond comes loose of Si piece	
16. Platelet Diamond Etch	Diamond mounted with PMMA495 on quartz carrier, 20 minutes 0_2, params see Ch.5	(d)
17. Hydrofluoric Acid Dip	40% Hydrofluoric Acid (HF), 10 minutes	(e)
18. Platelet Release Etch	Diamond clamped with quartz mask, 15 min Ar/Cl_2, O_2 until platelets are released (here 27 min), params see Ch.5	(f)

Table 9.1: Overview of fabrication steps used to fabricate diamond platelets. If not indicated otherwise, liquid processing steps are followed by dip in acetone and isopropanol, with subsequent dry-blowing with a nitrogen gun. We note that the platelets in this chapter were fabricated before optimization of the all-diamond photonic crystal fabrication process. We expect even smoother platelet sidewalls by replacing steps 10 through 15 with fabrication steps 2 through 10 in Tab. 8.1 of Ch. 8.

9
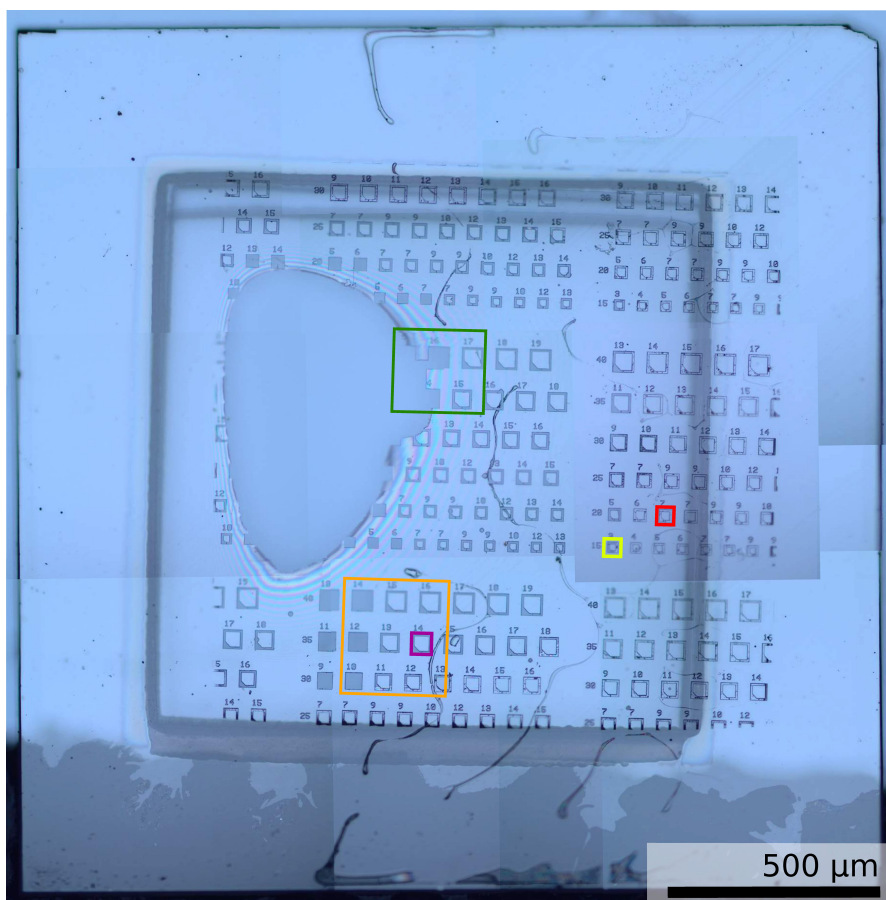
Figure 9.2: Overview of the fabricated diamond platelet device. Two black diamond squares resulting from micromasking at the edges of the quartz top mask during the two diamond deep etches are visible (see Ch. 5). Orange, red, purple and yellow solid lines indicate the areas which are depicted in Figs. 9.3 (a - d), while the green solid line highlights the region displayed in Figs. 9.5 (a - d).

9

As in Ch. 8, we then deposit a 200 nm thick layer of Si_3N_4 on the diamond via plasma-enhanced chemical vapour deposition (PECVD, 9), and mount the diamond on a silicon piece using PMMA495 (as described above). We then spin coat the sample with CSAR09 to form a uniform resist layer with a nominal thickness of 280 nm (Fig. 9.1(b), 10), and evaporate a 4 nm thin layer of gold (11) that serves to suppress charging effects during the subsequent electron beam lithography exposure step (12). After exposure, the gold is removed and the resist developed (13), before a Bosch etch process transfers the resist pattern into the Si_3N_4 etch mask (Fig. 9.1(c), 14). We then remove the resist (15), at which point the diamond comes loose from the silicon piece serving as a carrier, so we re-mount the diamond on the quartz carrier wafer with PMMA495 (see above). We transfer the Si_3N_4 pattern into the diamond (etch selectivity Si_3N_4 : Diamond ~ 30 : 1)
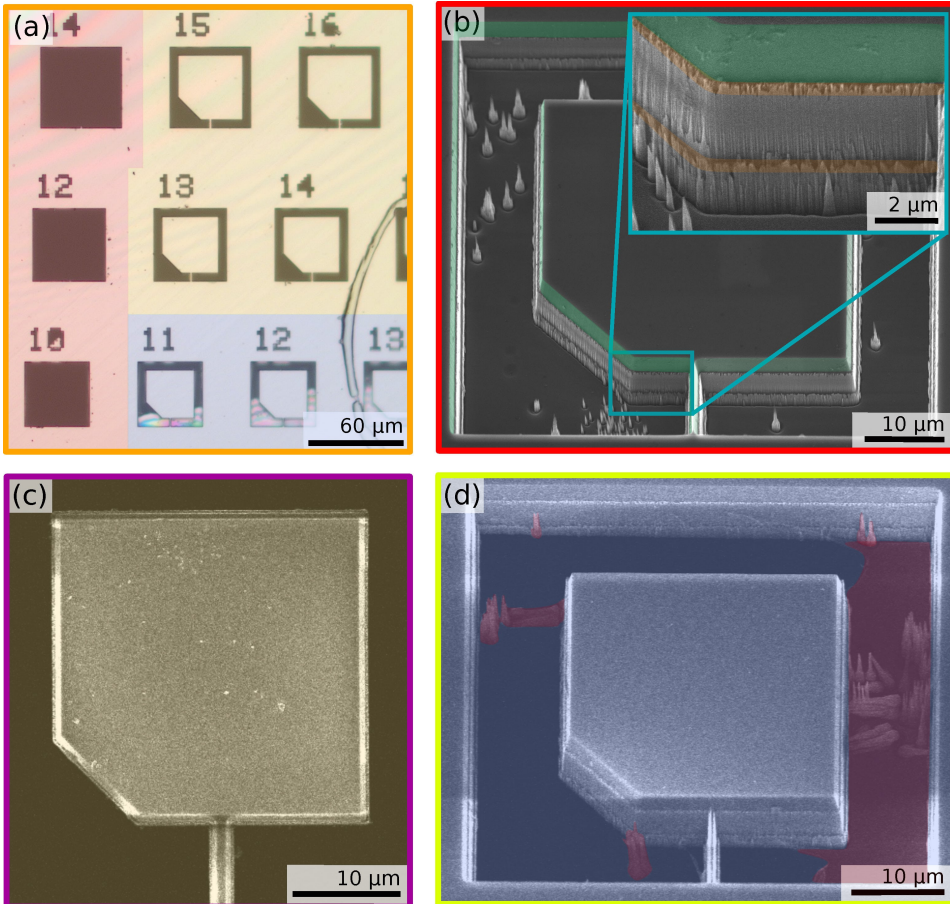
Figure 9.3: Optical and Scanning Electron Microscope (SEM) images of fabricated diamond platelets, still attached to the diamond frame, after all fabrication steps. Colors of the frames around images correspond to the colors in Fig. 9.2. (a) Optical microscopy image, showing regions for which platelets have been broken out (red shading), regions which contain platelets that are only held to the diamond via the holding bar (yellow shading), and regions which contain platelets which have not been fully released from the substrate (blue shading) due to a non-uniform height profile resulting from the diamond deep etch (see text). (b) SEM image of a platelet in a region where the deep etch has not reached the trenches (tilt 30 degrees). Pillars in the trenches resulting from local micromasking are visible. A cyan zoom in shows surface roughness of platelet sidewalls, with different highlighted regions resulting from gradual pattern transfer from the Si_3N_4 into the diamond during anisotropic platelet oxygen etch (green), and micromasking due to resist residuals after development and mask erosion (orange shaded lines). (c) SEM image of a fully released platelet (tilt 0 degrees). Some particles introduced by improper sample drying after wet processing are visible. (d) SEM image of a platelet that is partially released (tilt 30 degrees), showing fallen over pillars, and a thin remaining diamond layer in parts of the trenches (red shading).

with an anisotropic oxygen etch (Fig. 9.1(d), 16), and subsequently remove the remaining Si$_3$N$_4$ by dipping the sample in hydrofluoric acid (Fig. 9.1(e), 17), before we place the sample on a quartz carrier wafer for a second deep etch (clamping the diamond with a quartz mask from the top). This final step etches through the patterned trenches from the backside, and releases the platelets, which are at this point only attached to the diamond frame by small holding bars (Fig. 9.1(f), 18).

9.3. CHARACTERIZATION AND BONDING OF DIAMOND PLATELET DEVICES

Having fabricated diamond platelet devices, we now move on to their characterization, to see if the resulting structures fulfill the requirements defined in Sec. 9.1.

9.3.1. PLATELET CHARACTERIZATION

An optical microscope image of a final diamond device can be seen in Fig. 9.2. The numbers above each platelet indicate the written holding bar width in 10^{-7} m, while the numbers to the left of a platelet row indicate side length in µm (all plates have a square base shape); we vary these parameters to find a regime for which platelets are strongly attached to the support frame yet easy to break out with a micromanipulator, and can be successfully bonded to a mirror. As discussed in Ch. 5, the quartz etch mask lying on top of the diamond during deep etches leads to a position dependent etch rate on the diamond, as its finite thickness limits the plasma ion angles that contribute to the etch. As a result, the final device contains platelets of different thicknesses. For this particular sample an overestimation of the diamond thickness before the final etch lead to parts of the diamond being etched away during the platelet release etch, as evident by an elliptical hole in Fig. 9.2.

To gain a better understanding of the quality and directions for improvement of the fabricated platelet devices, we take optical and scanning electron microscope (SEM) images of platelets, as shown in Fig. 9.3. Fig. 9.3(a) shows three different platelet areas: shaded in red is a region for which fabricated platelets have been broken out with a micromanipulator, shaded in yellow is a region for which the platelet trenches have been fully opened during the platelet release diamond etch (resulting in the intended devices only attached to the support frame by the holding bars), and shaded in blue is a region for which the trenches have not yet been fully opened up. An asymmetric design with a cut corner is also visible. Together with the holding bar, this serves as a means to identify which side of the diamond one is looking at after a platelet has been broken out.

Figs. 9.3 (b), (c), and (d) show SEM images of platelets that are not released, fully released, and partially released, respectively. Pillars in the platelet trenches, created by local micro-masking of the diamond due to remaining Si$_3$N$_4$ particles during the platelet defining oxygen etch are visible. While the top sides of the diamond are smooth, the inset of Fig. 9.3(b) shows that this is not the case for the sidewalls; as mentioned above,the devices were fabricated when the photonic crystal process flow was still at an early stage of development. A non-optimal parameter regime of the Si$_3$N$_4$ etch resulted in relatively large horizontal etch rates. This causes an opening angle of the Si$_3$N$_4$, which transfers into the diamond during the following oxygen etch (stretched by the selectivity of Si$_3$N$_4$
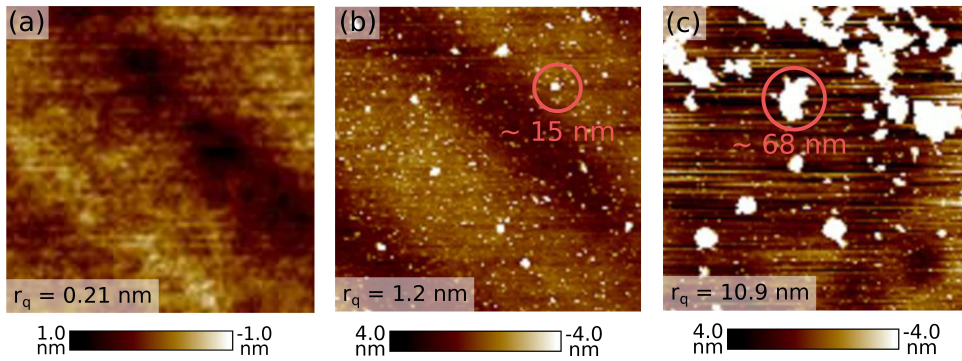
Figure 9.4: Atomic force microscope (AFM) images of a typical diamond membrane after a deep etch using argon-chlorine- and oxygen-based chemistries (a), and for a platelet sample lying on top of the mirror with the deep etched side (b) and pattern etched side (c) facing away from the mirror, after all fabrication. Red numbers indicate height of particles in accompanying circles. Images show quadratic area with side length of 3 μm.

: Diamond), explaining the green shaded area in the inset of Fig. 9.3(b). The orange shaded lines are a consequence of resist sidewall roughness after development (due to non-optimized etch parameters used during the Si_3N_4 etch [16, 17]), mask erosion leading to re-deposition, and resist residuals after development[2]. Ultimately, rough sidewalls should not impede bonding, and we expect that they only minimally contribute to the degradation of optical properties of NV centers when these are sufficiently far away from sidewalls ($\gtrsim$ μms).

To reduce unwanted scattering losses in the cavity, embedded diamond platelets need to be sufficiently smooth[3]. Fig. 9.4 shows atomic force microscope (AFM) images of a typical diamond membrane sample after the deep etch (Fig. 9.4(a)), and of diamond platelets broken out of the diamond frame and facing the mirror with the side originally patterned with a Si_3N_4 mask (Fig. 9.4(b)), and with the deep etched side (Fig. 9.4(c)), after all fabrication. While the diamond membrane shows a low surface roughness, this is not the case for the platelet sample. The bigger particles on the side originally covered with Si_3N_4 (Fig. 9.4(c), compared to the deep etched side, Fig. 9.4(b)) indicate that not all masking material has been successfully removed during wet etching, and / or that some dirt from contact with the carrier wafer employed during the subsequent deep etch has been picked up. Fig. 9.4(b) shows that the deep etched side is also covered in many, smaller particles[4]. Future research will focus on investigating the sources of this particle contamination, which might be associated with diamond debris resulting from non-clean breaking (see section below), and insufficient removal of the Si_3N_4 mask. Im-

---

[2]This is likely due to the fact that we did not employ a Piranha clean to remove all CSAR09 resist residues, a step that has proven to be crucial for photonic crystal fabrication, see Ch. 8. Importantly, however, for the optimized CSAR09 resist and Si_3N_4 etch parameters reported in Ch. 8, we expect these effects to be significantly reduced.

[3] $\lesssim 0.3$ nm r_q roughness for the cavity parameters considered in Chs. 5 and 6.

[4]As the particles on both platelet sides are not accompanied by holes (as observed for masking during etching in Ch. 5), we conclude that all particles visible are either introduced during wet processing or dry handling steps, after any etching.
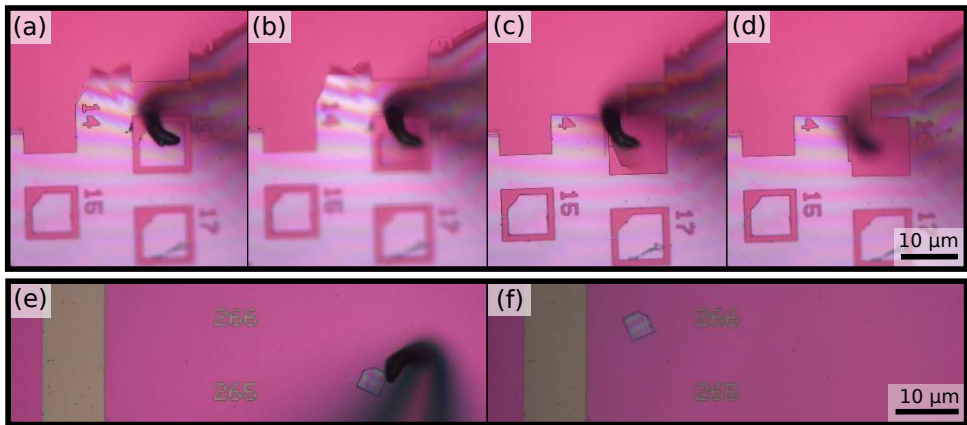
Figure 9.5: Breaking out of diamond platelets and their deterministic positioning on a patterned mirror. A microns-thin needle mounted on a piezo-controlled micromanipulator is used to break out diamond platelets that fall on a mirror lying below the diamond frame. Engagement of the needle with a platelet (a), initial (b) and final (c) flex of the platelet, just before breaking out (d). A broken out platelet that has landed on the mirror (e) is positioned next to a microwave stripline and marker (f) with the same manipulator. The mirror is patterned via an etching, gold deposition and liftoff procedure [1].

portantly, while the measured surface roughness of the fabricated and bonded diamond platelets is significantly above the desired value [r_q = (1.2 / 10.9) nm compared to a target value of r_q < 0.3 nm], the AFM measurements also show that the diamond surfaces are sufficiently smooth if the particles can be efficiently cleaned (i.e. no micromaksing leading to hole formation in surfaces during etches can be observed).

9.3.2. CONTROLLED BREAKING, MICROMANIPULATION, AND BONDING

To bond diamond platelet samples to a mirror patterned with markers and striplines [1], we place the full diamond structure containing platelets on the mirror (platelets facing away from the mirror), and use a microns-radius tungsten needle (American Probes and Technologies) mounted on a piezo-controlled micromanipulator (Imina Technologies) to break out individual platelets. Figs. 9.5(a - d) show optical microscope images of the process of breaking out a platelet with a nominal edge length of 40 μm, and a designed holding bar width of 1.6 μm. The platelet can be tilted almost 90 degrees (Fig. 9.5(c)) before it breaks out of the large support structure (Fig. 9.5(d)).

The platelet then falls down to the mirror surface ∼ 50 μm below (Fig. 9.5(e)), and can be moved with a micromanipulator to its final position close to a microwave stripline (Fig. 9.5(f)) to enable efficient microwave driving of NV spin states. We currently do not have a method to judge whether a platelet is bonded at this stage, as we do not observe a bending of the micromanipualator needle when trying to push a platelet device that is bonded to the mirror, as reported in Ref. [18]. This is most likely due to the fact that the needle in our setup has a ∼ 3 times larger diameter compared to the needles used in Ref. [18], making them too stiff to bend for the Van der Waals forces present in the system.

9.4. OUTLOOK

We have reported on the fabrication, controlled breaking and bonding of diamond platelet samples for operation in open micro-cavities. Current research is focusing on developing methods for further cleaning the diamond samples after fabrication, and on forming a cavity around a mirror with bonded platelets. Embedding the platelets in a cavity will allow to both confirm that the platelets are sufficiently bonded to the mirror (to both be not moved by potential electrostatic forces from the fiber and guarantee an electric-field node at the diamond-mirror interface to reduce unwanted cavity losses), and that the diamond-air interface is sufficiently smooth to avoid unwanted scattering losses. Furthermore, photoluminescence excitation scans will be performed, to confirm that embedded NV centers feature sufficient optical line stability. The thickness profile of this particular sample might enable a study of the optical coherence of NV centers formed via electron irradiation in sub-microns thin membranes, a regime unaccessible in our previous study (see Ch. 5). This could shed light on the mechanisms behind the optical line broadening of NV centers in sub-microns thin structures. Moreover, terminating the diamond oxygen etching with reduced etch rates has recently been linked with improved optical properties of near-surface NV centers, a method that we will investigate in future research [19]. Lastly, we expect that the experience gained in micormanipualting diamond platelets will be of help for the integration of all-diamond nanophotonic cavities (see Ch. 8) into hybrid integrated photonic circuits (see Ch. 10). Overall, we expect diamond platelet devices to be the building blocks for future cavity-enhanced quantum networks based on NV centers.

9

REFERENCES

[1] S. Bogdanović, M. S. Z. Liddy, S. B. van Dam, L. C. Coenen, T. Fink, M. Lončar and R. Hanson, *Robust nano-fabrication of an integrated platform for spin control in a tunable microcavity*, APL Photonics **2**, 126101 (2017).

[2] M. Ruf, M. IJspeert, S. van Dam, N. de Jong, H. van den Berg, G. Evers and R. Hanson, *Optically Coherent Nitrogen-Vacancy Centers in Micrometer-Thin Etched Diamond Membranes*, Nano Letters **19**, 3987 (2019).

[3] M. Ruf, M. Weaver, S. van Dam and R. Hanson, *Resonant Excitation and Purcell Enhancement of Coherent Nitrogen-Vacancy Centers Coupled to a Fabry-Perot Microcavity*, Physical Review Applied **15**, 024049 (2021).

[4] P. Maletinsky, S. Hong, M. S. Grinolds, B. Hausmann, M. D. Lukin, R. L. Walsworth, M. Loncar and A. Yacoby, *A robust scanning diamond sensor for nanoscale imaging with single nitrogen-vacancy centres.* Nature Nanotechnology **7**, 320 (2012).

[5] D. Riedel, D. Rohner, M. Ganzhorn, T. Kaldewey, P. Appel, E. Neu, R. J. Warburton and P. Maletinsky, *Low-loss broadband antenna for efficient photon collection from a coherent spin in diamond*, Physical Review Applied **2**, 1 (2014).

[6] P. Appel, E. Neu, M. Ganzhorn, A. Barfuss, M. Batzer, M. Gratz, A. Tschöpe and P. Maletinsky, *Fabrication of all diamond scanning probes for nanoscale magnetometry*, Review of Scientific Instruments **87**, 063703 (2016).

[7] K. K. Chang, *Scanning Magnetometry with NV Centers in Diamond*, Ph.D. thesis, ETH Zurich (2016).

[8] M. Radtke, R. Nelz, A. Slablab and E. Neu, *Reliable Nanofabrication of Single-Crystal Diamond Photonic Nanostructures for Nanoscale Sensing*, Micromachines **10**, 718 (2019).

[9] D. Riedel, I. Söllner, B. J. Shields, S. Starosielec, P. Appel, E. Neu, P. Maletinsky and R. J. Warburton, *Deterministic enhancement of coherent photon generation from a nitrogen-vacancy center in ultrapure diamond*, Physical Review X **7**, 1 (2017).

[10] K. Jensen, N. Leefer, A. Jarmola, Y. Dumeige, V. M. Acosta, P. Kehayias, B. Patton and D. Budker, *Cavity-enhanced room-temperature magnetometry using absorption by nitrogen-vacancy centers in diamond*, Physical Review Letters **112**, 1 (2014).

[11] S. B. van Dam, *Optical cavities, coherent emitters, and protocols for diamond-based quantum networks*, Ph.D. thesis, TU Delft (2019).

[12] H. Bernien, B. Hensen, W. Pfaff, G. Koolstra, M. S. Blok, L. Robledo, T. H. Taminiau, M. Markham, D. J. Twitchen, L. Childress and R. Hanson, *Heralded entanglement between solid-state qubits separated by three metres*, Nature **497**, 86 (2013).

[13] S. E. Grillo and J. E. Field, *The polishing of diamond*, Journal of Physics D: Applied Physics **30**, 202 (1997).

9

[14] H. A. Atikian, A. Eftekharian, A. Jafari Salim, M. J. Burek, J. T. Choy, A. Hamed Ma-
jedi and M. Lončar, *Superconducting nanowire single photon detector on diamond,*
Applied Physics Letters **104**, 122602 (2014).

[15] Y. Chu *et al.*, *Coherent Optical Transitions in Implanted Nitrogen Vacancy Centers,*
Nano Letters **14**, 1982 (2014).

[16] R. Benevides, M. Ménard, G. S. Wiederhecker and T. P. Mayer Alegre, *Ar/Cl 2 etch-
ing of GaAs optomechanical microdisks fabricated with positive electroresist,* Optical
Materials Express **10**, 57 (2020).

[17] M. Mitchell, D. P. Lake and P. E. Barclay, *Realizing Q > 300 000 in diamond microdisks
for optomechanics via etch optimization,* APL Photonics **4**, 0 (2019).

[18] D. Riedel, *Engineering of the photonic environment of single nitrogen-vacancy cen-
ters in diamond,* Ph.D. thesis, University of Basel (2017).

[19] I. Lekavicius, T. Oo and H. Wang, *Diamond Lamb wave spin-mechanical resonators
with optically coherent nitrogen vacancy centers,* Journal of Applied Physics **126**,
214301 (2019).

9

10

CONCLUSIONS AND OUTLOOK

This thesis focused on enhancing the spin-photon interface of color centers in diamond, making use of the Purcell effect. The research discussed can be loosely divided into two main directions. First, we presented theoretical and experimental progress towards cavity-enhanced quantum networks based on NV centers. We devised a method to create optically-coherent NV centers in a microns-thin diamond membrane, and used it to demonstrate resonant excitation and collection of coherent, Purcell-enhanced NV emission in a fiber-based micro-cavity. Second, we developed advanced nanofabrication capabilities that can be used to create all-diamond waveguides and photonic crystal cavities with embedded group-IV color centers, allowing for high emitter-waveguide or emitter-cavity coupling, potentially enabling near-deterministic spin-photon gates. In this final chapter, we present future research avenues towards realizing large-scale entanglement-based quantum networks employing color centers in diamond.

10.1. SUMMARY

This thesis describes theoretical and experimental progress towards cavity-enhanced quantum network nodes in diamond, focusing in particular on enhancing the spin-photon interface of embedded color centers. The results obtained can be summarized as follows:

- **Chapter 4** develops analytical methods to describe and improve the design of open, tuneable Fabry-Perot micro-cavities containing a microns-thin diamond slab. Our model suggests that reducing cavity length fluctuations, operating cavities with maximal electric-field localization in the diamond ("diamond-like" mode), and minimizing the air gap length of cavities have the biggest near-term optimization potential.

- **Chapter 5** describes a method to fabricate microns-thin diamond membranes that can be embedded in open cavities with high finesse. We optimize an etching sequence that allows us to remove tens of microns of diamond without degrading the surface of diamond membranes, and show that we can preserve the optical coherence of NV centers formed via electron irradiation in such structures.

- In **Chapter 6**, we couple optically coherent NV centers to a fiber-based cavity, and extract the resulting Purcell enhancement. We demonstrate resonant excitation and detection of coherent, cavity-enhanced NV center emission, as required for entanglement generation. A detailed theoretical model in excellent agreement with our results shows that such a cavity-based system can improve entanglement rates between distant NV centers by two orders of magnitude using near-term improvements to the setup.

- In **Chapter 7**, we outline a procedure for the optimization of photonic crystal cavities for highest Purcell enhancement of embedded color centers, including the effects of real-world fabrication imperfections. We also devise a method to efficiently interface these devices using tapered optical fibers.

- In **Chapter 8**, we develop a method to fabricate all-diamond photonic crystal cavities and waveguides, using a (quasi-) isotropic dry etching technique. We characterize the resulting structures, and outline a path towards a further improved process.

- **Chapter 9** describes a technique to fabricate microns-sized diamond plates that can serve as next generation open micro-cavity samples. We break these devices out of a diamond frame in a controlled way using a piezo-controlled micromanipulator, and position them on a mirror with microns-scale accuracy.

In the following sections, we discuss possible improvements and challenges on the path towards a large-scale entanglement-based quantum network based on color centers in diamond.

10.2. ENHANCING THE SPIN-PHOTON INTERFACE

Apart from the current challenges and future research directions for enhancing the spin-photon interface of color centers in diamond as discussed in the respective chapters of this thesis, we here shed light on some further directions that could be investigated.

10.2.1. NV CENTERS

UNDERSTANDING SURFACE NOISE EFFECTS*

Due to their permanent electric dipole moment, NV centers experience large spectral shifts on short timescales caused by charge fluctuations in the environment when close to surfaces (~ microns) [2]. As a result, despite reported Purcell factors of up to 70 in small mode-volume photonic crystal cavities [3], the regime of $C_{\mathrm{coh}} \geq 1$ has remained out of reach. We note that the origins of the surface noise are still a subject of active research, and that recent experiments geared at understanding the effect and origins of surface noise on the NV center spin [4], and the local electrostatic environment of NV centers [5] show promise towards understanding the causes of surface charge noise. Combined with proposals for active optical driving to reduce spectral diffusion effects [6], this could revive the field of NV centers in nanophotonic structures in the future.

OPTIMAL POSITIONING OF NVS IN OPEN CAVITIES*

Another active area of research is to create shallow, stable NV centers [7–9] at controlled locations; both the electron irradiation technique employed in Ref. [10], as well as recently introduced laser-writing techniques [11] can form optically coherent NV centers, but rely on native nitrogen in the sample to recombine with introduced lattice vacancies and thus miss precise control of the site of NV center formation. However, for maximal Purcell enhancement, NV centers should be positioned at an antinode of the cavity field. While such precision can be achieved using ion implantation, recent research has shown that NV centers created via this technique suffer from increased optical linewidths compared to NV centers formed during growth [12], even after extended high temperature treatments to restore the diamond lattice [13].

TOWARDS A CAVITY-ENHANCED COHERENT SPIN-PHOTON INTERFACE

As outlined in Ch. 6, there is a near-term path from the current $C_{\mathrm{coh}} \sim 0.1$ towards $C_{\mathrm{coh}} \sim 1$ and coherent photon collection efficiencies ~ 10% using near-term improvements to the system. In particular, recent results suggest that it should be possible to reach the required pm-scale cavity length fluctuations even in closed-cycle cryostats [14, 15], which would remove the need for a liquid helium infrastructure at each quantum network node. For our current cavity system, a proof-of-principle test showed that we can reduce the overall cumulative vibrations of the system at $T \sim 4$ K by about one third when using a real time controller (Dspace systems) that feeds back on the cavity length via a high bandwidth piezo [16], using the cavity transmission signal measured at the point of maximal slope. A new cavity system, centered around a custom cryostat design that combines a coldhead mounted off the optical table and a built-in vibration isolator is currently being installed (Montana Instruments). Initial measurements suggest a one-to-two order of magnitude improved vibration performance of the system can be achieved. Combining this system with active length stabilization via the Pound-Drever-Hall method

10

[16, 17] and photothermal feedback [14, 18] could allow for pm-scale vibration levels in the near-term future.

While it will remain challenging to achieve coherent cooperativites ≫ 1 (and thereby enter the near-deterministic spin-photon interface regime [19]), the open cavity approach is projected to speed up current emission-based entanglement generation by ∼ 2 orders of magnitude [10]. This could allow for continuous deterministic entanglement generation (generating high fidelity entanglement faster than it is lost), and enable experiments such as the formation of a quantum repeater surpassing direct transmission [20], and device-independent quantum key distribution [21] using NV centers. Additionally, in case two NV centers can be coupled to the same cavity and brought close to resonance, collective eigenstates of the two NV centers could be probed, which could allow entanglement of two NV centers in one cavity [22]. Since the collection of phonon sideband light that is typically used for optical NV state readout is projected to be about one order of magnitude lower than for current solid immersion based samples [23], it will likely be necessary to implement pulsed resonant readout schemes that make use of zero-phonon-line photon emission. To route entanglement between local spin-state readout and distant entanglement generation, fast, low-loss optical switches might be required [24]. Alternatively, if the cooperativity of the emitter-cavity system can be made sufficiently high, the NV state could be read out by spin-state-dependant cavity reflection- or transmission-based schemes [25, 26].

10.2.2. GROUP-IV COLOR CENTERS*

TUNING OF EMITTER FREQUENCIES

A key requirement for many remote entanglement generation schemes is the ability to tune two group-IV color centers located on separate chips to a common resonance frequency. So far, tuning the emission frequency of group-IV emitters has been demonstrated using strain [27–31], electric fields [32, 33], and Raman-type [25, 34] schemes (although the latter is only compatible with emission-based entanglement generation schemes), but only for single emitters, or several emitters in one structure. The first two tuning techniques deform the orbitals of the group-IV color centers, and thus the color's inversion symmetry is broken, leading to an observed increase in transition linewidths and spectral diffusion under applied external strain / electric field (potentially due to an increase in sensitivity to charge noise in the environment). We note that recent experiments indicate a larger tuning range of transitions for strain tuning (as compared to electric field tuning) for the same induced line broadening [31–33].

INCREASING THE STABILITY OF OPTICAL TRANSITIONS

While close-to-lifetime limited linewidths of group-IV color centers in nanophotonic structures have been observed, experiments still routinely show spectral shifts and charge instabilities, leading to broadening ∼ several lifetime-limited linewidths [22, 26, 31, 35], as well as large local strain fields. While dynamic strain tuning can be used to suppress slow spectral diffusion (seconds timescale) [30], it is challenging to improve the homogeneous linewidth (sub-microsecond timescale) that enters the coherent cooperativity using this approach. Typically, emitters are created by high-energy implantation, followed by a high temperature annealing step to form group-IV vacancy centers and to

reduce the effects of lattice damage from the implantation process [36–38]. However, there is evidence that even such high temperature treatments can not fully recover the original diamond lattice [12]. A recently developed promising method to overcome this limitation employs low energy shallow ion implantation, combined with overgrowth of diamond material [39]. Another strategy could be to combine low-density ion implantation with electron irradiation, to reduce the amount of damage created in the lattice via the (heavy) ion implantation [40]. Combined with controlled engineering of the diamond Fermi level [41–44], these techniques could increase the quality and stability of group-IV color center optical transitions [22, 26, 31, 35, 45, 46].

IMPROVING FABRICATION METHODS

Another area of active development involves the design and fabrication of the nanophotonic structures. Currently, all listed fabrication methods routinely achieve photonic crystal cavity quality factors $\sim 10^4$, about two orders of magnitude lower than simulated values [47]. These deviations are caused by a combination of surface roughness [26], non-uniform hole sizes [48], and deviations from the expected device cross-section [49]; we expect that an order-of-magnitude improvement in device quality factors is within reach upon further optimization. Furthermore, although photonic crystal nanocavities can be designed and fabricated to resonate at the ZPL frequency, they are especially sensitive to process variations, leading to a resonance wavelength spread of ~ 5 nm across devices [47]. Nonetheless, this spread in frequency may be overcome by cavity tuning methods [3, 25, 50], which are in any case needed for the precise overlapping of the ZPL and cavity frequency.

As nanofabrication methods are constantly refined, it is also likely that current methods of optimally aligning color centers within nanophotonic structures (to guarantee maximal overlap between the optical mode and the dipole emitter) can be further improved. Towards this end, various methods have already been demonstrated, including the targeted fabrication around pre-located centers [51], or ion implantation into devices using either masks [26] or focused implantation [25, 31]. Compared to the SiV center for which $C_{coh} \sim 100$ has been demonstrated, GeV and SnV centers have intrinsically higher radiative efficiencies and thus potentially higher cooperativities, which may increase cavity-QED-based protocol fidelities.

INTEGRATION IN OPEN MICRO-CAVITY SYSTEMS

We note that group-IV color centers in diamond are also suitable for integration into tuneable, open micro-cavities, as recently demonstrated for GeV [52] and SiV [53, 54] centers at room temperature. It should be possible to achieve $C_{coh} \gg 1$ for these systems, potentially providing a viable alternative to the more fabrication-intensive nanostructures.

10.3. ENHANCING THE MEMORY QUBITS*

We now discuss the state of the art and future research directions regarding the memory qubits of color centers in diamond.

10
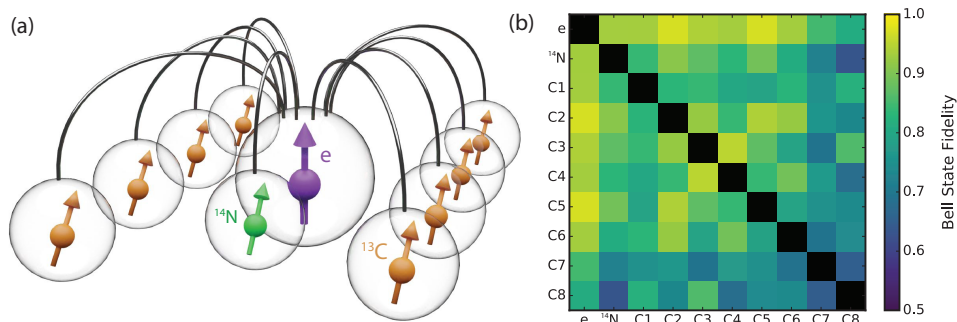
Figure 10.1: State-of-the-art research for increasing memory qubit numbers and control for color centers in diamond. (a) Schematic overview of a local 10-qubit quantum register in diamond, formed from a nitrogen-vacancy center (purple), a native ^{14}N nuclear spin, and 8 surrounding ^{13}C nuclear spins. (b) Connection map of the spin register in (a), demonstrating entanglement generation between all pairs of qubits in the register. Figure adapted with permission from Ref. [57], in accordance with creativecommons.org/licenses/by/4.0/legalcode.

STATE OF THE ART OF MEMORY QUBIT CONTROL

The most common isotope of carbon is ^{12}C. However, the ^{13}C isotope with natural abundance of about 1.1% carries a nuclear spin of 1/2. In the past decade, techniques have been developed (mostly on NV-based systems) to control these nuclear spins via the position-dependent hyperfine coupling. Universal nuclear spin control using electron decoupling sequences that are on resonance with a single ^{13}C spin has been demonstrated [55]. This has enabled the demonstration of coherence times above 10 seconds, and electron-nuclear gate fidelities ~ 98% for individual ^{13}C spins in NV-based systems [56, 57]. Additionally, up to one memory qubit per communication node has been used in an NV-based quantum network setting to date [56, 58]. For the case of SiV centers (and group-IV color centers in general), on the other hand, the spin-half nature of the system leads to a vanishing first-order sensitivity of decoupling sequences to individual ^{13}C hyperfine parameters, thus requiring long decoupling times (and / or potentially off-axis magnetic fields that are at odds with a high spin cyclicity of optical transitions) to isolate out single nuclear spins. So far, electron-nuclear gate fidelities have been limited to ~ 59% for SiV centers [59]; ^{13}C nuclear spins close to group-IV color centers have not yet been used in quantum networks experiments.

EXTENDING MEMORY QUBIT NUMBERS AND CONTROL

A first area of research is thus to extend the number of available nuclear spin qubits per network node, as well as their control speeds and fidelities. Recently developed gate schemes based on interleaving radiofrequency (RF) driving of ^{13}C nuclear spins (to control previously unaddressable qubits) with dynamical decoupling pulses (to decouple from the spin bath) have allowed the creation of a local quantum register of an NV communication qubit and up to 9 surrounding nuclear spin qubits [see Fig. 10.1(top)] that allow entangled state generation between all pairs of qubits [Fig. 10.1(bottom)], creation of a local 7-qubit GHZ state, as well as memory coherence times of single and two qubit states of over ten seconds [57]. This result (achieved on a similar device as used for dis-

tant entanglement generation [56, 58, 60]) shows that it is realistic to expect diamond-based quantum nodes containing many qubits in the near-term future. Such registers could enable scalable, modular quantum computation [61] and universal, fault-tolerant error correction [55, 62–64]. Additionally, we expect that RF driving of nuclear spins will overcome current limitations in manipulating nuclear spins for group-IV color centers, as the nuclear spin transition frequencies depend on the hyperfine parameters on first order in this case [26]. Overcoming issues related to sample heating and background amplifier noise could then also enable to address multiple nuclear spins simultaneously, thus reducing decoherence associated with long gate times [57]. Additionally, cross-talk between nuclear spins, as well as unwanted coupling to other spins could be reduced when using the full information of the environment of a color center [65] (potentially acquired while involving automated techniques [66]) to simulate and tailor gate sequences for a specific spin environment, and computationally optimizing them for overall protocol fidelity. Another way of extending the number of controllable nuclear spin qubits per node is to also employ the nuclear spin of a nuclear spin containing color center atom isotope, e.g. of ^{14}N (nuclear spin of 1) [67] or ^{29}Si (nuclear spin of 1/2) [68]. While the electron-nuclear gate times for these intrinsic nuclear spins can be relatively fast thanks to the strong (~ MHz), always-on hyperfine coupling to the color center's electron spin, they are for the same reason more susceptible to dephasing from uncontrolled electron dynamics during entanglement generation (see paragraph below). Thus, despite slower gate times, more weakly coupled 13C spins (~ kHz) are commonly used in experiments that require high fidelity storage of a quantum state during subsequent entanglement generation attempts [56, 58]. In general, the choice of memory qubit depends on the requirements of a specific application.

IMPROVING THE MEMORY'S RESILIENCE TO ENTANGLEMENT GENERATION ATTEMPTS

A second research direction is to increase the coherence time per available memory qubit under full network activity (in particular entanglement generation). The "always-on" nature of the hyperfine interaction of ^{13}C nuclear spin memory qubits and the NV center has limited memory coherence in quantum networks to ~ 500 entanglement generation attempts [58, 69]. Uncontrolled electron dynamics, which result for instance from control infidelities and stochastic electron spin initialization during an entangling sequence, cause dephasing of the nuclear spin memory qubits [69]. Techniques such as higher magnetic fields at the color center location can speed up gate times and shorten the entanglement generation element, thus reducing the time over which random phases can be picked up [58, 69]. Additionally, decoupling pulses on the memory qubits that suppress quasi-static noise in the environment have shown initial promise to prolong nuclear memory qubit coherence under network activity for NV centers [69]. Other promising routes to extend the nuclear spin memory coherence time involve reducing the color center's state-dependent coupling strength (the main dephasing channel), e.g. by employing decoherence-protected subspaces (formed from two or more individual spins, or pairs of strongly-coupled spins that mostly cancel the state-dependent hyperfine interaction term) [70–72], and using isotopically purified samples for which weakly coupled ^{13}C nuclear spin qubits can be controlled [73, 74]). Other methods are to engineer systems of coupled defects (e.g. involving a ^{13}C nuclear spin qubit coupled to a P1 center in the vicinity of an NV center [75], or to use the nitrogen nuclear spin of a

10

second NV center (whose nitrogen nuclear spin is used as a memory) in proximity to the communicator NV center [76, 77].

10.4. Towards large-scale quantum networks*

Having discussed the core quantum network components based on diamond color centers, we now turn to what is required to build these into a network capable of distributing entanglement over large distances at high rates.

Quantum frequency conversion

First, a future quantum internet will likely make use of existing fiber infrastructure. This necessitates the matching of the photon wavelength from the network node to the telecommunication bands using quantum frequency conversion. Recently, it has been demonstrated that spin-photon entanglement can be preserved after frequency down-conversion of a ~ 637 nm photon entangled with the spin-state of the NV center to telecommunication wavelengths (~ 1588 nm) [78]. Similar conversion techniques can be applied to other color centers and quantum systems [79–83]. Future work will focus on increasing the system efficiency and potentially integrating on-chip conversion (see below).

Real-world implementations

Second, it will be important to lower the footprint and cost of experimental setups. Since a large-scale quantum network will likely make use of already existing fiber connections, data centers are natural candidates for the placement of quantum repeater nodes. An important first step could thus be to shrink experimental setups to the standard 19-inch server racks used in industry [87], and ruggedize components so that the need for manual intervention can be kept to a minimum, and the systems can tolerate the conditions prevailing at such locations.

Scaling qubit numbers

Third, future quantum networks covering large distances will require many quantum repeater stations — each with a large number of qubits — for multiplexing, purification and error-correction. For example, 5-10 repeater stations with kilohertz entangled bit (ebit) rates need a total of $O(10^8)$ data qubits to reach mega-ebits per second communication [88]. Although color center devices are already produced using standard nanofabrication techniques, the needed scale for high-rate, high-fidelity networks would require large-scale manufacturing of quantum nodes. This task not only entails qubit and device production but also the packaging of efficient optical and microwave signals to and from many independent color centers at once.

Photonic integrated circuits for quantum applications

Optical technologies such as photonic integrated circuits (PICs) may play an important role in addressing these challenges. Their programmability [89] and access to a large number of spatial modes [90] are especially of interest to quantum network applications. Similar to their bulk optics counterparts, PICs comprise of low-loss on-chip components, such as waveguides, filters and switches. References [89–92] review the device
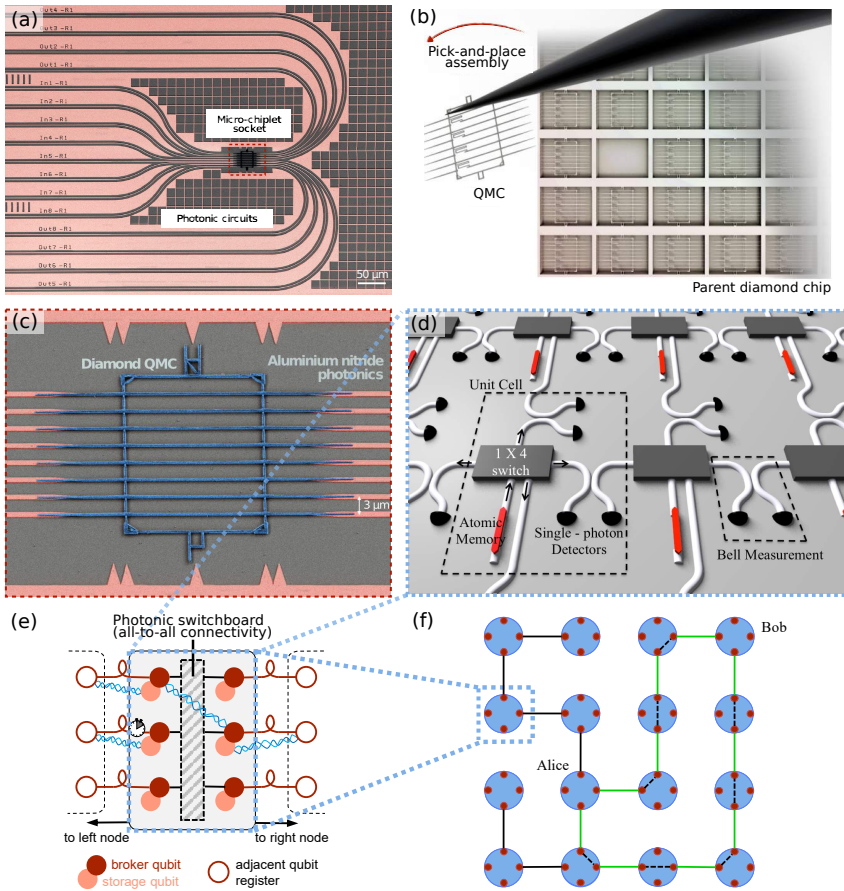
Figure 10.2: Schematic of realized and envisioned architectures for large-scale hybrid integrated circuits enabling entanglement routing. (a) False-color SEM image of a AlN-on-sapphire photonic integrated circuit (PIC), containing a diamond quantum microchiplet [QMC, red dashed area, enlarged view in (c)]. These microchiplets with embedded color centers are pre-fabricated and -characterized in the diamond host material, and transferred onto the PIC using a pick-and-place technique (b), allowing to optimize PICs and microchiplets separately. This technique has been used to generate a defect-free array of 128 nanophotonic waveguides containing individually addressable quantum emitters, coupled to the PIC [31]. Images (a-c) adapted with permission from Ref. [31]. (d) Integrated multi-quantum memory node in a modular architecture [84]. Each unit cell (black dashed line) contains a diamond-based atomic memory (red), a fast, reconfigurable switching network allowing all-to-all connectivity (realized e.g. via Mach-Zehnder interferometers), and photo-detectors. The atomic memory includes one communication and several memory qubits, with the communication qubit coupled to a diamond nanophotonic structure. Figure reprinted with permission from Ref. [84], in accordance with creativecommons.org/licenses/by/4.0/legalcode. (e) Entanglement routing in a quantum network. A multi-path routing algorithm (realized e.g. via re-configurable PICs, dashed black box) can improve the entanglement generation rate (wiggled blue lines) between distant nodes (white circles), compared to a linear repeater topology [85]. This allows concurrent communication links with only local information used in each node (f, data and communication qubits depicted in light and dark red, respectively). Figure (e) adapted with permission from Ref. [85]. Figure (f) reprinted with permission from Ref. [86], in accordance with creativecommons.org/licenses/by/4.0/legalcode.

10

concepts and state of the art of PIC technologies that may be relevant to quantum network applications. Driven by foundry adoption, as well as new frontiers in data communication [93, 94], photonic processors [95, 96] and optical quantum computing [97], integrated photonic circuits have advanced dramatically in manufacturability and complexity over the last decade. The first notable feature of PICs for quantum technologies is their compact footprint, which not only promotes dense integration, but also reduces phase errors in quantum interference of photons [89]. Next, phase modulators in PICs can implement on-chip switches for routing photons within an optical network [89], and material nonlinearities can be used for efficient frequency conversion between visible and telecommunication photons [98]. Finally, multi-channel optical access can be accomplished using standard fiber arrays, and electrical packaging for large-scale control of color centers can be achieved using potential metal layers in a PIC stack.

COMBINING PHOTONIC INTEGRATED CIRCUITS WITH DIAMOND NANOPHOTONICS

Photonic circuits in diamond have been previously demonstrated for optomechanics [99] and nonlinear optics [100]. Gallium phosphide-on-diamond photonics have also been used to route the emission from NV centers [101]. However, the non-deterministic creation and integration of color centers in devices, as well as the absence of single-crystal diamond wafers have limited the scale of diamond integrated photonics (see Sec. 10.2). One way to combine the functionalities and performance of industry-leading photonic circuits with diamond is through heterogeneous integration of diamond with other material systems. Also known as "hybrid photonics" [102, 103], this approach is akin to modern integrated circuits in that discrete chips are separately optimized and fabricated and then populated into a larger circuit board. Examples of heterogeneous integration include modulators and lasers in silicon photonics [104]. In the context of quantum photonics, recent successes include quantum emitters [102, 103] and single-photon detectors [105], which are otherwise difficult to achieve in a single material platform with high performance.

Heterogeneous integration of diamond color centers with PICs circumvents the yield issues associated with all-diamond architectures, thereby allowing potentially many addressable qubits within a single chip. A recent result showing the large-scale integration of color centers in diamond with hybrid photonic integrated circuits [31] is shown in Fig. 10.2(a-c). Diamond quantum micro-chiplets, each consisting of 8 diamond nanophotonic waveguides with at least one addressable group-IV color center, are integrated with PICs based on aluminum nitride [Fig. 10.2(c)]. After fabrication using the quasi-isotropic undercut technique (see Sec. 10.2), a total of 16 chiplets numbering to 128 waveguides were positioned with sub-microns accuracy on the PIC [Fig. 10.2(a)] using a pick-and-place technique [Fig. 10.2(b)]. The coupling of the color center to the waveguide can be as high as 55 %, and the diamond-PIC coupling and PIC-to-optical fiber coupling are reported to be 34 % and 11 %, respectively. In addition, electrodes in this hybrid PIC enabled the in-situ tuning of optical transition frequencies within this integrated device architecture [31]. The availability of multiple color centers per waveguide potentially allows for spectral multiplexing [106, 107], which is a hardware-efficient path to multiplying the total number of qubits to $N_s \times N_f$, where N_s and N_f are the number of spatial and frequency channels, respectively.

With further improvements in waveguide-emitter coupling as well as diamond-nanocavity integration with PICs, such a hybrid architecture could become an important building block of future quantum network nodes. Looking forward, we expect future developments to also focus on integrating chip components for color center technologies, such as CMOS-integrated microwave electronics for spin control [108], on-chip beam-splitters for photon quantum interference [97], optical switches for channel connectivity [89], single-photon detectors [105, 109–111] for heralded entanglement, and quantum frequency conversion [112, 113] or frequency tuning [114] on the same microphotonic platform. While these functionalities have been realized in other PIC platforms, a key challenge is to bring together various technologies and materials for implementing a chip-based node. Here, the advances in heterogeneous integration will be critical for controlling and deploying a large number of such chips.

Entanglement routing

As an example of such a chip, Fig. 10.2(d) shows a modular architecture with many unit cells per network node [84]. Each unit cell consists of atomic memories, photonic switches, and single-photon detectors. The atomic memories include communication qubits for inter-cell entanglement and memory qubits for long-term storage and intra-cell information processing. The switching network selects one of the adjacent cells, and the photo-detectors herald successful entanglement events between cells. Such a photonic architecture could allow for entanglement routing within a chip-based node, potentially boosting the communication rate [85, 115]. By establishing connectivity between unit cells using optical switches, the resulting network is scalable because adding nodes does not require any modification in the existing network.

Entanglement distillation and quantum error correction

Once multiple long-lived memory qubits that can be controlled with high fidelity are available per quantum network node, the entanglement fidelity can be greatly improved through entanglement distillation (purification), where low fidelity entangled pairs are employed as a resource and transformed to a smaller number of high fidelity pairs after local operations and classical communication [116, 117]. Such a scheme has recently been demonstrated in a proof-of-principle experiment between two distant NV centers that each have access to an additional ^{13}C memory [56]. While such distillation requires additional time resources as a result from two-way-classical-communication, quantum error correction [118] can achieve a more favorable key rate per qubit scaling[88]. Such error correction can be performed if the operational error is smaller than the threshold of a given code (e.g. ≈ 0.189 for the Calderbank-Shor-Stean (CSS) code [119]). If the photon-loss of a link is sufficiently small, heralded entanglement generation can also be replaced with error correction, allowing to move beyond two-way signalling associated with the heralding [120]. In addition, multi-qubit network nodes can be operated in a way that outperforms more simple linear repeater schemes. For example, Fig. 10.2(f) shows a 2D network with nearest-neighbor connectivity that allows multi-path entanglement routing [86]. Crucially, the algorithm only requires local knowledge about which of the entanglement generation attempts with its nearest neighbor succeeded while still achieving faster key distribution than a linear repeater chain [86].

10

10.5. CONCLUSIONS*

This thesis discussed the emerging field of quantum networks based on diamond color centers. Diamond color centers already define the state of the art in multi-node entanglement-based networks [58] and in memory-enhanced quantum key distribution [121]. We expect the next years to see rapid progress on photonic interfaces and integration of color centers, paving the way for first experiments on long-distance quantum links. From the basic building blocks, larger-scale devices will be designed and constructed. Control layers of higher abstraction – akin to the current Internet – are currently being developed [122, 123].

A future functional quantum network will support many interesting applications, such as distributed quantum computing [124], accessing a quantum server in the cloud with full privacy [125] and stabilizing quantum clocks [126, 127]. Color centers in diamond may play an essential role in these networks, as the "satisfactory repeater", or perhaps the "transistor of the quantum age."

10

REFERENCES

[1] M. Ruf, N. H. Wan, H. Choi, D. Englund and R. Hanson, *Quantum networks based on color centers in diamond,* Journal of Applied Physics **130**, 070901 (2021).

[2] M. Ruf, M. IJspeert, S. van Dam, N. de Jong, H. van den Berg, G. Evers and R. Hanson, *Optically Coherent Nitrogen-Vacancy Centers in Micrometer-Thin Etched Diamond Membranes,* Nano Letters **19**, 3987 (2019).

[3] A. Faraon, C. Santori, Z. Huang, V. M. Acosta and R. G. Beausoleil, *Coupling of Nitrogen-Vacancy Centers to Photonic Crystal Cavities in Monocrystalline Diamond,* Physical Review Letters **109**, 033604 (2012).

[4] D. Bluvstein, Z. Zhang and A. C. Jayich, *Identifying and Mitigating Charge Instabilities in Shallow Diamond Nitrogen-Vacancy Centers,* Physical Review Letters **122**, 76101 (2019).

[5] S. Sangtawesin *et al.*, *Origins of Diamond Surface Noise Probed by Correlating Single-Spin Measurements with Surface Spectroscopy,* Physical Review X **9**, 031052 (2019).

[6] H. F. Fotso, A. E. Feiguin, D. D. Awschalom and V. V. Dobrovitski, *Suppressing Spectral Diffusion of Emitted Photons with Optical Pulses,* Physical Review Letters **116**, 1 (2016).

[7] I. Lekavicius, T. Oo and H. Wang, *Diamond Lamb wave spin-mechanical resonators with optically coherent nitrogen vacancy centers,* Journal of Applied Physics **126**, 214301 (2019).

[8] M. Kasperczyk, J. A. Zuber, A. Barfuss, J. Kölbl, V. Yurgens, S. Flågan, T. Jakubczyk, B. Shields, R. J. Warburton and P. Maletinsky, *Statistically modeling optical linewidths of nitrogen vacancy centers in microstructures,* Physical Review B **102**, 075312 (2020).

[9] V. Yurgens, J. A. Zuber, S. Flågan, M. De Luca, B. J. Shields, I. Zardo, P. Maletinsky, R. J. Warburton and T. Jakubczyk, *Low-Charge-Noise Nitrogen-Vacancy Centers in Diamond Created Using Laser Writing with a Solid-Immersion Lens,* ACS Photonics **8**, 1726 (2021).

[10] M. Ruf, M. Weaver, S. van Dam and R. Hanson, *Resonant Excitation and Purcell Enhancement of Coherent Nitrogen-Vacancy Centers Coupled to a Fabry-Perot Microcavity,* Physical Review Applied **15**, 024049 (2021).

[11] Y.-C. Chen *et al.*, *Laser writing of individual nitrogen-vacancy defects in diamond with near-unity yield,* Optica **6**, 662 (2019).

[12] S. B. van Dam, M. Walsh, M. J. Degen, E. Bersin, S. L. Mouradian, A. Galiullin, M. Ruf, M. IJspeert, T. H. Taminiau, R. Hanson and D. R. Englund, *Optical coherence of diamond nitrogen-vacancy centers formed by ion implantation and annealing,* Physical Review B **99**, 161203 (2019).

10

[13] Y. Chu *et al.*, *Coherent Optical Transitions in Implanted Nitrogen Vacancy Centers,* Nano Letters **14**, 1982 (2014).

[14] B. Merkel, A. Ulanowski and A. Reiserer, *Coherent and Purcell-Enhanced Emission from Erbium Dopants in a Cryogenic High-Q Resonator,* Physical Review X **10**, 041025 (2020).

[15] Y. Fontana, R. Zifkin, E. Janitz, C. D. Rodríguez Rosenblueth and L. Childress, *A mechanically stable and tunable cryogenic Fabry–Pérot microcavity,* Review of Scientific Instruments **92**, 053906 (2021).

[16] E. Janitz, M. Ruf, Y. Fontana, J. Sankey and L. Childress, *High mechanical bandwidth fiber-coupled Fabry-Perot cavity,* Optics Express **25**, 20932 (2017).

[17] E. D. Black, *An introduction to Pound–Drever–Hall laser frequency stabilization,* American Journal of Physics **69**, 79 (2001).

[18] J. F. S. Brachmann, H. Kaupp, T. W. Hänsch and D. Hunger, *Photothermal effects in ultra-precisely stabilized tunable microcavities,* Optics Express **24**, 21205 (2016).

[19] J. Borregaard, A. S. Sørensen and P. Lodahl, *Quantum Networks with Deterministic Spin–Photon Interfaces,* Advanced Quantum Technologies **2**, 1800091 (2019).

[20] F. Rozpędek, R. Yehia, K. Goodenough, M. Ruf, P. C. Humphreys, R. Hanson, S. Wehner and D. Elkouss, *Near-term quantum-repeater experiments with nitrogen-vacancy centers: Overcoming the limitations of direct transmission,* Physical Review A **99**, 052330 (2019).

[21] G. Murta, S. B. van Dam, J. Ribeiro, R. Hanson and S. Wehner, *Towards a realization of device-independent quantum key distribution,* Quantum Science and Technology **4**, 035011 (2019).

[22] R. E. Evans *et al.*, *Photon-mediated interactions between quantum emitters in a diamond nanocavity,* Science **362**, 662 (2018).

[23] S. B. van Dam, *Optical cavities, coherent emitters, and protocols for diamond-based quantum networks,* Ph.D. thesis, TU Delft (2019).

[24] T. Đorđević, P. Samutpraphoot, P. L. Ocola, H. Bernien, B. Grinkemeyer, I. Dimitrova, V. Vuletić and M. D. Lukin, *Entanglement transport and a nanophotonic interface for atoms in optical tweezers,* Science **9917**, eabi9917 (2021).

[25] A. Sipahigil *et al.*, *An integrated diamond nanophotonics platform for quantum-optical networks,* Science **354**, 847 (2016).

[26] C. T. Nguyen *et al.*, *An integrated nanophotonic quantum register based on silicon-vacancy spins in diamond,* Physical Review B **100**, 1 (2019).

[27] S. Meesala *et al.*, *Strain engineering of the silicon-vacancy center in diamond,* Physical Review B **97**, 1 (2018).

10

[28] Y. I. Sohn *et al.*, *Controlling the coherence of a diamond spin qubit through its strain environment*, Nature Communications **9**, 17 (2018).

[29] S. Maity, L. Shao, Y.-I. Sohn, S. Meesala, B. Machielse, E. Bielejec, M. Markham and M. Lončar, *Spectral Alignment of Single-Photon Emitters in Diamond using Strain Gradient*, Physical Review Applied **10**, 024050 (2018).

[30] B. Machielse *et al.*, *Quantum Interference of Electromechanically Stabilized Emitters in Nanophotonic Devices*, Physical Review X **9**, 1 (2019).

[31] N. H. Wan, T. J. Lu, K. C. Chen, M. P. Walsh, M. E. Trusheim, L. De Santis, E. A. Bersin, I. B. Harris, S. L. Mouradian, I. R. Christen, E. S. Bielejec and D. Englund, *Large-scale integration of artificial atoms in hybrid photonic circuits*, Nature **583**, 226 (2020).

[32] L. De Santis, M. Trusheim, K. Chen and D. Englund, *Investigation of the Stark Effect on a Centrosymmetric Quantum Emitter in Diamond*, arXiv preprint (2021), arXiv:2102.01322 .

[33] S. Aghaeimeibodi, D. Riedel, A. E. Rugar, C. Dory and J. Vučković, *Electrical Tuning of Tin-Vacancy Centers in Diamond*, Physical Review Applied **15**, 064010 (2021).

[34] S. Sun *et al.*, *Cavity-Enhanced Raman Emission from a Single Color Center in a Solid*, Physical Review Letters **121**, 083601 (2018).

[35] A. E. Rugar, C. Dory, S. Aghaeimeibodi, H. Lu, S. Sun, S. D. Mishra, Z.-X. Shen, N. A. Melosh and J. Vučković, *Narrow-Linewidth Tin-Vacancy Centers in a Diamond Waveguide*, ACS Photonics **7**, 2356 (2020).

[36] T. Iwasaki, Y. Miyamoto, T. Taniguchi, P. Siyushev, M. H. Metsch, F. Jelezko and M. Hatano, *Tin-Vacancy Quantum Emitters in Diamond*, Physical Review Letters **119**, 253601 (2017).

[37] J. Görlitz, D. Herrmann, G. Thiering, P. Fuchs, M. Gandil, T. Iwasaki, T. Taniguchi, M. Kieschnick, J. Meijer, M. Hatano, A. Gali and C. Becher, *Spectroscopic investigations of negatively charged tin-vacancy centres in diamond*, New Journal of Physics **22**, 013048 (2020).

[38] P. Wang, T. Taniguchi, Y. Miyamoto and M. Hatano, *Low-Temperature Spectroscopic Investigation of Lead-Vacancy Centers in Diamond Fabricated by High-Pressure and High- Temperature Treatment*, arXiv preprint (2021), arXiv::2106.03413 .

[39] A. E. Rugar, H. Lu, C. Dory, S. Sun, P. J. McQuade, Z. X. Shen, N. A. Melosh and J. Vučković, *Generation of Tin-Vacancy Centers in Diamond via Shallow Ion Implantation and Subsequent Diamond Overgrowth*, Nano Letters **20**, 1614 (2020).

[40] C. A. McLellan, B. A. Myers, S. Kraemer, K. Ohno, D. D. Awschalom and A. C. Bleszynski Jayich, *Patterned Formation of Highly Coherent Nitrogen-Vacancy Centers Using a Focused Electron Irradiation Technique*, Nano Letters **16**, 2450 (2016).

10

[41] A. T. Collins, *The Fermi level in diamond,* Journal of Physics: Condensed Matter **14**, 3743 (2002).

[42] B. C. Rose *et al.*, *Observation of an environmentally insensitive solid-state spin defect in diamond,* Science **361**, 60 (2018).

[43] T. Murai, T. Makino, H. Kato, M. Shimizu, T. Murooka, E. D. Herbschleb, Y. Doi, H. Morishita, M. Fujiwara, M. Hatano, S. Yamasaki and N. Mizuochi, *Engineering of Fermi level by nin diamond junction for control of charge states of NV centers,* Applied Physics Letters **112**, 111903 (2018).

[44] T. Lühmann, R. John, R. Wunderlich, J. Meijer and S. Pezzagna, *Coulomb-driven single defect engineering for scalable qubits and spin sensors in diamond,* Nature Communications **10**, 4956 (2019).

[45] S. D. Tchernij *et al.*, *Single-Photon-Emitting Optical Centers in Diamond Fabricated upon Sn Implantation,* ACS Photonics **4**, 2580 (2017).

[46] M. E. Trusheim *et al.*, *Lead-related quantum emitters in diamond,* Physical Review B **99**, 1 (2019).

[47] S. Mouradian, N. H. Wan, T. Schröder and D. Englund, *Rectangular photonic crystal nanobeam cavities in bulk diamond,* Applied Physics Letters **111**, 021103 (2017).

[48] A. E. Rugar, S. Aghaeimeibodi, D. Riedel, C. Dory, H. Lu, P. J. McQuade, Z.-X. Shen, N. A. Melosh and J. Vučković, *Quantum Photonic Interface for Tin-Vacancy Centers in Diamond,* Physical Review X **11**, 031021 (2021).

[49] N. H. Wan, S. Mouradian and D. Englund, *Two-dimensional photonic crystal slab nanocavities on bulk single-crystal diamond,* Applied Physics Letters **112**, 141102 (2018).

[50] S. Mosor, J. Hendrickson, B. C. Richards, J. Sweet, G. Khitrova, H. M. Gibbs, T. Yoshie, A. Scherer, O. B. Shchekin and D. G. Deppe, *Scanning a photonic crystal slab nanocavity by condensation of xenon,* Applied Physics Letters **87**, 141105 (2005).

[51] N. H. Wan, B. J. Shields, D. Kim, S. Mouradian, B. Lienhard, M. Walsh, H. Bakhru, T. Schröder and D. Englund, *Efficient Extraction of Light from a Nitrogen-Vacancy Center in a Diamond Parabolic Reflector,* Nano Letters **18**, 2787 (2018).

[52] R. Høy Jensen, E. Janitz, Y. Fontana, Y. He, O. Gobron, I. P. Radko, M. Bhaskar, R. Evans, C. D. Rodríguez Rosenblueth, L. Childress, A. Huck and U. Lund Andersen, *Cavity-Enhanced Photon Emission from a Single Germanium-Vacancy Center in a Diamond Membrane,* Physical Review Applied **13**, 064016 (2020).

[53] S. Häußler, J. Benedikter, K. Bray, B. Regan, A. Dietrich, J. Twamley, I. Aharonovich, D. Hunger and A. Kubanek, *Diamond photonics platform based on silicon vacancy centers in a single-crystal diamond membrane and a fiber cavity,* Physical Review B **99**, 1 (2019).

10

[54] M. Salz, Y. Herrmann, A. Nadarajah, A. Stahl, M. Hettrich, A. Stacey, S. Prawer, D. Hunger and F. Schmidt-Kaler, *Cryogenic platform for coupling color centers in diamond membranes to a fiber-based microcavity,* Applied Physics B **126**, 131 (2020).

[55] T. H. Taminiau, J. Cramer, T. Van Der Sar, V. V. Dobrovitski and R. Hanson, *Universal control and error correction in multi-qubit spin registers in diamond,* Nature Nanotechnology **9**, 171 (2014).

[56] N. Kalb, A. A. Reiserer, P. C. Humphreys, J. J. Bakermans, S. J. Kamerling, N. H. Nickerson, S. C. Benjamin, D. J. Twitchen, M. Markham and R. Hanson, *Entanglement distillation between solid-state quantum network nodes,* Science **356**, 928 (2017).

[57] C. E. Bradley, J. Randall, M. H. Abobeih, R. C. Berrevoets, M. J. Degen, M. A. Bakker, M. Markham, D. J. Twitchen and T. H. Taminiau, *A Ten-Qubit Solid-State Spin Register with Quantum Memory up to One Minute,* Physical Review X **9**, 31045 (2019).

[58] M. Pompili, S. L. N. Hermans, S. Baier, H. K. C. Beukers, P. C. Humphreys, R. N. Schouten, R. F. L. Vermeulen, M. J. Tiggelman, L. dos Santos Martins, B. Dirkse, S. Wehner and R. Hanson, *Realization of a multinode quantum network of remote solid-state qubits,* Science **372**, 259 (2021).

[59] C. T. Nguyen, D. D. Sukachev, M. K. Bhaskar, B. MacHielse, D. S. Levonian, E. N. Knall, P. Stroganov, R. Riedinger, H. Park, M. Lončar and M. D. Lukin, *Quantum Network Nodes Based on Diamond Qubits with an Efficient Nanophotonic Interface,* Physical Review Letters **123**, 1 (2019).

[60] H. Bernien, B. Hensen, W. Pfaff, G. Koolstra, M. S. Blok, L. Robledo, T. H. Taminiau, M. Markham, D. J. Twitchen, L. Childress and R. Hanson, *Heralded entanglement between solid-state qubits separated by three metres,* Nature **497**, 86 (2013).

[61] N. H. Nickerson, J. F. Fitzsimons and S. C. Benjamin, *Freely scalable quantum technologies using cells of 5-to-50 qubits with very lossy and noisy photonic links,* Physical Review X **4**, 1 (2014).

[62] G. Waldherr, Y. Wang, S. Zaiser, M. Jamali, T. Schulte-Herbrüggen, H. Abe, T. Ohshima, J. Isoya, J. F. Du, P. Neumann and J. Wrachtrup, *Quantum error correction in a solid-state hybrid spin register,* Nature **506**, 204 (2014).

[63] J. Cramer, N. Kalb, M. A. Rol, B. Hensen, M. S. Blok, M. Markham, D. J. Twitchen, R. Hanson and T. H. Taminiau, *Repeated quantum error correction on a continuously encoded qubit by real-time feedback,* Nature Communications **7**, 1 (2016).

[64] M. H. Abobeih, *From atomic-scale imaging to quantum fault-tolerance with spins in diamond,* Ph.D. thesis, TU Delft (2021).

[65] M. H. Abobeih, J. Randall, C. E. Bradley, H. P. Bartling, M. A. Bakker, M. J. Degen, M. Markham, D. J. Twitchen and T. H. Taminiau, *Atomic-scale imaging of a 27-nuclear-spin cluster using a quantum sensor,* Nature **576**, 411 (2019).

10

[66] K. Jung, M. H. Abobeih, J. Yun, G. Kim, H. Oh, A. Henry, T. H. Taminiau and D. Kim, *Deep learning enhanced individual nuclear-spin detection,* npj Quantum Information **7**, 41 (2021).

[67] W. Pfaff, B. J. Hensen, H. Bernien, S. B. Van Dam, M. S. Blok, T. H. Taminiau, M. J. Tiggelman, R. N. Schouten, M. Markham, D. J. Twitchen and R. Hanson, *Unconditional quantum teleportation between distant solid-state quantum bits,* Science **345**, 532 (2014).

[68] B. Pingault, D. D. Jarausch, C. Hepp, L. Klintberg, J. N. Becker, M. Markham, C. Becher and M. Atatüre, *Coherent control of the silicon-vacancy spin in diamond,* Nature Communications **8**, 1 (2017).

[69] N. Kalb, P. C. Humphreys, J. J. Slim and R. Hanson, *Dephasing mechanisms of diamond-based nuclear-spin memories for quantum networks,* Physical Review A **97**, 062330 (2018).

[70] A. Reiserer, N. Kalb, M. S. Blok, K. J. M. van Bemmelen, T. H. Taminiau, R. Hanson, D. J. Twitchen and M. Markham, *Robust Quantum-Network Memory Using Decoherence-Protected Subspaces of Nuclear Spins,* Physical Review X **6**, 021040 (2016).

[71] M. H. Abobeih, J. Cramer, M. A. Bakker, N. Kalb, M. Markham, D. J. Twitchen and T. H. Taminiau, *One-second coherence for a single electron spin coupled to a multiqubit nuclear-spin environment,* Nature Communications **9**, 1 (2018).

[72] H. P. Bartling, M. H. Abobeih, B. Pingault, M. J. Degen, S. J. H. Loenen, C. E. Bradley, J. Randall, M. Markham, D. J. Twitchen and T. H. Taminiau, *Coherence and entanglement of inherently long-lived spin pairs in diamond,* arXiv preprint (2021), arXiv:2103.07961 .

[73] M. Pfender, N. Aslam, H. Sumiya, S. Onoda, P. Neumann, J. Isoya, C. A. Meriles and J. Wrachtrup, *Nonvolatile nuclear spin memory enables sensor-unlimited nanoscale spectroscopy of small spin clusters,* Nature Communications **8**, 834 (2017).

[74] M. Pfender, P. Wang, H. Sumiya, S. Onoda, W. Yang, D. B. R. Dasari, P. Neumann, X.-y. Pan, J. Isoya, R.-b. Liu and J. Wrachtrup, *High-resolution spectroscopy of single nuclear spins via sequential weak measurements,* Nature Communications **10**, 594 (2019).

[75] M. J. Degen, S. J. H. Loenen, H. P. Bartling, C. E. Bradley, A. L. Meinsma, M. Markham, D. J. Twitchen and T. H. Taminiau, *Entanglement of dark electron-nuclear spin defects in diamond,* Nature Communications **12**, 3470 (2021).

[76] T. Yamamoto, C. Müller, L. P. McGuinness, T. Teraji, B. Naydenov, S. Onoda, T. Ohshima, J. Wrachtrup, F. Jelezko and J. Isoya, *Strongly coupled diamond spin qubits by molecular nitrogen implantation,* Physical Review B - Condensed Matter and Materials Physics **88**, 1 (2013).

10

[77] M. J. Degen, *On the creation, coherence and entanglement of multi-defect quantum registers in diamond,* Ph.D. thesis, TU Delft (2021).

[78] A. Tchebotareva, S. L. Hermans, P. C. Humphreys, D. Voigt, P. J. Harmsma, L. K. Cheng, A. L. Verlaan, N. Dijkhuizen, W. de Jong, A. Dréau and R. Hanson, *Entanglement between a Diamond Spin Qubit and a Photonic Time-Bin Qubit at Telecom Wavelength,* Physical Review Letters **123**, 063601 (2019).

[79] V. Krutyanskiy, M. Meraner, J. Schupp, V. Krcmarsky, H. Hainzer and B. P. Lanyon, *Light-matter entanglement over 50 km of optical fibre,* npj Quantum Information **5**, 72 (2019).

[80] M. Bock, P. Eich, S. Kucera, M. Kreis, A. Lenhard, C. Becher and J. Eschner, *High-fidelity entanglement between a trapped ion and a telecom photon via quantum frequency conversion,* Nature Communications **9**, 1998 (2018).

[81] R. Ikuta, T. Kobayashi, T. Kawakami, S. Miki, M. Yabuno, T. Yamashita, H. Terai, M. Koashi, T. Mukai, T. Yamamoto and N. Imoto, *Polarization insensitive frequency conversion for an atom-photon entanglement distribution via a telecom network,* Nature Communications **9**, 1997 (2018).

[82] Y. Yu *et al.*, *Entanglement of two quantum memories via fibres over dozens of kilometres,* Nature **578**, 240 (2020).

[83] K. De Greve *et al.*, *Quantum-dot spin-photon entanglement via frequency downconversion to telecom wavelength,* Nature **491**, 421 (2012).

[84] H. Choi, M. Pant, S. Guha and D. Englund, *Percolation-based architecture for cluster state creation using photon-mediated entanglement between atomic memories,* npj Quantum Information **5**, 104 (2019).

[85] Y. Lee, E. Bersin, A. Dahlberg, S. Wehner and D. Englund, *A Quantum Router Architecture for High-Fidelity Entanglement Flows in Quantum Networks,* arXiv preprint (2020), arXiv:2005.01852 .

[86] M. Pant, H. Krovi, D. Towsley, L. Tassiulas, L. Jiang, P. Basu, D. Englund and S. Guha, *Routing entanglement in the quantum internet,* npj Quantum Information **5**, 1 (2019).

[87] I. Pogorelov *et al.*, *Compact Ion-Trap Quantum Computing Demonstrator,* PRX Quantum **2**, 020343 (2021).

[88] S. Muralidharan, L. Li, J. Kim, N. Lütkenhaus, M. D. Lukin and L. Jiang, *Optimal architectures for long distance quantum communication,* Scientific Reports **6**, 20463 (2016).

[89] W. Bogaerts, D. Pérez, J. Capmany, D. A. B. Miller, J. Poon, D. Englund, F. Morichetti and A. Melloni, *Programmable photonic circuits,* Nature **586**, 207 (2020).

10

[90] N. C. Harris, J. Carolan, D. Bunandar, M. Prabhu, M. Hochberg, T. Baehr-Jones, M. L. Fanto, A. M. Smith, C. C. Tison, P. M. Alsing and D. Englund, *Linear programmable nanophotonic processors,* Optica **5,** 1623 (2018).

[91] D. J. Blumenthal, R. Heideman, D. Geuzebroek, A. Leinse and C. Roeloffzen, *Silicon Nitride in Silicon Photonics,* Proceedings of the IEEE **106,** 2209 (2018).

[92] D. Zhu *et al.*, *Integrated photonics on thin-film lithium niobate,* Advances in Optics and Photonics **13,** 242 (2021).

[93] C. Sun *et al.*, *Single-chip microprocessor that communicates directly using light,* Nature **528,** 534 (2015).

[94] A. H. Atabaki *et al.*, *Integrating photonics with silicon nanoelectronics for the next generation of systems on a chip,* Nature **556,** 349 (2018).

[95] G. Wetzstein, A. Ozcan, S. Gigan, S. Fan, D. Englund, M. Soljačić, C. Denz, D. A. B. Miller and D. Psaltis, *Inference in artificial intelligence with deep optics and photonics,* Nature **588,** 39 (2020).

[96] B. J. Shastri, A. N. Tait, T. Ferreira de Lima, W. H. P. Pernice, H. Bhaskaran, C. D. Wright and P. R. Prucnal, *Photonics for artificial intelligence and neuromorphic computing,* Nature Photonics **15,** 102 (2021).

[97] J. Wang, F. Sciarrino, A. Laing and M. G. Thompson, *Integrated photonic quantum technologies,* Nature Photonics **14,** 273 (2020).

[98] C. Wang, C. Langrock, A. Marandi, M. Jankowski, M. Zhang, B. Desiatov, M. M. Fejer and M. Lončar, *Ultrahigh-efficiency wavelength conversion in nanophotonic periodically poled lithium niobate waveguides,* Optica **5,** 1438 (2018).

[99] P. Rath, S. Khasminskaya, C. Nebel, C. Wild and W. H. Pernice, *Grating-assisted coupling to nanophotonic circuits in microcrystalline diamond thin films,* Beilstein Journal of Nanotechnology **4,** 300 (2013).

[100] B. J. M. Hausmann, I. Bulu, V. Venkataraman, P. Deotare and M. Lončar, *Diamond nonlinear photonics,* Nature Photonics **8,** 369 (2014).

[101] M. Gould, E. R. Schmidgall, S. Dadgostar, F. Hatami and K. M. C. Fu, *Efficient Extraction of Zero-Phonon-Line Photons from Single Nitrogen-Vacancy Centers in an Integrated GaP-on-Diamond Platform,* Physical Review Applied **6,** 2 (2016).

[102] J. Kim, S. Aghaeimeibodi, J. Carolan, D. Englund and E. Waks, *Hybrid integration methods for on-chip quantum photonics,* Optica **7,** 291 (2020).

[103] A. W. Elshaari, W. Pernice, K. Srinivasan, O. Benson and V. Zwiller, *Hybrid integrated quantum photonic circuits,* Nature Photonics **14,** 285 (2020).

[104] T. Komljenovic, D. Huang, P. Pintus, M. A. Tran, M. L. Davenport and J. E. Bowers, *Photonic Integrated Circuits Using Heterogeneous Integration on Silicon,* Proceedings of the IEEE **106,** 2246 (2018).

10

[105] F. Najafi, J. Mower, N. C. Harris, F. Bellei, A. Dane, C. Lee, X. Hu, P. Kharel, F. Marsili, S. Assefa, K. K. Berggren and D. Englund, *On-chip detection of non-classical light by scalable integration of single-photon detectors,* Nature Communications **6**, 5873 (2015).

[106] E. Bersin, M. Walsh, S. L. Mouradian, M. E. Trusheim, T. Schröder and D. Englund, *Individual control and readout of qubits in a sub-diffraction volume,* npj Quantum Information **5**, 38 (2019).

[107] S. Chen, M. Raha, C. M. Phenicie, S. Ourari and J. D. Thompson, *Parallel single-shot measurement and coherent control of solid-state spins below the diffraction limit,* Science **370**, 592 (2020).

[108] D. Kim, M. I. Ibrahim, C. Foy, M. E. Trusheim, R. Han and D. R. Englund, *A CMOS-integrated quantum sensor based on nitrogen–vacancy centres,* Nature Electronics **2**, 284 (2019).

[109] G. Reithmaier, M. Kaniber, F. Flassig, S. Lichtmannecker, K. Müller, A. Andrejew, J. Vučković, R. Gross and J. J. Finley, *On-Chip Generation, Routing, and Detection of Resonance Fluorescence,* Nano Letters **15**, 5208 (2015).

[110] M. Schwartz, E. Schmidt, U. Rengstl, F. Hornung, S. Hepp, S. L. Portalupi, K. Llin, M. Jetter, M. Siegel and P. Michler, *Fully On-Chip Single-Photon Hanbury-Brown and Twiss Experiment on a Monolithic Semiconductor–Superconductor Platform,* Nano Letters **18**, 6892 (2018).

[111] S. Gyger, J. Zichi, L. Schweickert, A. W. Elshaari, S. Steinhauer, S. F. Covre da Silva, A. Rastelli, V. Zwiller, K. D. Jöns and C. Errando-Herranz, *Reconfigurable photonics with on-chip single-photon detectors,* Nature Communications **12**, 1408 (2021).

[112] X. Guo, C.-L. Zou, H. Jung and H. X. Tang, *On-Chip Strong Coupling and Efficient Frequency Conversion between Telecom and Visible Optical Modes,* Physical Review Letters **117**, 123902 (2016).

[113] M. Jankowski, C. Langrock, B. Desiatov, A. Marandi, C. Wang, M. Zhang, C. R. Phillips, M. Lončar and M. M. Fejer, *Ultrabroadband nonlinear optics in nanophotonic periodically poled lithium niobate waveguides,* Optica **7**, 40 (2020).

[114] Y. Hu, M. Yu, D. Zhu, N. Sinclair, A. Shams-Ansari, L. Shao, J. Holzgrafe, E. Puma, M. Zhang and M. Loncar, *Reconfigurable electro-optic frequency shifter,* arXiv preprint (2020), arXiv:2005.09621 .

[115] L. M. Duan and H. J. Kimble, *Scalable photonic quantum computation through cavity-assisted interactions,* Physical Review Letters **92**, 1 (2004).

[116] C. H. Bennett, G. Brassard, S. Popescu, B. Schumacher, J. A. Smolin and W. K. Wootters, *Purification of Noisy Entanglement and Faithful Teleportation via Noisy Channels,* Physical Review Letters **76**, 722 (1996).

10

[117] D. Deutsch, A. Ekert, R. Jozsa, C. Macchiavello, S. Popescu and A. Sanpera, *Quantum Privacy Amplification and the Security of Quantum Cryptography over Noisy Channels,* Physical Review Letters **77**, 2818 (1996).

[118] L. Jiang, J. S. Hodges, J. R. Maze, P. Maurer, J. M. Taylor, D. G. Cory, P. R. Hemmer, R. L. Walsworth, A. Yacoby, A. S. Zibrov and M. D. Lukin, *Repetitive readout of a single electronic spin via quantum logic with nuclear spin ancillae,* Science **326**, 267 (2009).

[119] D. Poulin, *Optimal and efficient decoding of concatenated quantum block codes,* Physical Review A **74**, 052333 (2006).

[120] J. Borregaard, H. Pichler, T. Schröder, M. D. Lukin, P. Lodahl and A. S. Sørensen, *One-Way Quantum Repeater Based on Near-Deterministic Photon-Emitter Interfaces,* Physical Review X **10**, 021071 (2020).

[121] M. K. Bhaskar, R. Riedinger, B. Machielse, D. S. Levonian, C. T. Nguyen, E. N. Knall, H. Park, D. Englund, M. Lončar, D. D. Sukachev and M. D. Lukin, *Experimental demonstration of memory-enhanced quantum communication,* Nature **580**, 60 (2020).

[122] A. Dahlberg, M. Skrzypczyk, T. Coopmans, L. Wubben, F. Rozpędek, M. Pompili, A. Stolk, P. Pawełczak, R. Knegjens, J. de Oliveira Filho, R. Hanson and S. Wehner, *A link layer protocol for quantum networks,* in *Proceedings of the ACM Special Interest Group on Data Communication* (ACM, New York, NY, USA, 2019) pp. 159–173.

[123] A. Pirker and W. Dür, *A quantum network stack and protocols for reliable entanglement-based networks,* New Journal of Physics **21**, 033003 (2019).

[124] D. Cuomo, M. Caleffi and A. S. Cacciapuoti, *Towards a distributed quantum computing ecosystem,* IET Quantum Communication **1**, 3 (2020).

[125] A. Broadbent, J. Fitzsimons and E. Kashefi, *Universal Blind Quantum Computation,* in *2009 50th Annual IEEE Symposium on Foundations of Computer Science* (IEEE, 2009) pp. 517–526.

[126] J. S. Hodges, N. Y. Yao, D. Maclaurin, C. Rastogi, M. D. Lukin and D. Englund, *Timekeeping with electron spin states in diamond,* Physical Review A **87**, 032118 (2013).

[127] P. Kómár, E. M. Kessler, M. Bishof, L. Jiang, A. S. Sørensen, J. Ye and M. D. Lukin, *A quantum network of clocks,* Nature Physics **10**, 582 (2014).

10

ACKNOWLEDGEMENTS

The last four years have been a tremendous journey, and I am very thankful for having been able to work on my PhD degree at the stimulating and fun place that is QuTech. None of this would have been possible without all the excellent people that I had the chance to interact and work with, and I would like to take the following pages to make an attempt at expressing my gratitude towards them.

First and foremost, I would like to thank my promoter, **Ronald Hanson**. Ronald, you are an exceptional scientist, team leader and visionary, and I think it is this rather unique combination of skills that are at the core of Team Diamond's success over the past years. You have given me countless opportunities, responsibility, and trust, right from the start of my journey in Delft. Attending a conference with you feels like going to a high school reunion, and has given me access to a vast network of experts in the field that have been crucial in tackling many challenges I encountered along the way. I am very grateful for all your advice and support over the last years, and I am looking forward to seeing the progress towards large-scale quantum networks that I have no doubt will come out of your lab.

Thank you to my co-promoter, **Tim Taminiau**, for the helpful advice and insightful discussions along the way. It has been impressive to witness your group expand, and the success you have had. I would also like to thank all other committee members for agreeing to evaluate this thesis. **Patrick Maletinsky**, several interactions with you and your group members have been very helpful along the way, and I will not forget your great hospitality during my visit in Basel. **Toeno van der Sar**, it has been great to expand the diamond fabrication team in Delft with you and your group members after your arrival in Delft. **Leo DiCarlo**, it feels like a circle closing with you serving on both my go / no go committee forming plans for my PhD, and now in the final graduation committee. I would also like to thank the other members of my committee, **Femius Koenderinck**, **Miriam Blaubooer**, and **Wolfgang Tittel** for agreeing to take part in my defense ceremony.

The work of Team Diamond is based upon a solid foundation of insights and tools developed by **previous generations of students and postdocs**, and I am glad I had the chance to meet many of them on several occasions, including at Ronald's Spinoza gathering, and the dinners at March meetings. Thank you for the great scientific and team environment that you have created.

When I arrived in Delft, I was lucky to find a close-to-working cavity setup in place. **Stefan Bogdanovic**, while we only overlapped briefly, it was great to learn about the cavity setup and, together with **Madelaine Liddy**, sample fabrication methods from you. Thanks for introducing me to the infamous Kloksteeg apartment. It was great to keep in touch during your next steps, and although working with you hasn't been possible due to COVID so far, I hope our paths will cross again at some point. **Suzanne van Dam**, it was great to witness your enthusiasm for your work, and to learn about the cavity setup from

you. Your structured approach to science has been great to learn from, and it was fun to discuss cavity physics with you. **Wouter Westerveld**, the documentation and functionality of your cavity vibration measurement code still amazes me to this day, and it is great to see you back in Delft, starting your own group. **Norbert Kalb**, it was great to learn from you about NV theory, operations and sample fabrication, and to dive into GST with you. I enjoyed our conversations on many different topics just as much, and I am still convinced that you should act as the founding director of the Norbert Kalb trust after your time as a software engineer. **Peter Humphreys**, thanks for the many interesting discussions about NV benchmarks and performance numbers, and for being a great housemate at Kloksteeg. **Maarten Degen**, my cleanroom mentor with the kites that are more often broken than not, I still vividly remember our first tries of fabricating mirrors with striplines - I think it is fair to say in hindsight that we didn't have a clue… I am glad I could introduce you to the man with the teeth in Rotterdam, thanks for this and many other fun times.

Matthew Weaver, your numerous contributions to this thesis are hard to put concisely, but let me try anyway: You arrived at a time when the samples just started to work out, and from that moment on we went on a great journey of trying to cavity enhance these NVs. I think it is fair to say that this proved to not always be easy, but as a team we managed to overcome the obstacles, and could finally demonstrate coherent cavity-enhanced NV emission. I admire your superb ability to do back-of-the-envelope theory calculations, and it was good to form a team to design a new cavity system and lab. Even though it did not work out in the end, it was equally fun to work on the NVNB project with you and the Groeblacher lab. Thanks for the extensive proof-reading of this thesis, for the many discussions about our next adventures, and for agreeing to be one of my paranymphs. Good luck at QPhox!

I had the privilege to supervise many bright bachelor and master students during their projects, and I have learnt a lot working with each of you: **Mark IJspeert**, my first student, your contributions to the diamond etching recipe were crucial to all work presented in my thesis. I had a lot of fun coming up with the auto-NV-search routine with you, and am still amazed by your dedication to science. The sight of you analyzing membrane fabrication results over some classical sonatas in the middle of the night, as well as suddenly talking to Takashi in fluent Japanese, will stick in my mind. **Jildou de Jong**, it was fun to have a closer look at the anti-reflection coated membranes, good luck with your startup. **Guus Evers**, your project turned out to be a tougher one than expected, but you never lost your smile and good mood. It was really fun having you on the team, good luck in your career as a data analyst. **Santi Sager la Ganga**, while I only supervised you for a few months, it was great to see your contributions to the automatization of cavity experiments. Thanks also for introducing me to some spanish culture. **Chris van Egmond**, it was great to start out the diamond photonic crystal fabrication in such a fun and relaxed way with you. I think you have left a lasting legacy in Delft. Enjoy your van.

During my time in Delft, I was lucky to be involved in the group-IV color center project from its very beginning, and I am happy to see its evolution into a full-sized project with a complete team. **Matteo Pasini**, you arrived right after we had gotten all basic spectroscopy equipment and samples, and have been instrumental in building up a measurement infrastructure and modifying the setup, and in taking the first SnV PLE

measurements in Delft. And thanks for your Italianness. **Hans Beukers**, it was great to see you decide to come back to our group for a PhD after finishing your medicine and physics studies. I especially enjoyed the entanglement schemes discussions with Matteo and you, and learnt a lot from it. **Nina Codreanou**, you have already developed a reputation for having magic hands in the cleanroom, and your dedication to nanofabrication work is truly impressive. You picked up all the diamond nanofabrication details in no time, and I am looking forward to many beautiful photonic crystal cavities in the future. I had a lot of fun working on the NVNB project with you. **Julia Brevoord**, while you just started, I have no doubts that you will be an excellent team member. Thanks for taking over the journal club organization. **Johannes Borregaard**, **Slava Dobrovitski** and **Fenglei Gu**, it has been very valuable to have your theoretical insights on the physics of group-IV color centers and entanglement schemes in our weekly meetings. **Lorenzo de Santis**, it was good to have you in our team during your COVID-instigated longer-than-expected stay in Delft.

When I started out my PhD in Delft, we had limited nanofabrication experience available in our group, and I am thankful for the veteran TNO fabrication team of Nick, Hans and Ruud for taking me under their wings initially. **Nick de Jong**, thanks for the fun visit in Basel, for knowing someone that can help with any obstacle one could face during their PhD within TNO, and for handling the depths of TNO budget codes. **Hans van den Berg**, thank you for teaching me basic dutch phrases, for bringing a relaxed atmosphere to our weekly meetings, and for fabricating many of the mirrors with striplines I used during my PhD. **Ruud Schmits**, thank you for managing the TNO part of the cleanroom, and for allowing me to use it. **Jasper Flipse**, you joined the team not long after, and provided very valuable support in the form of EDX measurements, fabrication assistance, and access to and handling of the micromanipulator. I am very grateful to **Richard Norte** for sharing all his knowledge about every aspect of the design and fabrication of nanophotonic structures with us after we had decided to fabricate photonic crystal cavities. **Simon Groeblacher**, you joined the team as one of Nina's supervisors, and have given invaluable hints on design and fabrication since. Thank you for sharing your group's photonic crystal cavity simulation files, they have been very helpful in designing optimized structures in diamond. I would also like to thank **Brecht Simon** — and very recently **Yufan Li** — for joining our diamond fabrication meetings, and for sharing their findings. It is very nice and useful to have all diamond fabrication knowledge in Delft bundled in one place and meeting, and it is great to see the tremendous growth in diamond nanofabrication expertise and experts in Delft over the last years.

It was very insightful to have active control experts in the persons of **Teun van den Dool**, **Gert Witvoet**, and **Robbert Voorhoeve** from TNO join our cavity efforts. It was fun to see you control our old cavity system with your computer that looked like it had been used to coordinate the first moon landing, and you provided great hints for the design of the new cavity system. **Tom Duivenvoorde**, thank you for all your help in making sure all the parts we wanted in the new system would actually fit in there, and thank you to the teams of **JPE** (**Bart van Bree** and **Huub Janssen**) and **Montana Instruments / LOT** (**Caleb Schreibeis**, **David Appel** and **Matt Ballinger**) for the numerous technical discussion on your systems, and your willingness to go the extra mile to make sure everything would fit together in our new system in the end. That new setup needed a place to be in, and

Hermans, it was great to overlap with you on the cavity project during my early time in Delft, and it has been fun to witness all the progress on quantum networks you were able to achieve in your PhD. Thank you for your help in translating my summary into Dutch. **Simon Baier**, thank you for the critical discussions on the cavity project, and for always having a smile on your face. **Arian Stolk**, while we have very different interpretations of the right taste in music, and of what forms a proper lunch, it was great to share this path with you, and hear your controversial opinions on many topics. **Kian van der Enden**, thanks for the tips about the stock market, and I wish you all the best on your quest to found a diamond startup. **Takashi Yamamoto**, thank you for all the diamonds you have been growing for us. **Marie-Christine Roehsner**, it is nice to see you come back to Delft for your postdoc, good luck with THE project, and with generating long-distance entanglement. **Sjoerd Loenen**, it was great to witness your thirst to understand every aspect of what we do in our groups. **Hans Bartling**, thanks for being (in the end not so) critical about my thesis cover design.

Thanks also to the newer members of the diamonds that I unfortunately did not have the chance to interact with so closely due to COVID: **Guido van de Stolpe**, **Damian Kwiatkowski**, **Benjamin Pingault**, and **Nicolas Demetriou**. I would also like to thank all MSc students that formed part of our group for the fun and insights they contributed during their stay in Delft: **Jesse Slim**, **Jaco Morits**, **Airat Galiullin**, **Romy van Es**, **Marianne Teng**, **Aletta Meinsma**, **Thomas Middleburg**, **Remon Berrevoets**, **Floris van der Gronden**, **Stein Faes**, **Asier Galicia**, **Annick Tepe**, **Kamiel Dankers**, **Lisa de Kluijver**, and **Laurens Feije**.

I would also like to take the opportunity to thank all the members of the technical staff at QuTech, TU Delft and TNO that are behind the smooth and steady running of this large ship, and make life as an experimental scientist as easy as can be. **Martin Eschen**, thank you for building and operating the laser ablation setup, for all your advice and help on optical systems design, and for many chats on any topic one can think of. **Mariya Sholkina**, thank you for your help in keeping our labs safe, and for helping with the building of various setups. The electronics wizards, **Raymond Schouten** and **Raymond Vermeulen**, thank you for teaching me the basics of electrical engineering, and for finding a solution to each and every problem I encountered. I am very grateful for the excellent technical staff of QuTech (in particular **Jason Mensingh**, **Olaf Benningshof**, **Mark Ammerlaan**, **Jelle Haanstra**, and **Remco Roeleveld**): you guys know a best practice / solution for every technical aspect of the work of an experimental physicist, and have helped me save many hours. The people at the reactor institute Delft, **Lennart van den Hengel**, **Wybe Roodhuyzen**, and **Marinus Hom**, for keeping that electron irradiation facility that looks like out of a 1960's Soviet movie up and running, and for always being very accommodating in all our electron irradiation requests. I am very grateful for the machine shop team around **Nico Alberts** for the many parts and sketches you made for us, and for always being willing to turn jobs around extra fast when our experiments were held up by a missing piece. I would like to thank all staff of the Kavli Nanolab Delft, in particular **Marc Zuiddam**, **Charles "Chuck" de Boer**, **Eugene Straver**, **Anja van Langen**, **Arnold van Run**, **Marco van der Krogt**, **Pauline Stevic**, and **Hozanna Miro**, for the many tips and tricks on nanofabrication, for keeping the cleanroom up and running at all times, and for being very positive even when we would break the etcher for the 5th

LIST OF PUBLICATIONS

10. *Directional excitation of a high-density magnon gas using coherently driven spin waves.*
    B. Simon, S. Kurdi, H. La, I. Bertelli, J. Carmiggelt, **M. Ruf**, N. de Jong, H. van den Berg, A. Katan, and T. van der Sar
    Nano Letters. Accepted for publication.

9. *Quantum networks based on color centers in diamond.*
    M. Ruf, N. Wan, H. Choi, D. Englund, and R. Hanson.
    Journal of Applied Physics 130, 070901 (2021). Invited perspective article.

8. *Resonant excitation and Purcell enhancement of coherent nitrogen-vacancy centers coupled to a Fabry-Perot micro-cavity.*
    M. Ruf*, M. J. Weaver*, S. B. van Dam, and R. Hanson.
    Physical Review Applied **15**, 024049 (2021). Featured as editor's suggestion.

7. *Flexure-tuned membrane-at-the-edge optomechanical system.*
    V. Dumont, S. Bernard, C. Reinhardt, A. Kato, **M. Ruf**, and J. Sankey.
    Optics Express **27**, 18 (2019).

6. *Optically coherent nitrogen-vacancy centers in micrometer-thin etched diamond membranes.*
    M. Ruf*, M. IJspeert*, S. B. van Dam, N. de Jong, H. van den Berg, G. Evers, and R. Hanson.
    Nano Letters **19**, 3987-3992 (2019).

5. *Near-term quantum-repeater experiments with nitrogen-vacancy centers: Overcoming the limitations of direct transmission.*
    F. Rozpędek*, R. Yehia*, K. Goodenough*, **M. Ruf**, P. C. Humphreys, R. Hanson, S. Wehner and D. Elkouss.
    Physical Review A **99**, 052330 (2019).

4. *Optical coherence of diamond NV centers formed by ion implantation and annealing.*
    S. B. van Dam*, M. Walsh*, M. J. Degen, E. Bersin, S. Mouradian, A. Galiullin, **M. Ruf**, M. IJspeert, T. H. Taminiau, R. Hanson, and D. Englund.
    Physical Review B **99**, 161203(R) (2019). Featured as editor's suggestion.

3. *Optimal design of diamond-air microcavities for quantum networks using an analytical approach.*
    S. B. van Dam, **M. Ruf**, and R. Hanson.
    New Journal of Physics **20**, 115004 (2018).

2. *High mechanical bandwidth fiber-coupled Fabry-Perot cavity.*
    E. Janitz, **M. Ruf**, Y. Fontana, J. Sankey, and L. Childress.
    Optics Express **25**, 20932 (2017).

1. *Fabry-Perot microcavity for diamond-based photonics.*
    E. Janitz, **M. Ruf**, M. Dimock, A. Bourassa, J. Sankey, and L. Childress.
    Physical Review A **92**, 043844 (2015).

---

*Equally contributing authors

MAXIMILIAN THOMAS RUF

July 2nd, 1992
Santa Clara, California
United States of America

2002 - 2011	Secondary school, Heinrich-Schliemann Gymnasium, Fürth, Germany
2011 - 2014	BSc in Physics, Ludwig-Maximilians-Universität, Munich, Germany Thesis: *"CO$_2$ laser microfabrication of optical fibers"* Thesis research undertaken at Quantum Optics & Sensing Lab, McGill University, Montreal, Canada Advisors: Prof. J.C. Sankey (Montreal) / Dr. D. Hunger (Munich)
2013	Research Internship, McGill University, Montreal, Canada. Scholarship of the German Academic Exchange Service (DAAD) Group: Quantum Optics & Sensing Lab Advisor: Prof. J.C. Sankey
2014 - 2016	Master of Science in Physics, McGill University, Montreal, Canada Thesis: *"Fiber-based Fabry-Perot microcavities"* Group: Quantum Optics & Sensing Lab Advisors: Prof. J.C. Sankey and Prof. L. Childress
2017 - 2021	Doctorate in experimental Physics, Delft University of Technology, Delft, The Netherlands. Thesis: *"Cavity-enhanced quantum network nodes in diamond"* Group: QuTech and Kavli Institute of Nanoscience Advisor: Prof. R. Hanson